Using Equalizers to Increase Data Rates in Organic Photonic Devices for Visible Light Communications Systems

Paul Anthony Haigh

Faculty of Engineering and Environment

Northumbria University

This dissertation is submitted for the degree of

Doctor of Philosophy

July 2014

To you, I dedicate this thesis…

Declaration

I hereby declare that except where specific reference is made to the work of others, the contents of this thesis are original and have not been submitted in whole or in part for consideration for any other degree or qualification in this, or any other university.

Paul Anthony Haigh
July 2014

Acknowledgements

Firstly, I would like to offer apologies in case I have missed anyone, this was certainly not intentional.

Secondly, before I move on to the individuals that have helped to shape my PhD and made my studies such an enjoyable experience, I would like to acknowledge all financial support received, including a full university PhD scholarship and the multiple IEEE and university grants that I have received for conference attendance and journal charges. I would also like to acknowledge the financial support of the Hong Kong Polytechnic University for my secondment there. Furthermore, I would like to gratefully acknowledge the financial support of the European Union IC1101 COST program and the Technical University of Graz, Austria for approving my short term scientific mission and supporting it financially. Finally I must acknowledge the support given to me by all of the research students, staff and administrators that I came into contact during my PhD and also during my spell as a visiting researcher at University College London.

The first person I would like to thank is my principle supervisor, Fary Ghassemlooy who has carefully guided me from a time before I even started my PhD, to the very end and beyond. Fary offered his full confidence, enthusiasm, support and belief in me at every turn and this is reflected in the numerous collaborations that I established through my work. Without Fary I would not have had the opportunity to study for my PhD at such a young age and I thoroughly understand the advantages and privileges from which I have benefited as a direct result of Fary's confidence in me. Thank you sincerely, Fary.

Secondly, Ioannis Papakonstantinou has repeatedly gone above and beyond what is necessary to be an excellent supervisor; usually at the expense of his own time. I would like to note the outstanding support that you have given me over the years, including our time together at CERN. Furthermore, the year I spent as a visiting researcher in your research group at University College London (UCL) were some of the most productive days of my PhD. This was an exceptional platform to achieve some of the results shown in this thesis. Thank you for every opportunity you have given to me.

Thanks to Hoa Le Minh for supporting me through this work, especially at the early stages of my PhD where you very elegantly helped to point me in the direction of visible

light communications and offer substantial support throughout all of the stages of the work.

To Sujan Rajbhandari, University of Oxford, thank you for being such a close friend and colleague of mine throughout this work. I would suggest that without our time together spent in the laboratories, this work would have been substantially less enjoyable. I look forward to a continuation of this in the future.

I am indebted to Sandro Francesco Tedde, Francesco Arca and Oliver Hayden of Corporate Technology, Siemens AG, Erlangen, Germany. I must thank each of you individually not only for the production of the organic photodetectors used in several chapters of this work and the continuous support over the duration of my PhD, but also for the individual lessons that you have all taught me. I have thoroughly enjoyed our collaboration and look forward to future endeavours developing this technology together.

In my PhD I was able to collaborate closely with a number of colleagues, but none was more productive than my work with Francesco Bausi working with organic polymer diodes produced in the Physics department of UCL. I have thoroughly enjoyed our work together in our respective laboratories, and particularly the personal aspect of this research and getting to know you very well, which has been my privilege. This research was made possible by Franco Cacialli, who helped to establish and support this work, whilst delivering his insight and knowledge to enable our rapid progress. I also look forward to our continued collaboration.

I offer special thanks to Lu Chao and Erich Leitgeb of Hong Kong Polytechnic University and the Technical University of Graz, respectively who both supported my secondment into their groups at various stages of my PhD. I had a very good time both academically and socially in both Hong Kong and Graz and look forward to meeting you again in the future.

Further thanks to Wasiu Popoola of Glasgow Caledonian University, for his excellent input to improve the quality of work in the second half of my PhD work. I am sure that our work together will continue as productively as ever in the future.

I would like to offer sincere thanks to my internal and external examiners, Dr Xuewu Dai and Professor Izzat Darwazeh, respectively, for giving me a very thorough and professional examination platform that I ultimately enjoyed very much.

Sincere thanks must go to Andrew Bradley, to whom I owe a tremendous debt of gratitude. You spent considerable time helping me in a hard time, and it is a direct result of that investment that I have been able to come this far and complete this work, so thank you.

To James Savage, thank you very much for distracting me from the work at every opportunity, and for honouring me by making me your best man.

Thanks to my parents and Helene, you already know how much I appreciate everything you have done for me.

Abstract

This thesis proposes to marry two separate technologies together. The first technology is that of visible light communications (VLC), and the second is small molecule and polymer organic photonic devices. These two technologies both offer outstanding potential in their respective fields of information communications and optoelectronics, with both being proposed as two of the most important technologies about to emerge in the next decades by their respective research communities. As such, it is imperative to investigate and analyse the performance of organic photonic devices in the context of VLC broadcasting networks. There have been no experimental results in the literature reporting on organic-VLC systems until the work proposed in this thesis and therefore the focus is on improving transmission speeds.

The reason for this is that organic devices typically have bandwidths that are orders of magnitude smaller than inorganic devices, and hence improving the transmission speed to similar levels is the foremost challenge available to address. Therefore this work investigates four separate links to find the maximum capacity possible in each case:

1. A small molecule organic light emitting diode (OLED) as the transmitter, with an inorganic photodetector (PD) as the receiver.
2. An inorganic LED as the transmitter, with an organic PD (OPD) as the receiver.
3. An SMOLED as the transmitter, with an OPD as the receiver.
4. A polymer LED (PLED) as the transmitter, with an inorganic PD as the receiver.

The modulation schemes focused on were non-return-to-zero (NRZ) on-off keying (OOK) and pulse position modulation (PPM). The improvement in transmission speed using the artificial neural network (ANN) (links 1 — 3) and least mean squares (link 4) equalizer is presented here in terms of bit error rate (BER) performance in comparison to the unequalized case.

The key results presented in this work show that in spite of the relatively low bandwidths (hundreds of kHz), transmission speeds in the region of Mb/s can be comfortably achieved

using equalization techniques. The maximum transmission speeds demonstrated in this work are 2.7, 3.75, 1.15 and 10 Mb/s for links 1, 2, 3 and 4 in Chapters 4, 5, 6 and 7, respectively.

Table of contents

List of figures

List of tables

Chapter 1

Introduction

1.1 Introduction to Visible Light Communications

Due to the exponentially growing demand for data and bandwidth by the end-users, researchers are increasingly turning to optical communication technologies due to their broad bandwidths, licence free spectra and low implementation costs. The current UK radio frequency (RF) allocation chart is depicted in Fig. 1.1 (from [14]), which shows substantial overcrowding, leading to premium license fees and highly restricted bandwidth.

Optical wireless communications (OWC) is a subset under the wider optical communication umbrella; which also consists of infra-red fibre, visible light communications (VLC), free-space communication (FSO) technologies [15]. Further communications technologies include microwave technologies such as radar and RF as mentioned. Their spectrum allocations are shown in Fig. 1.2 (adopted from adopted from [16]), where the visible wavelengths with a bandwidth of $\sim$ 400 THz are highlighted; around 10,000 times higher than the RF bandwidth.

OWC operates in both the indoor and outdoor environments; with the indoor split into three categories based on their operating wavelength; ultra-violet, visible light and infrared (IR) while the outdoor environment is colloquially known as FSO and mainly works in the IR region where the major challenge remains to be fog and other weather impediments [4]. Indoor communications carried on the visible wavelengths (380 — 780 nm) is known as VLC and is a relatively new technology first proposed roughly a decade prior to this thesis. VLC was first proposed as an alternative to indoor IR access technologies [17, 18] with a dual purpose of data communication and room illumination; transmission by means of intensity modulation and direct detection (IM/DD) of a light-emitting diode (LED) and photodetector(s) (PD), respectively. Development of the VLC technology was encouraged by rapid developments in gallium nitride (GaN) blue LED technologies that can be con-

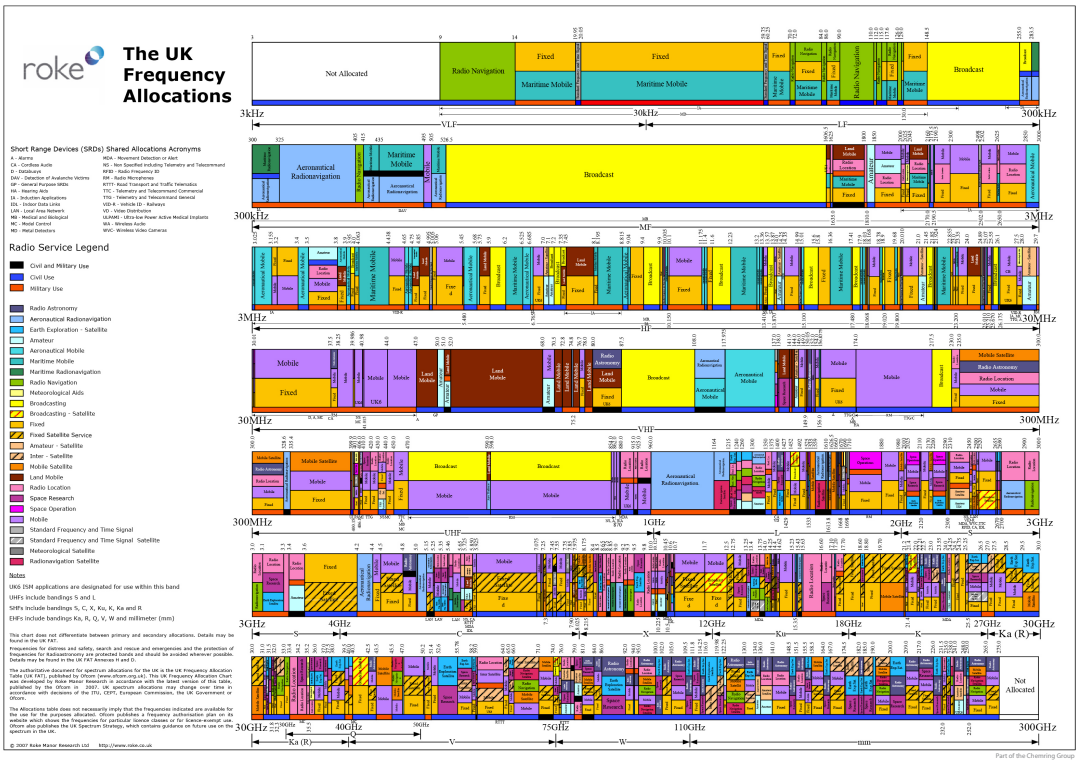

Fig. 1.1 UK radio frequency spectrum showing significant overcrowding

verted to emit white light by coating the photoactive area with a yellowish cerium doped yttrium aluminium garnet (Ce:YAG) phosphor, known as white phosphor LEDs (WPLEDs) [19–21]. The first reports of VLC using WPLEDs emerged from Japan via a series of conference publications [22–25] and it took several years before the first article was published [26]. Following this, the idea was popularized and the visible light communications consortium (VLCC) was established in Asia (i.e. Japan) in 2003, allowing technical discussion and collaboration between developers and for researchers working in the field. This lead to the standardisation of VLC by the Institute of Electrical and Electronics Engineers (IEEE), namely IEEE 802.15.7 in 2012 [27] which outlines the individual layer standards required for industrial implementation.

Data communications is the primary function of VLC and it is necessary to provide full connectivity regardless of the illumination level, which can easily be set using a direct current (DC) bias value. This leads to a further challenge considering the linearity of the LED electro-optic response; signal distortion can occur if the device is improperly biased outside of the linear region while the SNR is also degraded if the received optical power is low. Most of the research aiming to tackle the dimming problem has focused on the

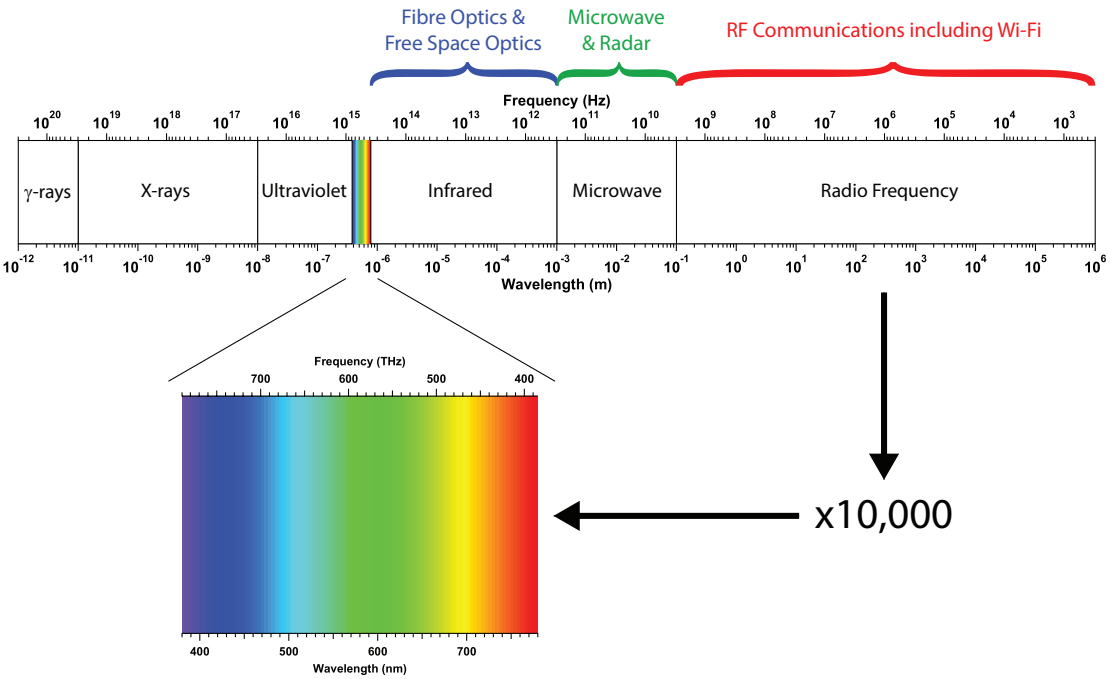

Fig. 1.2 Visible light in the electromagnetic spectrum in the context of other communications technologies

modulation format selected. Pulse width modulation (PWM) is the standard way to control the average optical power output; by controlling the duty-cycle so that the required optical power level can easily be reached. The PWM signal does not carry any information though, and modulation schemes such as OOK, PPM and discrete multi-tone (DMT) have been added to the PWM signal to maintain information transmission at various illumination levels [28–36].

As mentioned the most popular type of LEDs used in VLC systems are WPLEDs because of their simplicity, high optical power and reasonable bandwidth in the MHz region after phosphor conversion. At the receiver, it is possible to undo the effect of the phosphor and remove the yellowish wavelengths to recover the faster response of the GaN diode using a short wavelength pass filter at the receiver (known colloquially as a blue filter). This causes a significant challenge in VLC in terms of how to drive up the transmission speed, which has attracted widespread attention within the research community at large. The first significant reports of high speed VLC systems using WPLEDs emerged based on introducing resonant circuits matched to the frequency response of the transmitter in order to expand the bandwidth and hence the transmission speed. The resonant drive circuit consists of three sub-drivers each with dissimilar resonant frequencies for equalizing different regions of the system frequency response. Using a single WPLED (2.5 MHz raw bandwidth) and OOK, an

equalized bandwidth of 40 MHz was achieved leading to a transmission speed of 80 Mb/s at a BER of 10^{-6} [37]. In [38] this scheme was extended by introducing a 4×4 matrix of 16 WPLEDs with a drive circuit that resonates with the aggregate frequency response of the WPLEDs. However the bandwidth achieved with such a configuration was reduced to 20 MHz with a transmission speed of 40 Mb/s, or a reduction by half in comparison to [37]. The reason for this reduction is not stated in either report; however the most likely cause for this is that the resonant matching in the single WPLED is much better than the multiple WPLEDs, thus offering a higher bandwidth. On the other hand, in [38] it is shown that by introducing multiple WPLEDs the distance can be substantially improved to 0.5 m, compared to a back-to-back link scenario in [37].

Subsequently, a 100 Mb/s link (BER of 10^{-9}) based on a WPLED was reported in [39] that offered a reduction in complexity over [37, 38] by removing the resonant circuits at the transmitter. Instead, a single resistor-capacitor (RC) analogue high pass filter (HPF) was introduced at the receiver [39]. The raw bandwidth of the WPLED remains at 2.5 MHz, however in [39] a blue filter was introduced resulting in bandwidth of 14 MHz at the cost of a 20 dB power penalty (at low frequencies). Using the HPF a bandwidth extension up to 50 MHz is recorded with a transmission speed of 100 Mb/s [39]. However, there is a major drawback using HPF equalization and that is the introduction of the baseline wander (BLW) phenomenon, which occurs when the low-frequency components of a baseband modulation format are attenuated by the coupling capacitors and HPFs. In [39] the BLW effect is not investigated. Note that with a link using HPF and a simple threshold detector it would not be possible to recover the low frequency component including the DC level. BLW has been thoroughly investigated in the literature [40–42] and is commonly treated as random noise with a Gaussian distributed noise variance. The low frequency power penalty increases exponentially with increasing cut-on frequency [40].

Each of the passive equalization methods discussed here are not without drawbacks. The performance of each method is dependent on each of the components in the circuits and WPLED. Therefore a generalized solution cannot exist as each WPLED will have slightly different characteristics while WPLEDs from different manufacturers will vary significantly, thus this solution is not optimum.

Alterative modulation formats can protect against BLW depending on the spectral allocation of the information. For instance PPM has a low spectral content at DC that decreases with an increasing order of bits per symbol. However, PPM has not emerged as a popular modulation format for the highly bandlimited VLC because the bandwidth requirement increases exponentially with the modulation order and is at least twice that of OOK in the best case [43], thus undesirably offering a low spectral efficiency. An alternative frequency based

modulation is DMT modulation, the basis of which is the parallel transmission of multiple orthogonally spaced subcarriers (commonly called 'tones' in RF technologies) that allows high order complex modulations such as quadrature amplitude modulation (QAM). Complex modulation formats such as QAM are desirable because they have the same power and bandwidth requirements as pulse amplitude modulation (PAM) except with a spectral efficiency that is M times higher, where M is the modulation order [44]. Further, with DMT it is possible to load selected subcarriers with redundant information (i.e. those spaced around DC and the low frequencies), effectively nullifying the effect of BLW. In [45] a 1 Gb/s link with a WPLED is implemented based on DMT modulation, offering a tenfold improvement over [39], albeit with a higher white bandwidth of 30 MHz; around ten times higher than the blue filtered bandwidth in [39]. This is a significant aspect because it meant that there was no need for any blue filtering due to the additional power penalty it would incur on the system frequency response and SNR. In order to improve the transmission speed further, two additional techniques were used: firstly adaptive bit loading was implemented. Adaptive bit loading consists of recording the SNR measurement of the system (i.e. the subtraction of the frequency response (dB) from the noise floor (dB)) and allocating a given number of bits per symbol depending on the measured SNR. For instance, the theoretical relationship between SNR and the error vector magnitude (EVM) for several orders of QAM can be found in [46] and used to decide the appropriate SNR threshold levels. Doing this means that the individual subcarriers are modulated by constellations that they have the required SNR to transmit, thus avoiding introducing errors into the system and allowing higher throughput. The second technique is adaptive power loading, which can be thought of as a very similar process as RC HPF equalization because it aims to distribute power across the spectrum by measuring the received power of each subcarrier and feeding back the information to the transmitter. The transmitter than makes a decision about which subcarriers to redistribute power from based upon the SNR availability and requirements.

WPLEDs are not the only common method of producing white light for VLC links. Another method is based on combining individual red, green and blue LEDs (RGBLEDs) as illustrated in Fig. 1.3.

While WPLEDs are a more simplistic choice, RGBLEDs clearly offer at least two significant advantages for communications including higher system capacity due to the unrestricted bandwidths of the individual components in the triplet and the potential for parallel transmission using wavelength division multiplexing (WDM). RGBLEDs have a downside, however and that is in terms of lighting, it is very difficult to provide a constant white colour balance since the individual LEDs are switched on at arbitrary and uncorrelated intervals. No work in VLC using RGBLEDs has addressed this challenge at the time of writing.

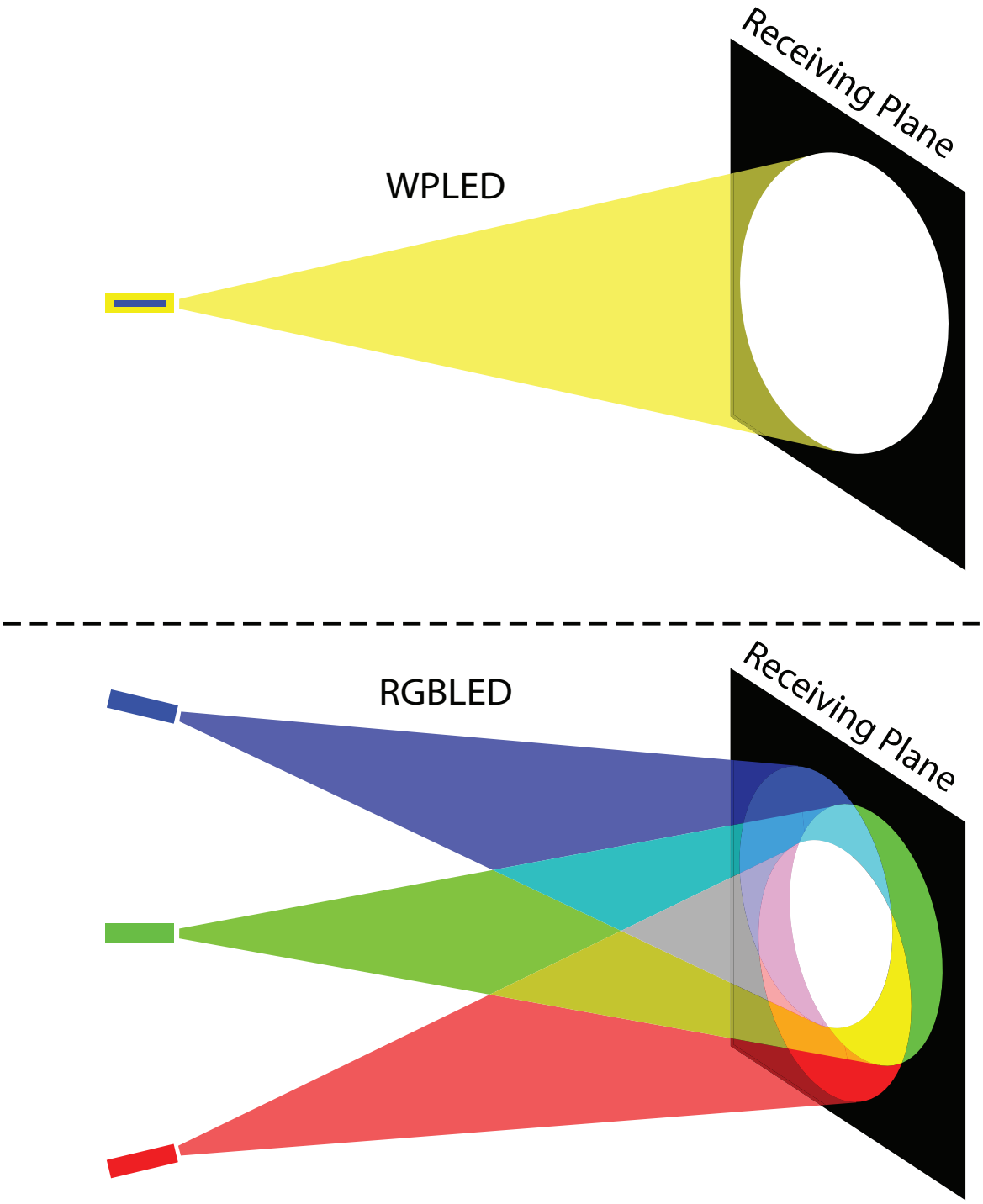

Fig. 1.3 White light generation from WPLED and RGBLED link topologies; note that the beam profile is indicated in yellow for WPLED for enhanced visibility but in reality the emission is white

A comparison of the optical spectra of an RGBLED and a WPLED is shown in Fig. 1.4. The RGBLED has peaks at 450 (B), 520 (G) and 635 (R) nm. In WPLEDs, the GaN emission occurs at 445 nm while the Ce:YAG phosphor has a wide spectral emission peaking around 555 nm (green).

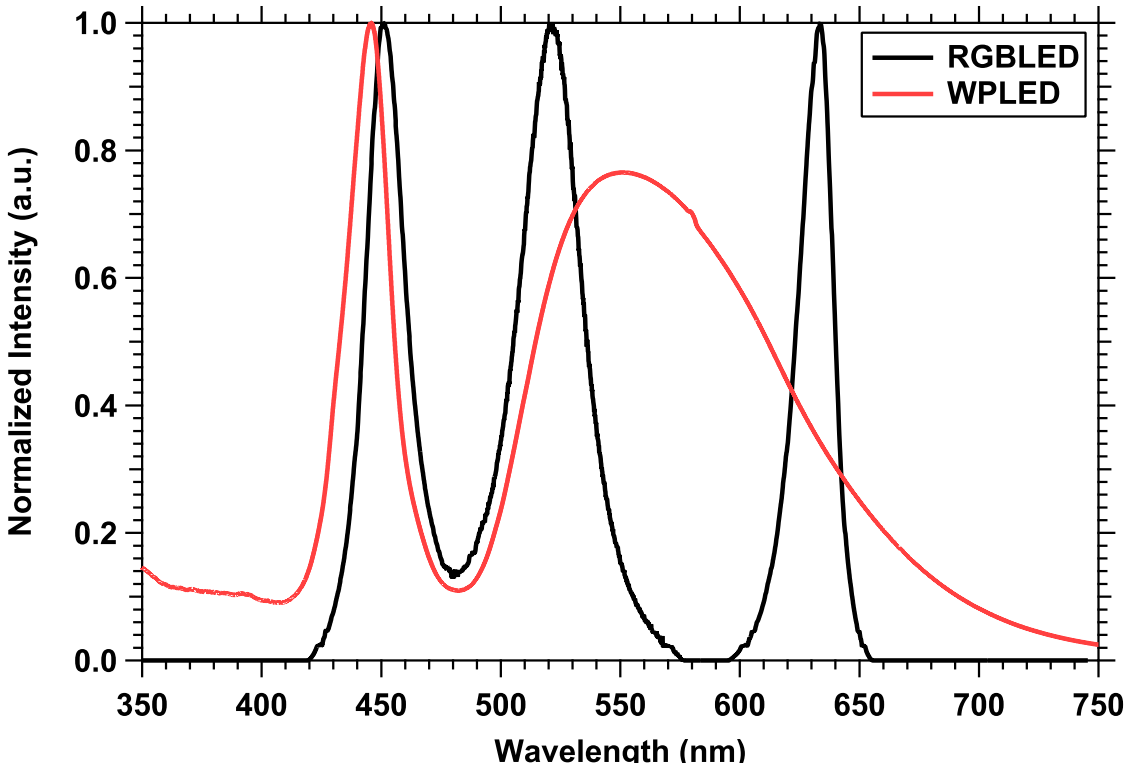

Fig. 1.4 Optical spectra of an RGBLED (data from [1]) and an WPLED (measured using ThorLabs CCS2000)

Research using RGBLEDs has simply expanded on the 1 Gb/s DMT link reported in [45]. The adaptive DMT modulation format is extended onto the three separate wavelengths, resulting in a gross transmission speed of 3.4 Gb/s [47], an approximate increase of threefold as expected. The downside of such an adaptive DMT modulation format is the requirement to feed back the system frequency response to the transmitter in order to establish how to distribute the bits and power. VLC is inherently a half-duplex technology considering the typical aesthetic layout of home and office solid state light (SSL) systems and there has been strong disagreement in the VLC community about a feedback medium and a lack of reports proposing a fully duplex link. There are strong arguments that an RF antenna is suitable due to the lower capacity of the uplink, whilst there is also a case for using an IR uplink. Both have built-in problems and as such neither provides a clear case for implementation. Thus using a modulation format that heavily depends on a feedback channel is not the optimum

case and alternatives should be explored.

Equalization is a well-established subject that has been extensively studied and is widely covered in the literature [48]. Equalizers can undo the effects of inter-symbol interference (ISI) caused by data transmission outside of the modulation bandwidth. No technical details are given in this introduction as they are covered in Chapter 3. There are two broad types of equalizer; analogue and digital which consist of different types of equalizer as illustrated in Fig. 1.5.

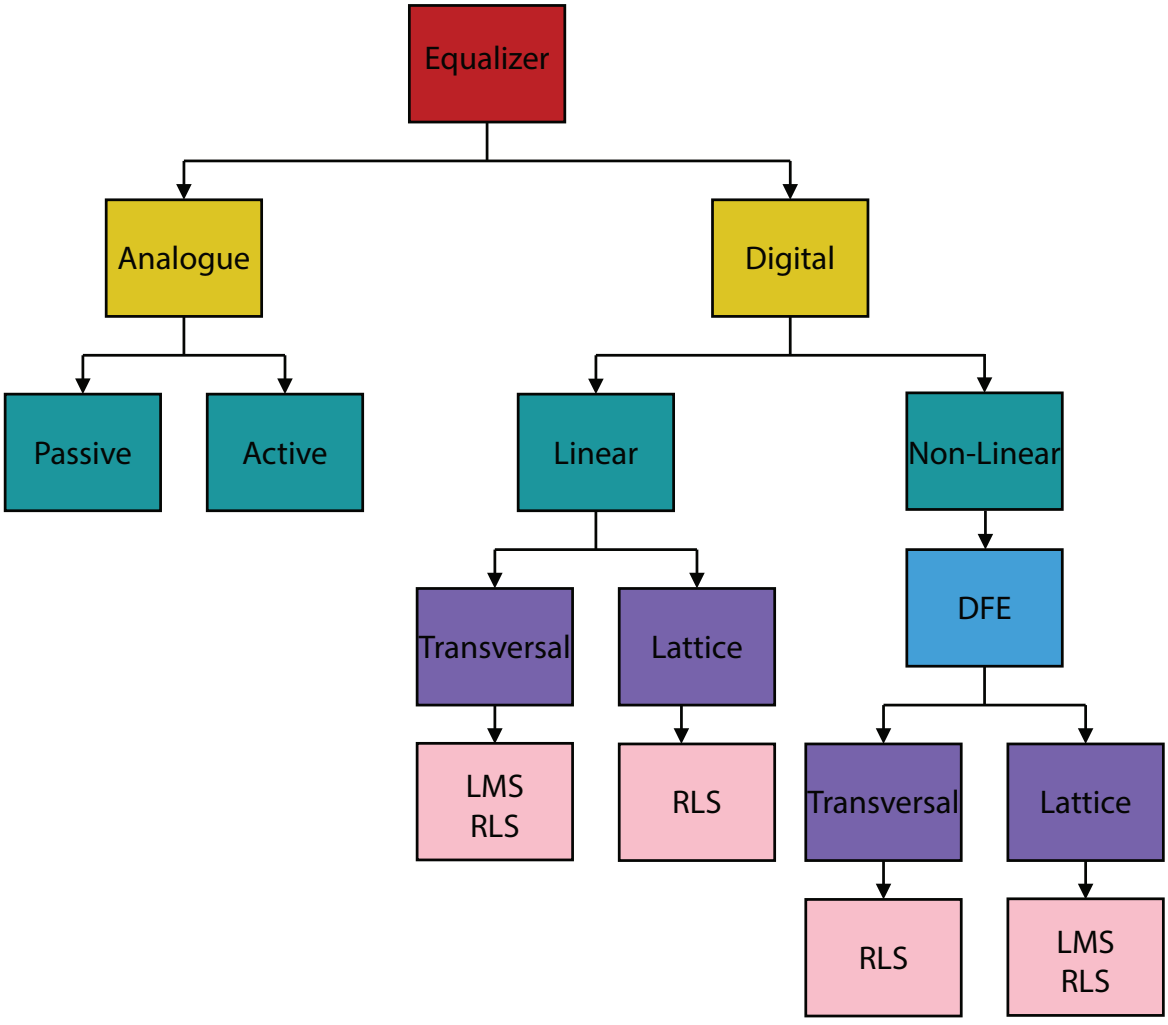

Fig. 1.5 List of the most popular equalizers, adapted from [2]

Analogue equalizers consist of passive components such as resistors, capacitors and inductors as already discussed; or active components that add power into the system such as operational amplifiers. Passive analogue equalizers are low in complexity but typically offer a limited improvement over the modulation bandwidth due to the associated power penalties. Demonstrations of active analogue equalizers have only recently started to emerge; in

[49] the first results are reported. The concept proposed is the same as the passive equalizers except using an active filter. Thus it is possible to introduce additional power into the frequency response, flattening the overall response whilst avoiding the attenuation of the low frequencies. The transmission speed achieved with active equalization is 300 Mb/s at a BER of 10^{-9} [49].

Digital equalizers can be separated into linear and non-linear methods. Linear equalizers are less complex than non-linear equalizers at the cost of reduced BER performance (but more complex than the analogue with better BER performance). Digital equalizers work on the principle of removing ISI by calculating the contribution of energy in the current symbol from previously transmitted symbols. Digital equalizers can make this estimation by comparing a known data sequence stored in memory with the received version of the same sequence at the start of any transmission sequence, thus not requiring a feedback path as in adaptive DMT. This is known as training and the estimation is made by updating a set of equalizer coefficients using an iterative method.

There is one additional type of equalizer that is not shown in Fig. 1.5 because it operates in a different way. That is the ANN, which can be thought of as classifiers as opposed to a traditional equalizer because they classify a signal based on highly non-linear boundaries which are formed by an adaptive learning sequence.

Bearing in mind that OOK is the most commonly used modulation scheme in VLC and is compatible with digital equalizers, there is a noticeable lack of research in this area and the only major reports are based on the analogue equalization as previously discussed. An increase in performance can be expected using digital equalizers but there are no reports to provide any further results for a WPLED VLC system aside from [50]. Further, there are no reports that provide any comparison between an adaptive DMT link and OOK with equalization, or an RGBLED with digital equalization.

A substantial problem with using either WPLEDs or RGBLEDs as the transmitter in VLC systems is scalability. LEDs produced with metal alloys such as GaN by epitaxial thermal evaporation methods result in brittle crystals that cannot easily be fashioned into large area panels which are desirable for VLC, SSL and other applications such as screens and displays. One possible solution to this is organic optoelectronic devices as a direct replacement for WPLEDs and RGBLEDs, which offer low heat dissipation, mechanical flexibility, cheap production and arbitrarily large photoactive areas. Organic electroluminescent polymers were first discovered by Burroughes in 1990 [51] and are now commonly known as polymer LEDs (PLEDs). Alternatively, small molecule based organic electroluminescent devices known as small molecule organic LEDs (SMOLEDs) were proposed prior to PLEDs in 1987 by Tang and VanSlyke [52]. Aside from the length of molecules used in the

semiconductor, PLEDs are more complex, based on long chains of π–conjugated polymers, the main difference between PLEDs and SMOLEDs is the processing method. SMOLEDs are generally thermal-vacuum evaporated while PLEDs can be solution processed which is the cheaper (and thus more desirable) method.

Organic devices are based on thin film technology; the general structure for a photonic device is two or more organic semiconductor materials sandwiched by oppositely polarized electrodes. The most important manufacturing processes are solution processing [53], spray coating [54], doctor blading [55], spin coating [56] and inkjet printing [57] all of which are wet processed techniques that can offer potentially low mass production in the future. The total stack thickness for any OLED (either SMOLED or PLED) produced with any manufacturing process is between 100 — 200 nm, which is a very exciting prospect for future displays, considering the common desire to miniaturise electronics as far as possible.

Aside from the transmitter, the receiver in VLC systems is also of the utmost importance and is generally taken to be an individual positive-intrinsic-negative (PIN) Si PD [39], or less commonly, a Si avalanche PD (APD) [58]. Si PDs have responsivity in the range of 200 — 1100 nm and are very well established in free space optical communications operating in the NIR wavelengths, where they offer high responsivity [4]. On the other hand, the responsivity is very low in the visible range which is undesirable for VLC links where the information is mostly carried on the blue wavelengths. Thus, additional optical power must be added in order to achieve a useful signal voltage level. It is not surprising that a dedicated material has not emerged for high speed, high responsivity PDs in the visible range because previously no communications technology has utilized this region of the electromagnetic spectrum. Although solar cells typically operate in the visible region with reasonable efficiencies (refer to Fig. 1.6), they harvest the DC power and as such there hasn't been any investigation into improving the bandwidths.

As most of the focus in VLC systems is focused on the transmitter and not on the receiver, in spite of the drawbacks mentioned in the previous paragraph, OPDs (polymer-based) have emerged as an attractive prospect for VLC systems not only due to the low materials costs ($<$ £0.20/cm^2 [59]) but also due to the fact that OPDs can be spray deposited with higher efficiencies than Si [54] to different photoactive area devices. Furthermore, due to the band gap energies of conjugated polymers (1 — 4 eV, encompassing the entire visible range); OPDs can be tailored for visible light whilst rejecting the entire IR region by careful selection of the semiconductor materials.

The organic electronics sector is now large enough to be considered as a separate industry (the so-called printed electronics industry) to the Si electronics industry. According to market forecasters IDTechEx, the printed electronics industry will be valued at $330 billion

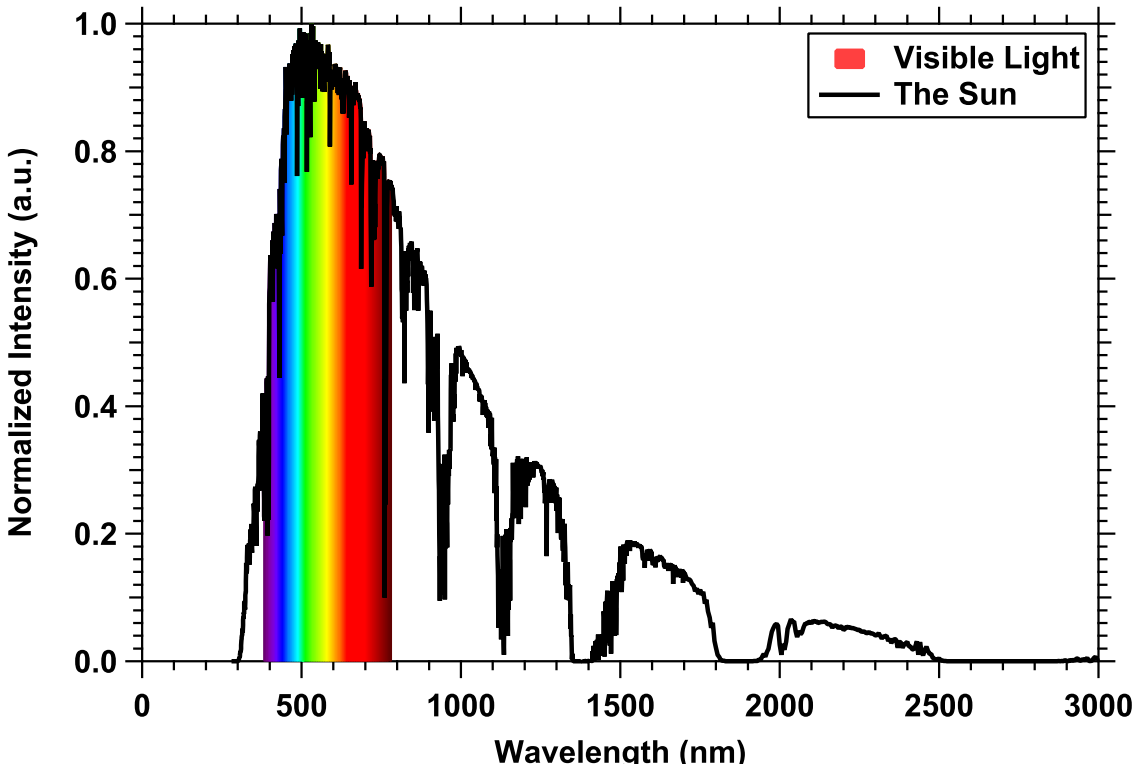

Fig. 1.6 The received solar spectrum with highlighted visible region; data obtained from [3]

as early as 2027 - more than the gross value of the Si market today ($225 billion) [60].

Organics are not without their disadvantages and challenges. The development of inorganics has been undertaken for a number of decades and homogenous devices can be produced that are almost free from impurities and imperfections. This is not the case for organics; every manufacturing process without exception introduces impurities and defects that can lead to charge traps and short circuits. Charge traps are poised to emerge as an extremely important consideration in OVLC systems as the available device bandwidth is directly related to filling traps with charge carriers [61]. Furthermore the charge transport mobility of organics is around three orders of magnitude lower than amorphous Si [59]. It should be noted that this is due to highly disordered polymer crystallinity [62] which severely restricts the movement of charge carriers through the device, causing a bandwidth limitation. This is not the same problem as the Ce:YAG phosphor limiting device bandwidths because that problem can easily be solved using a short pass optical filter. As such this thesis takes on this challenge with the aim of firstly introducing organic VLC (OVLC) systems and subsequently achieving a high capacity using electronic equalization techniques.

Further, it is well known that inorganic LEDs are inherently non-linear devices and this is reflected in their optical power – drive current – voltage (L-I-V) relationships. OLEDs

exhibit the same non-linearity and the candidate proposed a model for an SMOLED in [63].

The idea of organic photonics for communications had been conceived previously and the first postulation of organic photonic devices for a communications system came in 1992 [64] on organic optical fibre communications. A summary of potential organic communications systems was outlined in [65], which raises some very important points. Perhaps the most crucial point is that organics should not be taken as a direct replacement for inorganic devices, as such a transition will never occur due to the strong placement of inorganics in the market and the cost of switching. On the other hand, [65] reports that organics should be seen as a strong alternative technology for use in markets that inorganics cannot penetrate. A good example of this would be an OVLC system where thin films and large area panels are extremely desirable such as deployment in laptop computers, mobile phones and multifunctional displays.

To date, research and development in organic communications systems has been limited even though reports are starting to emerge that allude to the prospect of organic optical communications systems but they do not explicitly test important performance metrics such as BER [65–70]. The root of this could be down to the fact that the device structure has not yet been optimized. For example the semiconductor interlayer influences the device wavelength and charge transport characteristics, while the layer structure and organization can affect efficiency characteristics [71, 72].

1.2 Problem Statement

As introduced in the previous section, low charge transport mobility is a serious impediment to high capacity OVLC systems because the devices simply cannot offer similar bandwidths to IVLC systems. On the other hand, organics offer a variety of advantages that are ideally suited to the applications of VLC; first and foremost the materials costs are extremely low (£0.20/cm^2 for P3HT:PCBM) and can be dissolved into solvents that allow screen printing or spray deposition to produce large diodes that are simply impossible using inorganics.

As such, in this thesis organic devices are worthy of investigation as the transmitter and receiver for VLC systems. A number of transmitter/receiver configurations are tested:

- A small molecule/polymer OLED as the transmitter and a Si PD as receiver.
- A WPLED as the transmitter and an OPD as the receiver.
- A completely OVLC system.

By adopting these configurations the maximum individual and collective potential of organic devices can be found for VLC. As mentioned, the bandwidths of organics are significantly

lower than their inorganic counterparts due to lower charge transport mobility, thus when used for data communications the achievable data rates are highly restricted. If the transmission speed exceeds the modulation bandwidth of the system, ISI where the energy of the previous pulses is carried over to the next pulses can be introduced into the system. Subsequently, equalization techniques are implemented in order to find the maximum bit rates for each topology. The overall results of each experiment will offer a first perspective on whether or not organic photonic devices are suitable for VLC links using state-of-the-art components.

1.3 Research Aims and Objectives

This work introduces a new domain to the VLC technology by using organic photonic components as the transmitter and receiver, respectively. This is an important development because of the cost reduction, large photoactive areas and increasing popularity of thin film devices in modern technologies, all of which are important for SSL and VLC equally. Additionally, establishing the OVLC domain has prompted research and developments from many research groups throughout the world that are starting to build on the results reported in this thesis, indicating the impact of this work.

The major challenge in using organic components as the optoelectronic devices in VLC systems is the low charge transport mobility that leads to slow spontaneous recombination of holes/electrons in the semiconductor and hence slow extinction of the luminescence and low transmission bandwidths. Therefore a significant challenge remains to increase the transmission speeds in OVLC systems. As a result three main themes will occur in this thesis:

- Three OVLC topologies are proposed, experimentally investigated and demonstrated for the first time:
  - VLC with an SMOLED as the transmitter and a Si PD as receiver.
  - A WPLED as the transmitter and an OPD as receiver.
  - OVLC comprised of both an SMOLED and OPD.
  - A PLED as the transmitter and a Si PD as receiver.
- OOK and PPM modulation schemes are tested due to their bandwidth and power efficiencies, respectively.
- Due to low bandwidths, the suitability of a series of equalization methods to achieve high data rates are investigated. The equalizers tested were:

  - Digital FIR equalizers as outlined previously.
  - The ANN classifier implemented as an equalizer.

- Further, each equalizer has been implemented using an online filter on a Texas Instruments (TI) TMS320C6713 digital signal processing (DSP) board to ensure accurate performance is reported where appropriate.

- Due to the nature of OPDs, which can be patterned arbitrarily, MIMO is experimentally demonstrated with a solitary OPD consisting of four diodes patterned on to the same substrate.

The key achievement from these contributions was in each case to demonstrate megabits per second (Mb/s) data rates using online equalization from system bandwidths in the kHz region. This is a significant achievement for OVLC systems because it demonstrates that there is considerable potential in these systems. As the physical chemistry of organics improves to support higher charge transport properties, the bandwidths will improve and subsequently data rates will improve even further as is required for the optical backbone.

The key areas for research are highlighted in Fig. 1.7 where the coloured blocks indicate the path taken through this work.

The outcome of this research demonstrated some extremely important results which are listed next.

1.4 Original Contributions to Knowledge

The key contributions to knowledge that are derived in this thesis are as follows:

- In Chapter 4 the SMOLED to Si PD system is demonstrated and it is shown that a gross transmission speed of 2.7 Mb/s can be achieved with a $\sim$90 kHz bandwidth, offering an increase in data rate over the raw bandwidth of $\sim$ 30 times. In order to achieve this result, an ANN equalizer was required and the modulation format was OOK.

- In Chapter 5 the WPLED to OPD system is demonstrated, showing a gross transmission speed of 3.75 Mb/s with the same OOK and ANN equalizer topology as in Chapter 4. As mentioned, the OPD has a dynamic bandwidth as a function of incident light density and the communications performance is outlined for a series of bandwidths. The minimum transmission speed achieved is 1 Mb/s.

- In Chapter 6 the SMOLED to OPD system is demonstrated; the world's premier OVLC link. The transmission speed achieved was 1.15 Mb/s and required ANN signal processing.

- In Chapter 7 the PLED to Si PD link results are shown; with transmission speeds up to 10 Mb/s and 20 Mb/s available using LMS and ANN equalizers, respectively.

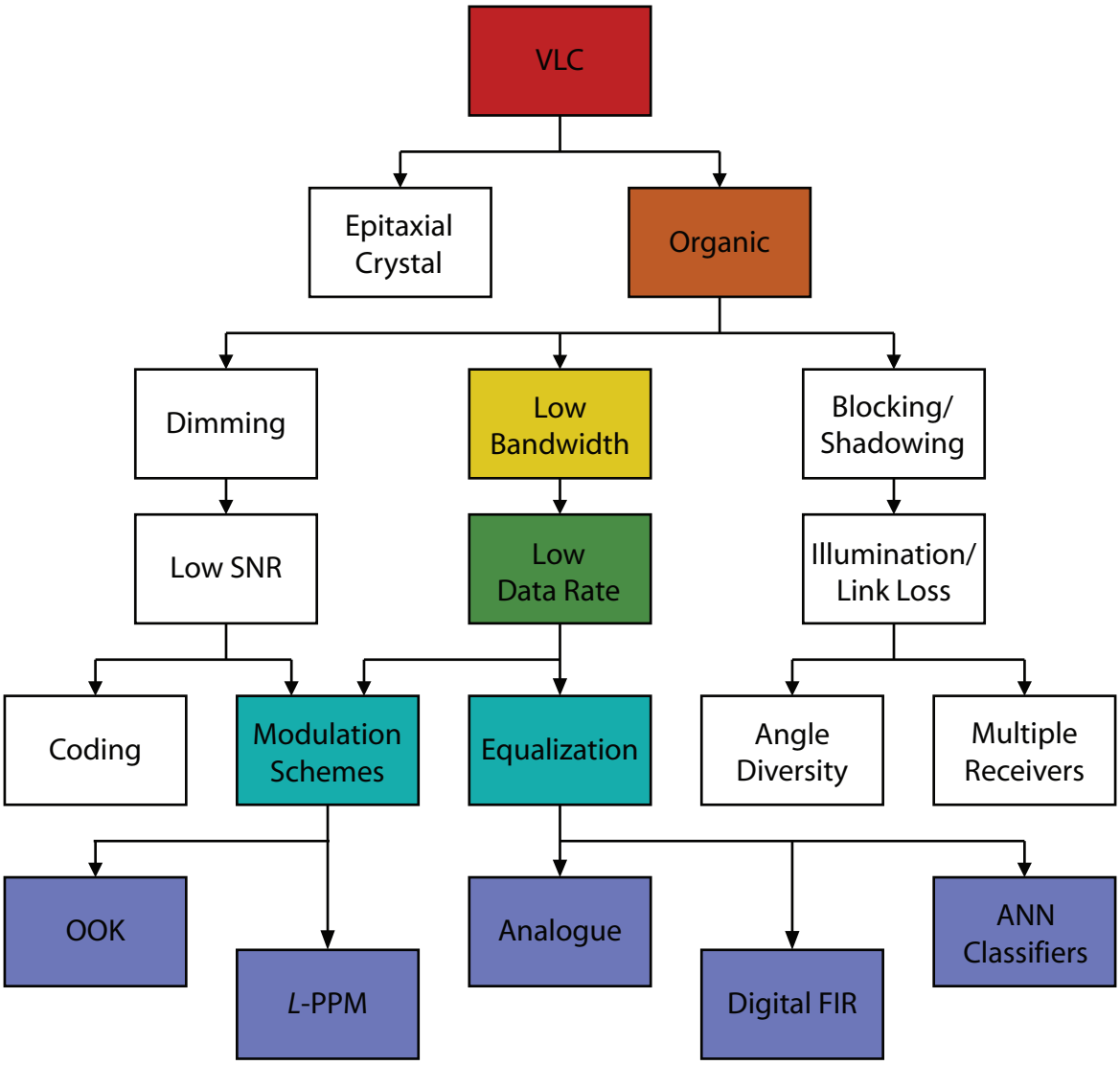

Fig. 1.7 VLC current challenges and thesis contributions

1.5 List of Publications and Awards

1.5.1 Peer Reviewed Journal Papers

1. **P. A. Haigh**, F. Bausi, T. Kanesan, S. T. Le, S. Rajbhandari, Z. Ghassemlooy, I. Papakonstantinou, W. Popoola, A. Burton, H. Le Minh, A. D. Ellis and F. Cacialli, "A 20-Mb/s VLC link with a polymer LED and a multi-layer perceptron equalizer," *IEEE Photonics Technology Letters*, vol. PP, 2014.

2. S. T. Le, T. Kanesan, F. Bausi, **P. A. Haigh**, S. Rajbhandari, Z. Ghassemlooy, I. Papakonstantinou, W. O. Popoola, A. Burton, H. Le Minh, F. Cacialli and A. D. Ellis, "10-Mb/s visible light transmission system using a polymer light-emitting diode with orthogonal frequency division multiplexing," *Optics Letters* vol. 39, pp. 3876-3879, 2014.

3. **P. A. Haigh**, Z. Ghassemlooy, I. Papakonstantinou, F. Arca S. F. Tedde, O. Hayden, and E. Leitgeb, "A 1-Mb/s visible light communications link with low bandwidth organic components," *IEEE Photonics Technology Letters*, vol. 26, pp. 1295-1298, 2014.

4. **P. A. Haigh**, Z. Ghassemlooy, S. Rajbhandari, I. Papakonstantinou and W. Popoola, "Visible light communications: 170-Mb/s using an artificial neural network equalizer in a low bandwidth white light configuration," *Journal of Lightwave Technology*, vol. 32, pp. 1807-1813, 2014.

5. **P. A. Haigh**, F. Bausi, Z. Ghassemlooy, I. Papakonstantinou, H. Le Minh, C. Fléchon and F. Cacialli, "Visible light communications: Real time 10-Mb/s link with a low bandwidth polymer light-emitting diode," *Optics Express*, vol. 22, pp. 2830-2838, 2014.

6. **P. A. Haigh**, Z. Ghassemlooy, S. Rajbhandari and I. Papakonstantinou, "Visible light communications using organic light emitting diodes," *IEEE Communications Magazine*, vol. 51, pp. 148-154, 2013.

7. **P. A. Haigh**, Z. Ghassemlooy, I. Papakonstantinou and H. L. Minh, "2.7 Mb/s With a 93-kHz White Organic Light Emitting Diode and Real Time ANN Equalizer," *IEEE Photonics Technology Letters*, vol. 25, pp. 1687-1690, 2013.

8. S. Rajbhandari, **P. A. Haigh**, Z. Ghassemlooy and W. Popoola, "Wavelet-neural network VLC receiver in the presence of artificial light interference," *IEEE Photonics Technology Letters*, vol. 25, pp. 1424-1427, 2013.

9. Z. Ghassemlooy, **P. A. Haigh**, F. Arca, S. F. Tedde, O. Hayden, I. Papakonstantinou and S. Rajbhandari, "Visible light communications: 3.75 Mb/s data rate with a 160 kHz bandwidth organic photodetector and artificial neural network equalization [Invited]," *Photonics Research*, vol. 1, pp. 65-68, 2013.

10. **P. A. Haigh**, Z. Ghassemlooy and I. Papakonstantinou, "1.4-Mb/s white organic LED transmission system using discrete multi-tone modulation," *IEEE Photonics Technology Letters*, vol. 25, pp. 615-618, 2013.

11. **P. A. Haigh**, Z. Ghassemlooy, H. Le Minh, S. Rajbhandari, F. Arca, S. F. Tedde, O. Hayden and I. Papakonstantinou, "Exploiting equalization techniques for improving data rates in organic optoelectronic devices for visible light communications," *Journal of Lightwave Technology*, vol. 30, pp. 3081-3088, Oct 1 2012.

1.5.2 Peer Reviewed Conference Papers

1. **P. A. Haigh**, Z. Ghassemlooy, F. Bausi, I. Papakonstantinou, H. L. Minh, S. F. Tedde, O. Hayden and F. Cacialli, "Organic visible light communications: Recent progress [invited paper]," in *IEEE ICTON 2014*, Graz, Austria, 2014.

2. **P. A. Haigh**, F. Bausi, T. Kanesan, S. T. Le, S. Rajbhandari, Z. Ghassemlooy , I. Papakonstantinou, W. O. Popoola, A. Burton, H. Le Minh, A. D. Ellis and F. Cacialli, "A 10-Mb/s visible light communication system using a low bandwidth polymer light-emitting diode [invited]," in *IEEE CSNDSP 2014*, Manchester, UK, 2014.

3. **P. A. Haigh**, Z. Ghassemlooy, S. Rajbhandari and E. Leitgeb, "A 100-Mb/s visible light communications system using a linear adaptive equalizer," in *Network and Optical Communications (NOC) and Optical Cabling and Infrastructure (OC&i)* 2014, Milan, Italy, pp. [accepted], 2014.

4. **P. A. Haigh**, F. Bausi, Z. Ghassemlooy, I. Papakonstantinou, H. Le Minh, C. Flechon and F. Cacialli, "Next generation visible light communications: 10-Mb/s with polymer light-emitting diodes," in *Optical Fiber Communication Conference*, San Francisco, California, 2014, p. Th1F.4.

5. **P. A. Haigh**, Z. Ghassemlooy, I. Papakonstantinou and S. Rajbhandari, "Online artificial neural network equalization for a visible light communications system with an organic light emitting diode based transmitter," in *Network and Optical Communications (NOC) and Optical Cabling and Infrastructure (OC&i) 2013*, Graz, Austria, pp. 153-158, 2013.

6. **P. A. Haigh**, Z. Ghassemlooy, I. Papakonstantinou, F. Arca, S. F. Tedde, O. Hayden and S. Rajbhandari, "A MIMO-ANN System for Increasing Data Rates in Organic Visible Light Communications Systems," in *IEEE ICC 2013 - Wireless Communications Symposium (ICC'13 WCS)*, Budapest, Hungary, 2013.

7. Z. Ghassemlooy, H. Le Minh, **P. A. Haigh** and A. Burton, "Development of Visible Light Communications: Emerging Technology and Integration Aspects [Invited Paper]," in *OPTIC 2012*, Taiwan, 2012.

8. A. Burton, H. Le Minh, Z. Ghassemlooy, S. Rajbhandari and **P. A. Haigh**, "Performance analysis for 180^{c}*irc*; receiver in visible light communications," in *Fourth International Conference on Communications and Electronics (ICCE)*, 2012, pp. 48-53.

9. A. Burton, H. Le Minh, Z. Ghassemlooy, S. Rajbhandari and **P. A. Haigh**, "Smart receiver for visible light communications: Design and analysis," in *8th International Symposium on Communication Systems, Networks & Digital Signal Processing (CSNDSP)*, pp. 1-5, 2012.

10. **P. A. Haigh**, T. T. Son, E. Bentley, Z. Ghassemlooy, H. Le Minh and L. Chao, "Development of a Visible Light Communications System for Optical Wireless Local Area Networks," in *IEEE Computing, Communications and Applications Conference (ComComAp)*, pp. 351-355, 2012.

11. H. Le Minh, Z. Ghassemlooy, A. Burton and **P. A. Haigh**, "Equalization for Organic Light Emitting Diodes in Visible Light Communications," in *IEEE Globecom*, Houston, Texas, USA, 2011.

1.6 Thesis Organization

This thesis is organized as follows: in Chapter 2 a brief review of the theory of inorganic and organic semiconductors is presented and in Chapter 3 a review of the theory of communications and equalization is given. In Chapter 4 the first original chapter is presented based on the link BER evaluation of a SMOLED to Si PD system. It is found that a maximum 2.7 Mb/s transmission speed can be supported. In Chapter 5 an original WPLED to OPD link is evaluated in terms of BER performance and a 3.75 Mb/s link is demonstrated for the first time. In Chapter 7 a VLC link employing exclusively organic (SMOLED, OPD) optoelectronic components is discussed, including a transmission speed of 1.15 Mb/s. In Chapter 8

a PLED based VLC system is introduced and evaluated in terms of BER performance; first demonstrating that 10 Mb/s can be supported with an LMS equalizer and 20 Mb/s can be supported using an ANN.

Chapter 2

Principles of Organic Photonic Devices

2.1 Introduction

The theory of operation of inorganic semiconductors is well known and covered extensively in the literature [73], so is not repeated here in detail. This chapter discusses a basic outline of electron/hole generation and recombination followed by the theory for some of the organic photonic devices used in this work, based on availability of the structure from the manufacturers.

2.2 Review of Conventional Semiconductors

Semiconductors have electrically conductivity somewhere between a conductor such as copper often used in wires or an insulator like ceramic which can be commonly found insulating power lines. LEDs and PDs are based on the operation of semiconductor devices; hence it will be useful to give a detailed review of the physics that is employed. Si and gallium (Ga) are two of the most important semiconductor materials in the fields of microelectronics and photonics. In terms of light emitters, GaN has undergone something of a revolution over the last few decades and now dominates the LED market due to high efficiency and high power output [74, 75]. Gallium arsenide (GaAs) is generally heralded as the most important semiconductor material for light absorption due to its high responsivity in the IR range, but offers no detection in the visible range of the electromagnetic spectrum. On the other hand, Si encompasses the entire visible to IR range, making it the most important inorganic semiconductor material for VLC detectors, currently.

The reason for the difference in absorption wavelength is down to band theory. The valence and conduction bands are separated by the band gap energy. The smaller the band

gap energy, the higher the conductivity of the device, thus insulators have large band gaps ($>$ 3 eV [76]) and conductors have very small (or no) band gaps ($<$ 0.1 eV [76]). Si and GaAs have band gap energies of 1.11 and 1.42 eV at 300 K, respectively which means that an incoming photon must have at least this energy if it is to excite an electron across the forbidden zone.

Optoelectronic devices rely on the transport of current across the boundary between the p (hole injection) and n (electron injection) type regions. When forward biased, electrons and holes recombine to generate electron-hole pairs that emit photons. In reverse bias conditions, a photon incident to the semiconductor can generate a charge carrier where the electron and hole are attracted to the n and p type regions, respectively inducing a photocurrent.

2.3 Photon Generation and Absorption

The simplest form of semiconductor has two bands; the conduction band containing holes and the valence band containing electrons as illustrated in Fig. 2.1. The depletion region is exaggerated in size for emphasis.

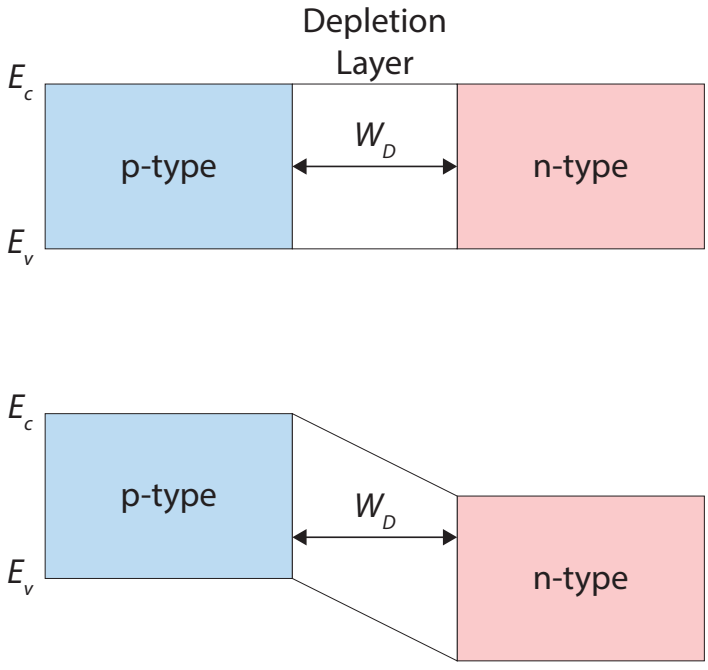

Fig. 2.1 $p-n$ junction with exaggerated depletion layer; top; device under no bias, bottom; device under bias (Fermi level not shown in either device)

Each band has an associated energy level, E_c and E_v for the conduction and valence

bands, respectively and the band gap energy E_g is the difference between them:

$$E_g = E_c - E_v \tag{2.1}$$

It is possible to promote an electron from the valence band into the conduction band by overcoming the band gap energy, resulting in the generation of a photon with energy that is slightly less than E_g before the electron drops back into the valence band. Equally, an incoming photon of sufficient energy ($> E_g$) is capable of breaking the valence bonds between atoms and freeing an electron, promoting it from the valence band into the conduction band generating a so called photocurrent. These processes are known as radiative generation and recombination of electron hole pairs and are outlined in Fig. 2.2. Non-radiative recombination is not in the primary focus of this work and is not covered here, for further reading see [77].

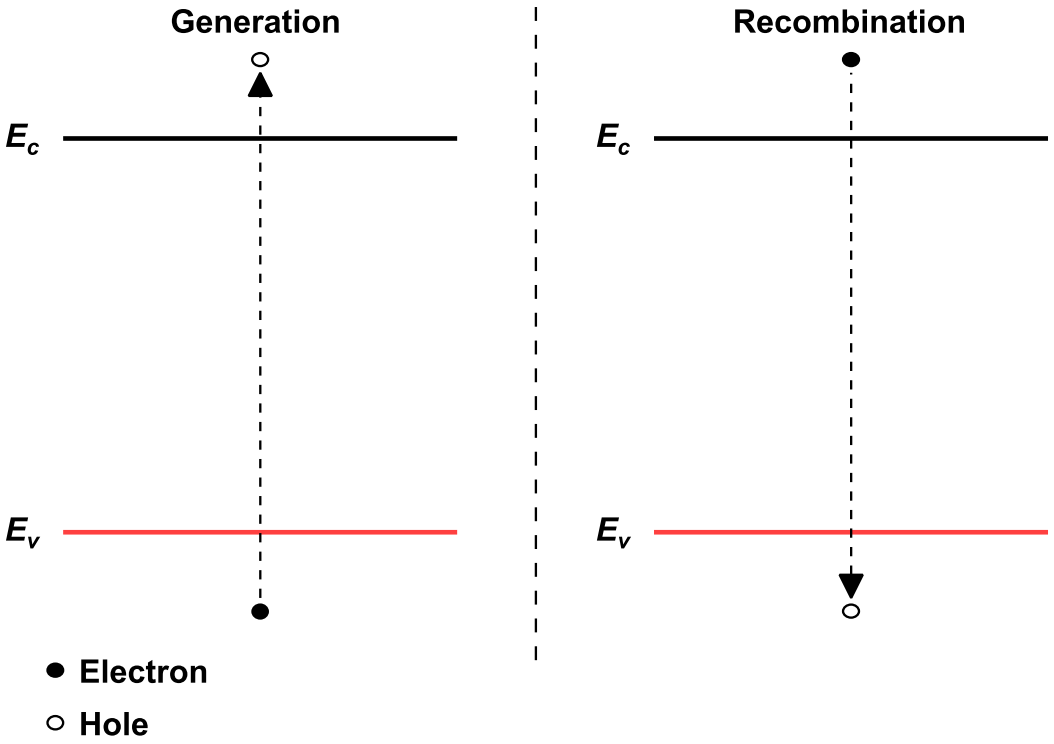

Fig. 2.2 Electron hole pair generation and recombination

2.3.1 Radiative Recombination of Electrons and Holes

Without the influence of a bias voltage, at a given temperature the concentrations of holes p_0 and electrons n_0 are equal to the intrinsic carrier concentration n_i, that is [77]:

$$n^2 = n_0 p_0 \tag{2.2}$$

In the presence of a bias voltage the concentration of charge carriers is given by [77, 78]:

$$n = n_0 + \delta n \tag{2.3}$$

$$p = p_0 + \delta p \tag{2.4}$$

where δn and δp are the excess charge carriers generated proportional to the bias voltage. As previously mentioned, the concentration of each type of charge carrier is not necessarily equal. The recombination rate is directly proportional to the charge carrier concentrations and the relationship is given by the bimolecular rate equation for light emitting diodes as follows [77, 78]:

$$R = Bnp \tag{2.5}$$

where B is the bimolecular recombination coefficient ($\mathrm{cm}^3\ \mathrm{s}^{-1}$), given by [77]:

$$B = 3 \times 10^{-10} \left(\frac{300}{T}\right)^{3/2} \left(\frac{E_g}{1.5}\right)^2 \tag{2.6}$$

Assuming either an n- or p-type semiconductor, the majority carrier concentration greatly exceeds the injected concentration (i.e. $\delta n \ll (n_0 + p_0)$ or $\delta p \ll (n_0 + p_0)$) then the following is obtained, assuming $\delta n = \delta p$ because generation and recombination occur in pairs [77, 78]:

$$R = B(n_0 + p_0 + \delta n)\delta n \tag{2.7}$$

The radiative lifetime is given by [77]:

$$\tau_{lifetime} \simeq \frac{1}{B(n_0 + p_0 + \delta n)} \tag{2.8}$$

which gives the carrier lifetime $\tau_{lifetime}$ for any p - n junction semiconductor. For high level injection such as modern high powered LEDs [79] and semiconductor lasers [78] the injected concentration of charge carriers is far in excess of the majority charge carriers (i.e.

$\delta n \gg (n_0 + p_0)$ or $\delta p \gg (n_0 + p_0)$):

$$R_{sp} \simeq B\delta n^2 \simeq Bn^2 \tag{2.9}$$

The recombination rate for high level injection is called the spontaneous recombination rate R_{sp} and is commonly associated with LEDs. Laser diodes are also subject to this recombination as well as stimulated emission of photons, which can be referred to in [77]. The recombination rate is of the utmost importance in optical communications because it is one of the main parameters controlling LED bandwidth [77].

In VLC systems (described in Chapter 4) the carrier lifetime is not something that can be explicitly controlled since the LEDs are typically commercial devices; however it is necessary to understand the origin of this phenomenon in order to understand the device limitations. The key method to overcome the carrier lifetime limitations in optical communications is to model the device as an equivalent RC circuit (for simplicity). Both LEDs and PDs can be modelled as filters with low pass transfer functions.

2.3.2 Equivalent Model of the Light Emitting Diode

The Shockley diode equation describes the current - voltage relationship of LEDs and is given by [80]:

$$J = J_0 \left[e^{\frac{qV_B}{k_B T}} - 1 \right] \tag{2.10}$$

where J_0 is the saturation current density which has an expression given in [73], q is the charge of an electron, V_B is the bias voltage, k_B is the Boltzmann constant and T is the temperature (K). The Shockley equation is illustrated in Fig. 2.3 where the voltage normalization factor is qV_B/k_BT. The forward bias region is where LEDs operate. The reverse bias region is for PDs which is discussed in the next section.

An LED is a p - n junction and therefore has a depletion region with width W_D given by [77]:

$$W_D = \sqrt{\frac{2\varepsilon_r \varepsilon_0 (V_D - V_B)(N_A^+ + N_D^-)}{qN_A^+ N_D^-}} \tag{2.11}$$

where ε_r is the dielectric constant of the material,ε_0 is the relative permittivity of a vacuum, N_A^+ and N_D^- is the concentration of acceptor and donor atoms, respectively and V_D is the diffusion voltage given in [77]. Taking the charge carrier parameters as constant at any

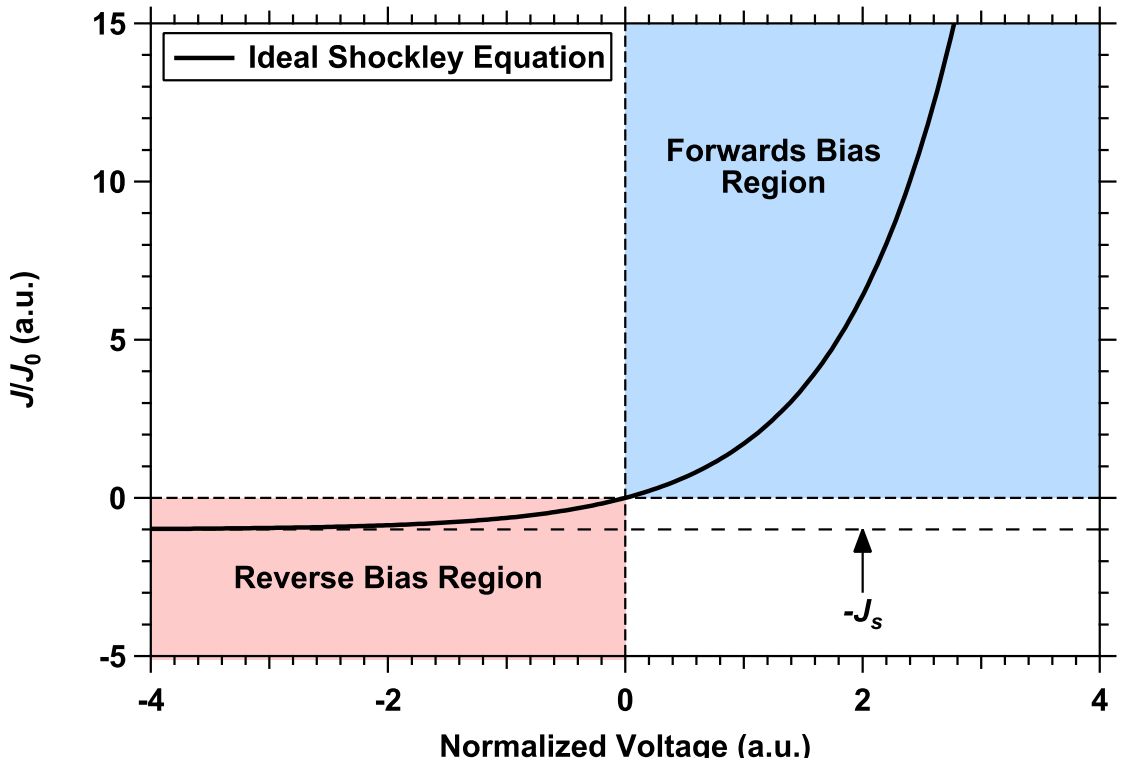

Fig. 2.3 Ideal Shockley equation showing the V-I relationship for a p - n junction

instantaneous time, clearly the width of the depletion region is related to the difference between the diffusion voltage and the bias voltage. If the bias voltage is negative the width increases and charge carriers require more energy to cross the semiconductor; this is a good condition for PDs and is known as reverse bias. While a positive bias voltage (forward bias) reduces the width and means that less energy is required for the charge carriers to diffuse, clearly a desirable condition for LEDs.

The capacitance of the depletion layer C_j (F) is given by [81]:

$$C_j = \frac{\varepsilon\varepsilon_0}{W_D} = \sqrt{\frac{\varepsilon\varepsilon_0 q N_A^+ N_D^-}{2(V_D - V_B)(N_A^+ + N_D^-)}} \tag{2.12}$$

which by inspection is similar to the expression for parallel plate capacitance, thus introducing a term for the cross sectional area A_D (m^2), the junction capacitance becomes:

$$C_j = \frac{\varepsilon\varepsilon_0 A_D}{W_D} \tag{2.13}$$

The plate capacitance of silicon (dielectric constant 11.7) is illustrated in Fig. 2.4.

Recalling that charge carriers have a definite and finite lifetime, it is clear that devices

such as LEDs have a low pass transfer function and it is trivial to produce an equivalent first order RC_j low pass filter model, since the junction capacitance in conjunction with a load resistance causes a cut-off frequency [59, 82].

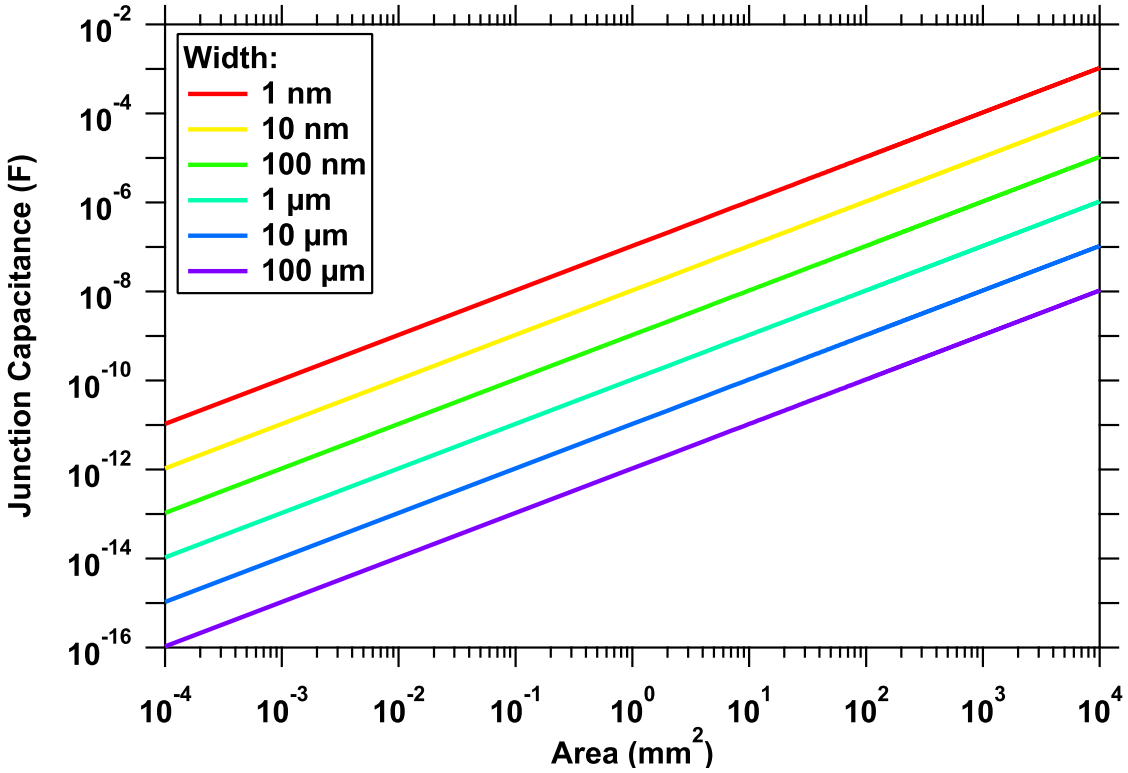

Fig. 2.4 Theoretical p - n depletion layer capacitance as a function of area and width

2.4 Photodetectors

Photodetectors generate an electrical current proportional to the square of the optical field incident to the photoactive area of the device. Therefore the generated photocurrent I_p magnitude is clearly proportional to the strength of the optical power P_i at the receiver [83]:

$$I_p = \eta \frac{qP_i}{h\upsilon}\left[1 - e^{-\alpha l}\right] \tag{2.14}$$

where h is the Planck constant (eVs) and υ is the photon frequency (m s^{-1}), l is the length of the photoactive region and α is the absorption coefficient, which is the fraction of optical power absorbed in a unit length of the absorption medium. The absorption medium is commonly selected as Si for visible light while gallium alloys are preferred for the NIR to IR range. The quantum efficiency η is the ratio of generated charge carriers that contribute to

the generated photocurrent. The responsivity $\Re$ (A/W) is the ratio of generated photocurrent to received optical power [83]:

$$\Re = \frac{I_p}{P_i} = \frac{\eta q}{h\upsilon}\left[1 - e^{-\alpha l}\right] \tag{2.15}$$

After transmission through the optical channel, the received signal is generally very weak and a high responsivity is a desirable characteristic. The responsivity of semiconductor materials and their band gap energies are shown in Fig. 2.5.

The organic polymer semiconductor, poly(3-hexylthiophene) (P3HT) is introduced here for illustrative purposes and will be discussed in detail later in this chapter. For now though, observe the high responsivity in comparison to Si and the sharp cut-off wavelength around 650 nm, which is a significant advantage for VLC systems as IR noise is intrinsically filtered. Germanium (Ge) and indium gallium arsenide (InGaAs) do not pass visible wavelengths. The semiconductor material is extremely important as it defines the range of wavelengths over which the device is capable of operating.

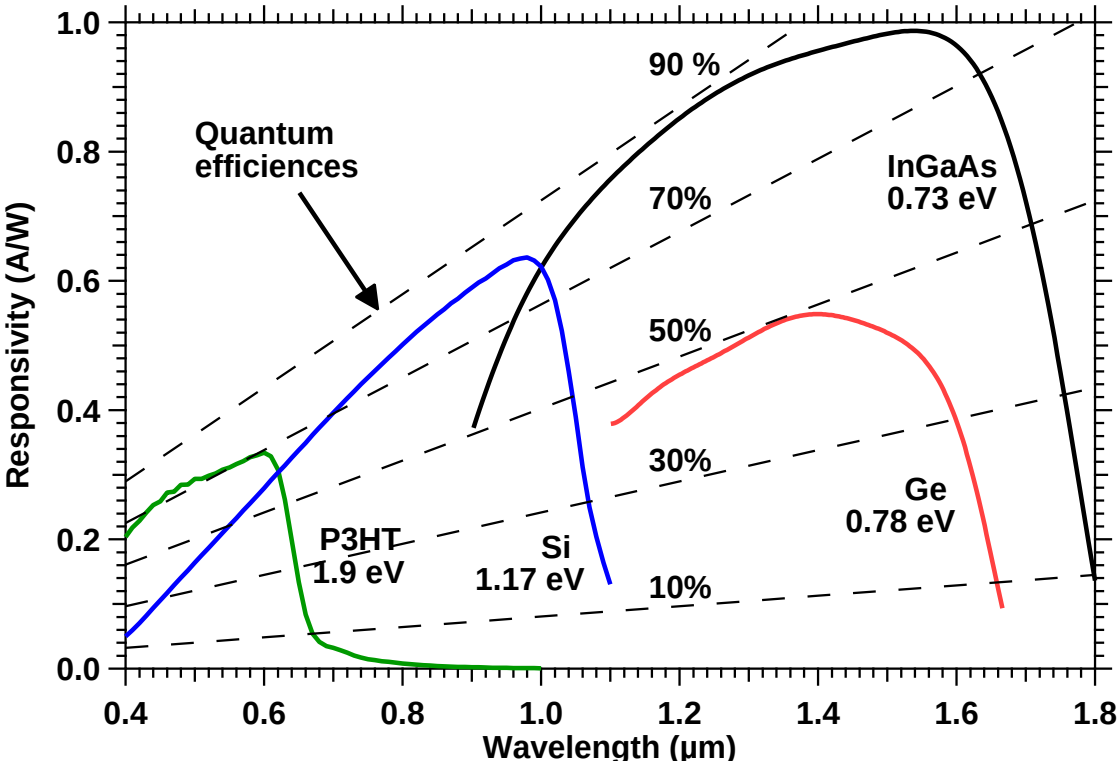

Fig. 2.5 Responsivity and band-gap energy of a number of semiconductor materials, abbreviations as follows; indium gallium arsenide (InGaAs), germanium (Ge), Si and P3HT; adapted from [4] and developed

An incident photon must have at least enough energy to overcome the band gap, generating an electron-hole pair. The upper cut-off wavelength λ_c (m) can be found using E_g and is given by [73]:

$$\lambda_c = \frac{hc}{E_g} = \frac{1.24 \times 10^{-6}}{E_g} \tag{2.16}$$

Most PDs used in optical communications are not $p-n$ junctions because the RC_j time constant is large and there is low optical absorption in the diffusion lengths [78]. An intrinsic layer is introduced as the major absorber in order to aid the absorption in comparison to $p-n$ junctions. PINs have the structure shown in Fig. 2.6, where V_b is in reverse bias configuration and R_L is the load resistor.

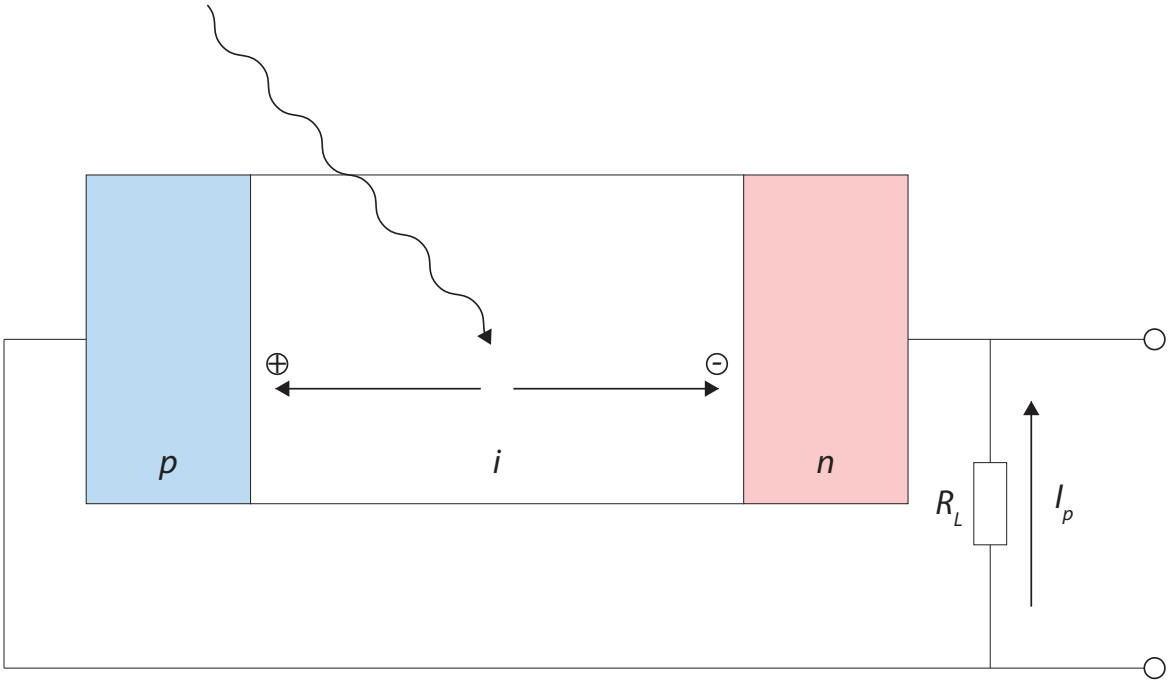

Fig. 2.6 The structure of a PIN type photodetector

The Shockley equation (Equation (2.10) is used to plot the I-V relationship of PDs, as well as LEDs and examples of the dark and illumination current can be seen in Fig. 2.7. A reverse bias is required in order to ensure that the active region is absent of charge carriers. PINs consist of a wide intrinsic semiconductor with p-type and n-type material regions. Increasing the reverse bias voltage causes an increase in the intrinsic region width; thus causing an decrease in capacitance and a higher bandwidth (refer to Fig. 2.4). The bandwidth of most PDs is limited by the combination of several parameters.

The most important are the resistor-capacitor (RC_j) time constant and charge carrier

lifetime as has been demonstrated previously. The PIN structure can be thought of as similar to the $p-n$ junction however with a larger depletion region (the intrinsic region) and therefore the mathematics of charge carrier transport through the device remains the same [78]. The equivalent circuit is therefore still low pass, however since the absorbed photons are generating the photocurrent, at least one current source must be included to indicate the photocurrent and the dark current as illustrated in Fig. 2.8.

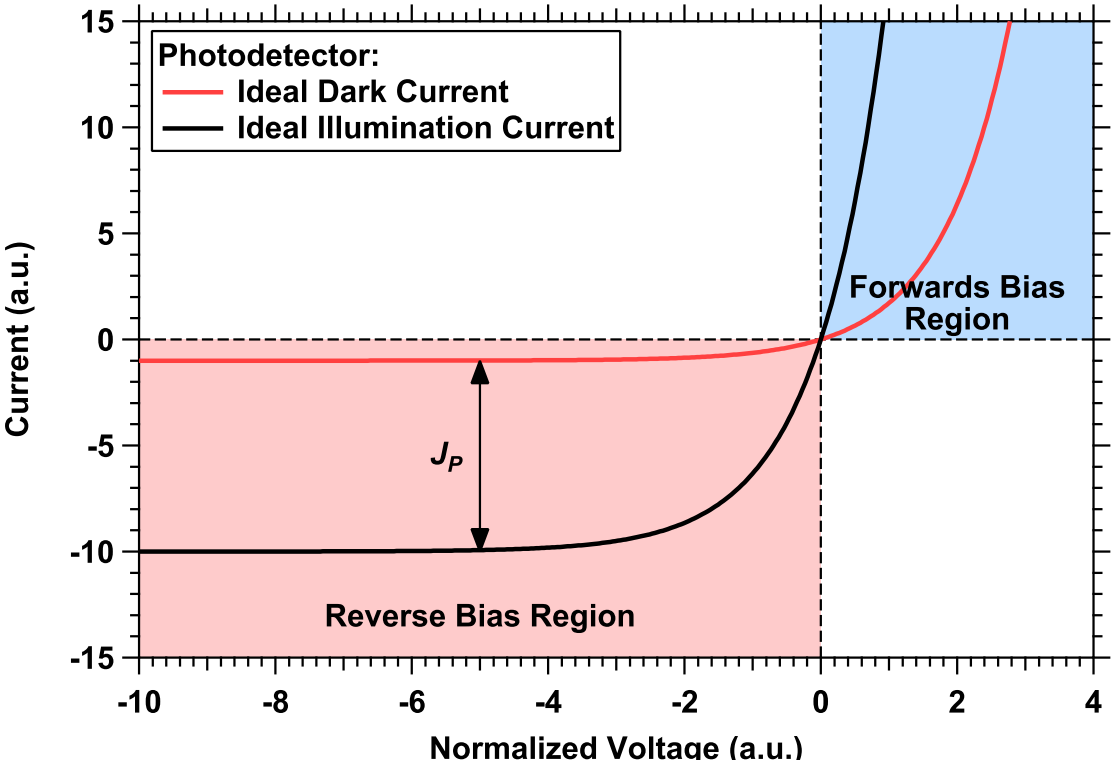

Fig. 2.7 Ideal PD I-V relationship

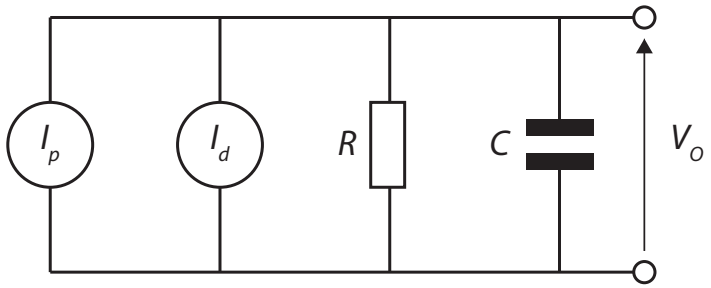

Fig. 2.8 Equivalent model of a PIN PD; a first order RC low pass filter with two current sources; the photocurrent I_p and the dark current I_d

The noise source in a PD is of crucial importance because it imposes the device lower

sensitivity limit. The main noise sources are shot I_S and thermal I_T (also called Johnson) noise, while there is also a contribution from the $1/f$ noise I_f which isn't covered here [5]:

$$I_{noise} = \sqrt{I_S^2 + I_T^2 + I_f^2} \tag{2.17}$$

As opposed to thermal noise, which is introduced by thermal fluctuations in the passive components within the electronic circuitry the shot noise is introduced by fluctuations in the current flow. Shot noise is given by [5]:

$$I_S = \sqrt{2qI_d\Delta f} \tag{2.18}$$

where Δf is the noise bandwidth. Thermal noise is given by [5]:

$$I_T = \sqrt{\frac{4kT}{R}\Delta f} \tag{2.19}$$

The noise equivalent power (NEP) is another important noise metric that is defined as the optical power required to produce a photocurrent equal to the total noise current [5]:

$$NEP = \frac{I_{noise}}{\Re} \tag{2.20}$$

The NEP is clearly dependent on the physical characteristics of the PD such as the responsivity and also the frequency of the incoming signal. A small area device yields a lower NEP value which is desirable.

2.5 Organic Semiconductors

A semiconductor is considered organic if the materials are mainly made up of either carbon or nitrogen [5]. Organic semiconductors are a unique category of materials because they possess similar properties to metallic semiconductors and polymers simultaneously. They can offer electronic characteristics as previously discussed whilst offering superior mechanical and processing characteristics including mechanical flexibility, a variety of flexible substrates and low cost manufacturing. These attributes are extremely attractive for future electronics and a new type of industry is beginning to emerge; organic electronics. Within the organic electronics domain, a wide variety of applications is starting to emerge. The most popular are OLEDs and also organic solar cells (OPVs) and there is enormous potential to provide extremely large scale general electronics at low cost. The first completely organic microcontroller was recently reported in [84] that offers a fully functional

8-bit flexible interface based on 3381 transistors. In comparison to the microcontrollers of today, where the number of transistors has scaled up into the billions approximately according to Moore's law [85] (the Intel i7 has $\sim$ 1.4 billion transistors on-chip) this is a very small amount. However, when the organic microcontroller is compared with the 4-bit Intel 4004 which was one of the first examples of a Si microcontroller in 1971, the number of transistors is $\sim$ 50% higher and the power consumption is reduced by five orders of magnitude [84] which demonstrates considerable potential.

The conductivities of some of the most common conductive polymers are shown in Fig. 2.9 along with the molecular structure where appropriate. As can be seen, the conductivities of such materials are orders of magnitude lower than metal conductors which are a serious impediment to high speed devices. A polymer is created by a reaction between neighbouring atoms causing energy to be released and mixing between orbitals, or the so-called hybridization of orbitals. The fine details of hybridization can be obtained from [5, 86] with a general outline presented here.

2.5.1 Hybridization

Hybridization causes the bonds between molecules. After polymer formation has occurred it is not possible to describe the position of any single atom, and hence delocalized densities of electrons must be considered which are known as π-bonds which are weak due to their electron dislocation. There is also σ-bonds where the atomic location of each bonding electron can be known; hence σ-bonds are far stronger than π-bonds so it is easier to procure an electron from the latter [5, 86].

Linear Combination of Molecular Orbitals

The previous discussion only concerns the orbitals of individual atoms. In order to understand the behaviour of molecules, it is necessary to perform the linear combination of atomic orbitals (LCAO). LCAO means adding the two atomic orbitals to form a bonding and anti-bonding orbital for the overall molecule. Atomic orbitals have phase in exactly the same way as a standing wave. Combination of out-of-phase orbitals produces an anti-bonding orbital while combining two in-phase orbitals produces a bonding orbital. An anti-bonding orbital contains no electrons between the nuclei of the adjoined atoms aiding the repulsion mechanism between positively charged nuclei, thus raising the relative energy level in comparison to the unbounded molecules. A bonding orbital is the opposite; electrons can be found between the nuclei of the two atoms and therefore a drop in relative energy level occurs as the electrons are shared. This concept can be illustrated in an energy level diagram

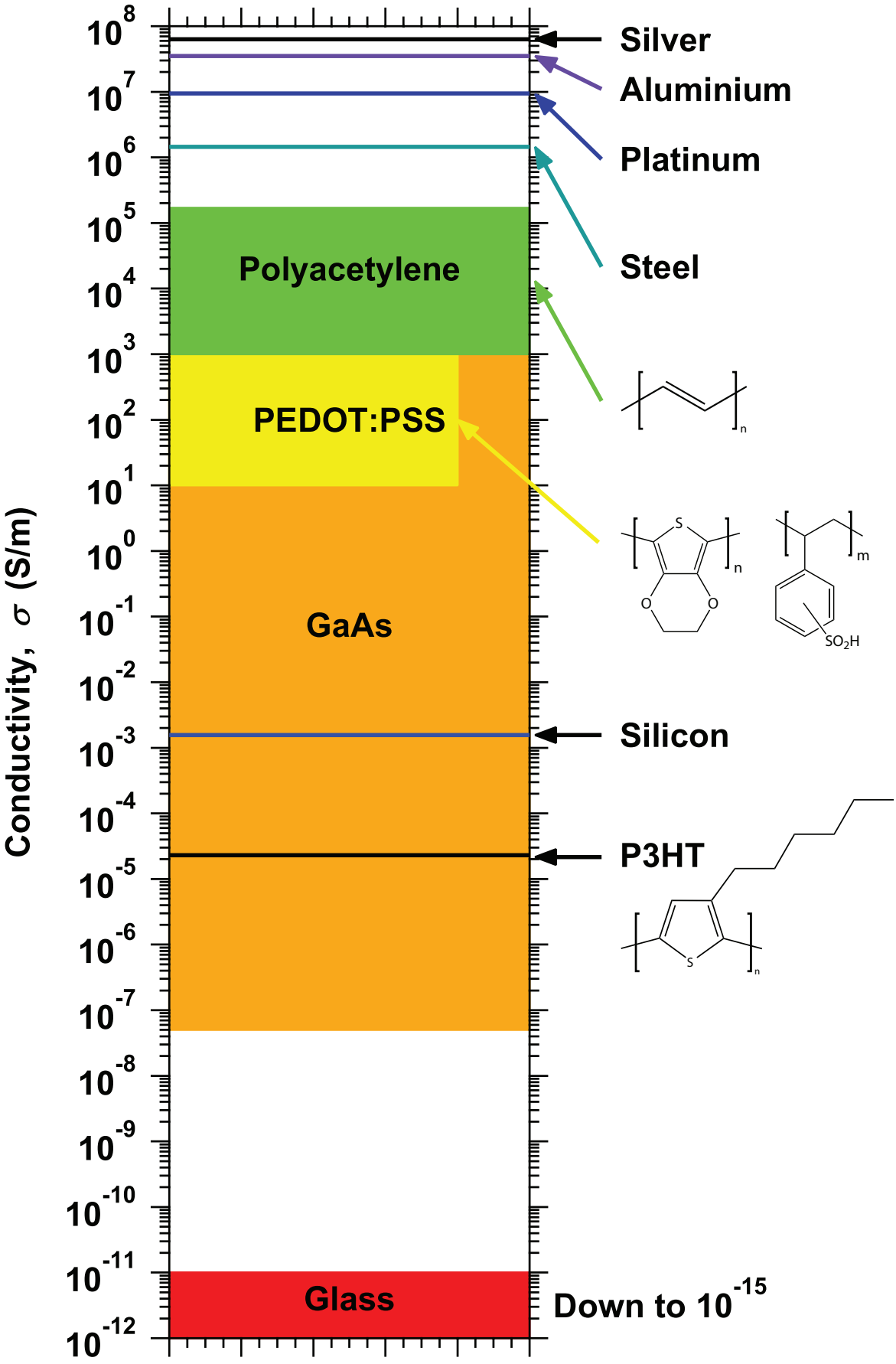

Fig. 2.9 Conductivity of some common organic polymers in comparison to common metal conductors and electrical insulators

(Fig. 2.10) and it should be noted that this is a σ-bond as the location of the electrons can be known.

When two atoms with electrons in the p orbitals meet, both σ-bonds and π-bonds are produced as shown in Fig. 2.11 where the $*$ indicates the anti-bonding combination. Clearly less energy is required to promote an electron between π-bonds than σ-bonds. It should be noted that at lower energy levels the $1s$ and $2s$ combinations also exist but are not shown here.

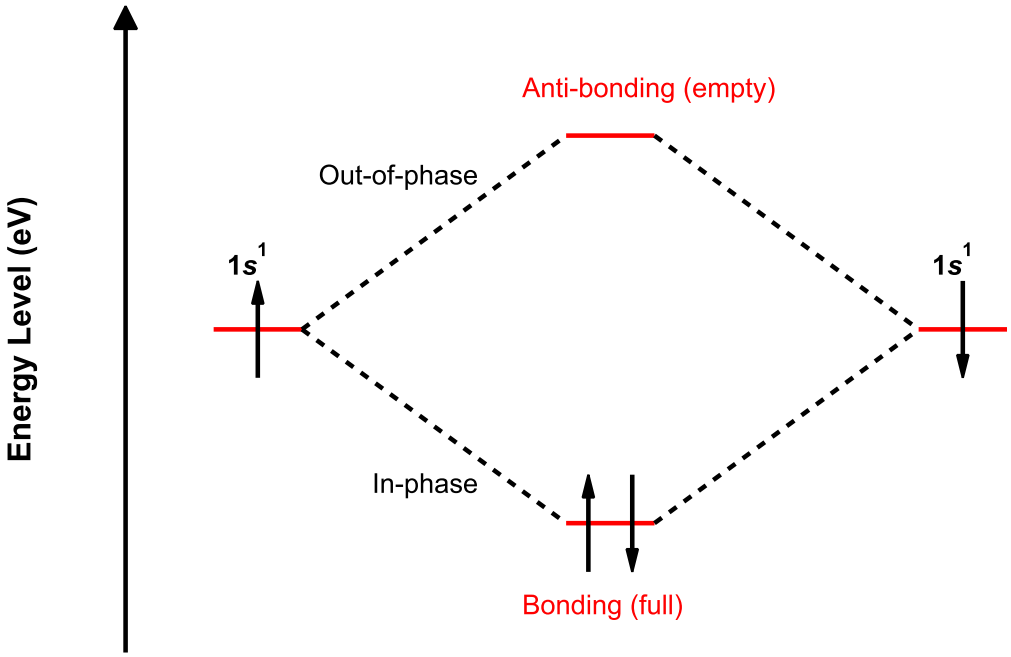

Fig. 2.10 Energy level diagram of bonding between two hydrogen atoms, electron spin is indicated by the arrows

If molecules combine that are not of the same type, they will still bond but they will mix and form a hybrid molecular orbital that retains the number of orbitals before the mixing process. For example combining an s orbital with each of the p orbitals results in a hybrid sp^3 orbital (i.e. one part s, three parts p) which has a signature shape determined by the constructive and destructive superposition of the standard atomic orbitals and angle between hybrid orbitals as is illustrated in [5, 86, 87]. The main types of hybrid orbital in organic semiconductors are sp^3 and sp^2.

It is π-bonds that are responsible for the conduction of current through the polymer due to complete delocalization across the whole bond chain. The band gap energy increases

for an increasing number of bonds until the so-called long chain limit is reached at around 20-30 bonds. The band gap energy is given by [5]:

$$E_g = E_{LC} + \frac{k_p}{N_\pi} \tag{2.21}$$

where E_LC is the energy gap of the long chain limit, N_π is the number of π-bonds and k_p is a proportionality constant. It should be noted that this relationship was derived experimentally and a theoretical solution also exists that can be found in [5]. The band gap energy of conjugated polymers typically lies between 1 — 4 eV, encompassing the entire visible light range.

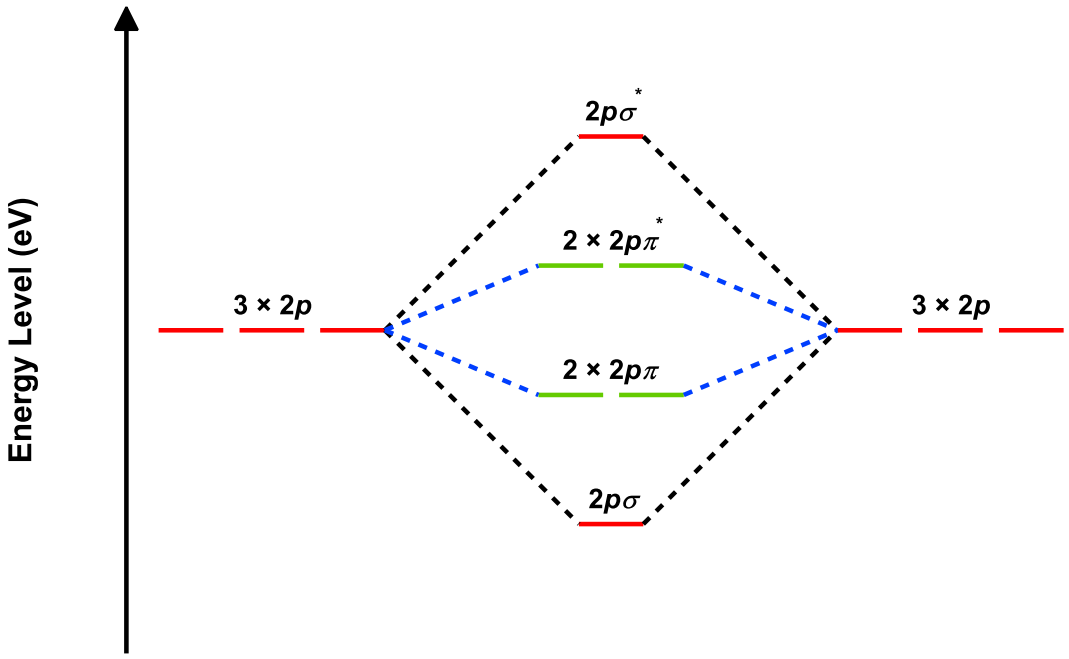

Fig. 2.11 Energy level diagram of π and σ bond generation by LCAO

The lowest unoccupied molecular orbital (LUMO) is the lowest energy level bond in which there are no electrons. Similarly, the highest occupied molecular orbital (HOMO) is the highest energy level in which electrons exist. Generally the LUMO is given by $\pi*$ while the HOMO is given by π. The LUMO and HOMO are comparable to the conduction and valance bands, respectively, in metallic semiconductors and thus the band gap energy is given by the difference between them. For emission of photons, electrons must be promoted from the HOMO to the LUMO (π to $\pi*$) and the wavelength corresponds to the energy gap

between them and for absorption of photons the energy of the impinging photon must exceed that of the band gap energy, with both processes exactly as in inorganics. From the previous section the concepts of generation and recombination were introduced and these are not applicable to organic semiconductors because the charge carriers are not free to move back to their respective electrodes. Instead excitons must be introduced which are quasi-particles that represent a bound electron-hole pair which exists for a fraction of a second (typically in the order nanoseconds) before photon emission. In order to separate an exciton, energy greater than the bounding energy (which is higher than inorganics) must be applied in both the generation and recombination processes. There are several variations on the generic exciton which are classified according to their binding energy; Frenkel excitons, charge transfer excitons and Mott-Wannier excitons in order of high to low. The most abundant in organics are Frenkel excitons and therefore the others are not considered here, although they can be referred to in [5, 88–90]. The Frenkel exciton can move through the polymer chain freely.

Conductive polymers are not ordered crystals as in metallic semiconductors and consist of a localized density of states (DOS) and the most common estimation of the positions and energy level of each site within the density is a Gaussian distribution [5, 91, 92] and can be described as follows [91, 93]:

$$DOS(E) = \frac{N_t}{\sigma\sqrt{2\pi}} \exp\left\{ -\left(\frac{E - E_0}{\sigma\sqrt{2\pi}} \right)^2 \right\} \tag{2.22}$$

where E_0 is the Gaussian centre, N_t is the effective DOS and σ is the DOS Gaussian variance. This concept is illustrated in Fig. 2.12 where the movement of electrons and holes are shown in section 1a and 1b for the LUMO and HOMO, respectively. It should be noted that the majority charge carrier here are holes and they occupy every vacant state. Electrons are shown for simplicity and vice-versa for holes in the HOMO. In section 2 trap states are indicated inside the dashed boxes for holes and electrons. Traps are a negative effect as they restrict charge transport properties and restrict the generation and recombination processes as will be discussed in the following paragraphs. Finally in section 3 a Frenkel exciton is generated and a photon is emitted with energy approximately equivalent to the energy gap of the semiconductor. For absorption of a photon, the opposite process occurs. Starting at section 3, if a photon with energy greater than the band gap impinges on the photoactive area a Frenkel exciton is generated and gets separated into an electron and a hole which are attracted to their relative electrodes through section 1a and 1b. Alternatively, these carriers can fall into the traps indicated in section 2 to restrict the generated photocurrent.

The mobility of charge carriers is perturbed by the addition of trap states at the interfaces

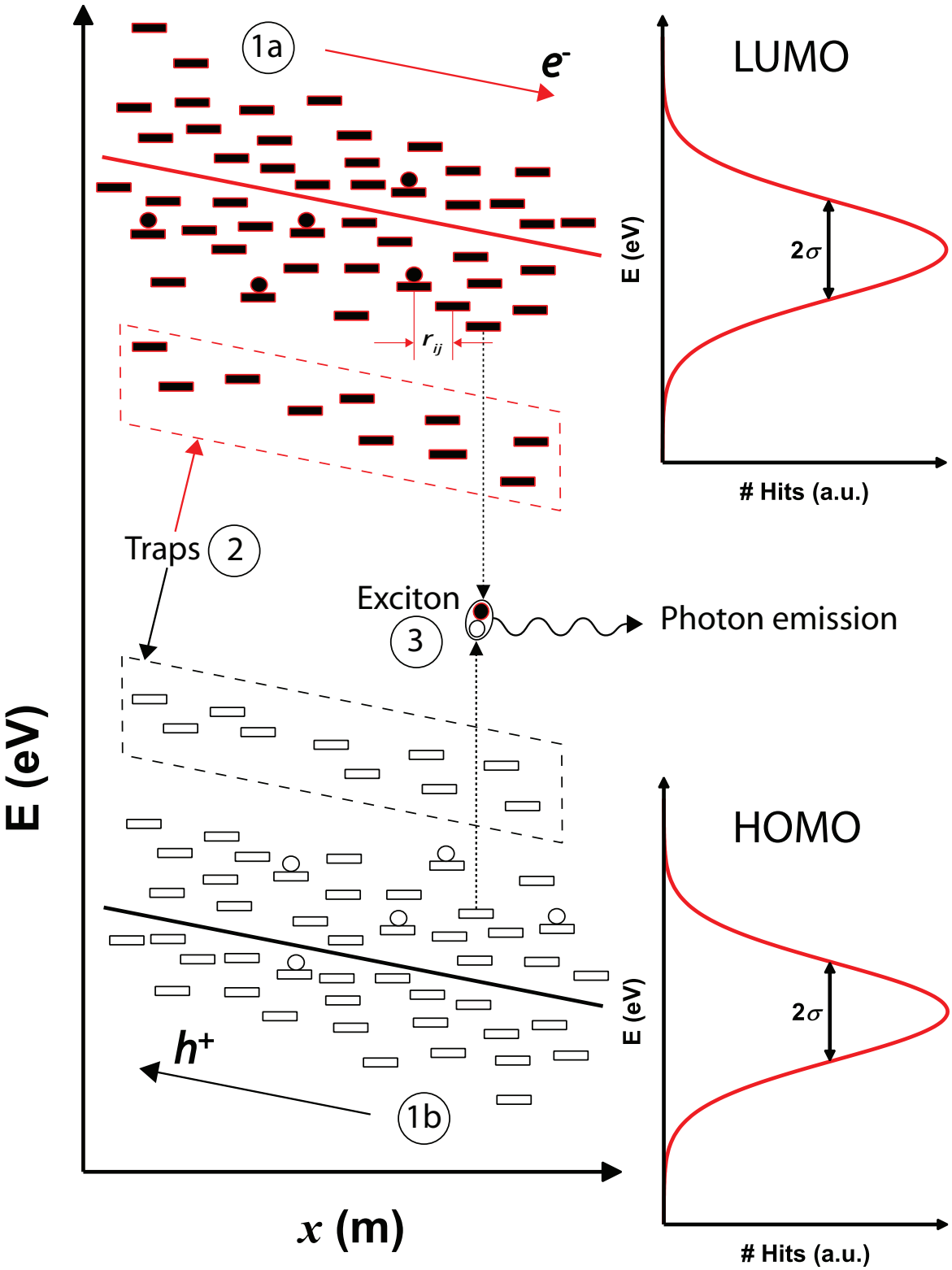

Fig. 2.12 Density of states for an organic semiconductor and the processes for photon emission with respect to the HOMO and LUMO levels; electrons and holes hope through localized states in the direction of the $e-$ and $h+$ arrows in sections 1a and 1b, respectively. Trap states exist and the electrons and holes must avoid being restricted in these states to recombine to form a photon. In section 3 a Frenkel exciton is generated (bonding distance $\sim$5 Å (1 Å = 1×10^{-10} m) [5]) and a photon is emitted

(intrinsic traps) and due to defects in the layers and production processes (extrinsic traps). Both types of trap impede transport properties of organics as they interfere with the recombination and generation processes by introducing new energy levels that have energy levels between the HOMO and LUMO levels meaning charge carriers must drop into the traps as they propagate across the device [94], refer to Fig. 2.12. Clearly if a charge carrier is confined inside a trap, it cannot assist with the overall generation of photons or photocurrent. Besides organic photonic devices, traps are also known to cause a shift in turn-on threshold voltage in organic field effect transistors (OFETs) [94]. The issue of trapping is one of the key challenges facing physical chemists who are researching organics.

Charge carriers (and therefore current flow) can be considered to be 'hopping' from state to state in the localized densities previously mentioned. The hopping rate υ_{ij} between localized states i and j is known as the Miller-Abrahams rate [95]:

$$\upsilon_{ij} = \upsilon_0 \exp\left(-2\gamma r_{ij}\right) \begin{cases} \exp\left(\frac{E_j - E_i}{k_B T}\right) & \text{if } E_j \geq E_i \\ 1 & \text{if } E_j \leq E_i \end{cases} \tag{2.23}$$

where υ_0 is a pre-factor, γ is the inverse localization length, r_{ij} is the distance between localized states and $E_j - E_i$ is the energetic barrier that the charge carrier must overcome (as in Fig. 2.12).

2.6 The Bulk Heterojunction

In terms of PDs, in order to separate excitons into individual charge carriers, a larger energy is required than inorganics due to the high binding energy as mentioned in the previous section. To offer a solution to this problem, the concepts of electron donor and electron acceptor must be introduced. Electron donors have lower electron affinity (the difference between the band edge and the vacuum energy) than electron acceptors. It should be noted that a high electron affinity is desirable for electron acceptors and vice-versa for electron donors. It is possible to disassociate the exciton at the interface of an electron donor/acceptor configuration due to the unbalanced electron affinities (i.e. the unbalanced energy levels). In this thesis only radiative decay of excitons is considered (non-radiative decay is also possible as previous) and with the influence of an external voltage the generated electrons and holes are attracted to their respective electrodes. The bulk heterojunction (BHJ) is an interpenetrated blend of electron donor and electron acceptor that provides such an interface that is distributed across the entire photoactive area of the organic photonic device as illustrated in Fig. 2.13. The reason for interpenetration is due to the fact that radiative decay of excitons

depends on the distance of exciton generation from the electron acceptor-electron donor border (for distances $>$ 10 nm the exciton will not offer radiative decay [5]). BHJs were first introduced in [96] and are popular in OPVs and OPDs due to the fact that they are soluble and provide extremely low cost processing [54].

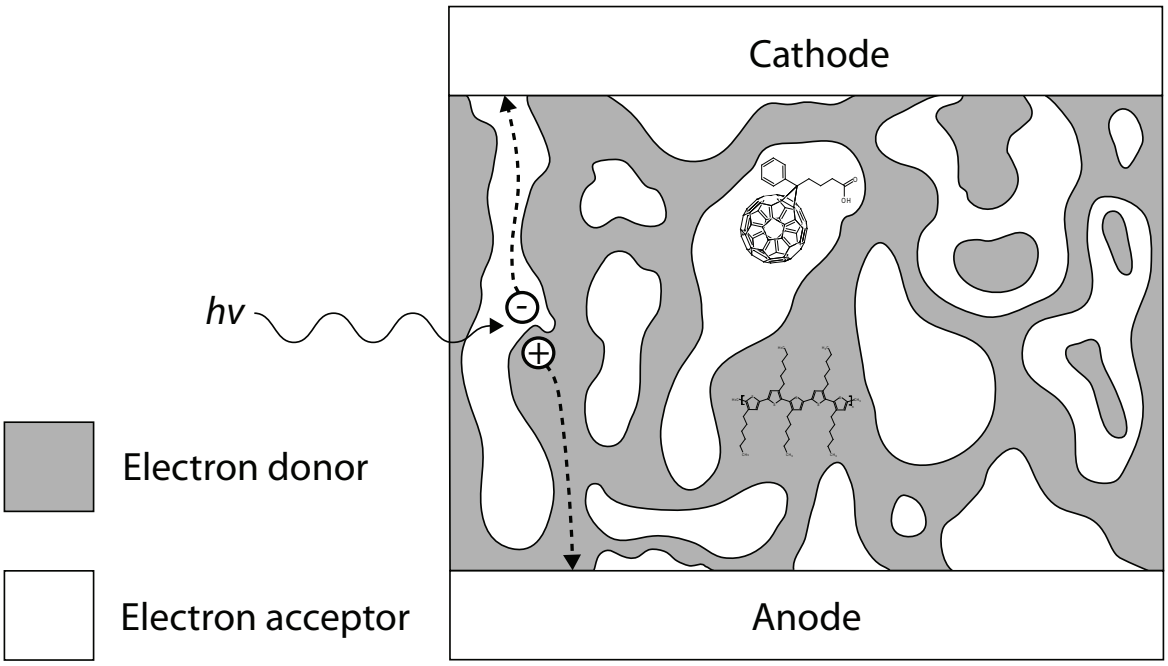

Fig. 2.13 The bulk heterojunction concept made up of electron acceptor and electron donor including electron acceptor and electron donor materials, PCBM and P3HT, respectively

As illustrated in 2.13 the materials selected for electron acceptor and electron donor are [6,6]-phenyl-C_{61}-butyric acid methyl ester (PCBM) and P3HT, respectively. PCBM is a Buckminsterfullerene derivative (the 1996 Nobel Prize in Chemistry was awarded for the discovery of Buckminsterfullerene) that offers the advantage of having high electron affinity to produce efficient electron transfer. PCBM is also soluble. P3HT is a conductive polymer (the 2000 Nobel Prize in Chemistry was awarded for its discovery) consisting of π–conjugated orbitals which are advantageous for photoactive devices. In this thesis, the OPDs are based on the BHJ principle and are manufactured by Siemens AG, Corporate Technology. Top and bottom view photographs of the OPD are provided in Fig. 2.14 and 2.15, respectively.

The bottom view features most of the features that are important to the OPD and a digitally produced model of the OPD highlights these key aspects in Fig. 2.16.

The OPDs share the aluminium electrode (the cathode) and have an individually structured anode that allows each diode to read out an independent data stream. The anode is made from indium tin oxide (ITO) which is a transparent conductive metal. The fact that

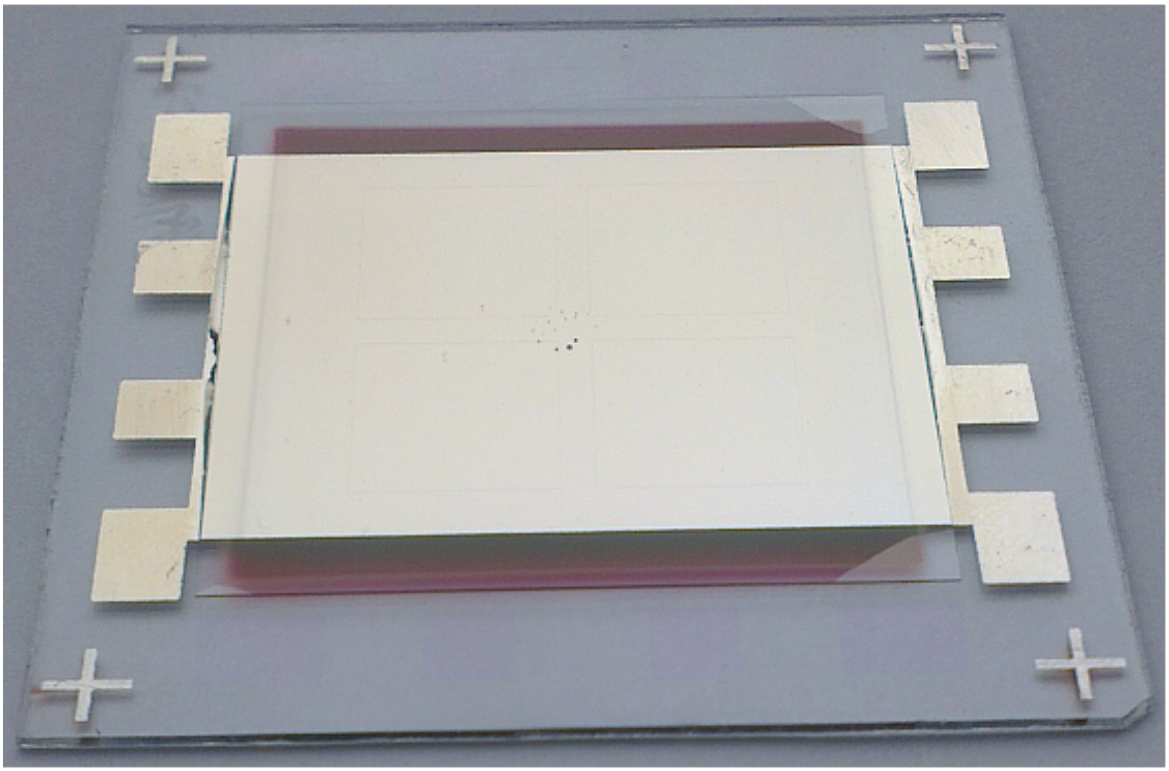

Fig. 2.14 Top view of the OPD used in this thesis

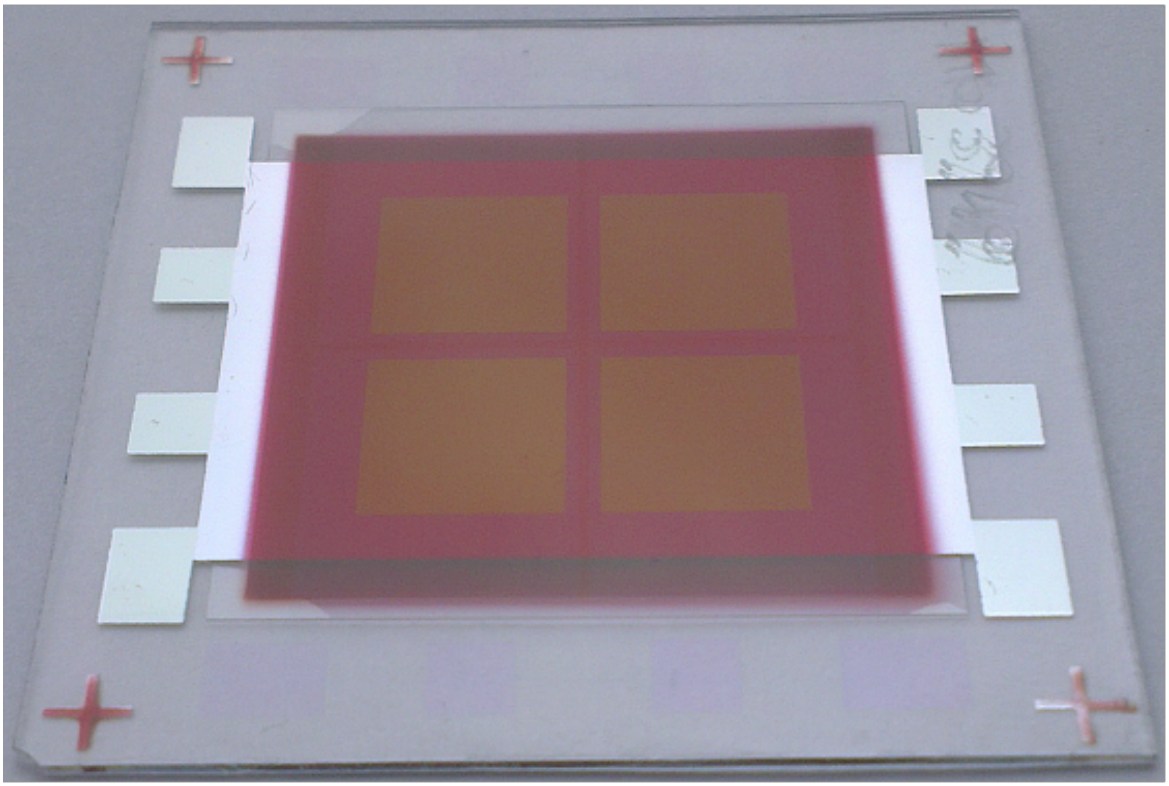

Fig. 2.15 Bottom view of the OPD used in this thesis (four 1 cm^2 diodes)

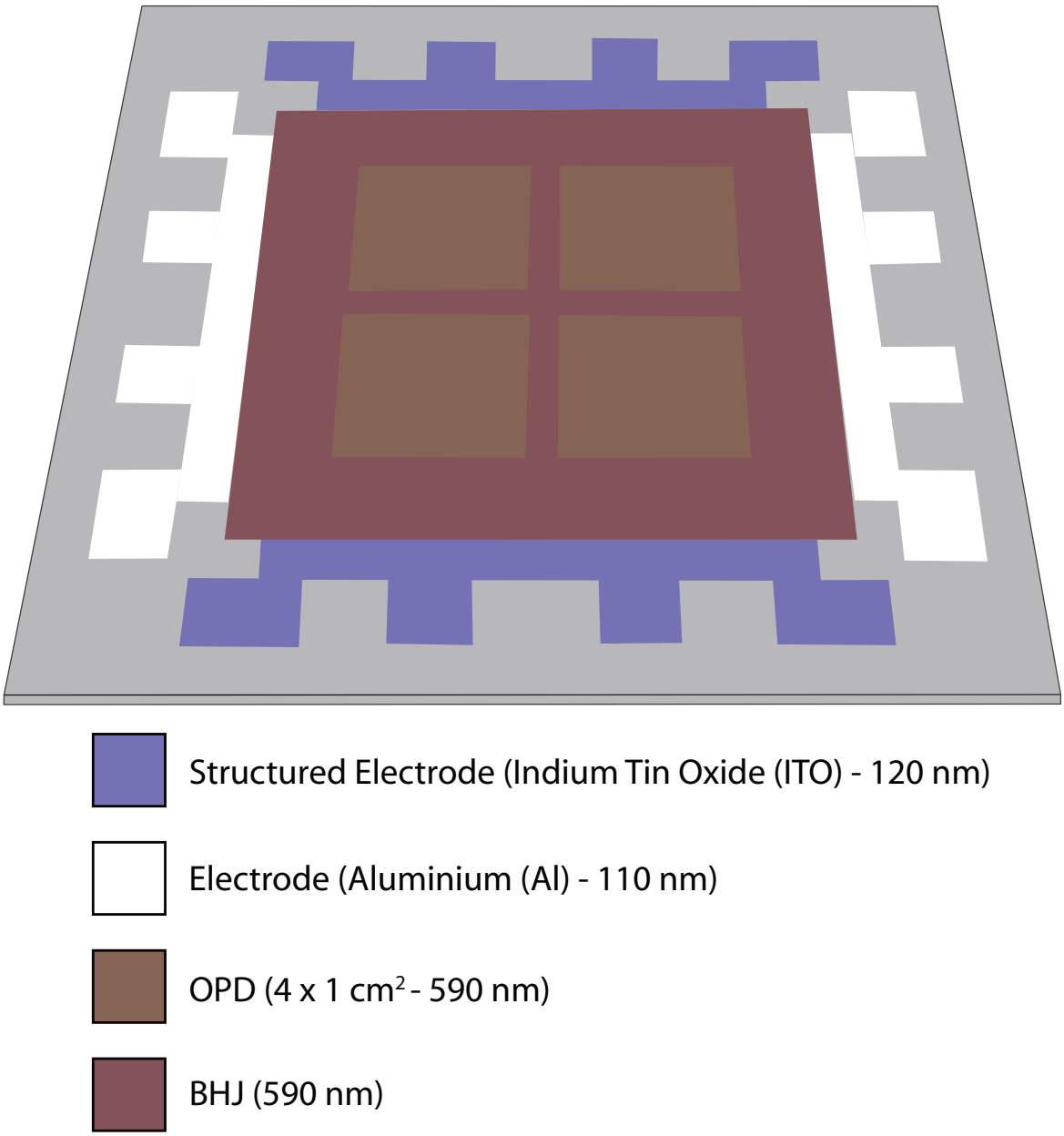

Fig. 2.16 Digital version of the OPD bottom view highlighting the key areas of the device

the ITO is structured leads to an arbitrary number of photoactive sections on the substrate, in this case 4×1 cm^2 devices. This is an important feature of the device as it immediately allows many applications that Si PDs cannot provide in such a simple manner. The most important application for a communications system is multiple-input multiple-output (MIMO), a highly parallel transmission scheme that is covered later in this thesis [97]. Another notable application is position sensing. The BHJ is deposited using the spray coating technique proposed in [54] where the materials are dissolved into a solvent and sprayed onto

the substrate, offering significant cost reduction at the cost of surface roughness which can increase dark currents.

Each BHJ interface can be considered as a miniature $p-n$ junction leading to an expanded Shockley equation (Equation (2.10)) that defines the I-V relationship [5]:

$$J_{MPN} = J_0 \left[\exp \left[\frac{qV}{n_{ID} k_B T} \right] - 1 \right] \tag{2.24}$$

Notice that there is an extra term in the denominator of the exponential term. The additional term is the so-called ideality factor n_{ID} that takes into account bulk morphology as illustrated in Fig. 2.17. Clearly as $n \to 0$ the diode reaches the J_0 saturation current at $V \to 0$ which is advantageous since a lower bias voltage is required.

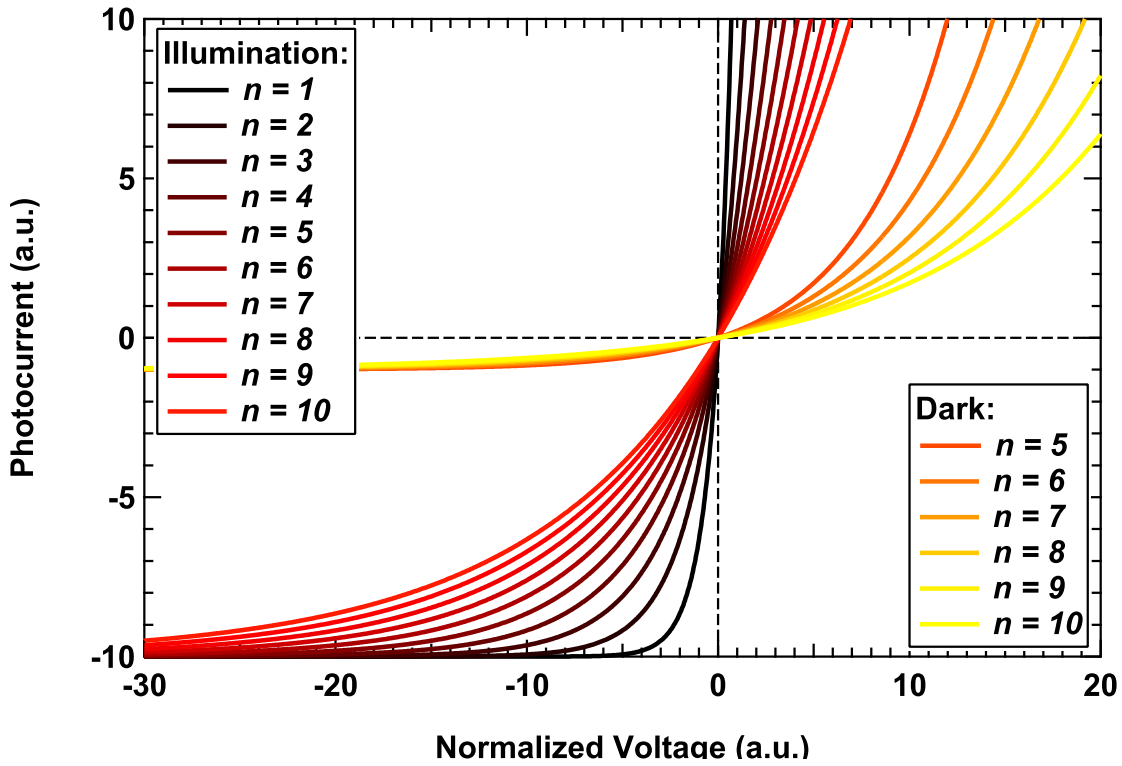

Fig. 2.17 Shockley equation for an expanded $p-n$ junction considering ideality factor n; the influence of n is illustrated here - clearly for decreasing n the diode reaches the saturation current with less bias voltage which is advantageous

Organic semiconductors are typically vertical devices and therefore some insight into the device structure must be given. The substrate can be almost anything in organics including paper [98], plastic [99, 100] and glass [54]. In this thesis the substrate for both the OLED and OPD is glass which is beyond the control of the author; device samples were

received from project partners and hence the material stacks are presumed to be optimized on the glass substrate. It would be extremely interesting to perform measurements with a flexible device in order to examine the effects on the communications performance under different flex stresses. The anode is generally made from transparent ITO although there is a growing argument for using graphene due to the emergence of high efficiency devices with graphene anodes [101]. The next layers are the organic layers. In state-of-the-art OLED devices the organic layers are made up of (from bottom to top) a hole injection layer, a hole transport layer, an emissive layer, an electron transport layer, an electron injection layer followed by the cathode which is generally aluminium since it is cheap and not necessary to be transparent. There are many devices that offer an increase in performance at the cost of increased complexity such as multiple photon emitters that are not covered here but are referred to in [71]. In BHJ OPDs the stack structure is significantly less complex; requiring only the two electrodes, the BHJ and an optional interlayer; selected as P3HT in this thesis because it offers the highest bandwidth [61]. The interlayer is not covered here, however it can have a profound effect on the performance of critical parameters of the device such as bandwidth; for a detailed analysis, refer to [61]. As mentioned, the BHJ is an interpenetrated blend of P3HT:PCBM which are extremely popular materials in BHJ devices due to their relatively high efficiency and solubility. The band gap energy of P3HT:PCBM is ~ 2 eV which is ideal for VLC applications as the cut-off wavelength is ~ 650 nm which cuts a portion of the red wavelengths that would possibly be useful for WDM. By introducing a further, low band gap material into the BHJ blend such as poly[2,6-(4,4-bis-(2-ethylhexyl)-4H-cyclopenta[2,1-b;3,4-b']dithiphene)-alt-4,7-(2,1,3-benzothiadiazole)] (PCPDTBT) the BHJ band gap can be reduced so the absorption spectrum extends into the NIR region and allows the absorption of such wavelengths. The working principles of P3HT:PCBM and similar BHJs are well covered in literature and the reader is encouraged to refer to [5, 54, 96] since no details are given here.

2.7 Summary

In this chapter, the prerequisite theoretical knowledge for organic semiconductors is outlined, starting with the essential band theory from inorganic semiconductors, including the generation and absorption of photons. This is subsequently related to the dislocated clouds of charge carriers that exist in organic semiconductors due to the linear combination of orbitals. The HOMO and LUMO energy levels are introduced and are related to inorganics for the readers understanding. Finally details of the OPDs used in this work are provided.

Chapter 3

Principles of Visible Light Communications

3.1 Introduction

In this chapter the basic theory of VLC is outlined plus the theory of the modulation schemes. There are a number of possible link configurations as illustrated in Fig. 3.1. Firstly there is the directed line-of-sight (LOS) method where the LED is pointed directly at the receiver with no offset in order to maximize SNR and hence increase the data rate until there the bandwidth limitations are met. Another LOS configuration is the non-directed link which essentially provides the system with mobility and aims to flood the receiving plane with optical power. There are also some non-LOS (NLOS) configurations shown where the link relies on reflections from the walls and ceiling to receive the data. The difference between the directed and non-direct configurations is just the focusing of the beam; that is to say that the directed NLOS method requires either beam tracking or no mobility in order to recover the data and the non-directed NLOS configuration (often called diffuse) does not care about the position of the PD on the receiving plane. This thesis focuses on the directed LOS topology since it offers the highest SNR and is the most popular VLC topology. Further, as was shown in the previous chapter the bandwidth of the OPD is directly proportional to the incident light density and it is desirable to maximize this constraint in order to maximize the system capacity.

The block diagram of a typical VLC system is shown in Fig. 3.2. A pseudorandom binary sequence (PRBS) x_i is generated either by MATLAB or by a field programmable gate array (FPGA) using shift registers. The data must then be formatted into an appropriate modulation scheme d_i, generally non-return-to-zero OOK and L^{th} order PPM are used in

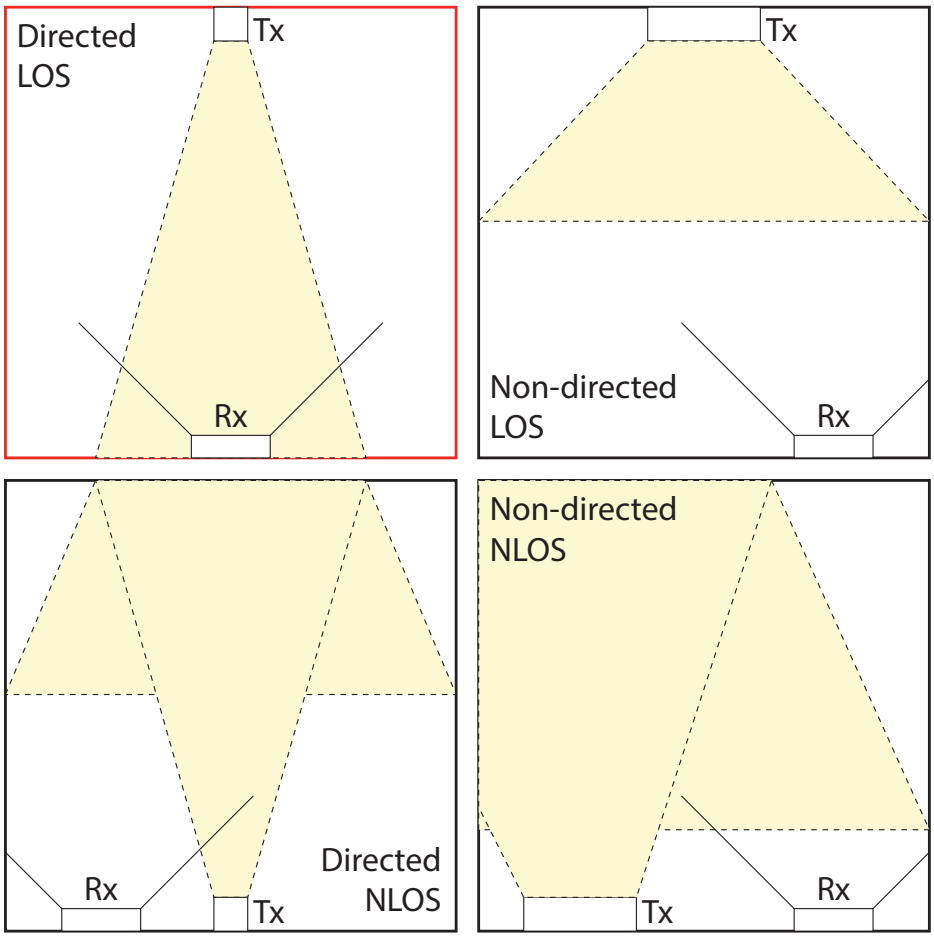

Fig. 3.1 Possible VLC link configurations - highlighted in red is the one used in this thesis

VLC systems. The data must then be passed through a pulse shaping filter $R(t)$ with unit height and symbol duration width to convert the samples into a rectangular pulse $g(t)$ (or raised cosine, or any shape of filter).

Optical power must be non-negative and satisfy the following condition:

$$x(t) \geq 0 \tag{3.1}$$

where $x(t)$ is the continuous optical signal. Therefore the signal must be superimposed onto a bias current using a driving circuit, denoted by $g'(t)$. The intensity of light is a continuous signal $x(t)$ with amplitude P_t (Watts), which can vary depending on the modulation scheme

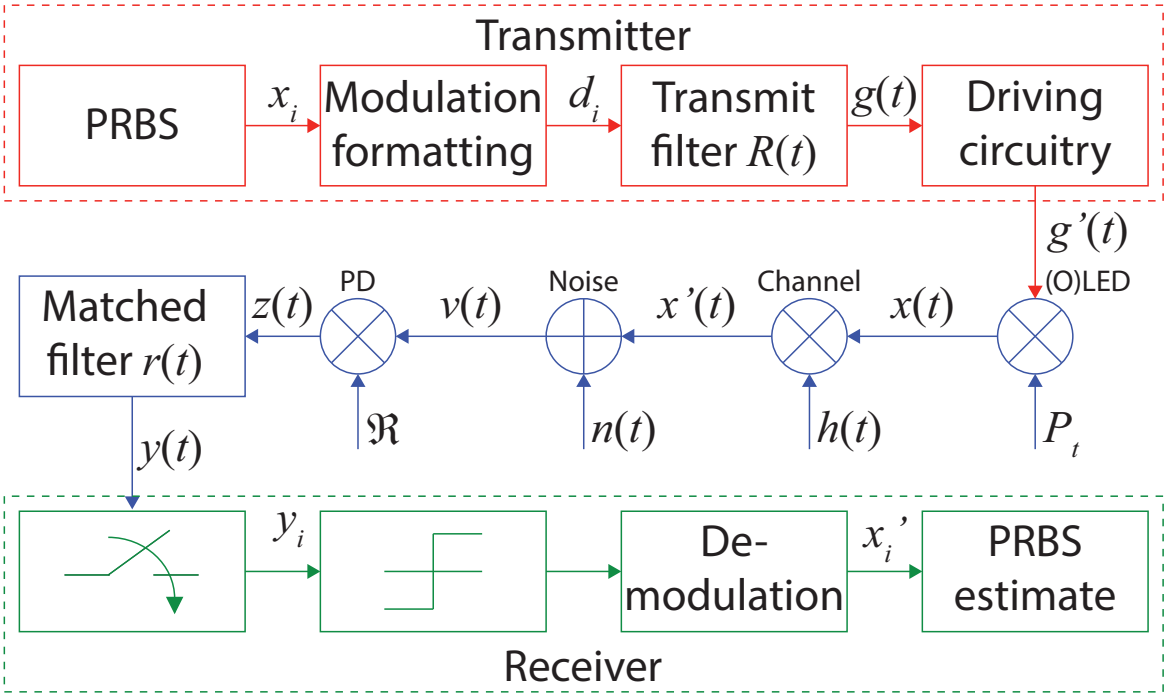

Fig. 3.2 Block diagram of a typical indoor VLC link

as is outlined later in this section. The average power P_{avg} given by [17]:

$$P_{avg} = \frac{1}{2T} \int_{-T}^{T} x(t)\, \mathrm{d}t \tag{3.2}$$

The optical source in VLC links is generally an (inorganic or organic) LED that follows Lambert's cosine law, that is [102]:

$$R_0(\theta) = \frac{m+1}{2\pi} \cos(\theta)^m \tag{3.3}$$

where R_0 is the luminous intensity, θ is the angle of emission and m is the Lambertian order given by [17]:

$$m = -\frac{\ln(2)}{\ln\left[\cos\left(\theta_{1/2}\right)\right]} \tag{3.4}$$

where $\theta_{1/2}$ is the transmitter semi-angle, note the negative operator. Only when $m = 1$ ($\theta_{1/2} = 60°$) is the source a Lambertian transmitter, while the source gets more directed for increasing m. In Fig. 3.3 several generalized theoretical Lambertian radiation patterns are plotted for a series of Lambertian orders. The curved axis shows the angle of observation in

degrees while the flat axis is the normalized emission intensity. Lambertian emitters ($m = 1$) have the same perceived intensity at any observation angle, unlike any other value for m. It is assumed that $m = 1$ for WPLEDs and OLEDs as has widely been reported [103, 104].

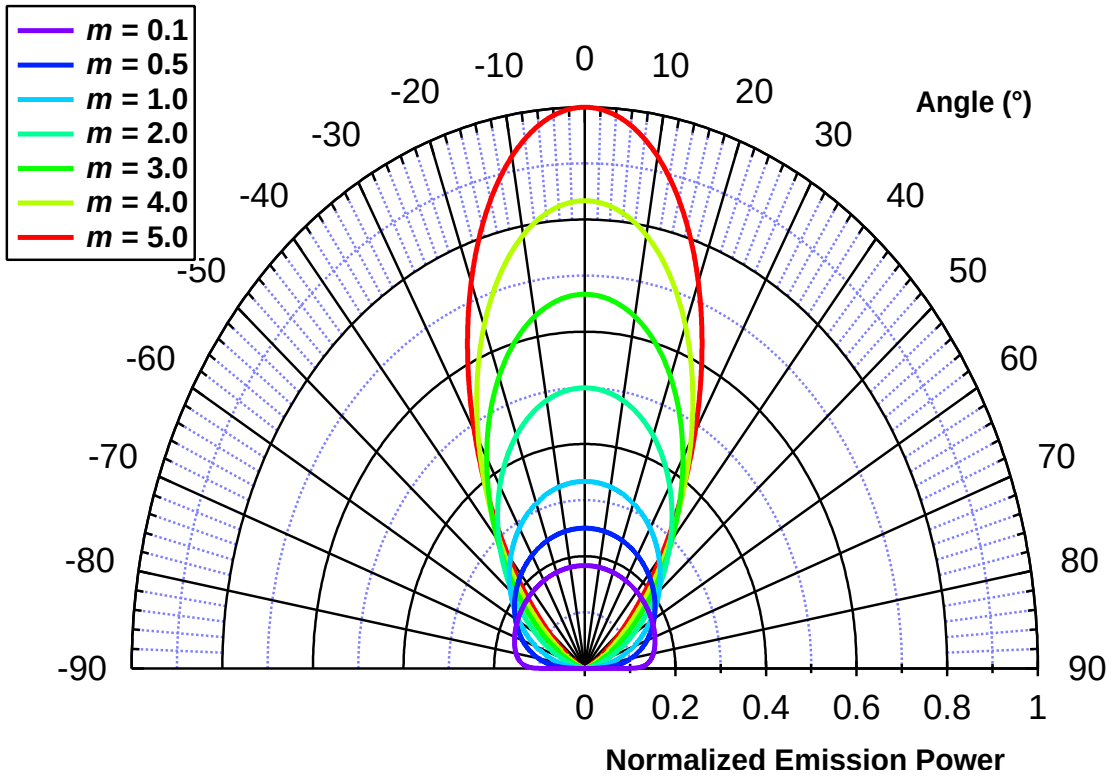

Fig. 3.3 Lambertian emission profiles of several Lambertian orders

In order to maximize the luminous intensity it is necessary to set $\theta = 0°$ and thus directed LOS link will provide the best signal quality. While it is possible to use external modulation methods such as a Mach-Zander modulator (MZM) in fibre optic links, to date VLC has exclusively used intensity modulation, where the electrical signal amplitude is reflected in the intensity of the optical power. Each device has a transfer function known as the L–I curve, where L is the optical power and I is the drive current) and an example of intensity modulation is illustrated in Fig. 3.4. The operating point is selected due to its linearity. Each device has a pseudo-linear and safe operating region where extended operation can occur. If the drive current is pushed into the roll-over region or beyond signal distortion can occur in conjunction with significant device degradation. Next, the indoor channel $h(t)$ must be taken into account. The intensity of the optical power transmitted over the channel drops by a factor of $1/d^2$, where d is the distance to the receiving plane.

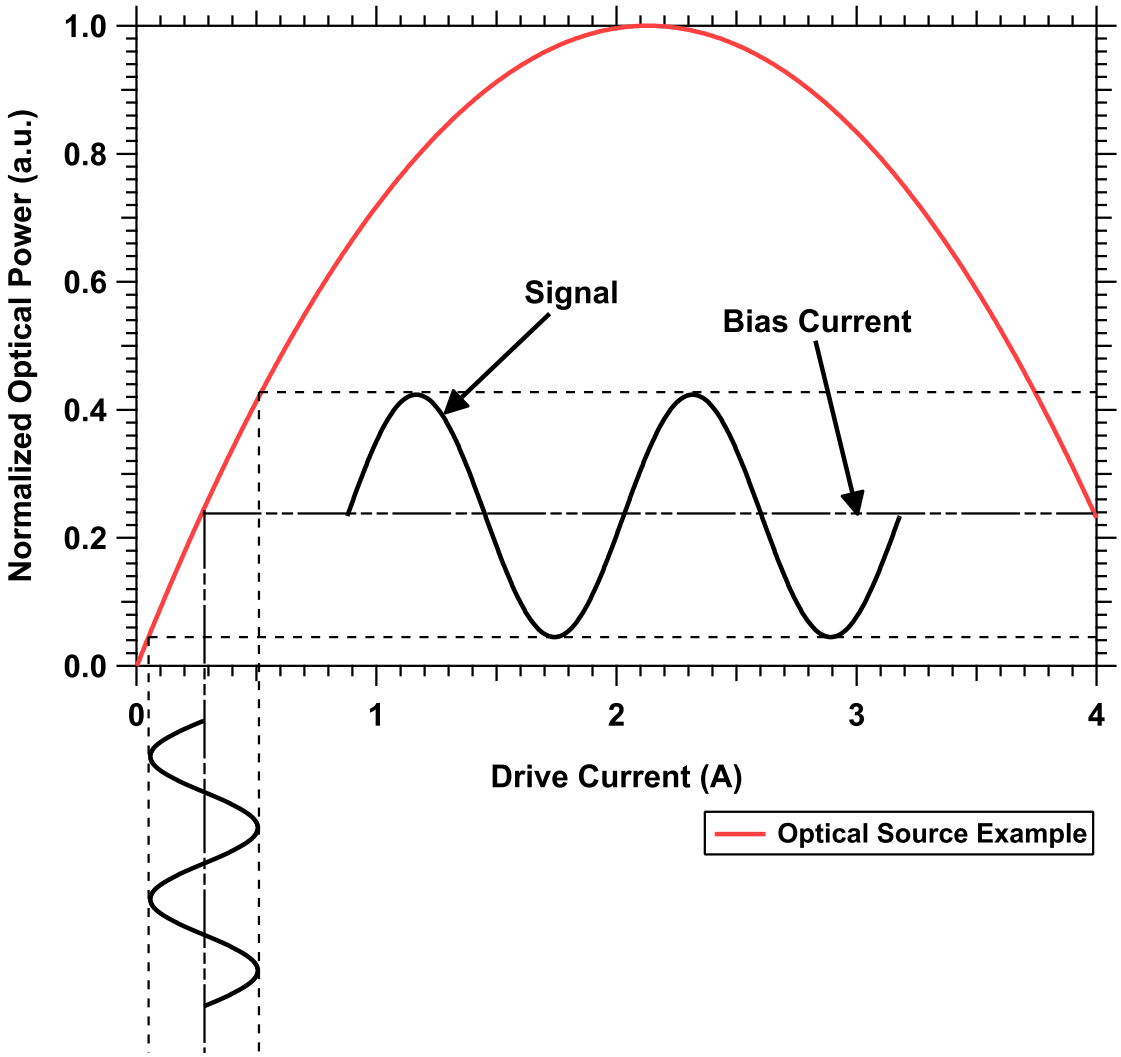

Fig. 3.4 Example L-I curve for intensity modulation of an optical source

The channel can be described either in terms of the impulse or frequency response, i.e.:

$$H(f) = \int_{-\infty}^{\infty} h(t)\, e^{-2\pi f t}\, \mathrm{d}t \tag{3.5}$$

The frequency response is the most popular choice, as the channel $H(f)$ represents a DC gain less than unity [17, 26]:

$$H(0) = \frac{A_r}{d^2} R_0(\theta) \cos(\varphi) \tag{3.6}$$

where A_r is the photoactive area of the PD and φ is the angle of incidence to the PD.

The main source of noise $n(t)$ in VLC links is shot noise which is independent of and uncorrelated to the signal. IR and thermal noise also contribute but they are considered negligible in comparison to the shot noise. The additive white Gaussian noise (AWGN) model can be adopted with single sided power spectral density N_0 [17, 105]:

$$N_0 = 2qI_D \tag{3.7}$$

where q is the charge of an electron and I_D is the PD dark current. The noise and channel perturbed signal, $v(t) = x(t) \otimes h(t) + n(t)$, (refer to Fig. 3.2) is detected by a PD with responsivity $\Re$ which is less than unity for PIN PD.

The received optical power P_r impinging on the PD is given by:

$$P_r = H(0) P_t \tag{3.8}$$

Clearly neither the wavelength nor the signal frequency influences the average received optical power and there are no non-linear affects for the wavelengths and frequencies concerned. It is not clear where this assumption breaks down and non-linear effects occur because in general the bandwidths of the components are significantly lower than the channel. The photocurrent denoted $z(t)$ is generally converted into a voltage by a transimpedance amplifier (TIA) which is not shown in Fig. 3.2. The SNR at the receiver is given by [17, 105]:

$$SNR = \frac{(\Re P_r)^2}{R_b N_0} = \frac{\Re^2 H(0)^2 P_t^2}{R_b N_0} \tag{3.9}$$

It is well known that PDs are square law detectors, hence the square term. It is clear that the SNR is a function of the transmission speed. A higher transmission speed causes a reduction in SNR due to an enhancement of noise [17]. The reason for this is due to the additional bandwidth requirement causing a higher susceptibility to noise.

Typically a matched filter $r(t)$ is used in order to maximize the SNR at the receiver. The matched filter can only be used when the pulse shape is known at the receiver, i.e. in OOK and L-PPM links. The matched filter is simply a tool to ensure that the signal is at its maximum amplitude at the sampling instance and aims to undo the dispersion caused by the channel or bandwidth limitations. There are numerous methods including the use of the autocorrelation function, a transversal linear filter or the 'integrate and dump' method [106], which is the most simple and is outlined here. For the mathematical proof of the matched filter, refer to [106, 107].

The signal SNR is defined by the level of received power in comparison to the level of AWGN noise. The integrate and dump is a special case of the matched filter which

improves the SNR by performing the cumulative sum of the amplitude over the bit period, then returning to zero and repeating for the next symbol period. Therefore the amplitude at the output of the filter at end of the symbol period is much larger than the amplitude at any point before the filter, as can be seen in Fig. 3.5. The decision on the symbol can be made using a sampler that samples at the rate of the symbol duration when the amplitude is at its peak as indicated by the dashed line. Subsequently an average level threshold can be used to decide the absolute level of the bits.

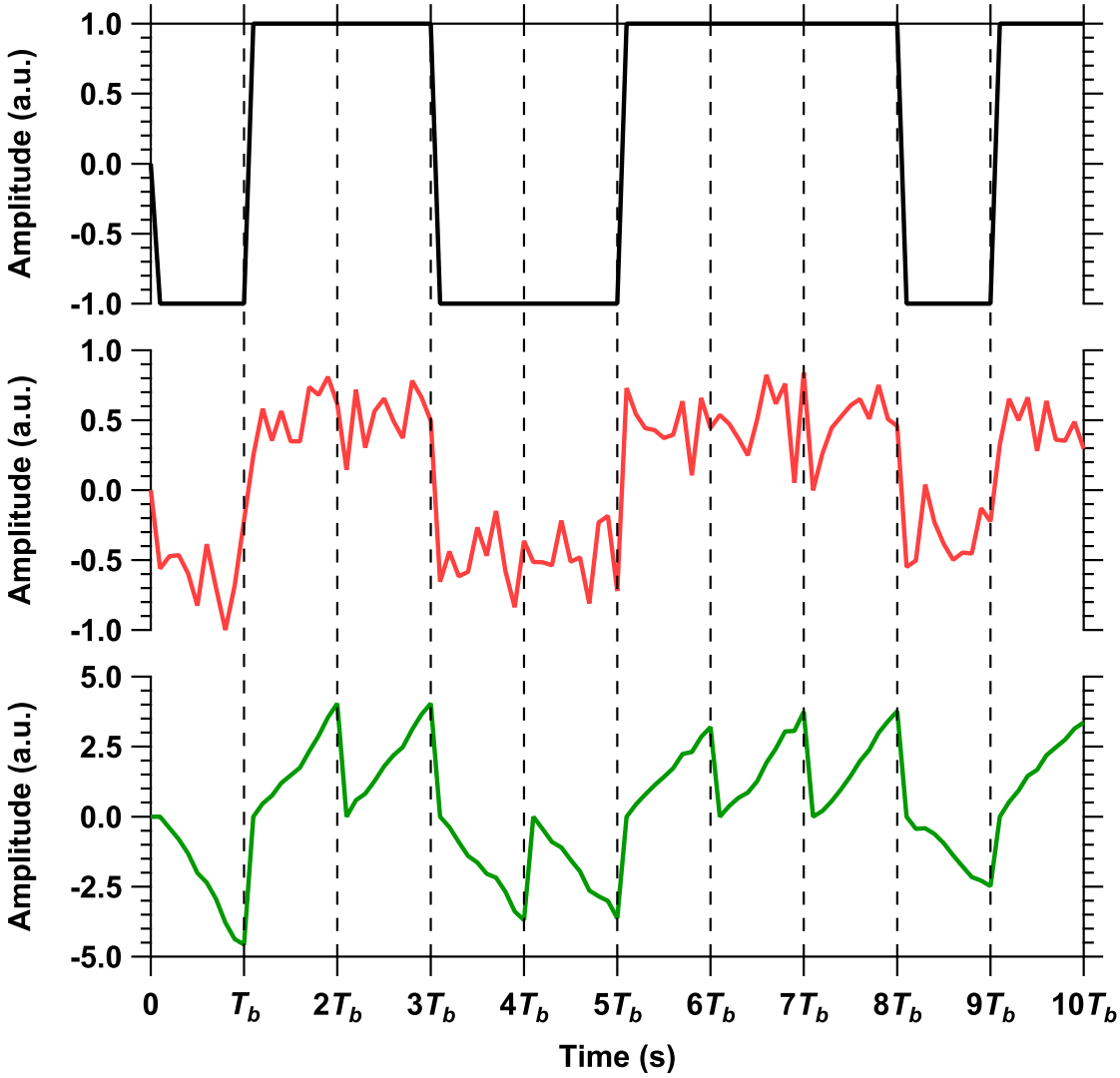

Fig. 3.5 Operation of matched filter; the data (top) is perturbed by noise (middle) and the output of the matched filter (bottom) is much larger in magnitude in comparison to the noise level than the noisy signal (note the y-axis magnitude), which is reflected in an increased SNR

The data is then de-mapped from the modulation format and the BER performance is

measured, either by Q-factor or by exact comparisons between transmitted and received data. Typically in VLC, BER $= 10^{-6}$ is deemed sufficient [59]. Q-factor is given by:

$$Q = \frac{\upsilon_H - \upsilon_L}{\sigma_H + \sigma_L} \tag{3.10}$$

where υ_H and υ_L are the mean received voltages and σ_H and σ_L are the standard deviations of the 1-level and 0-level signals before being sliced, respectively. There are a number of modulation schemes in common use for VLC systems; the most popular are M-PAM and L-PPM. M-PAM offers unrivalled bandwidth efficiency while L-PPM is the most power efficient scheme. A block diagram for each modulation scheme is also presented with the various receiver topologies. The mathematical theory of each of the modulation schemes is covered here in order to understand their bandwidth, power requirements and probability of error performance and thus their suitability for future OVLC links.

3.2 Modulation Schemes

The reason no further modulation schemes other than M-PAM and L-PPM are selected is because of their bandwidth and power requirement characteristics, respectively. PAM is the most bandwidth digital modulation scheme (aside from QAM) while PPM is the most power efficient. This is reflected in Fig. 3.6 which shows the spectral efficiency of a number of modulation schemes at a BER target of 10^{-6} including phase shift keying (PSK) and frequency shift keying (FSK) which have characteristics closest to those of the modulation schemes under test. Every other digital modulation scheme offers performance somewhere between PAM and PPM so are not tested in this thesis. M-PAM/QAM approaches the capacity limit as $M \to \infty$ while L-PPM approaches the power limit under the same condition.

By far the most popular modulation scheme is OOK due to the simplicity of implementation and bandwidth efficiency [58]. OOK is the lowest order of M-ary pulse amplitude modulation where the order of modulation is $M = 2^k$ for $k > 0$. OOK is based on two levels so $M = 2$.

3.2.1 M-ary Pulse Amplitude Modulation

The intensity of the optical power is made proportional to the amplitude of the electrical current. Therefore in the case of unipolar OOK, in order to transmit a binary 1-level a pulse of energy is transmitted over the symbol period T_b. To transmit a binary 0-level there is an

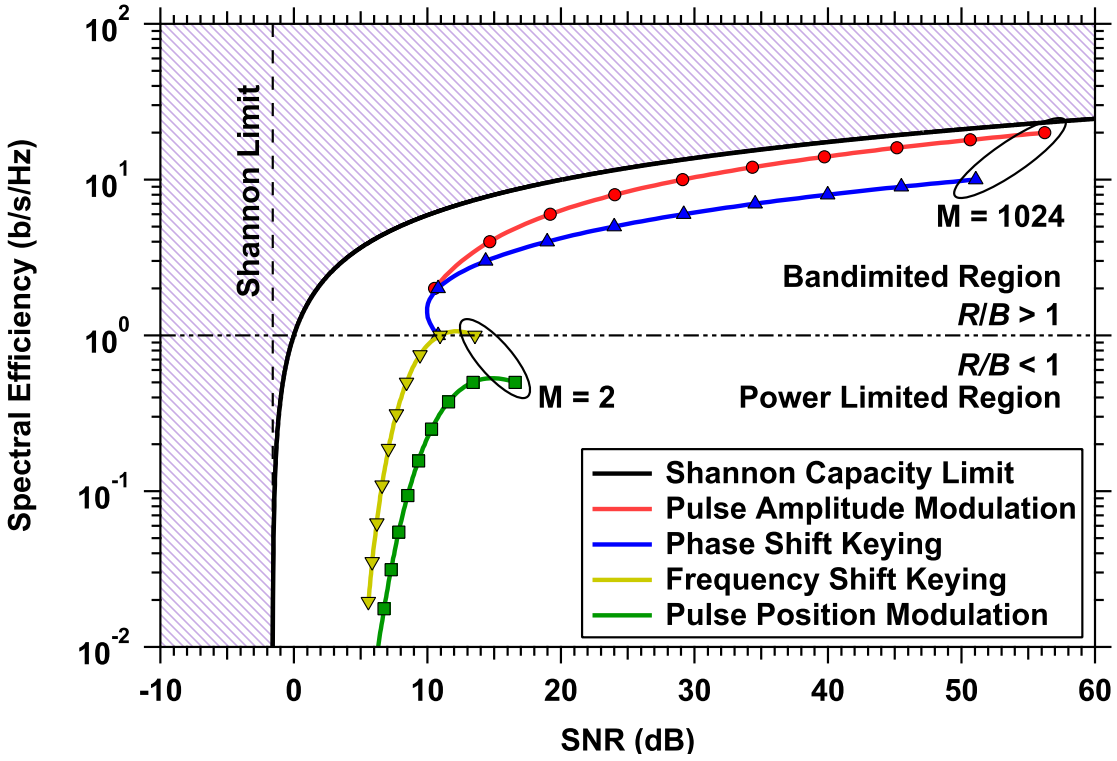

Fig. 3.6 Spectral efficiency of several modulation schemes as a function of SNR; all the modulation schemes are bound by the Shannon capacity where the untenable region is highlighted with a dashed line

absence of energy and the envelope is as follows [105, 108]:

$$p(t) = \begin{cases} P_0 & \text{if } 0 \leq t < T_b \\ 0 & \text{elsewhere} \end{cases} \tag{3.11}$$

where p is the M-PAM signal and P_0 is the transmitted power ($P_0 = 2P_{avg}$ if P_{avg} is the average transmitted power over the symbol interval). The mapping of OOK is shown in Fig. 3.7. The bandwidth requirement of M-PAM is given by [108]:

$$B = \frac{R_b}{\log_2 M} \tag{3.12}$$

where R_b is the bit rate. For a given bit rate, increasing the order of M increases the bandwidth efficiency of the system due to increasing the number of bits per symbol. The bandwidth requirement for a series of arbitrary bit rates is shown in Fig. 3.8. Decreasing the bandwidth requirement is a significant advantage in VLC systems as they are band-limited.

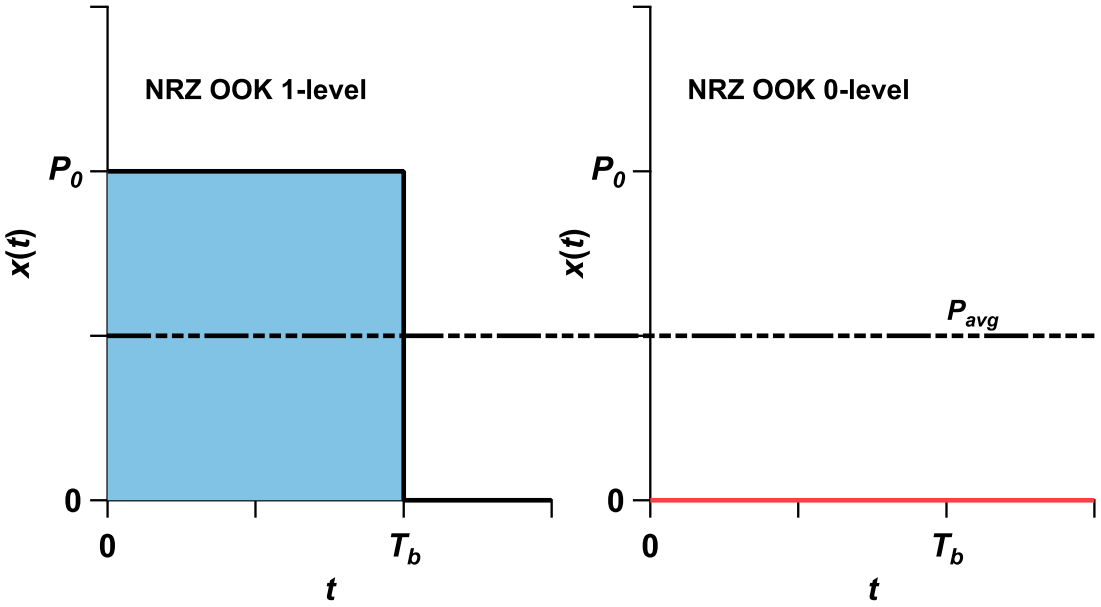

Fig. 3.7 Transmitted waveforms for NRZ-OOK for the 1- and 0-levels

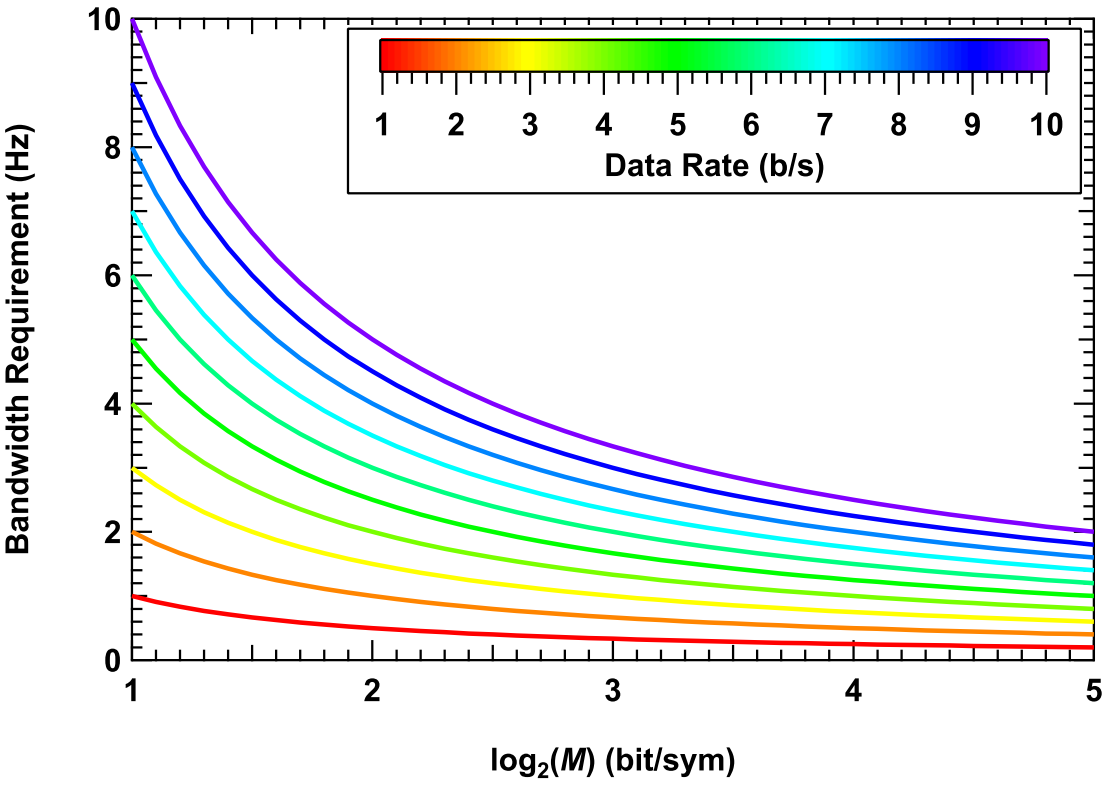

Fig. 3.8 Bandwidth efficiency of M-PAM, recalling that 2-PAM is OOK

The power spectral densities (PSDs) $P(f)$ of M-PAM are given by [105, 106]:

$$P(f) = (P_{avg}\Re)^2 T_b \left(\frac{\sin(\pi f T_b)}{\pi f T_b}\right)^2 [1 + R_b \delta(f)] \tag{3.13}$$

recalling that $\Re$ is the PD responsivity, f is the frequency and $\delta(f)$ is the Dirac delta function. The PSDs of several orders of M-PAM are plotted in Fig. 3.9. The x-axis (frequency)

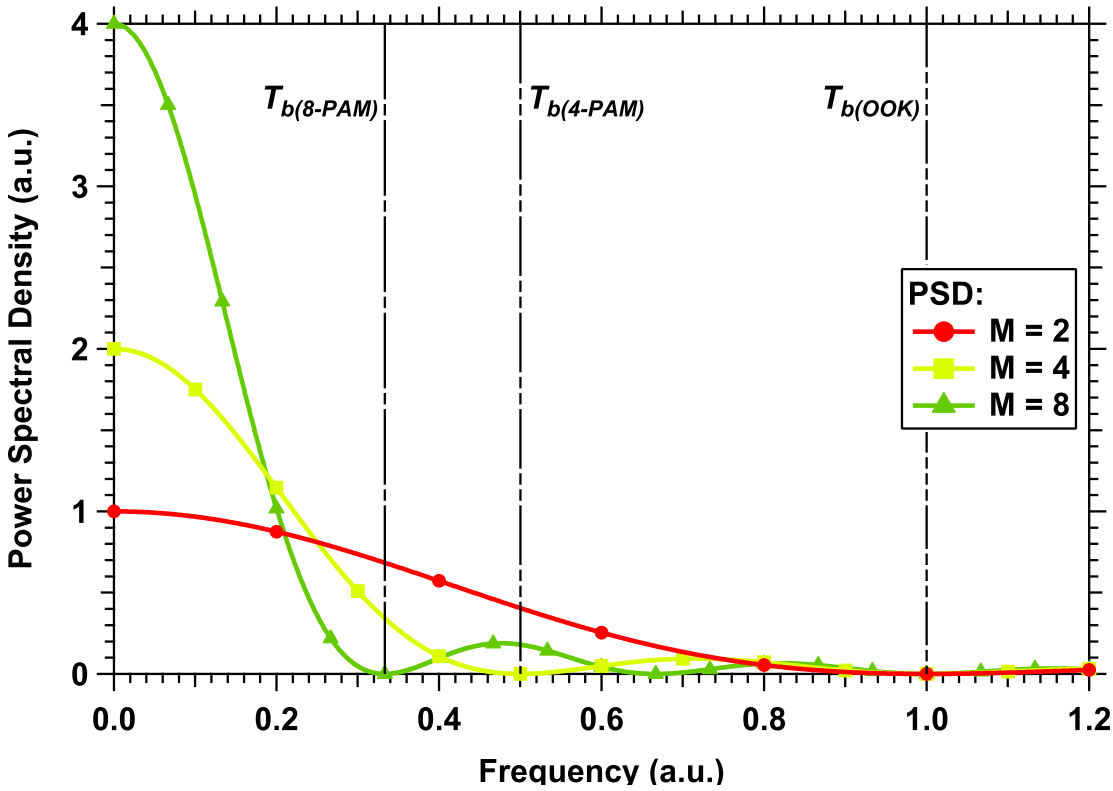

Fig. 3.9 Power spectral densities of M-PAM with box axes normalized to OOK

is normalized to an OOK bit rate of 1 arbitrary unit for $M = 2$ and the y-axis (PSD) is also normalized to OOK. Therefore it is clear that as the order of M increases, the power requirement also increases while the required symbol period a decrease, assuming that the transmission speed is the same and the distance between symbols is also equal in each case. Also noteworthy from Fig. 3.9 is there are significant spectral contributions around the DC and low frequency regions which can introduce the baseline wander phenomenon (that is described later in this Chapter) and make threshold detection impossible [41].

A system block diagram for M-PAM is shown in Fig. 3.10. The NRZ coded PRBS data x_i is passed through a rectangular unit-amplitude pulse shaping filter with a symbol period impulse response in order to produce a continuous signal. The output of the transmit filter

$g(t)$ is given by:

$$g(t) = \sum_{i=-\infty}^{\infty} x_i R(t - iT_b) \tag{3.14}$$

where i is the current bit and $R(t)$ is the pulse shaping rectangular transmit filter with unity height and length of a symbol duration. The signal is transmitted using an optical source; an (organic) LED with power P_0, given by $x(t)$. The signal is perturbed by noise $n(t)$ which is assumed to be dominated by the electrical shot noise; although background optical noise and thermal noise also contribute [17, 105].

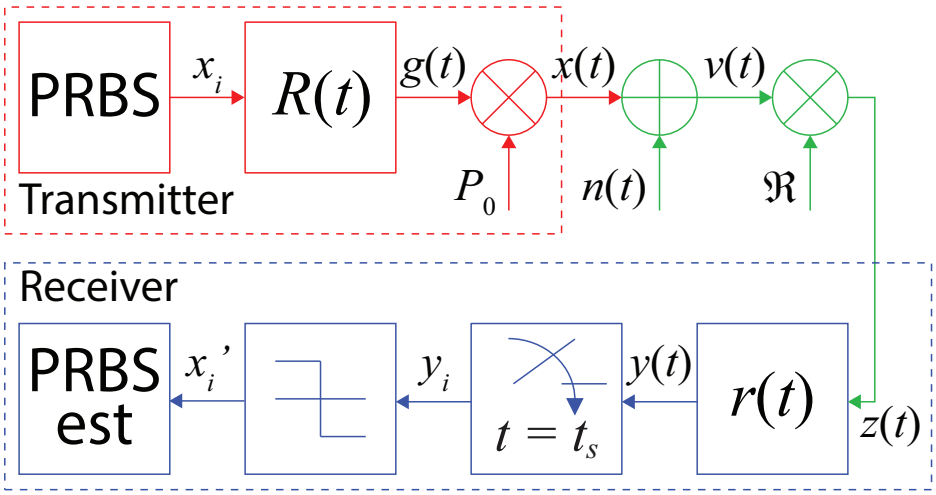

Fig. 3.10 OOK block diagram

The optical power is converted into electrical photocurrent by a PD. The PD responsivity $\Re$ is not constant for its operating range of wavelengths and therefore it must be factored in. The received photocurrent is given by:

$$z(t) = \Re \upsilon(t) = \Re[x(t) + n(t)] \tag{3.15}$$

where $\upsilon(t)$ is the noise influenced optical signal.

Assuming a system that has unlimited bandwidth, the maximum likelihood receiver is the best performing. A receive filter $r(t)$ is matched to the shape of the transmit filter in order to maximize SNR by cross correlation of the signal [109]. The signal is then sampled at the end of each symbol period and sliced with an average level threshold in order to find an estimate of the original data x_i'. The average level threshold Λ is given by [105, 108]:

$$\Lambda = \Re P_0 \sqrt{T_b} \tag{3.16}$$

Maximum likelihood detection induces decision regions due to the threshold as can be seen in Fig. 3.11 for the generalized M-PAM case.

Samples above the Λ_i threshold are assigned an $\Lambda_i + 1$ level and samples below are assigned the Λ_i level. The Euclidean distance between points is $2d$ and the probability of error depends on this distance as will be demonstrated later.

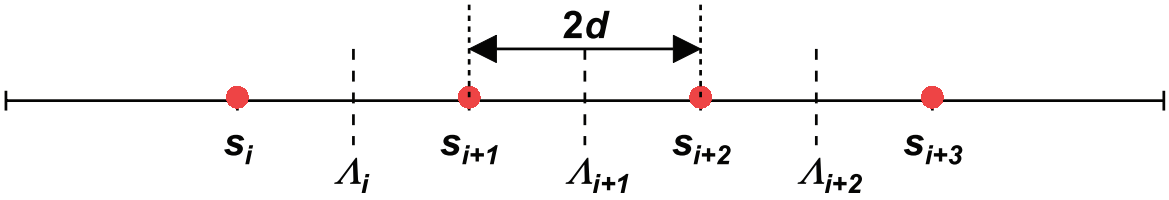

Fig. 3.11 Constellations for M-PAM

The output of the sampler is given by:

$$y_i = z(t_s) \otimes r(t_s) \tag{3.17}$$

where t_s is the sampling interval and $t_s = iT_b$ where i is an integer and $\otimes$ is the convolution operator. The matched filter is defined as follows [105]:

$$r(t) = \frac{p(-t)}{\sqrt{\mathscr{E}_p}} \tag{3.18}$$

where $\mathscr{E}_p$ is the energy in the received pulse which in the case of OOK is given by [105]:

$$\mathscr{E}_p = \begin{cases} (\Re P_0)^2 T_b & \text{if } a_i = 1 \\ 0 & \text{if } a_i = 0 \end{cases} \tag{3.19}$$

The probability of error P_e is given by [44]:

$$P_e = \frac{2(M-1)}{M} Q\left[\sqrt{\frac{2d^2}{N_0}}\right] \tag{3.20}$$

where d is given by [44]:

$$d = \sqrt{\frac{3\mathscr{E}_{av}}{M^2 - 1}} \tag{3.21}$$

$\mathscr{E}_{av}$ is the average transmitted signal energy which is related to the average energy per sym-

bol $\mathscr{E}_s = \mathscr{E}_{av}/\log_2(M)$, thus the probability of error can be rearranged as [44]:

$$P_e = \frac{2(M-1)}{M} Q\left[\sqrt{\frac{6\mathscr{E}_s \log_2(M)}{(M^2-1)N_0}}\right] \tag{3.22}$$

where $Q[.]$ is the well-known Q-function, $Q(x) = \frac{1}{2\pi}\int_{-x}^{\infty} \exp\left[\frac{t^2}{2}\right] \mathrm{d}t$ and $\mathscr{E}_s/N_0$ is the SNR for each symbol. The theoretical probability of error as a function of $10\log_{10}(\mathrm{SNR})$ is illustrated in Fig. 3.12. Taking a constant bit error rate of 10^{-6}, it is clear that an extra ~ 5 dB is required for increasing orders of M in comparison to the previous order.

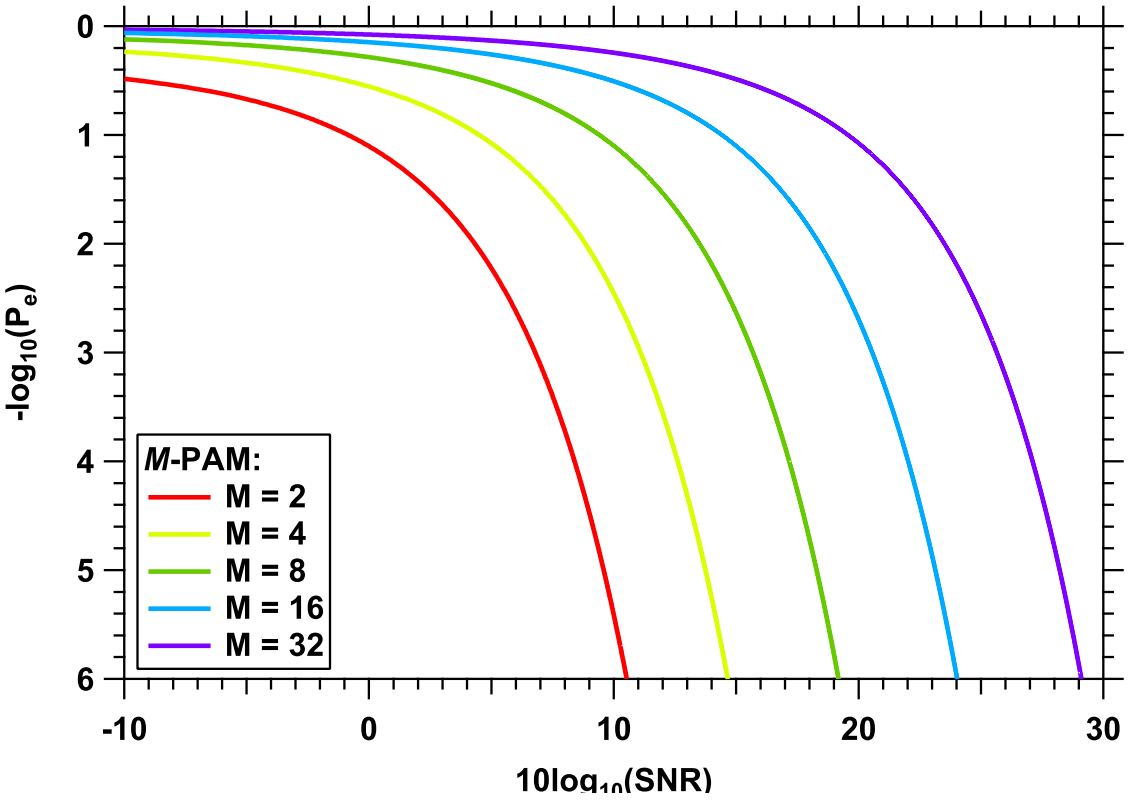

Fig. 3.12 Probability of error curves for increasing orders of M-PAM

3.2.2 L-ary Pulse Position Modulation

PPM is an orthogonal baseband modulation format that is popular in optical communications [29, 33, 110] due to its superior power efficiency to M-PAM. The format of L-PPM, where $L = 2^k$ is the modulation order ($k > 0$) is illustrated in Fig. 3.13 for 4-PPM.

The symbol period is split into L slots and a pulse of energy is placed into a solitary slot with the position of the pulse reflecting the value of the PRBS data, which is drawn from

the set $i = 0, \ldots, L\check{}1$. The rest of the slots are left empty. The slot duration T_L is found as follows [105]:

$$T_L = T_b \frac{i}{L} \tag{3.23}$$

The L-PPM envelope is given by [111]:

$$s(t) = \begin{cases} 1 & \text{if } (i-1)\,T_L \leq t < kT_L \\ 0 & \text{elsewhere} \end{cases} \tag{3.24}$$

The L-PPM signal $x(t)$ is therefore given by [111]:

$$x(t) = LP_0 \sum_{l}^{L-1} C_l R(t - lT_L) \tag{3.25}$$

where the L-PPM code word $C_l = [C_0,\ C_1,\ \ldots,\ C_{L-1}]$.

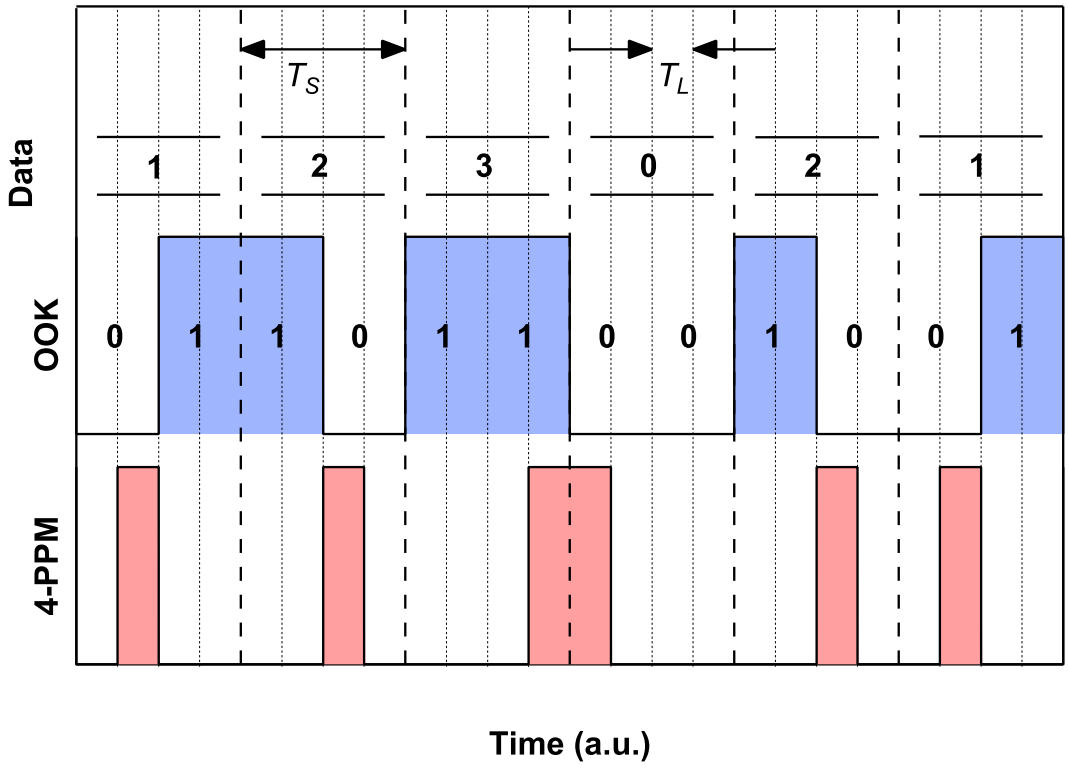

Fig. 3.13 Raw data code into the 4-PPM format with a comparison to OOK

The pulse shaping function $R(t)$ once more has unity height and duration T_L and LP_{avg}

is the peak optical power of the L-PPM symbol. The cost of the aforementioned power efficiency is an additional bandwidth requirement. The lowest two orders of L-PPM require twice the bandwidth of OOK while for $L > 4$ the requirement is much larger. The bandwidth requirement increases as follows [43]:

$$B = \frac{LR_b}{\log_2 L} \tag{3.26}$$

This is reflected in Fig. 3.14 where it is evident that the bandwidth requirement for any data rate increases as a function of $L/\log_2 L$.

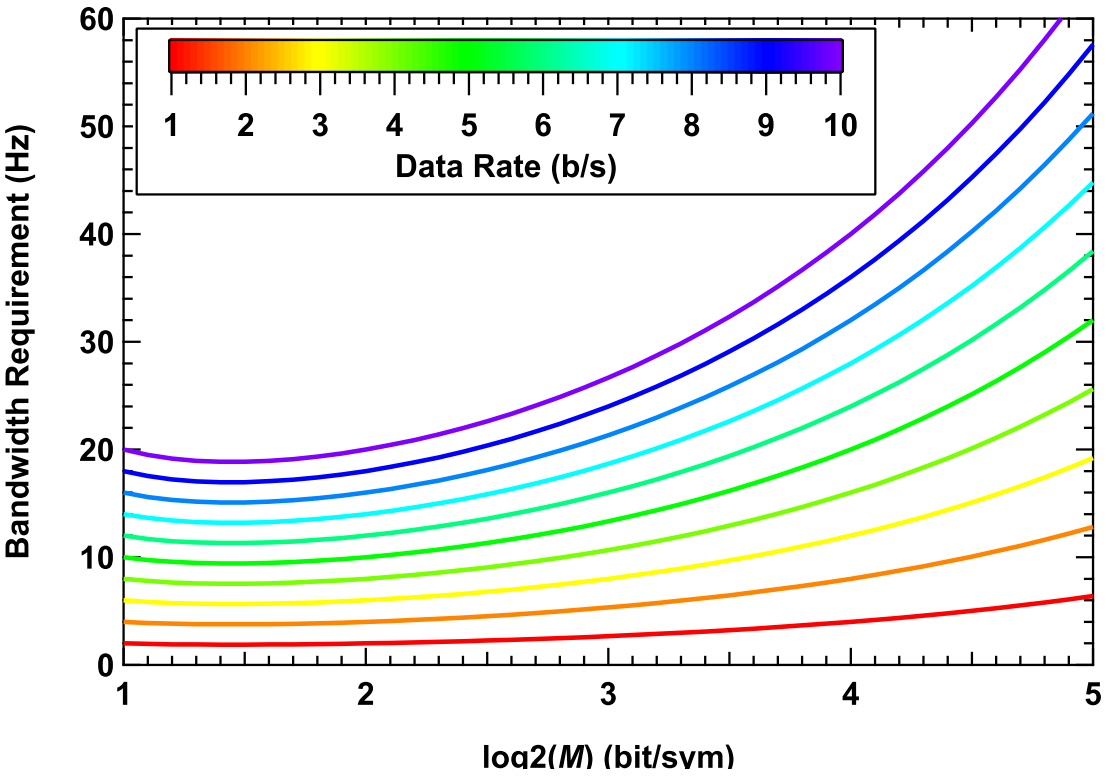

Fig. 3.14 Bandwidth requirements for L-PPM, note that for $L = 2$ and $L = 4$ the requirement is identical

In optical communications PPM is the most widely used modulation format [111, 112]. This is because typically the system and channel bandwidths far exceed the required data rate, and saving power is a much more important parameter. Further, due to the fact that energy exists in exactly one slot as L increases the DC and low frequency contribution is reduced. This is reflected in the power spectral density of L-PPM $\mathcal{S}(f)$ which are given by

[111]:

$$\mathcal{S}(f) = |\mathcal{R}|^2 [\mathcal{S}_c(f) + \mathcal{S}_d(f)] \tag{3.27}$$

where $\mathcal{R}(f)$ is the Fourier transform of the pulse shape and $\mathcal{S}_c(f)$ and $\mathcal{S}_d(f)$ are as follows [111]:

$$\mathcal{S}_c(f) = \frac{1}{LT_L}\left[\left(1-\frac{1}{L}\right) + \frac{2}{L}\sum_{l}^{L-1}\left(\frac{l}{L}-1\right)\cos(2\pi f l T_L)\right] \tag{3.28}$$

$$\mathcal{S}_d(f) = \frac{2\pi}{(LT_L)^2}\sum_{l=-\infty}^{\infty}\delta\left(f-\frac{l}{T_L}\right) \tag{3.29}$$

The bit rate is 1 arbitrary unit. It is clear that the bandwidth requirements increase as the order of L increases. Also it is important to notice that the spectral components around DC and the low frequencies are insignificant in comparison to M-PAM. This has several advantages including protection from baseline wander and artificial light interference due to high pass filtering [40, 41]. The PSDs are illustrated in Fig. 3.15.

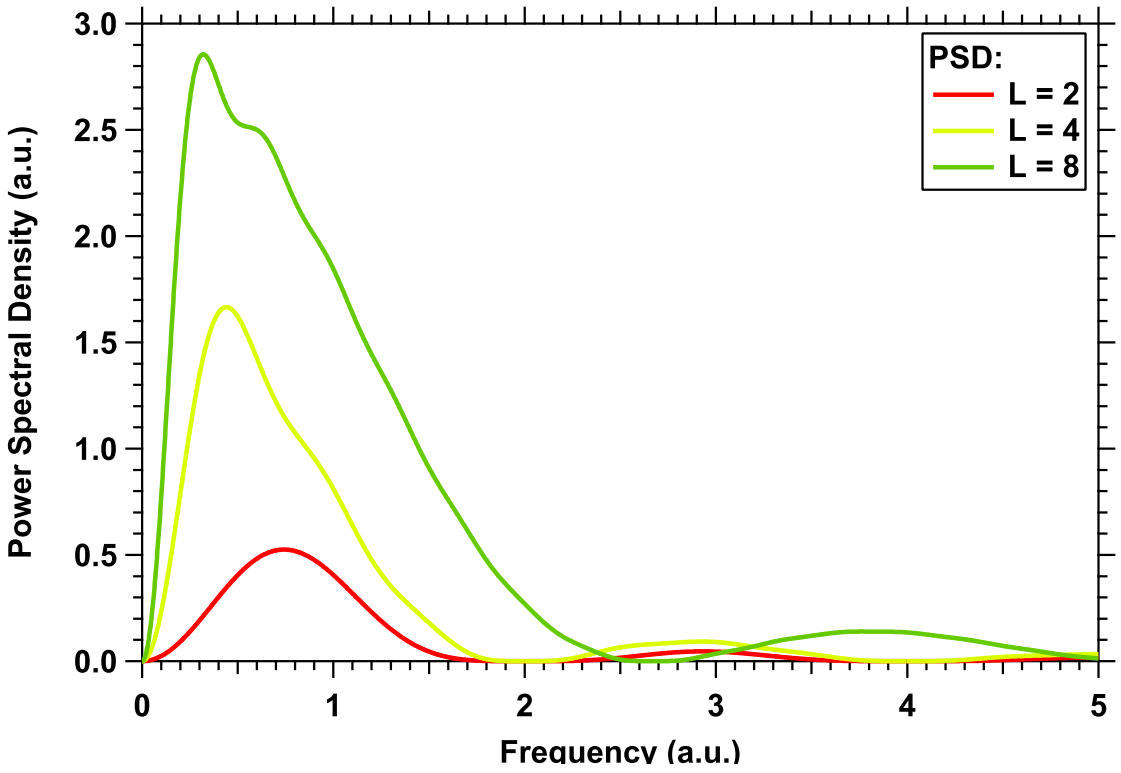

Fig. 3.15 PSDs of L-PPM; note that 2-PPM and 4-PPM have the same bandwidth requirement

A system block diagram for L-PPM is shown in Fig. 3.16.

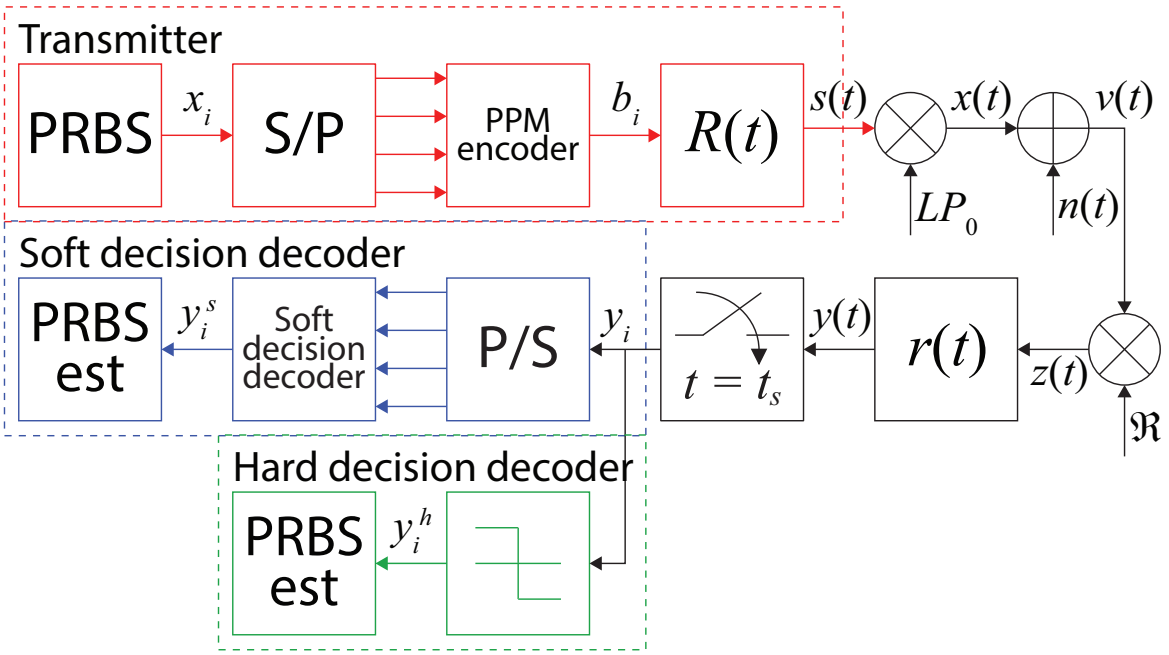

Fig. 3.16 L-PPM block diagram with both soft and hard decision decoding

The data a_i $(i = 0, \ \ldots, \ k-1)$ is generated and immediately converted into L parallel streams and passed through the transmitter filter $R(t)$. Similarly to OOK, the data is then transmitted by an optical source with peak power LP_{avg}. AWGN noise $n(t)$ is added and the signal is detected by the PD with responsivity $\Re$. A matched filter $r(t)$ with unit energy and impulse response equal to $R(t)$ is used to maximize SNR. There are two options for the receiver in an AWGN channel. Firstly there is the hard decision decoder using an average level threshold as in OOK. Secondly a soft decision decoder can be used, using maximum a posteriori or maximum likelihood detection, which offers a 1.5 dB gain in SNR over a hard decision decoder due to increased information for all slots [113, 114].

The hard decision decoder the average level threshold Λ_p decides whether to assign each slot a 1-level or a 0-level depending on the received amplitude. Recalling that the matched filter has unit energy and is rectangular in pulse shape, the peak output must be $\sqrt{E_L} = L\Re P_{avg}\sqrt{T_L}$ for the slot containing the pulse of energy and zero for all other slots. Thus, the probability of a slot error P_s for hard decision decoding is given by [105]:

$$P_s = \frac{1}{L}Q\left(\frac{L\Re P_{avg}\sqrt{T_L} - \Lambda}{\sqrt{N_0/2}}\right) + \frac{L-1}{L}Q\left(\frac{\Lambda}{\sqrt{N_0/2}}\right) \tag{3.30}$$

where $P(1) = L^{-1}$ and $P(0)$ is $(L-1)/L$ where $P(.)$ indicates probability. The probability

of a pulse is generally far exceeded by that of the probability of an empty slot by a factor of $L-1$ so selecting $\Lambda = \sqrt{E_L}/2$ is not optimal but is a good approximation [105, 111]and one that simplifies the slot error probability to [111]:

$$P_s = Q\left(\sqrt{\frac{E_L}{2N_0}}\right) \tag{3.31}$$

This can be converted into the bit error probability in order to make a like-for-like comparison with OOK as follows [111]:

$$P_e = \left(\frac{L}{2(L-1)}\right) - (1-P_s)^L \tag{3.32}$$

The probability of a bit error is illustrated in Fig. 3.17. It is clear that for increasing orders of L and a fixed probability of error (i.e. 10^{-6}) the power requirement is required, which is contrary to the M-PAM modulation format where the power requirement increases for higher orders of M.

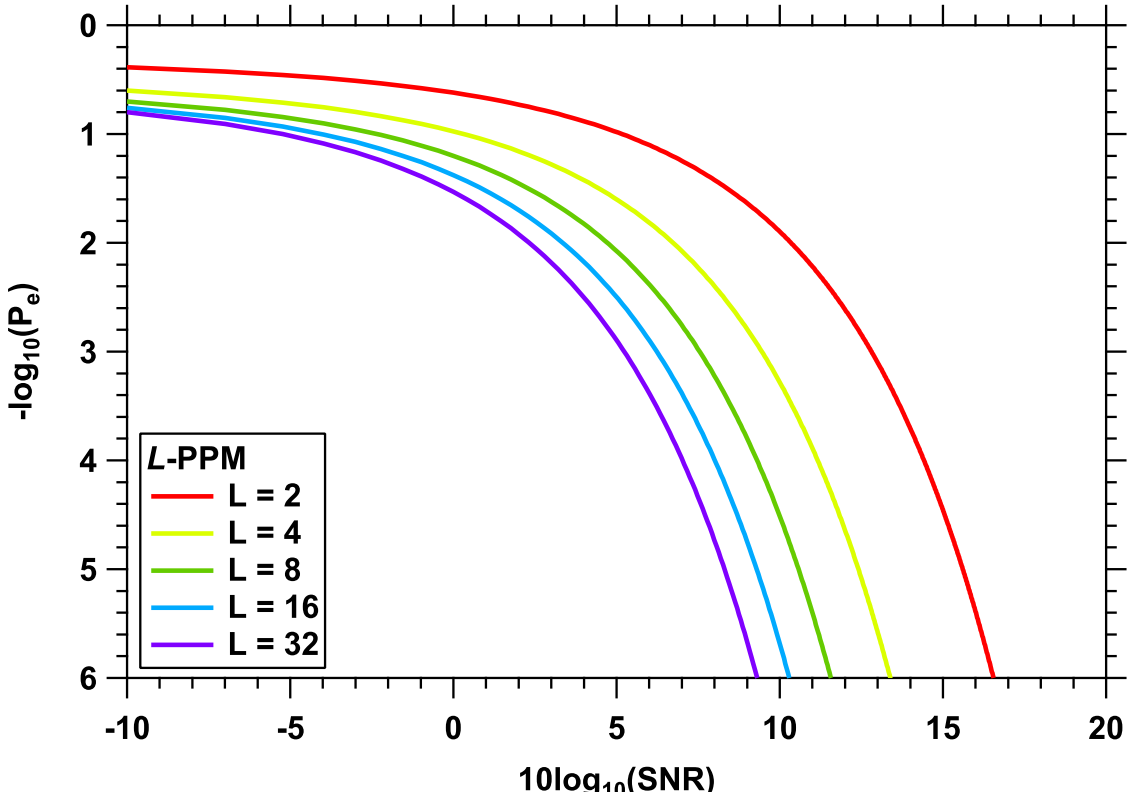

Fig. 3.17 Probability of error curves for increasing orders of L-PPM

Soft decision decoding treats the PPM signal as a block code. The output of the matched

filter is rearranged into an L-column matrix and selects the highest value as the 1-level and the remaining values as a 0-level, removing the reliance on a threshold as follows [115]:

$$y^s = \begin{bmatrix} 1 & 0 & 0 & 0 \\ 0 & 1 & 0 & 0 \\ 0 & 0 & 1 & 0 \\ 0 & 0 & 0 & 1 \end{bmatrix} \begin{bmatrix} y_i & y_{i+1} & y_{i+2} & y_{i+3} \end{bmatrix} = \begin{bmatrix} y_i \\ y_{i+1} \\ y_{i+2} \\ y_{i+3} \end{bmatrix} \tag{3.33}$$

Thus, a decision is made on which bit should be correctly assigned the 1-level. This method has been demonstrated to offer at least 1.5 dB gain in electrical SNR in non-directed LOS links such as the one implemented in this thesis.

3.2.3 Summary of Modulation Schemes

The modulation schemes used in this thesis, M-PAM and L-PPM have been outlined in detail and are summed up as follows. The key advantages are as follows: the bandwidth requirement of M-PAM is lower than any other modulation scheme other than M-QAM which requires an imaginary channel. An imaginary channel is not possible in VLC and therefore QAM cannot be implemented easily. Since OVLC systems are highly bandlimited it is desirable to aim for a modulation scheme that can transmit more symbols per bit with a bandwidth that is as small as possible. The next closest modulation scheme is M-PSK; however the bandwidth requirement for PSK is twice that of PAM. Furthermore, PSK is a pass-band modulation while PAM is a baseband modulation which is more suitable for the low-pass transfer functions exhibited in OVLC systems. The other modulation scheme under test is L-PPM which is the most power efficient scheme. This is also importance due to the electro-optic characteristics of OLEDs; i.e. commercial devices are not as efficient as inorganic LEDs yet and thus the lower optical modulation index must be taken into account. Therefore a power efficient modulation must be considered and there is no modulation scheme more power efficient than L-PPM currently. M-FSK is similar to PSK in that it is a pass-band modulation scheme. However, the power requirement is twice that of PPM. Therefore only PAM and PPM are considered in this thesis.

3.3 Equalization Theory

In this section the fundamental theory of equalizers is given. First equalization as an information theory problem and potential solutions are outlined. Then a different view is

procured where equalization is taken as a classification problem, which is the currently the best solution. The requirement for equalizers emerges when a system is bandlimited. Data transmission at a rate that exceeds the system bandwidth by a factor of two in OOK (the Nyquist rate) introduces a phenomenon called ISI where the symbol pulse energy exceeds the symbol duration and effectively "spills over" into successive symbols.

3.3.1 Equalization as an Information Theory Problem

The overall aim of an equalizer in its simplest form is to inverse the undesirable effects of the system response, generally expressed in consideration of the overall system frequency response as follows [59]:

$$H(f) = \frac{1}{Y(f)} \tag{3.34}$$

where $Y(f)$ is the Fourier transform of the output of the system response at the output of the matched filter, i.e. $Y(f) = \mathcal{F}\{R(t) \otimes g'(t) \otimes h(t) \otimes r(t)\} = R(f)G'(f)H(f)r(f)$, recalling that $R(t)$, $g'(t)$, $h(t)$ and $r(t)$ are the transmit filter, intensity modulation, channel and matched filter responses, respectively, whilst assuming that the optical transmission power and PD responsivity are unity in conjunction with negligible noise, referring to Fig. 3.18.

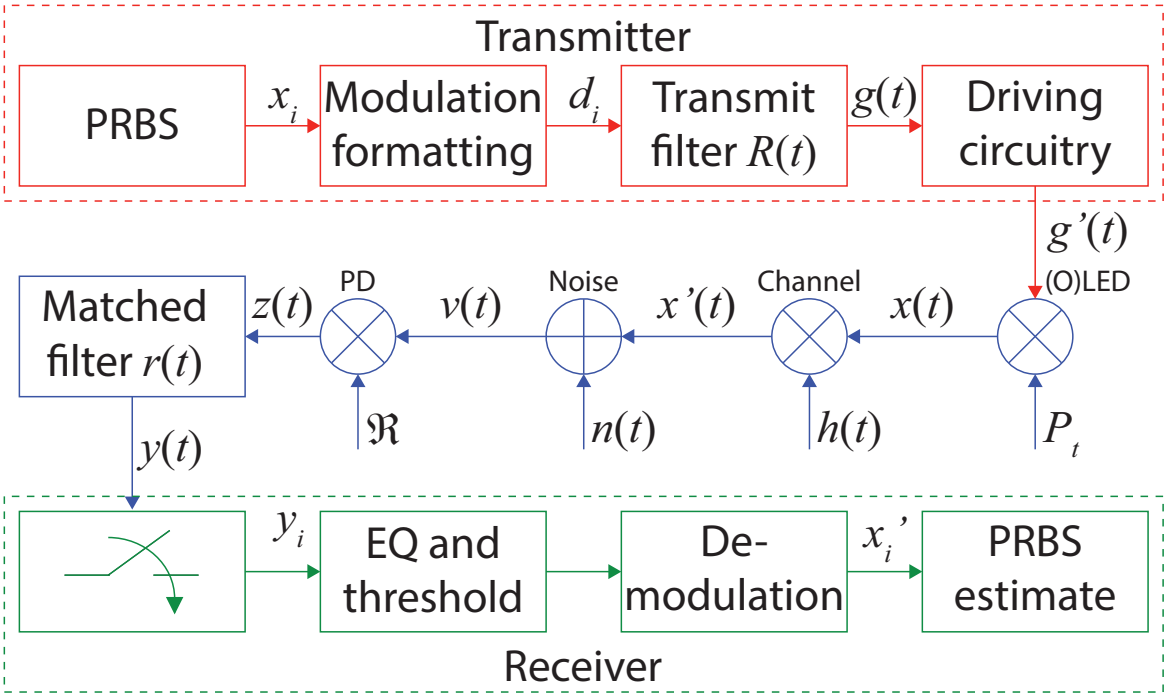

Fig. 3.18 General VLC block diagram with equalizer

Equalizers are typically used to equalize the channel response which can be dispersive or have fading properties in the outdoor environment. In this thesis the channel response is not being equalized as it is independent of wavelength and frequency, see equations (3.5)–(3.5). Therefore $H(f)$ is just a constant. The output of the matched filter can be listed as follows [116]:

$$y(t) = \sum_{k=-\infty}^{\infty} a_k p(t - kT_b) + n(t) \tag{3.35}$$

where $p(t) = R(t) \otimes g'(t) \otimes h(t) \otimes r(t)$ and a_k is the k^{th} OOK symbol. Assuming $y(t)$ is being sampled at a rate of $t_s = iT_b$ then the output of the matched filter becomes [116]:

$$y(t_s) = \sum_{k=-\infty}^{\infty} a_k p[(i-k)T_b] + n(t_s) \tag{3.36}$$

which can be expanded to [116]:

$$y(t_s) = a_i + \sum_{\substack{k=-\infty \\ k \neq i}}^{\infty} a_k p[(i-k)T_b] + n(t_s) \tag{3.37}$$

where a_i indicates the amplitude of the i^{th} received symbol. The summand indicates the contribution of ISI from the preceding and subsequent symbols to the system, and it is therefore possible to state that in order to achieve zero ISI, the following must be realised [116]:

$$p[(i-k)T_b] = \begin{cases} 1 & \text{if } i = k \\ 0 & \text{if } i \neq k \end{cases} \tag{3.38}$$

which would mean that the receiver output would become [116]:

$$y(t_s) = a_i \tag{3.39}$$

i.e. the system is not affected by ISI.

Considering the system response $p(t)$, the factor that is deteriorating the overall system response and introducing ISI is the low pass transfer functions of the organic devices as was demonstrated in Chapter 2. Equalizing the low pass response will allow the data rate to be increased significantly in the presence of a high SNR. It should also be noted that the equalizers do not equalize the effects of noise.

The system response is found by pilot signal and careful filter design is required in order to maximize the effectiveness of the equalizer. There are two main types of filter; analogue and digital. In the analogue domain a high pass filter RC equalizer is the only real choice while in the digital domain the zero forcing (ZF) and the decision feedback (DF) equalizers are the most popular. Both types have intrinsic advantages and disadvantages which are documented here.

3.3.2 RC Equalizer

An RC equalizer consists of a resistor and capacitor arranged into a high pass filter that is placed between the data source and the optical source (pre equalizer), or the receiver and the terminal (post equalizer). The frequency response of the RC equalizer $H_{RC}(f)$ is given by [39]:

$$H_{RC}(f) = k^{-1}\frac{1+j2\pi f\tau}{1+\frac{j2\pi f\tau}{k}} \tag{3.40}$$

where $k^{-1} = R_L/(R+R_L)$ is the DC co-efficient of the RC equalizer, R is the equalizer resistor value, R_L is the load resistor (typically 50 Ω) and $\tau = RC$ is the RC time constant. The magnitude response is given by [39]:

$$|H_{RC}(f)| = k^{-1}\sqrt{\frac{1+4\pi^2 f^2\tau^2}{1+\left(\frac{4\pi^2 f^2\tau^2}{k^2}\right)}} \tag{3.41}$$

In order to equalize the low pass frequency response, the high pass slope must be opposite, i.e. $S_L = -S_H$ where S_L and S_H are the low and high pass filter slope responses, respectively, where S_H is given by [39]:

$$S_H = \frac{6\pi\tau}{\sqrt{\frac{1}{1-[2/k^2]}}} \tag{3.42}$$

Which leads to an approximate bandwidth B of [39]:

$$B \leq \frac{20\log_{10}(k)}{S_H} \tag{3.43}$$

Clearly, the bandwidth is dependent on k. Selection of k decides the margin of equalization for the system; a high value of k allows for more equalization and vice-versa. There is a restriction on the selection of k, however, it cannot be increased indefinitely. The restriction

is caused by the dynamic input range of the receiver $\Delta P = P_{max} - P_{sense}$, where P_{max} is the saturation power of the receiver and P_{sense} is the minimum power the receiver can sense controlled by the NEP. The restriction is given by [39]:

$$20\log_{10}(k) \leq \Delta P \tag{3.44}$$

The advantages of the RC equalizer are that it is extremely simple to implement and has been demonstrated experimentally to offer a significant improvement in data rate in VLC systems [39], however as is shown in Chapter 2, the improvement is not as large as can be provided with a classifying equalizer. The disadvantages are major. By introducing a high pass filter, there is an exponential power penalty that is introduced around the low frequencies. This is compounded by the fact that introducing that power penalty leads directly to the baseline wander effect due to the removal of the low frequencies.

The Baseline Wander Phenomena

BLW is a phenomenon whereby the signal randomly deviates from the DC level caused by the attenuation of the low frequency components by a high pass filter or coupling capacitor. The shape of BLW is can be expressed as an exponentially decaying tail of an isolated pulse is as follows [117]:

$$y(t) = \begin{cases} \frac{A}{2}\exp\{-2\pi f_c t\} & \text{if } 0 \leq t < T_b \\ -\frac{A}{2}\left(\exp\{-2\pi f_c T_b\} - 1\right)\exp\{-2\pi f_c t\} & \text{if } T_b \geq t \end{cases} \tag{3.45}$$

where A is the signal amplitude and f_c is the cut-on frequency of the high pass filter. The origin of the wander is clear; the contribution of each individual pulse is added at the output of the receiver by the principle of linear superposition as follows:

$$y(t) = \sum_{i=1}^{\infty} \frac{A_i}{2}\left(1 - \exp\{-2\pi f_c t\}\right)\left(\exp\{-2\pi f_c t\}\right)^{i-1} \tag{3.46}$$

Increasing the cut-on frequency increases the portion of the frequencies that are removed and the exponential decay becomes more severe. This concept is illustrated in Fig. 3.19 with eye diagrams inset for cut-on frequencies of $R_b/100f_s$, $R_b/10f_s$ and $R_b/2f_s$, respectively. The BLW phenomenon has an approximately Gaussian distribution [41, 111], as shown in Fig. 3.20, for $f_c = R_b/10f_s$, which shows the vertical histogram.

The normalized optical power penalty for varying f_c is shown in Fig. 3.21 which also shows 4-PPM and 8-PPM. Since BLW can be treated as non-white Gaussian noise [41, 111]

it also has variance σ^2_{BLW}, reducing the system SNR. The optical power penalty is a measure of how much extra power is required in order to achieve the same BER (10^{-6}) for the ideal AWGN system and is normalized to OOK for each modulation scheme [111].

Clearly, as expected for high cut-on frequencies the power penalty is more severe and increases exponentially. The performance of the analogue equalizer is limited by the BLW effect and is not a viable candidate for future OVLC systems as is experimentally demonstrated later in Chapter 5 and [9]. Therefore a move into the digital domain is required and the simplest digital equalizer is the ZF equalizer.

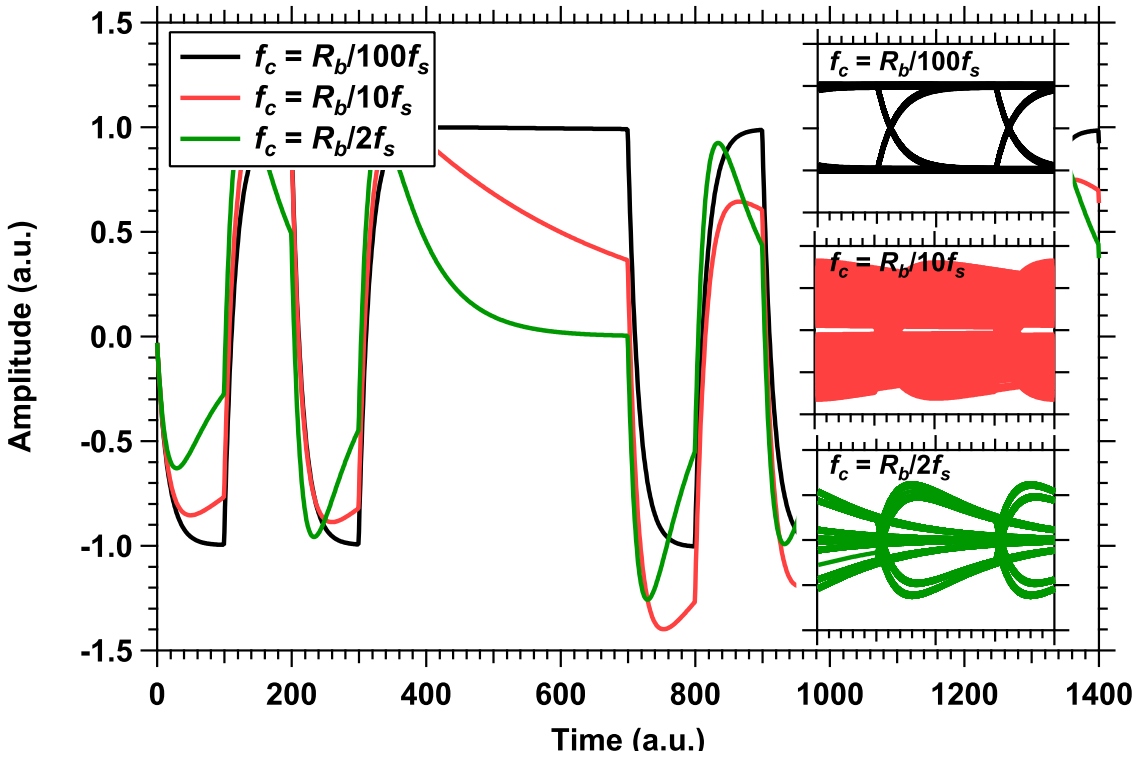

Fig. 3.19 BLW for three different high pass filter cut-on frequencies

3.3.3 Zero-Forcing Equalizer

The ZF equalizer selects its transfer function as $H(f) = 1/Y(f)$ as previously mentioned, i.e. it tries to force a flat magnitude response by removing the ISI. The ZF is linear equalizer with transversal format that has a number of adjustable tap coefficients $\{w_n\}$, as illustrated in Fig. 3.22. The delay given by Z^{-1} is inversely proportional to the filter oversampling rate ξ and is either selected equal to the symbol period (symbol spaced) or at a frequency higher than the symbol rate, typically $\xi = T_b/2$ (fractionally spaced). In fractionally spaced

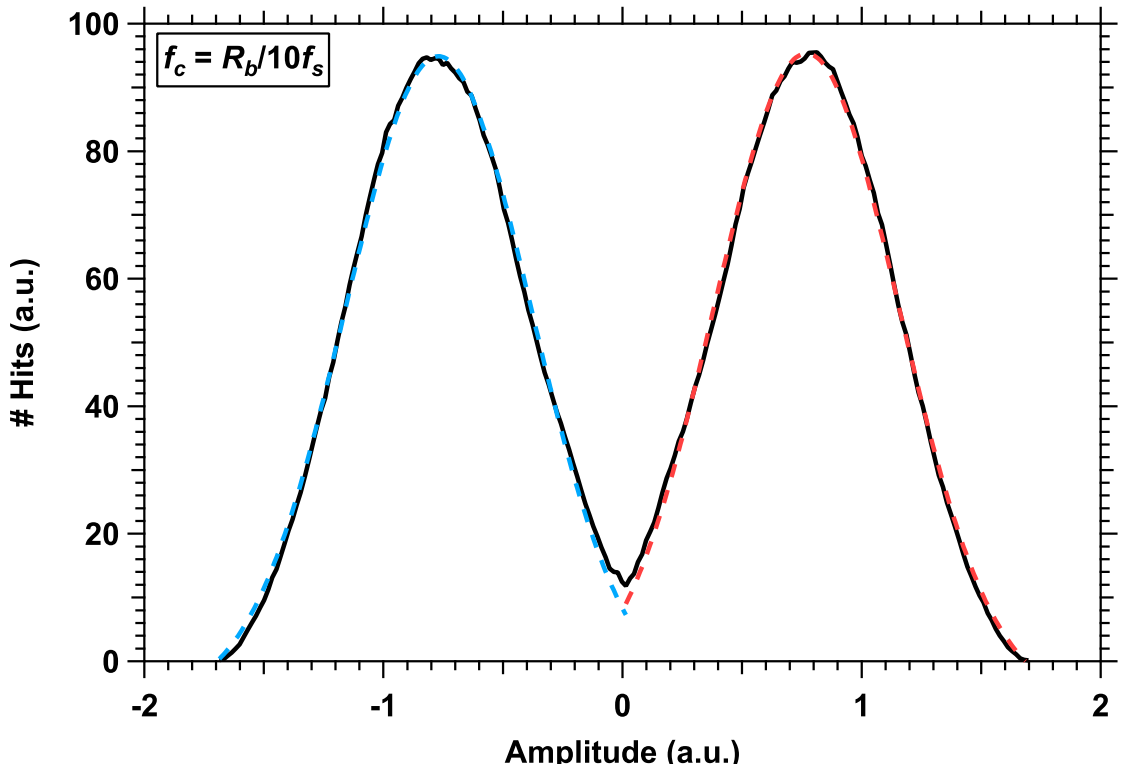

Fig. 3.20 Gaussian distribution of BLW

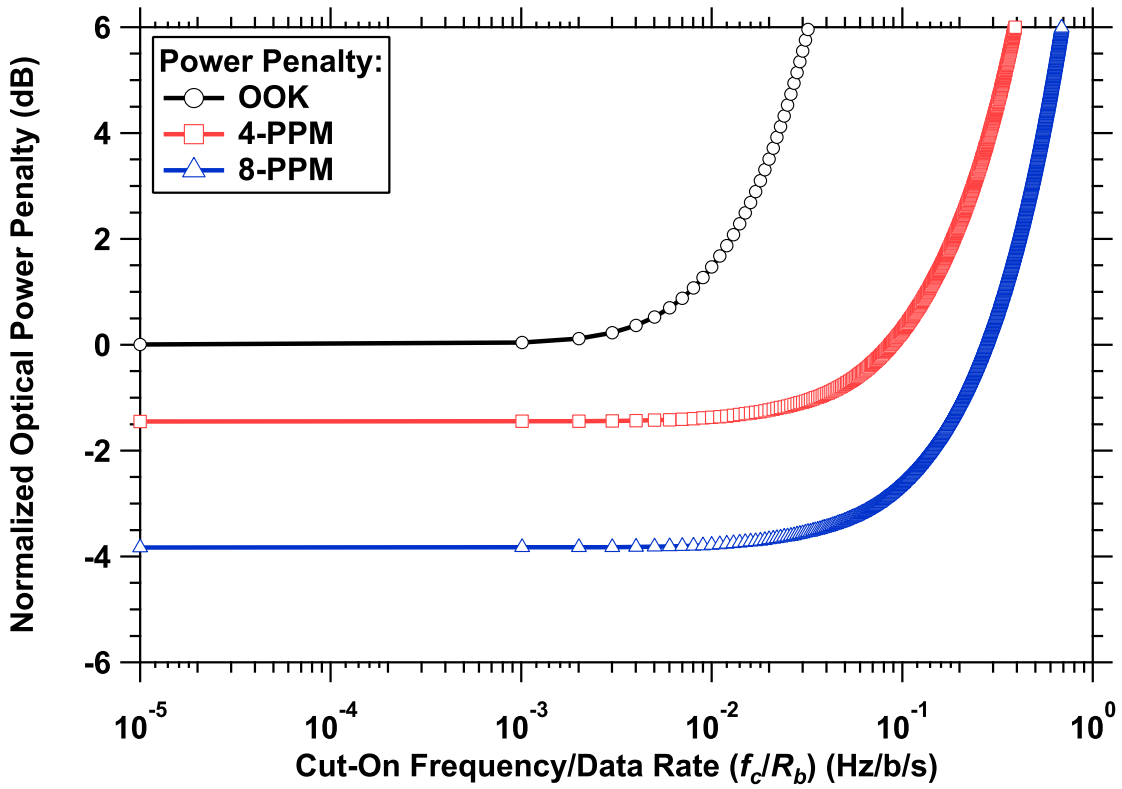

Fig. 3.21 Normalized Optical Power Penalty for OOK, 4-PPM and 8-PPM; clearly PPM has a better power penalty performance than OOK

configuration the output of the filter is also sampled at this rate, as opposed to the symbol rate.

The impulse response of the ZF is given by [44]:

$$q(t) = \sum_{n=-N}^{N} w_n \mathbf{Y}(t - n\xi) \tag{3.47}$$

where $Y(t)$ is the incoming impulse response and is built up into an $N \times N$ matrix in order to find the transfer function of the system. The number of taps must be selected in order to span the entire length of the ISI and is must be symmetrical around the current sample to take into account the previous and next samples, i.e. $L \leq 2N+1$ where L is the number of samples that the ISI spans and N is introduced as a factor in order to make the number of taps symmetrical around the current sample.

The condition to force zero ISI is given in Equation (3.38) and can be equated to $q(t)$. Sampling the output at the symbol rate $t = mT_b$ leads to [44]:

$$q(mT_b) = \sum_{n=-N}^{N} w_n \mathbf{Y}(mT_b - n\xi) = \begin{cases} 1 & \text{if } m = 0 \\ 0 & \text{if } m = \pm 1,\ \pm 2,\ \ldots,\ \pm N \end{cases} \tag{3.48}$$

The output of the filter can be displayed in matrix form as follows:

$$\begin{bmatrix} y_0 & \cdots & y_{-N} & \cdots & y_{-2N} \\ \vdots & \ddots & \vdots & \iddots & \vdots \\ y_N & \cdots & y_0 & \cdots & y_{-N} \\ \vdots & \iddots & \vdots & \ddots & \vdots \\ y_{2N} & \cdots & y_N & \cdots & y_0 \end{bmatrix} \begin{bmatrix} w_{-N} \\ \vdots \\ w_0 \\ \vdots \\ w_N \end{bmatrix} = \begin{bmatrix} 0 \\ \vdots \\ 1 \\ \vdots \\ 0 \end{bmatrix} \tag{3.49}$$

Therefore the tap coefficients are found by training the equalizer. A known sequence (i.e. a single pulse) is transmitted over the system in order to formulate the channel response. In the ZF method all of the weights are updated at the same time as follows:

$$\mathbf{w} = \mathbf{Y}^{-1}\mathbf{q} \tag{3.50}$$

where $\mathbf{q}$ represents the impulse response observation vector of the system. When all of the symbols in the observation vector are considered for calculating the weights and error, this is known as the least squares method.

The filter coefficients are then convoluted into the system and periodically updated in case the system response has been modified in some way. Clearly a training sequence is required here in order to build up the impulse response of the system; the longer the training sequence is the better the representation of the system response becomes.

It is crucial to notice that the ZF is clearly very susceptible to the effects of noise as any random noise in the training sequence will cause an inaccurate picture of the system response. VLC systems generally exhibit very large SNRs; however the power penalty for exceeding the system bandwidth is significant, thus the ZF is not the optimal equalizer for VLC systems.

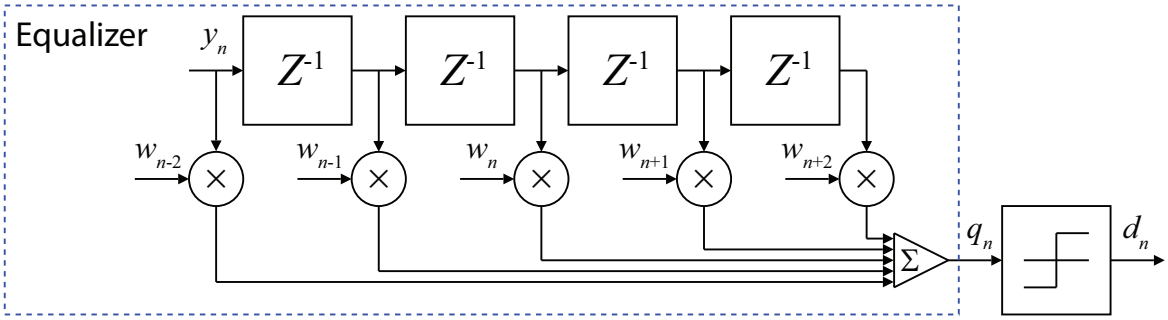

Fig. 3.22 Zero forcing equalizer in linear transversal filter format; it should be noted that the nomenclature y_n is exactly the same as $y(n)$

3.3.4 Adaptive Linear Equalizer

An increase in performance can be obtained if an adaptive algorithm is introduced to find the tap weights as illustrated by Fig. 3.23. There are several adaptive algorithms, most notable are the least mean squares (LMS) and recursive least squares (RLS) and the others are typically variations of these algorithms. In order to find the tap weights the adaptive algorithm requires training against a header sequence of data symbols that is known at the receiver.

Least Mean Squares

The LMS algorithm is a gradient vector descent (based on the minimum square error criterion) on an error cost function $E\left\{e^2(n)\right\}$ and is very simple to implement due to the lack of matrix inversions or correlation function calculations. The tap weights are given by [2]:

$$w(n+1) = w(n) + \frac{1}{2}\mu\left[-\nabla\left(\mathbf{E}\left\{e^2(n)\right\}\right)\right] \tag{3.51}$$

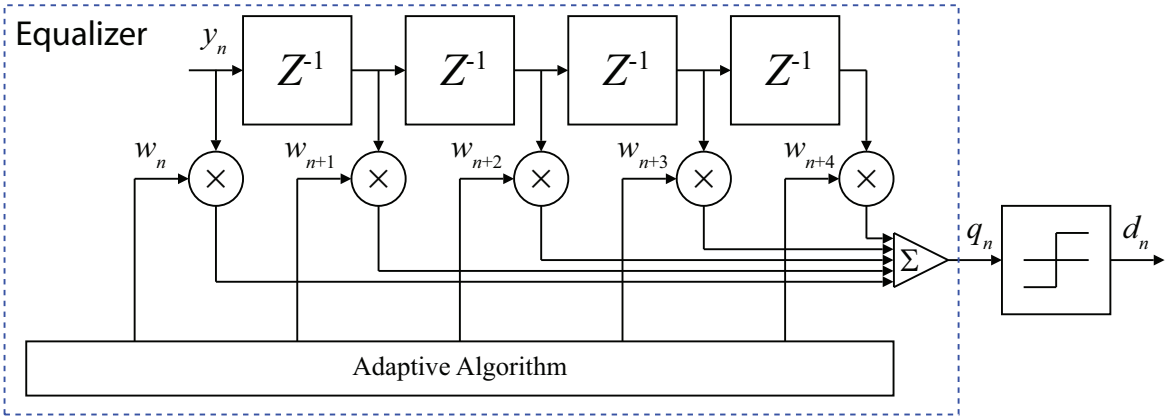

Fig. 3.23 Adaptive linear transversal equalizer

where μ is the step-size parameter that controls the rate of convergence to the minimum square error and the dell operator ∇ indicates a gradient descent. The square error is given by the difference between the known symbols $d(n)$ in the training header and the estimated symbols (given by $w^H x(n)$, where H is the conjugate transpose), as given by [2]:

$$e^2(n) = \left[d(n) - w^H x(n)\right]^2 \tag{3.52}$$

It is not possible to directly measure the gradient vector at an arbitrary sample interval as prior knowledge of the channel would be required and therefore the gradient descent is an estimate given by [2]:

$$\nabla\left(\mathbf{E}\left\{e^2(n)\right\}\right) = -2\mathbf{p} + 2\mathbf{R}w(n) \tag{3.53}$$

where $\mathbf{p}$ and $\mathbf{R}$ are covariance instantaneous estimators obtained from the estimated symbol sample at the output of the filter and the incoming sample at the input to the filter which are given as [2]:

$$\mathbf{p}(n) = d(n)x(n) \tag{3.54}$$

$$\mathbf{R}(n) = x(n)x^H(n) \tag{3.55}$$

Thus equation (3.53) becomes [2]:

$$\nabla\left(\mathbf{E}\left\{e^2(n)\right\}\right) = -2d(n)x(n) + 2x(n)x^H(n)w(n) \tag{3.56}$$

Hence, the tap weight update equation is modified to [2]:

$$w(n+1) = w(n) + \mu x(n) \left[-d(n) x(n) + x^H(n) w(n) \right] \tag{3.57}$$

Thus, the LMS algorithm can be summed up in three key equations, the filter output, estimation error and tap weight update equation, respectively [2]:

$$y(n) = w^H(n) x(n) \tag{3.58}$$

$$e(n) = d(n) - y(n) \tag{3.59}$$

$$w(n+1) = w(n) + \mu x(n) \left[-d(n) x(n) + x^H(n) w(n) \right] \tag{3.60}$$

At $n = 0$ the weight values are arbitrary and are traditionally set as zero and the step-size parameter is selected as $0 < \mu < 1$.

The RLS algorithm is now introduced and a comparison of LMS and RLS will follow.

Recursive Least Squares

The major difference between the RLS and LMS algorithms is that the RLS algorithm recursively reduces the linear least squares weighted error cost function while the LMS algorithm aims to reduce the mean square error.

A weighting factor $\beta(i,n)$ (where i is the length of observable data in the filter and n is still the sampling instance) must be introduced to the RLS error cost function $\varepsilon(i)$ [2]:

$$\varepsilon(i) = \sum_{n}^{i} \beta(i,n) |e(n)|^2 \tag{3.61}$$

where $e(n)$ is the same as equation (3.59), i.e. the difference between desired and estimated responses. The vector input to the filter is given by [2]:

$$\mathbf{x}(n) = [x(n),\ x(n-1),\ \ldots,\ x(n-M+1)]^T \tag{3.62}$$

where T is the vector transpose and M is the number of taps. The weight vector is given by [2]:

$$\mathbf{w}(i) = [w_0(i),\ w_1(i-1),\ \ldots,\ w_{M-1}(i-M+1)]^T \tag{3.63}$$

The weighting factor is also known as the forgetting factor $(0 < \beta(i,n) \leq 1)$ is generally expressed in exponential terms and is used to control the influence of previous data samples on the current sample which is advantageous in a time varying environment. The forgetting

factor is given exponentially by [2]:

$$\beta(i,n) = \lambda^{i-n} \tag{3.64}$$

The error cost function is therefore updated to [2]:

$$\varepsilon(n) = \sum_{n}^{i} \lambda^{i-n} |e(n)|^2 \tag{3.65}$$

Before minimizing the error cost, the so-called normal equations are introduced which establish the input correlation matrix $\Phi(n)$ and the cross-correlation matrix $z(n)$ to find the optimum tap weight values [2]:

$$\Phi(i)\,\mathbf{w}(i) = \mathbf{z}(i) \tag{3.66}$$

where the $(M \times M)$ input correlation matrix is given by [2]:

$$\Phi(i) = \sum_{n}^{i} \lambda^{i-n} \mathbf{x}(n)\,\mathbf{x}(n)^H \tag{3.67}$$

The cross-correlation vector finds the agreement between the input samples to each tap and the desired response and is defined by [2]:

$$\mathbf{z}(i) = \sum_{n}^{i} \lambda^{i-n} \mathbf{x}(n)\,d(n) \tag{3.68}$$

Reformulating equation (3.67) to sum every term except $n = i$ yields [2]:

$$\Phi(i) = \left[\sum_{n}^{i-1} \lambda^{i-1-n} \mathbf{x}(i)\,\mathbf{x}(i)^H\right] \lambda + \mathbf{x}(i)\,\mathbf{x}(i)^H \tag{3.69}$$

which is an important result as the expression inside the brackets is the previous input correlation matrix and can therefore be rewritten to show a clear recursion [2]:

$$\Phi(i) = \lambda\,\Phi(i-1) + \mathbf{x}(i)\,\mathbf{x}(i)^H \tag{3.70}$$

The term to the right of the addition operand is known as the correction term when updating the taps. The cross-correlation matrix can be shown recursively following the same method

[2]:

$$\mathbf{z}(i) = \lambda \mathbf{z}(i-1) + \mathbf{x}(i)\, d(i) \tag{3.71}$$

Now, to find the tap weights a matrix inversion of $\phi(i)$ is required which is undesirable due to the time constraints that accompany matrix inversion, especially considering larger values of M. The inverse of a matrix can be found using the matrix inversion lemma which indirectly inverts the matrix of interest. There are two key relations in the matrix inversion lemma as follows [2]:

$$\mathbf{A} = \mathbf{B}^{-1} + \mathbf{C}\mathbf{D}^{-1}\mathbf{C}^{H} \tag{3.72}$$

$$\mathbf{A}^{-1} = \mathbf{B} - \mathbf{B}\mathbf{C}\left(\mathbf{D} + \mathbf{C}^{H}\mathbf{B}\mathbf{C}\right)^{-1}\mathbf{C}^{H}\mathbf{B} \tag{3.73}$$

Clearly by multiplication of equations (3.72) and (3.73) the result is the identity matrix as expected. Therefore this technique can be applied to the problem of matrix inversion facing the RLS algorithm. Since it is the input correlation matrix that is to be inverted, the following can selected [2]:

$$\mathbf{A} = \Phi(i) \tag{3.74}$$

$$\mathbf{B}^{-1} = \lambda \Phi(i-1) \tag{3.75}$$

$$\mathbf{C} = \mathbf{x}(i) \tag{3.76}$$

$$\mathbf{D} = 1 \tag{3.77}$$

Making the appropriate substitutions:

$$\Phi^{-1}(i) = \lambda^{-1}\Phi^{-1}(i-1) - \frac{\lambda^{-2}\Phi^{-1}(i-1)\,\mathbf{x}(i)\,\mathbf{x}(i)^{H}\,\Phi^{-1}(i-1)}{1+\lambda^{-1}\mathbf{x}(i)^{H}\,\Phi^{-1}(i-1)\,\mathbf{x}(i)} \tag{3.78}$$

This is a complex formulation and will be used in the tap weight update equations, so for simplicity it is necessary to reformulate take $\mathbf{P}(i) = \Phi^{(}-1)(i)$ and take $\mathbf{k}(i)$ as:

$$\mathbf{k}(i) = \frac{\lambda^{-1}\mathbf{P}(i-1)\,\mathbf{x}(i)}{1+\lambda^{-1}\mathbf{x}(i)^{H}\,\mathbf{P}(i-1)\,\mathbf{x}(i)} \tag{3.79}$$

which yields a simpler expression for $\mathbf{P}(i)$:

$$\mathbf{P}(i) = \lambda^{-1}\mathbf{P} - \mathbf{1}(i) - \lambda^{-1}\mathbf{k}(i)\,\mathbf{x}(i)^{H}\,\mathbf{P}(i-1) \tag{3.80}$$

Rearranging equation (3.79) to show that $\mathbf{k}(i)$ is a function of $\mathbf{P}(i)$ yields:

$$\mathbf{k}(i) = \mathbf{x}(i)\left[\lambda^{-1}\mathbf{P}(i-1) - \lambda^{-1}\mathbf{k}(i)\mathbf{x}(i)^H\mathbf{P}(i-1)\right] = \mathbf{P}(i)\mathbf{x}(i) \tag{3.81}$$

Thus the so-called gain vector which is the transformation of the filter input by the correlation matrix and is given by [2]:

$$\mathbf{k}(i) = \Phi(i)\mathbf{x}(i) \tag{3.82}$$

Updating the taps requires knowledge of the input correlation matrix and cross-correlation matrix as the update is based on the previous values, thus the previous mathematics is crucial to updating the taps and it is trivial to notice that the RLS algorithm is significantly more complex than the LMS. The tap weight updates as follows, using equation (3.66) and (3.71) by [2]:

$$\mathbf{w}(i) = \Phi^{-1}(i)\mathbf{z}(i) = \mathbf{P}(i)[\lambda\mathbf{z}(i-1) + \mathbf{x}(i)d(i)] \tag{3.83}$$

Substituting equation (3.80) for P(i) and recalling equation (3.82), a recursive update can be demonstrated [2]:

$$\mathbf{w}(i) = \mathbf{w}(i-1) + \mathbf{k}(i)\xi(i) \tag{3.84}$$

where $\xi(i) = d(i) - w^H(i-1)x(i)$ is the *a priori* estimation error where the product of $w^H(n-1)x(n)$ is the estimate of the symbol using the previous tap weights. The *a priori* error is cascaded back into the algorithm to update the taps while there is also the *a posteriori* error which is the error out of the filter based on the current set of weights, i.e. $e(i) = d(i) - w^H(i)x(i)$.

To sum up, in order to implement the RLS algorithm, the following equations are required in this order:

$$\mathbf{k}(i) = \frac{\lambda^{-1}\mathbf{P}(i-1)\mathbf{x}(i)}{1 + \lambda^{-1}\mathbf{x}(i)^H\mathbf{P}(i-1)\mathbf{x}(i)} \tag{3.85}$$

$$\xi(i) = d(i) - \mathbf{w}^H(i-1)\mathbf{x}(i) \tag{3.86}$$

$$\mathbf{w}(i) = \mathbf{w}(i-1) + \mathbf{k}(i)\xi(i) \tag{3.87}$$

$$\mathbf{P}(i) = \lambda^{-1}\mathbf{P} - \mathbf{1}(i) - \lambda^{-1}\mathbf{k}(i)\mathbf{x}(i)^H\mathbf{P}(i-1) \tag{3.88}$$

Then repeated this sequence for each sample until an acceptable error level is met or the training interval ends.

The quality of an equalizer is defined by how fast it converges on the target error. A generic OOK VLC link with a 5-tap linear equalizer is outlined in Fig. 3.24 and simulated in MATLAB. The effect of the bias tee is not included in Fig. 3.24 but is set to $f_c = R_b/10$ so that the effect of BLW is included in the performance analysis and the simulation is representative of the real system. Since the real-world channel bandwidth is significantly higher than the optical transmitter/receiver and is simply a DC gain less than unity, the ideal channel is considered here. The ISI is introduced by the optical transmitter (the cut-off frequency of the transmitter is set as one fifth of the symbol rate) as highlighted in red in Fig. 3.24 due to bandwidth limitations as previously described. The LMS mean square error convergence is examined under a series of different SNRs first (Fig. 3.25), with a training sequence of 10,000 symbols, followed by the RLS least squares convergence (Fig. 3.26) under the same conditions. The difference between mean square error and least squares error is that the mean square error considers only error of the symbol at the output of the filter while least squares considers the total error of the symbols in the observation vector.

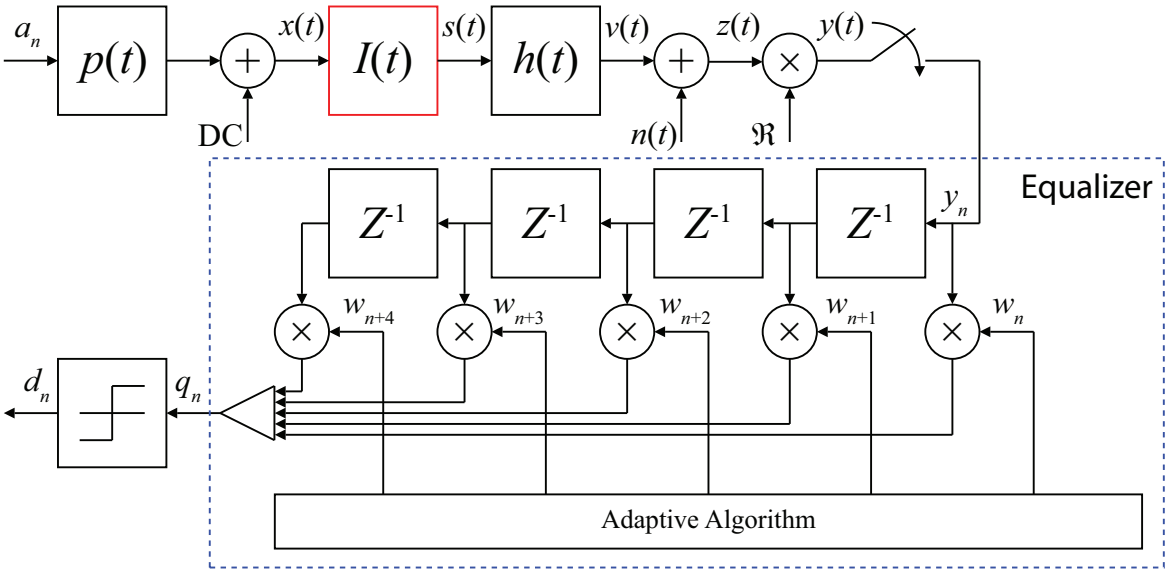

Fig. 3.24 OOK link with linear 5-tap transversal equalizer

The key information in Fig. 3.25 is decreasing the step-size parameter causes a better convergence to the minimum error possible at the cost of increased convergence time. On the other hand, setting the step-size parameter excessively is that the filter becomes unstable (not shown here) and will not convergence on the optimum filter weights. The improvement by decreasing the step size parameter is very slight in this case and does not offer a significant improvement to justify the increased convergence time.

The RLS algorithm with exponentially weighted forgetting factor is trained on the same

dataset and generally demonstrates much faster convergence than LMS as illustrated in Fig. 3.26, although not always to a lower error in the case of small forgetting factors (note the difference in range on the y-axis). An increasing forgetting factor offers a faster convergence to the least squares error than the LMS equalizer at a lower error value and there is little difference in performance in each SNR case.

As illustrated by Fig. 3.25 and Fig. 3.26, the RLS algorithm is much faster to converge than the LMS which comes at the cost of increased complexity. The DF equalizer can be trained with both the LMS and RLS algorithms and offers an improvement in performance over the linear equalizer.

3.3.5 Decision Feedback Equalizer

The performance of an equalizer is directly related to the severity of the ISI experienced in the system. In heavy ISI linear equalizers will fail due to their inability to produce non-linear relationships between input and output. Further, if a system transfer function exhibits a deep spectral null a linear equalizer will struggle to compensate as it will set some of the tap coefficients to be excessively high [44]. Therefore it is necessary to introduce the non-linear DF equalizer which works on the principle of estimating the influence of ISI in the current symbol based upon the previously detected symbol. Two filters are required, the feedforward and feedback filters. The feedforward filter is exactly the same as the adaptive linear filters in the previous section and operates in the same way while the feedback filter is made up of past symbols in order to estimate the contribution of ISI on the current symbol. The output of each filter is subtracted and a decision is made as follows:

$$q_m = \sum_{i=0}^{N_1} c_n y_{m-n} - \sum_{i=1}^{N_2} b_n \hat{d}_{m-n} \tag{3.89}$$

where c_n is coefficient value of the i_{th} feedforward tap and y_{m-n} is the current symbol. The estimate of the previous symbol is given by $\hat{d}_{m-n}$ and the feedback filter tap coefficients are given by b_n.

The DF equalizer is not examined in this thesis but is briefly introduced since it should offer a level of performance somewhere between the linear equalizer and the ANNs that are introduced in the next section.

3.3.6 Equalization as a Classification Problem

While traditional equalizers such as the ones shown in the previous section are very popular they do not offer the best performance. ANN classifiers were first introduced in by McCul-

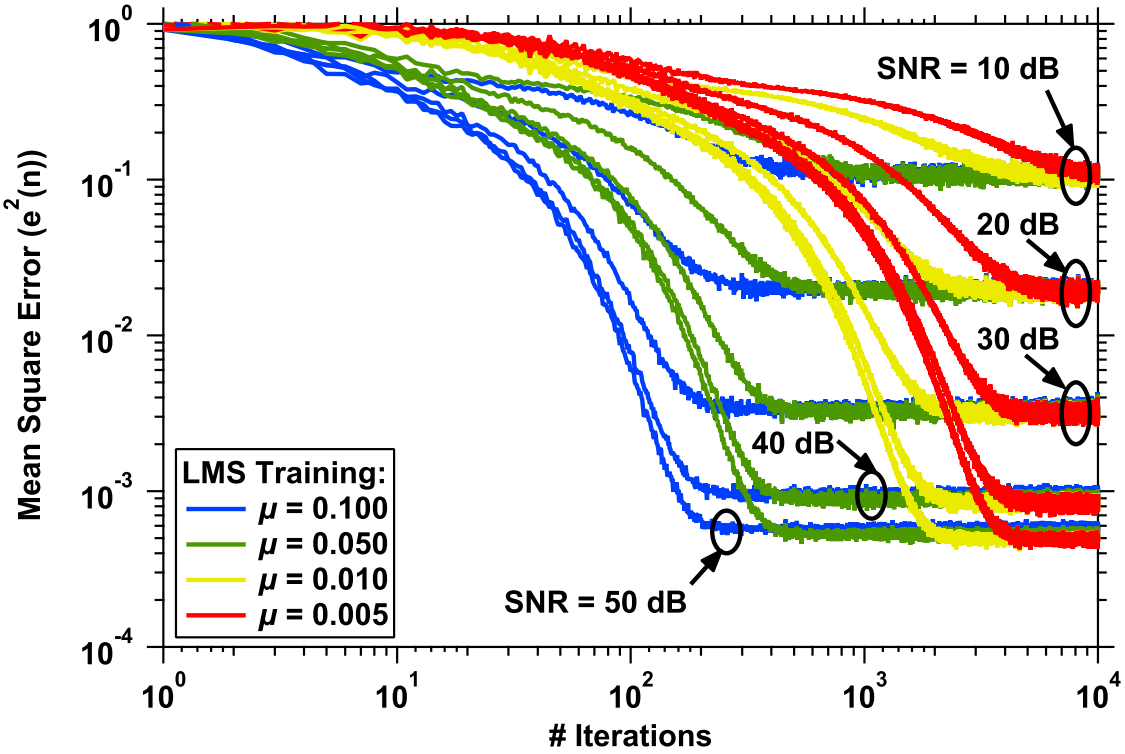

Fig. 3.25 Convergence on the error target using an LMS linear equalizer and varying the step-size, error cost function related to equation (3.52)

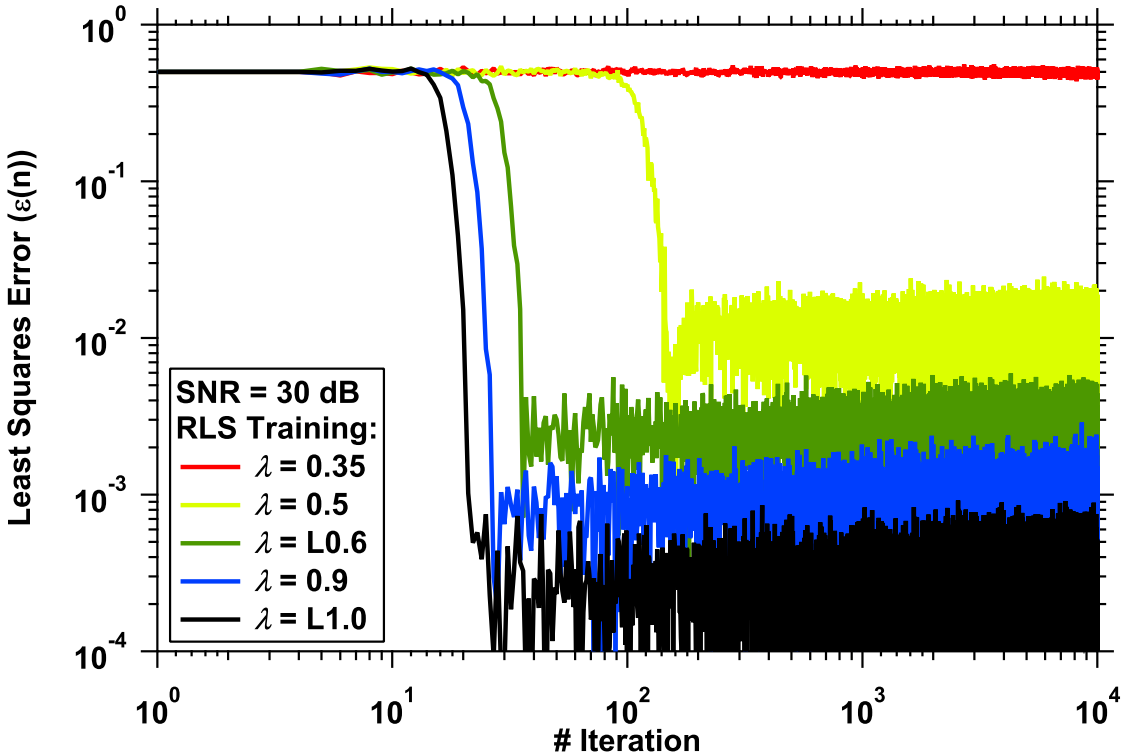

Fig. 3.26 RLS convergence speed with varying exponential forgetting factor, error cost function related to equation (3.61)

loch and Pitts in 1943 [118] but did not gain popularity for a number of years due to their high computational complexity that was simply not available at the time. ANNs were then effectively forgotten until a re-emergence in the 1960s due to advances in perceptrons [119]. Based on the results in [119] which showed that perceptrons do not always converge on the correct pattern due to some theoretical limits, a further lull was experienced in the popularity of ANNs for another two decades. Research interest has been renewed somewhat with advances in signal processing and computational technologies. A complete ANN history can be found in [120] and there are many applications for ANNs across many industries including finance [121], medical imaging [122] and pattern recognition [123].

One of the most common applications is as equalizers in communications systems which operate based on forming decision boundaries based on a training scheme. This is in opposition to calculating the contribution of ISI from each received symbol such as transversal equalizers. The decision boundaries formed aim to classify the received symbols into groups that belong to the desired symbol value. The boundaries are formed using neurons which can be thought of as being similar to those found in the human brain (see Table 3.1 for a comparison between computer and biological systems) and adjust their size in reaction to the training sequence such as tap weights in transversal filters. The major difference between ANNs and transversal equalizers is the structure; the former are arranged into a highly parallel form that allows non-linear mapping as each input is connected to each neuron. The latter are obviously highly linear (not considering DF) since each input is connected only to its corresponding weight. The schematic of a single neuron is shown in Fig. 3.27.

Each neuron in the network has a number of associated weights. The contribution from each input that is scaled by the weight is then summed. The summation can be biased using an external input but in this thesis there is no bias so it is not considered any further. The output of the summation uk is given by [124]:

$$u_k = b_k + \sum_{i=1}^{N} x_j w_{kj} \tag{3.90}$$

where the N^{th} input is given by x_N and the weight associated with the N^{th} input is given by w_{kN}. The output of the activation function is given by [124]:

$$y_k = \varphi(u_k) \tag{3.91}$$

The activation function can be any differentiable function but is most commonly one of three; the threshold function, the piecewise-linear function (see Fig. 3.28) and the (log)

Table 3.1 Table comparing computer systems such as microprocessors or sequential logic with biological (and pseudo-biological) systems such as the neural networks; adopted from [6, 13]

	Computer System	Biological System
Processor	Complex High speed (ns) One	Simple Low speed (ns) A large number
Memory	Localized Addressable	Distributed Addressable
Computing	Centralized Sequential Stored programs	Distributed Parallel Supervised/self Learning
Reliability	Vulnerable	Robust
Power Consumption	High	Low

sigmoid function, given by [124]:

$$\varphi = \frac{1}{1+e^{-\alpha u_k}} \tag{3.92}$$

where α is the so-called slope parameter which has been varied as $\alpha = \{0.1 : 0.1 : 5\}$ in Fig. 3.29, which shows the log-sigmoid function, one of the most popular activation functions for multilayer perceptrons.

This is due to its inherently non-linear structure which allows highly non-linear mapping. Clearly as $\alpha \to 0$ the slope becomes increasingly linear and as $\alpha \to \infty$ the log-sigmoid function first approximates to the piecewise linear function, then to the threshold function.

There are many ANN architectures that can be used as equalizers in communications systems; including single and multilayer feedforward networks, and feedback networks. The topologies of each network are shown in Fig. 3.30, Fig. 3.31 and Fig. 3.32 for single, multilayer and DF networks, respectively.

The number of layers does not include the input layer since no processing occurs, so in single layer networks the neurons and activation function make up the output layer as previously in Fig. 3.27 while the inputs are generated using tap delay lines. Single layer networks cannot extract higher order statistics from the data and there is requirement for multilayer networks that can (assuming there is a sufficient amount of neurons) form arbitrarily complex decision boundaries, see Fig. 3.33.

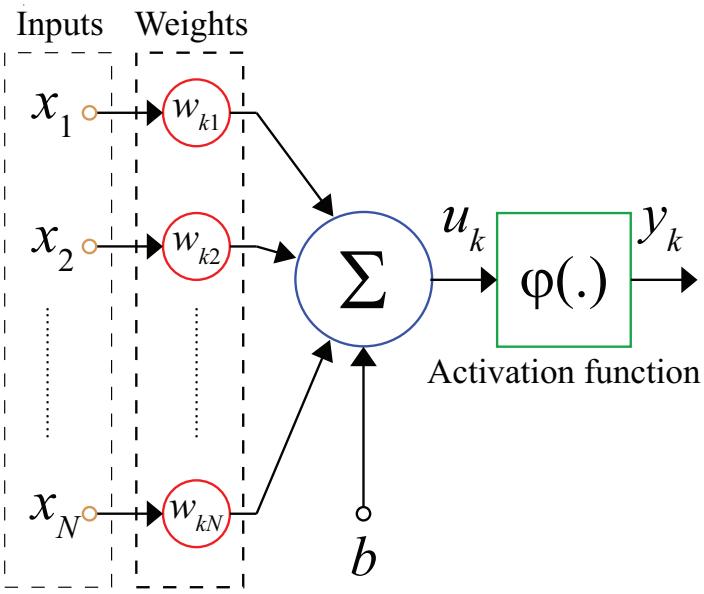

Fig. 3.27 Simple overview of a neuron

Multilayer networks consist of at least two layers (not including the input layer as mentioned) where any layers between the input and output layers are so-called hidden layers which simply contain neurons. In general a two layer feedforward network is sufficient for equalization [59, 105, 125].

DF-ANNs are similar to multilayer networks except the output is fed back into one or more inputs which offer a performance increase in the same way DF equalizers offer an improvement over linear transversal equalizers. It is clear from comparison of Fig. 3.31 and Fig. 3.32 that there is no difference in computational complexity between the DF-ANN and multilayer ANN.

For equalization using classification, ANNs require training similar to transversal equalizers. The training sequence simply allows the ANN to adjust the neuron weights according to a gradient descent on the error cost function is satisfied. There are a number of training methods including LMS and RLS and scaled conjugate gradient (SCG) learning but the most popular is the Levenberg-Marquardt back propagation (LMBP) algorithm because it is simple to implement in hardware due to low complexity but requires the most memory. SCG training should converge to a lower error value but requires a longer training period and is more complex for hardware implementation so is not examined here. Having a short training sequence is of paramount importance because it reduces the amount of redundancy in the system, especially if the system is non-stationary and therefore requires frequent retraining to update the input-output map.

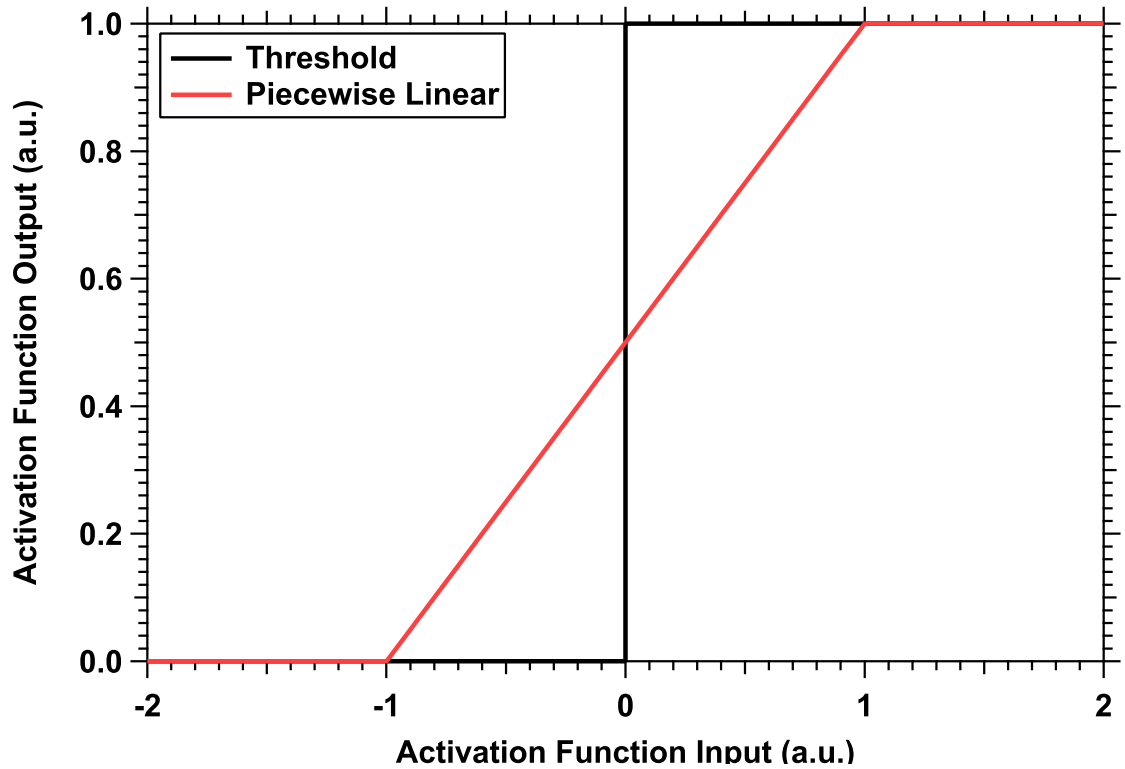

Fig. 3.28 Normalized threshold and piecewise linear activation functions

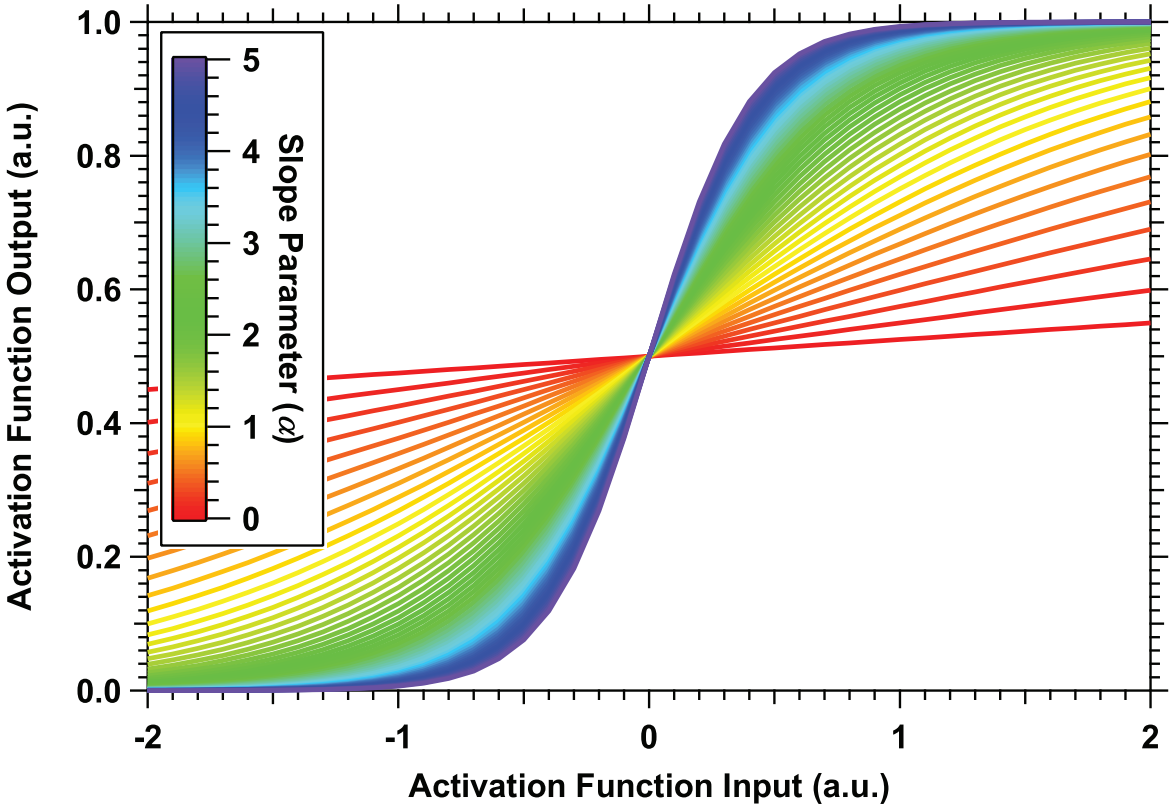

Fig. 3.29 Log-sigmoid activation function with $\alpha = \{0.1 : 0.1 : 5\}$

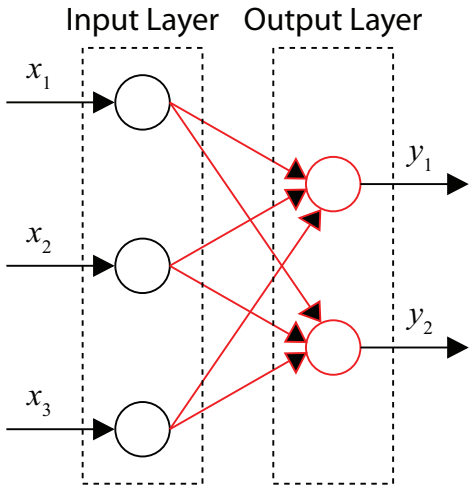

Fig. 3.30 Single layer ANN

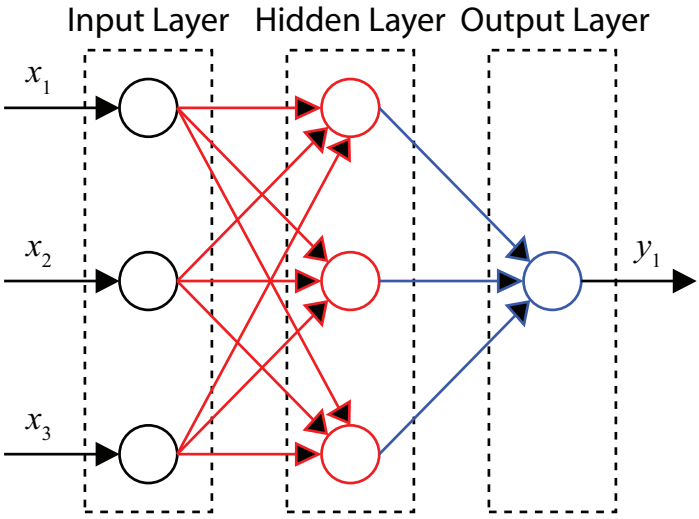

Fig. 3.31 Multilayer ANN

Levenberg-Marquardt Back Propagation Algorithm

The error cost function $(e(n))$ is no different to the same function described in the LMS and RLS algorithms; i.e. the difference between the desired symbols and the received symbols. The neuron weights are updates as follows [124]:

$$w_{kj}(n+1) = w_{kj}(n) - \eta \frac{\partial E(n)}{\partial w_{kj}(n)} \tag{3.93}$$

where $E(n)$ is the error cost function and η is the learning rate parameter. Immediately it is noticeable that the weight updates have an important difference between the previously outlined algorithms; that is there is no matrix inversion which reduces the training com-

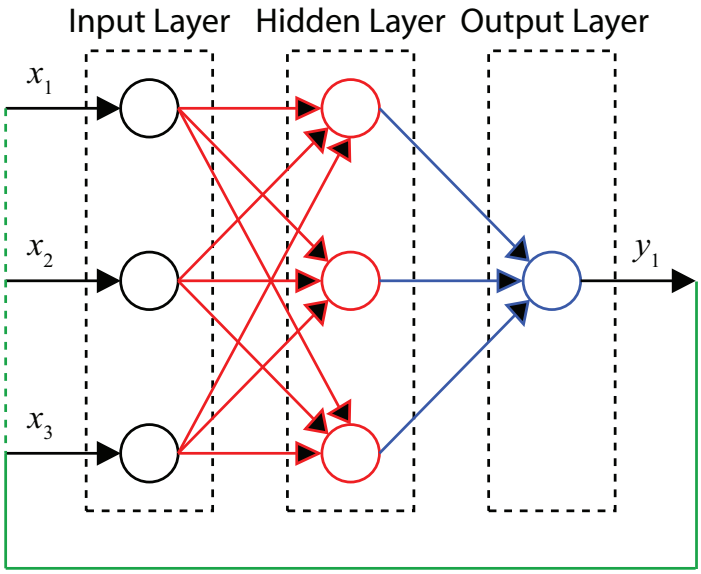

Fig. 3.32 Feedback ANN

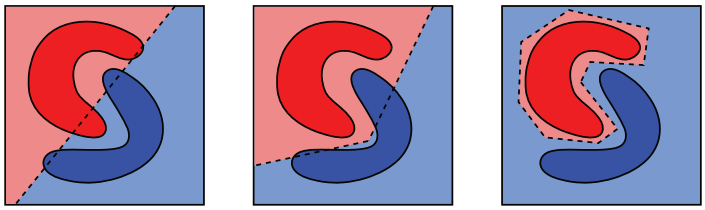

Fig. 3.33 Decision boundaries for two different classes based on different layer structures, adapted from [6]

plexity. It should also be noted that the LMBP algorithm is a supervised training method where a training sequence is known at the receiver. Unsupervised training is also possible but is not examined in this thesis so the reader should refer to [126]. The learning rate parameter controls the rate of convergence. Slow convergence or instability can occur if η is selected inadequately or excessively and a solution for this has been proposed in [127] that implements an adaptive learning rate that automatically adjusts the learning rate parameter according to the error cost performance and this method is adopted to select the learning rate parameter in this thesis. Training can be problematic since convergence on a local minimum rather than the global minima is possible, meaning that the system converges on a minimum that is not the true minimum as illustrated in Fig. 3.34 Local minima in error convergence during training. Clearly if the ANN converges on the local minimum the performance would be significantly worse than if convergence was to the global minima since there is a difference of more than ten orders of magnitude in error level.

The local minima problem has been well studied in the literature [127, 128] and a pop-

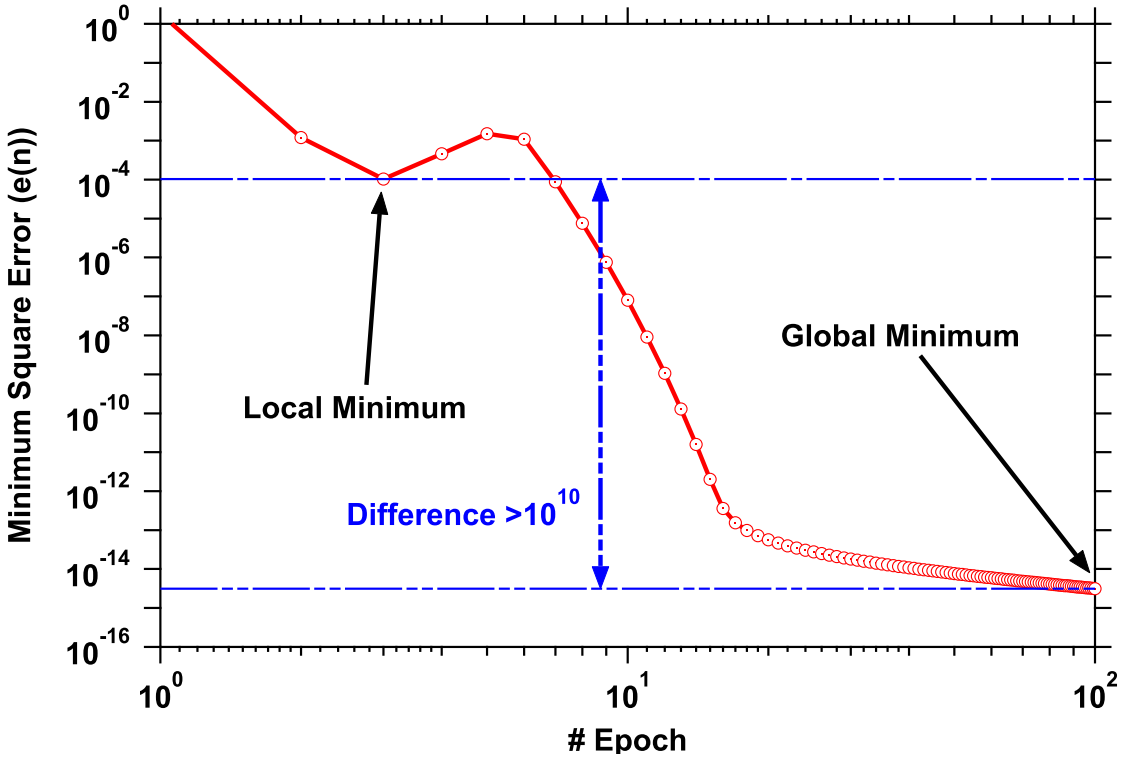

Fig. 3.34 Local minima in error convergence during training; convergence is on global minimum due to adaptive learning rate algorithm

ular solution widely used is the adaptive learning rate algorithm previously mentioned that guarantees convergence on the global minima, based on a series of conditions that can be found in [127].

There are many variations of ANN that can be used for equalization. The most common are multilayer perceptrons (MLPs), radial basis function (RBF) ANNs, functional link ANNs (FLANNs) and support vector machines (SVMs). Literature has demonstrated that two layer MLPs offer similar performance to RBFs and SVMs [129] with the advantage of having less complexity and hence is used as the feedforward ANN in this thesis since any gain obtained using other feedforward ANNs would be marginal with increased hardware complexity.

In Fig. 3.35, the error convergence is shown for several different MLPs; the one (1H) and two hidden (2H) layer feedforward and 1 hidden layer DF structures are considered using the same setup as previous equalizers (Fig. 3.24) with an SNR $= 30$ dB, number of input taps and neurons is 5 and training length of 1000, ten times less than in the linear transversal equalizer case.

It is immediately clear that the LMBP training reaches a lower minimum error value

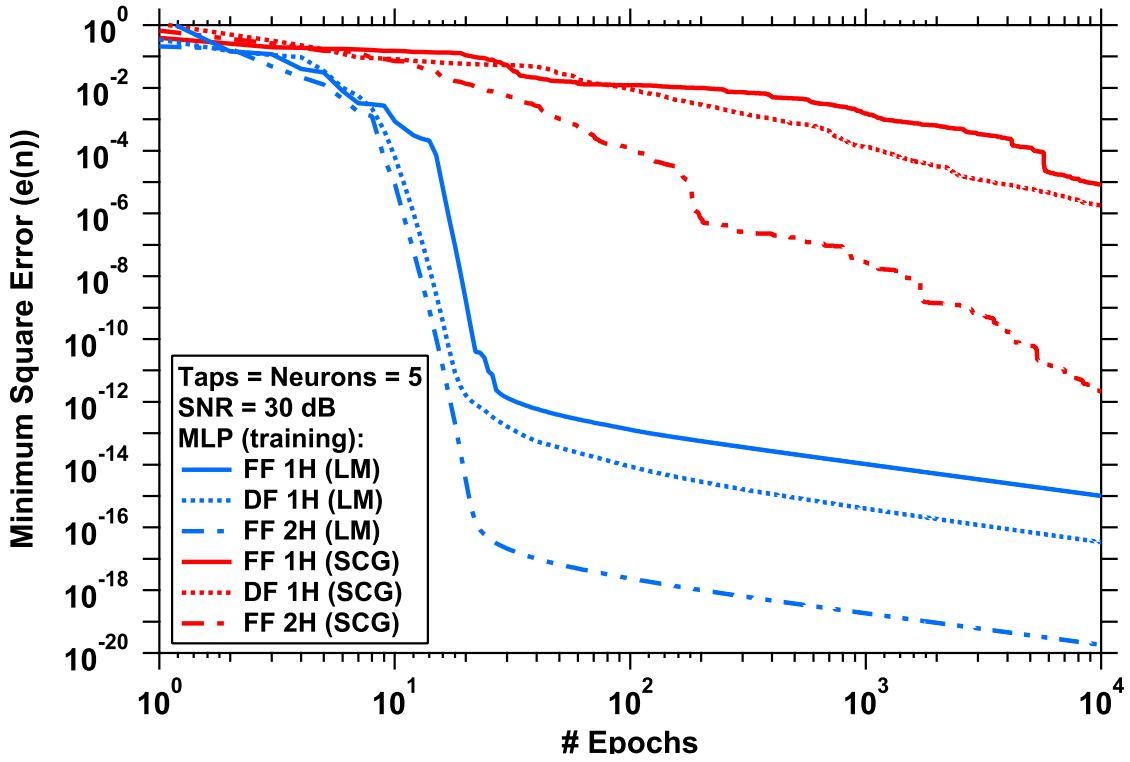

Fig. 3.35 Comparison of different ANN structures (1H = 1 hidden layer, 2H = 2 hidden layers) and training schemes with SNR = 30 dB; the training length is 1000

than the SCG training for all cases. Using the DF-MLP offers an improvement over the 1H FF-MLP using both training methods of a few orders of magnitude. The 2H FF-MLP offers a significant improvement in each case. However this improvement has largely been shown to be theoretical and experimental results have shown that there is little difference between single and two hidden layer structures [130] provided an appropriate number of neurons are selected. Therefore in this thesis the 1H FF-MLP is selected.

3.4 Summary

VLC has attracted considerable interest in recent years and is growing rapidly as a subject and is expected to be worth £6,318 million by 2018 according to Markets and Markets, a leading market research company. The significant advancement in GaN LEDs in the preceding decades spurred VLC as a solution for the "last-metre" bottleneck due to advantages such as practically unlimited (in comparison to the currently available components), unregulated and license free bandwidth.

VLC certainly should not be seen as replacement for radio frequency technologies such

as Wi-Fi, but as a complimentary technology that can provide access in places where Wi-Fi cannot such as hospitals and airplanes. Further VLC has a wider bandwidth (around 10,000 times) than radio frequencies and therefore has the potential to significantly improve the transmission speed to the end user.

A substantial amount of research has been conducted into intensity modulation schemes for both VLC and indoor IR communications. The most popular are OOK because it is very simple to implement and bandwidth efficient and L-PPM due to its power efficiency which often has more importance than bandwidth efficiency in optical links due to the high bandwidths. In general this thesis only investigates M-PAM and L-PPM for these reasons, however there are a number of standard techniques such as DMT and a plethora of novel techniques that could equally be used in place of M-PAM and L-PPM.

Chapter 4

Visible Light Communications with Organic Light Emitting Diodes

4.1 Introduction

In the next four chapters, four communications systems are analysed; VLC with an SMOLED transmitter and Si PIN PD receiver in this chapter, VLC with a WPLED transmitter and OPD as receiver in Chapter 5. In Chapter 6, a VLC link with an SMOLED transmitter and OPD receiver is examined and finally in Chapter 7 a PLED transmitter and Si PD receiver link is examined.

The general working principles of organic devices were given in Chapter 2 and are therefore not covered here. The first commercial SMOLED used was an Osram Orbeos CMW-031 with 79 mm diameter and a luminous efficacy of 23 lm/W. The normalized measured optical spectrum is shown in Fig. 4.1 illustrating that the device is made from individual RGB components with peaks at 610 (R), 514 (G) and 480 (B) nm. The peak at 480 nm is not as pronounced as the other peaks and this is attributed to the poor conversion efficiency of blue materials in comparison to red and green [131, 132].

The empirically measured normalized azimuth emission profile of the SMOLED is shown in Fig. 4.2 along with the theoretical normalized Lambertian emission profile. It is clear that the plots closely match and the OLED is approximately Lambertian in emission which is supported in the literature [104, 133–135].

The OLED L-I-V curve was measured using the setup shown in Fig. 4.3 under autonomous LabVIEW control.

The measured intensity is a unit-less quantity which is relative to the integration time and the sensitivity of the pixels. The integration time is set to 30 ms which was found

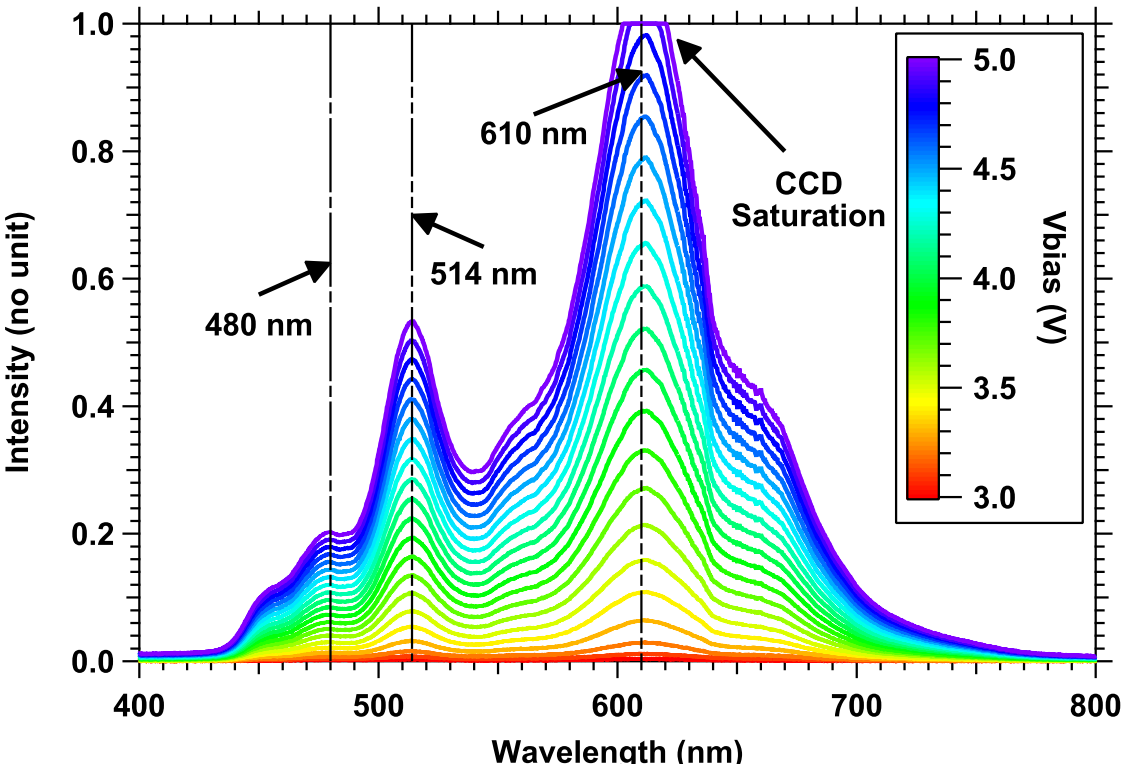

Fig. 4.1 Optical spectrum of the Osram Orbeos CMW-031 SMOLED under test with peak wavelengths marked

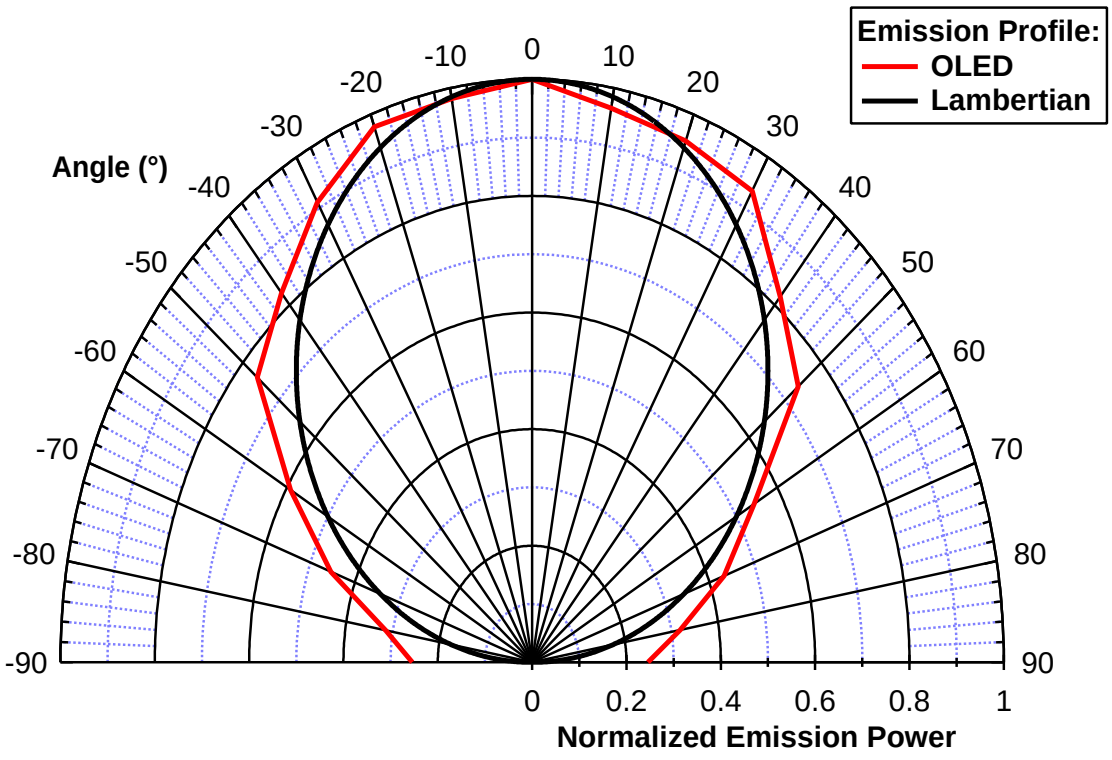

Fig. 4.2 Polar plot showing the normalized measured emission profile of the SMOLED, which is in close agreement to the normalized Lambertian emission profile $(m = 1)$

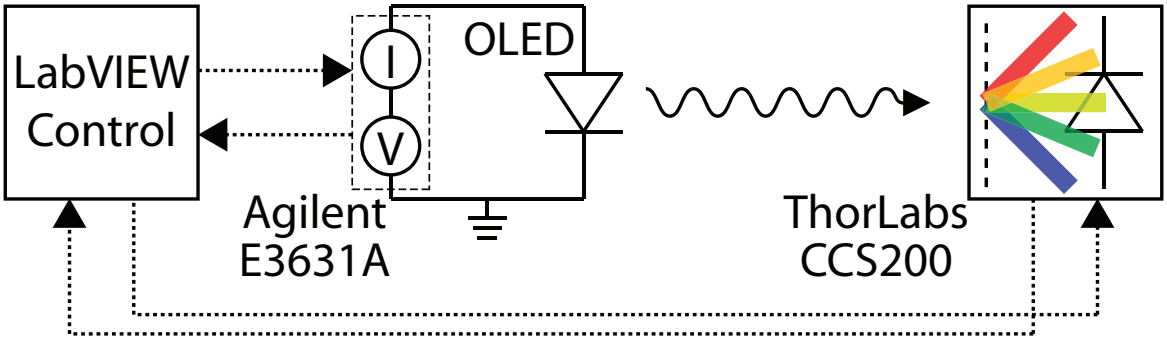

Fig. 4.3 Measurement setup for obtaining the SMOLED L-I-V curve

empirically. The measured intensity would be integrated over the active wavelengths for every bias voltage if it were a continuous signal; however the discrete samples are summed in order to find the total light output as follows:

$$L = \frac{1}{n} \sum_{\lambda=1}^{n} I(\lambda) \tag{4.1}$$

Then the L-I-V curve is produced as in Fig. 4.4. First note that the OLED goes through a transition phase where the optical power and voltage both drop as a function of time in the first few hours of operation. This could be due to the thermal destruction of unstable molecules and processing defects such as short circuits. This is a common feature of new SMOLEDs and PLEDs and is colloquially known as 'burning-in'. The device then reaches a steady state region. Note that the data shown in Fig. 4.4 was for the first twelve hours of seven days of continuous measurements. The device remains in the steady state for the remaining time.

The SMOLED bandwidth is measured using the setup in Fig. 4.5. A swept since wave (1 V_{pp}) is transmitted over the free space link. The bias tee has a cut-on frequency of 7 kHz and the receiver used is a ThorLabs PDA36A-EC with in-built TIA set to 10 dB gain; reducing the Si PD bandwidth to 5 MHz. The entire system including the voltage source (Agilent E3631A) supplying the SMOLED bias voltage is controlled by LabVIEW.

The measured spectrum (measured at point X in Fig. 4.5) is shown in Fig. 4.6 and its normalized version is in Fig. 4.7 where the bias voltage is varied for each spectrum measurement. The injection current can be measured from the I-V curve in Fig. 4.4. The range of bias voltages is from 2.9 – 5 V. For voltages below 2.9 V, the SMOLED is effectively not switched on, as can be inferred from Fig. 4.4

The ESA is not sensitive to frequencies below 9 kHz and therefore the attenuation of the low frequencies caused by the bias tee cannot be noticed. The output light intensity

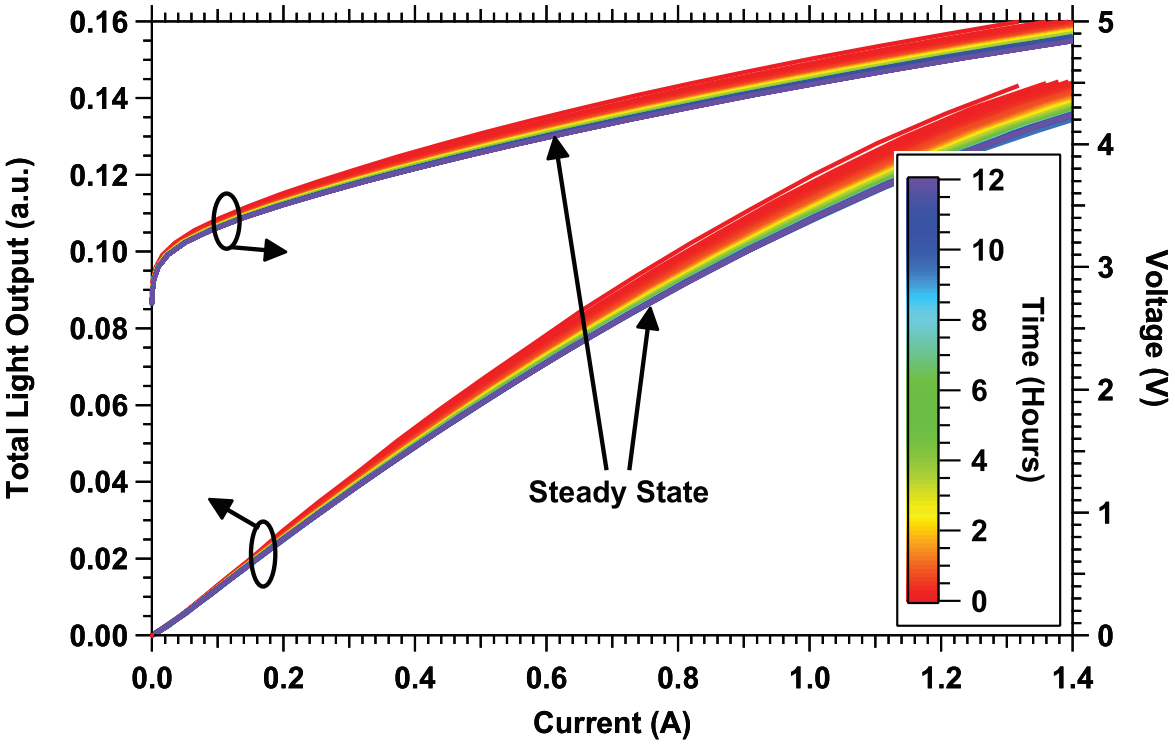

Fig. 4.4 Measured SMOLED L-I-V curve for a range of bias currents over a period of 12 hours

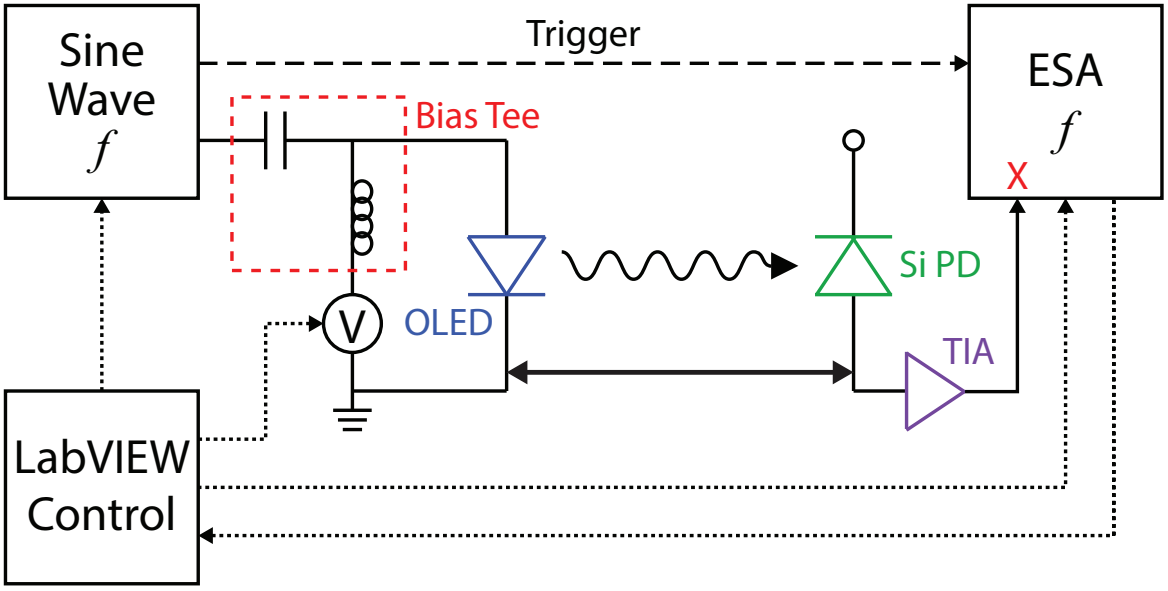

Fig. 4.5 SMOLED bandwidth test measurement; the bias tee cut-on frequency is 7 kHz while the Si PD bandwidth is 5 MHz (in 10 dB gain mode) as used in this work

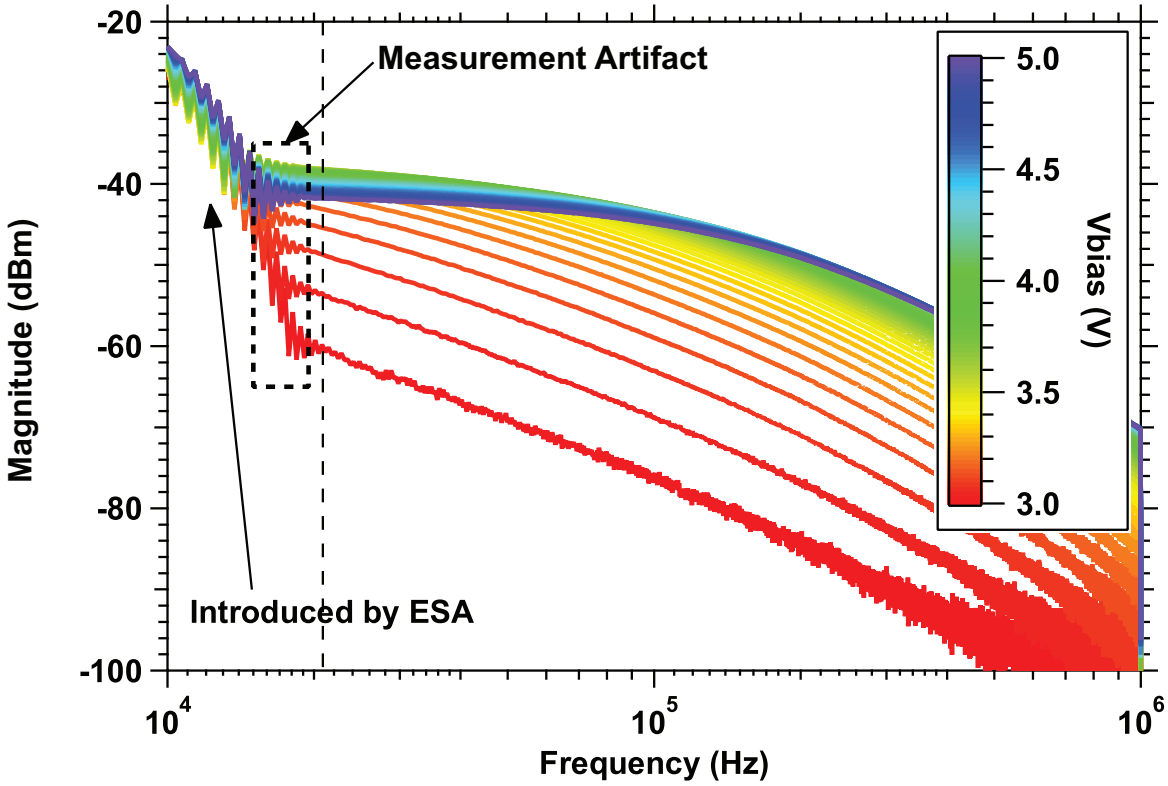

Fig. 4.6 Raw magnitude response of the SMOLED under test including large low frequency components introduced by the ESA, measured at point *X* in Fig. 4.5

is clearly proportional to the injection current as expected and the amplitude is within the range of -60 dBm to -40 dBm. It is clear from Fig. 4.6 that under the operating conditions used to measure the magnitude response (resolution bandwidth (RBW) and video bandwidth (VBW) are both 10 kHz), the ESA is still insensitive to frequencies $<$ 20 kHz as highlighted. Therefore each response is cut at the dashed line in MATLAB and normalized for like-for-like comparison, see Fig. 4.7.

It is immediately clear from inspection that the SMOLED bandwidth is dependent on the injection current and this is a phenomenon that has never been reported for SMOLED devices (but has been reported in OPDs [61]). At high injection currents (and therefore bias voltages) the bandwidth extends to 96 kHz while for low injection currents the bandwidth decreases to 26 kHz; a difference of 72 kHz. Research into organic semiconductors has demonstrated clearly that there are well pronounced trap states in the conductive polymer layers that exist within (at most) a few eV of the HOMO and LUMO energy levels and are introduced by production defects and material impurities [61, 94, 136]. Such traps inhibit charge carrier recombination by confining a charge carrier in a fixed space making it unavailable for radiative recombination.

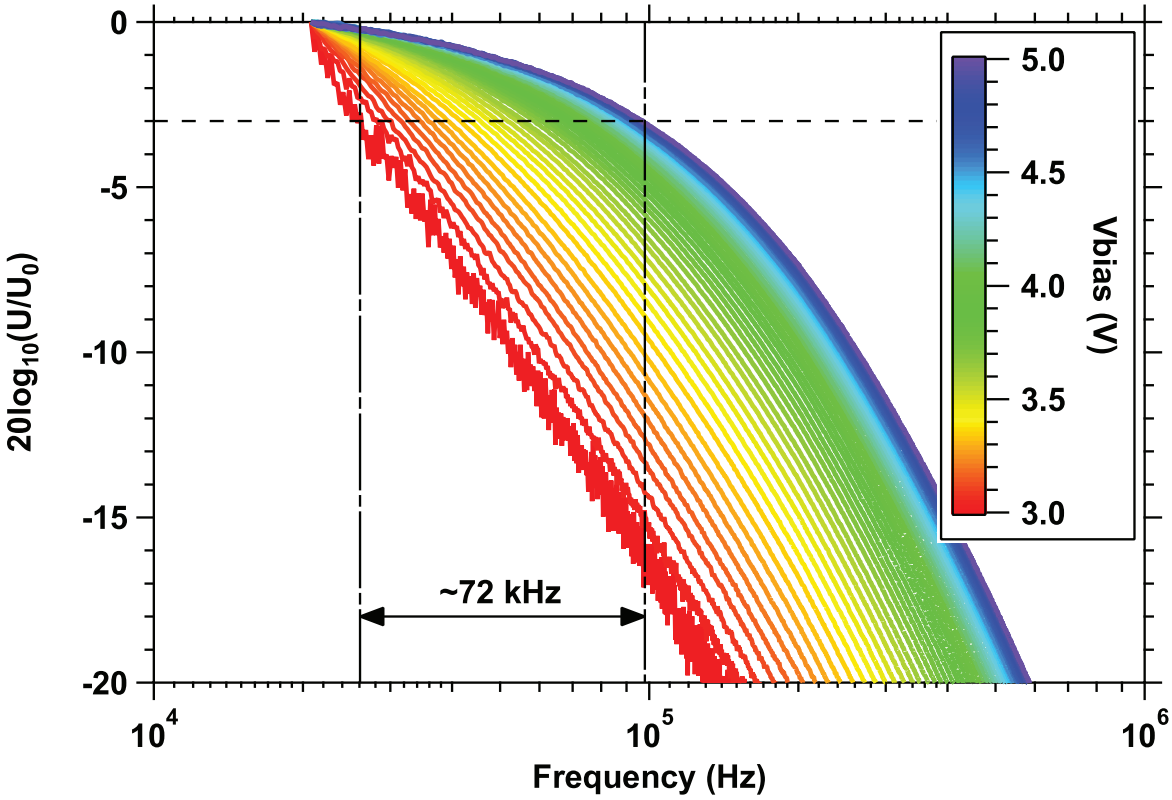

Fig. 4.7 Cut and normalized magnitude response of the SMOLED under test. Clearly the bandwdith incraeses with bias voltage (and therefore injected current); the bandwidth in the best case is 98 kHz and in the worst case is 26 kHz giving a difference of 72 kHz. The ratio of U/U_0 on the y-axis refers to the normalization against the first sample

The charge carrier will eventually recombine either non-radiatively or radiatively freeing the trap to inhibit another charge carrier. Thus the traps have an associated time constant, depending on the quantity of traps occupied; defining the bandwidth as a function of injection current beneath the capacitive limit, which is reached when all the traps are full under a sufficient injection current. It should be noted that for OPDs the process is the same; i.e. traps control the bandwidth; however the medium of energy is reversed. The magnitude of the incident light density to the OPD active area controls the bandwidth and the output is the photocurrent. For high light densities, the capacitive limit is reached.

There are currently no reports that quantitatively describe the trap-bandwidth relationship to the best of the authors' knowledge. The next step to providing such research is to examine a range of small molecules and/or polymers to measure the frequency response for a variety of injection currents in order to define a relationship between traps, injection current and bandwidth could be derived. This is out of scope for this thesis however, but is included in the future work. In the scope of this work, it is enough to simply acknowledge

that the interface traps exist and hence careful transmitter and receiver design is necessary. It should be noted that the bandwidth was measured at the beginning of the SMOLED lifetime and slightly decreased by a few kHz when the VLC links were implemented.

4.2 Communications Performance

VLC using OLEDs is described in this section. The modulation schemes adopted are OOK and *L*-PPM since they are simple to implement in hardware and are respectively the most bandwidth and power efficient pulse modulation schemes currently available. For future OVLC links, Mb/s transmission speeds are desirable and are demonstrated in SMOLED-VLC with a PIN Si PD in this section.

It should be noted that higher order PAM (i.e. 4-PAM, 8-PAM) formats are not tested. The reason for this is because there is an ISI power penalty of at least 6 dB between OOK and 4-PAM and even higher for further orders resulting in lower BER performance with increasing levels [137].

Two link setups are illustrated in Fig. 4.8 where (*a*) utilizes a bias tee as transmitter and (*b*) uses a NAND gate driver adopted from [138]. The latter scheme has two advantages; (*i*) no signal voltage is dropped in the bias-tee components therefore the modulation depth can be increased to 100% from $< 10\%$, and (*ii*) neither the DC nor low frequency components are removed, thus no BLW phenomena, thus the data rate can be extended in comparison to [59]. Furthermore it is entirely and easily scalable to incorporate multiple OLEDs to increase the light output if desired.

In both cases, a dataset is generated in MATLAB and shaped with a unity height rectangular pulse shaping filter that is mapped to OOK, 2-PPM and 4-PPM. A custom LabVIEW script, which autonomously controls every instrument in the setup, is used to output the data at 2 Vpp. In Fig. 4.8(*a*) the pulsed data is mixed via a bias tee with a DC voltage (4.25 V) that is supplied by an Agilent E3631A controlled by LabVIEW, which corresponds to ~ 90 kHz bandwidth and also provides a large symmetrical swing in the pseudo-linear region of the L-I-V curve.

In Fig. 4.8(*b*) the data is passed through a unit buffer NAND gate and mixed with the bias voltage; (generated using the E3631A) and mixed with the signal via an NPN transistor, which is then output to the SMOLED. In both cases the receiver used is a ThorLabs PDA36A-EC Si PIN PD as previous in 10 dB configuration with responsivity of 0.25, 0.30 and 0.375 A/W at 480, 514 and 610 nm, respectively [139]. The intensity modulated OLED transmits the information across the channel which was given in Chapter 3. The link distance is 0.10 m to ensure that an illumination level of 400 lux is measured which is around

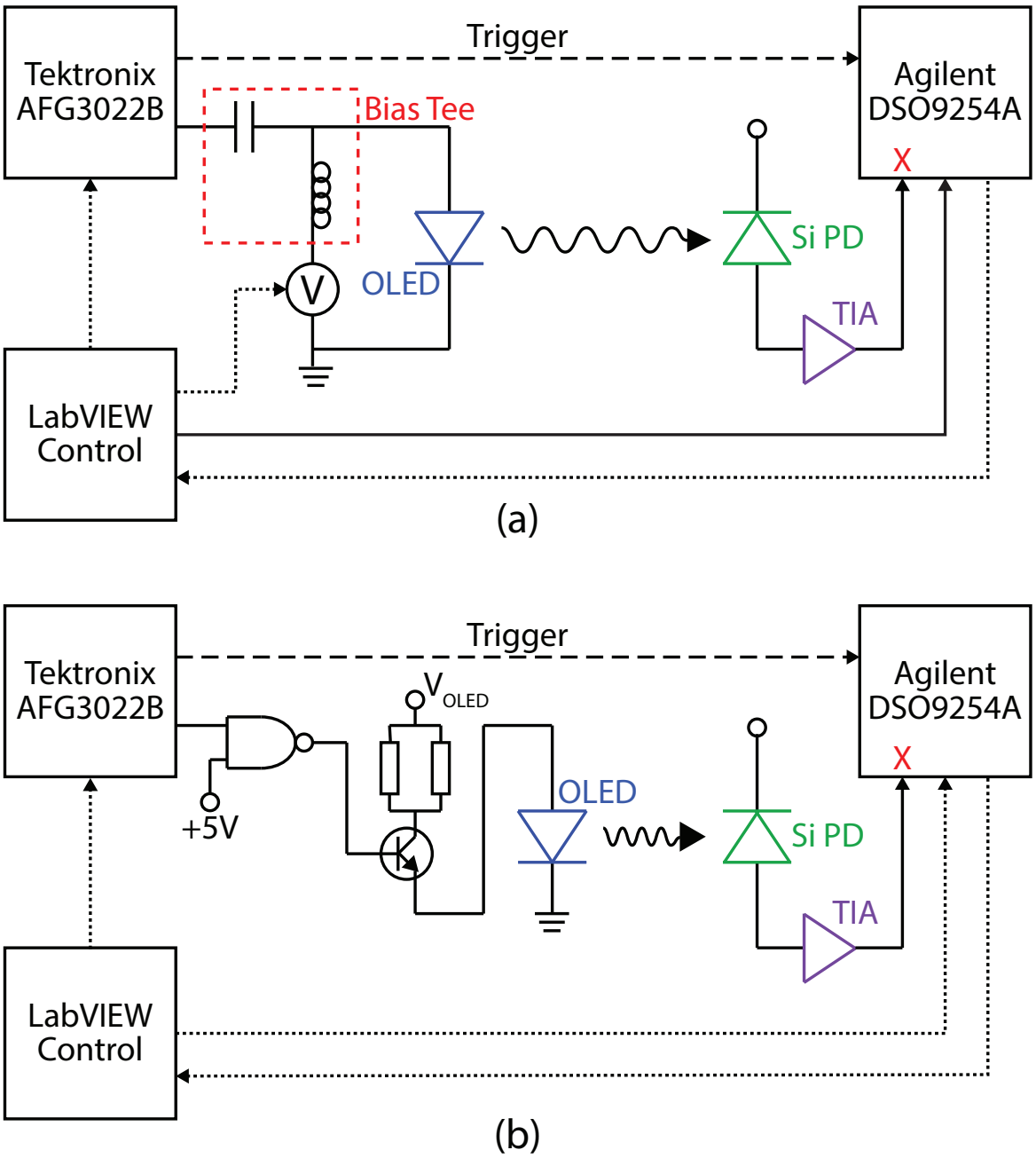

Fig. 4.8 Communications test setup for the SMOLED-VLC with a driver consisting of (*a*) a bias tee and (*b*) a NAND gate driver

the recommended region for home and office lighting [140]. The incoming signal is sampled and acquired using an Agilent DSO9254A real time oscilloscope controlled by LabVIEW. At least 10×10^6 symbols were captured and the BER was calculated in MATLAB by comparing the transmitted and received bits symbol-by-symbol.

The measured system SNR, bandwidth and the noise floor using a frequency sweeping

sine wave and an Agilent MXA N9010A electrical spectrum analyser as can be seen in Fig. 4.9.

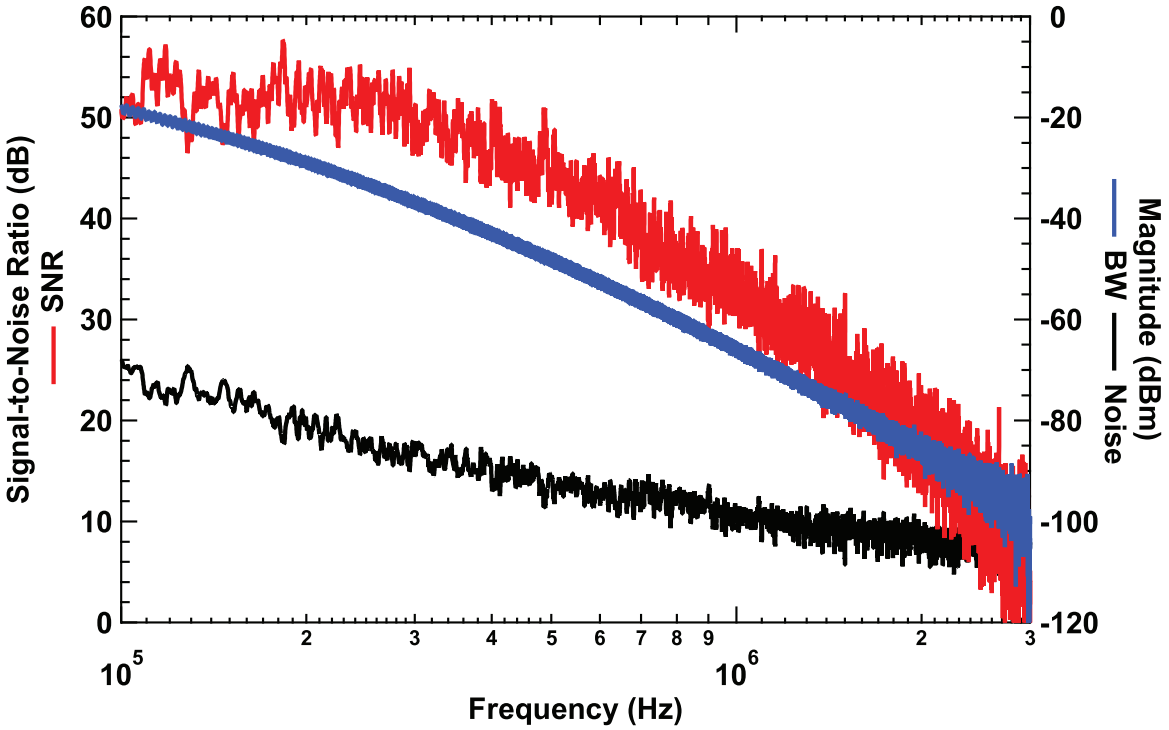

Fig. 4.9 Measured SNR (red) (left), system bandwidth (BW) (blue) (right) and receiver noise (black) (right)

The bandwidth and noise amplitudes referred to the right hand axis were measured directly by the electrical spectrum analyser with the OLED on (bandwidth) and off (noise). The SNR was measured by subtracting the bandwidth and noise amplitudes and indicates a high quality signal with SNR $>$ 30 dB for frequencies $<$ 1 MHz. For frequencies $>$ 1 MHz the SNR quickly degrades. Note that at $\sim$ 2.7 MHz the SNR drops to $\sim$ 10 dB and at $\sim$ 3 MHz the signal has descended into the noise floor.

4.2.1 On-Off Keying

The BER performance of both driving circuits is shown in Fig. 4.10. An improvement in achievable data rate of $>$ 100 kb/s can be observed with the NAND driver over the bias-tee driver which can offer transmission speeds of 250 and 75 kb/s, respectively. Some insight into the data rate increase can be provided by considering the frequency spectrum of each driver. In the bias-tee driver, the selection of capacitor is crucial as it has an associated cut-on frequency f_{co}. If the capacitor value is selected too high the cut-off frequency is

reduced (which is desirable) but more power is dissipated meaning that the modulation depth decreases. Improperly selecting too low means f_{co} increases, inducing the BLW phenomena as the DC and low frequency components below f_{co} are significantly attenuated. This is reflected in the magnitude response as illustrated in Fig. 4.11 which clearly shows three sections of an arbitrary system with a bias tee driver that has similar characteristics to a band pass filter.

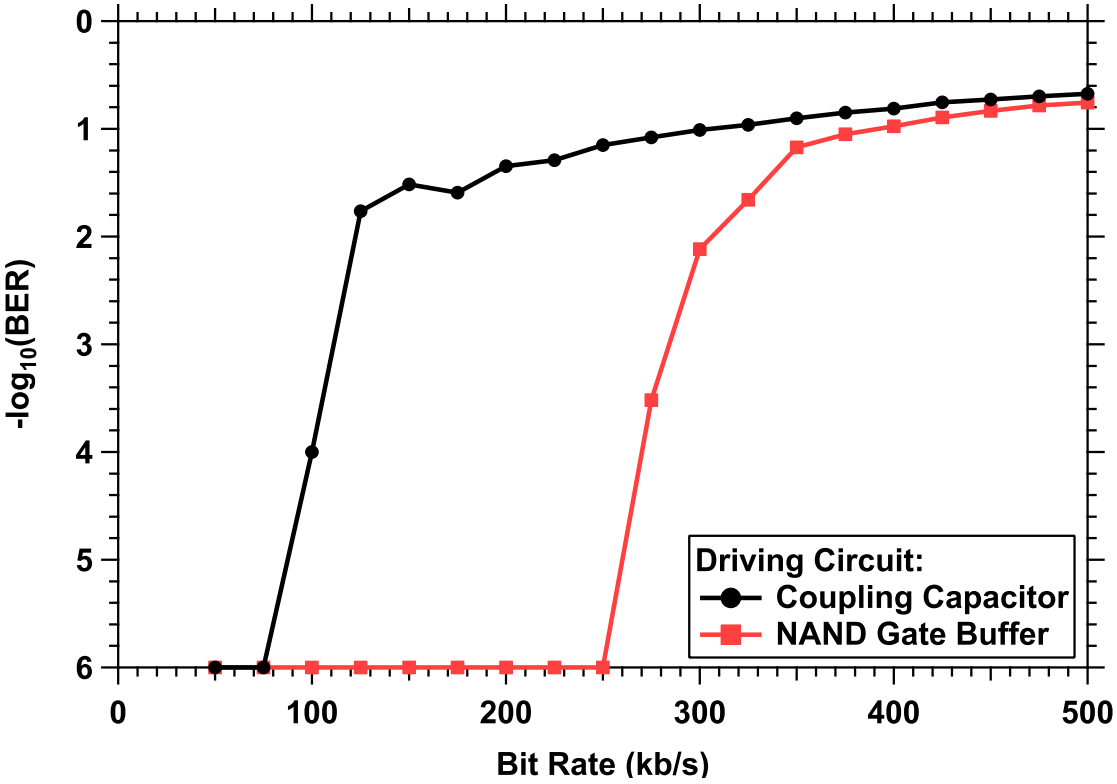

Fig. 4.10 BER performance of each driving circuit; data rates of 250 and 75 kb/s can be achieved using the NAND gate and bias tee drivers, respectively

In section A the low frequency components are attenuated, which is the root of the BLW. Sections B and C show a normal low pass response where all frequencies in section C are outside the system modulation bandwidth. The difference in drivers is further reflected in the eye diagrams produced from the received symbols at 100 kb/s data rate shown in Fig. 4.12 and Fig. 4.13 as in Fig. 4.11 there is a clearly a dominating BLW effect caused by the bias tee driver. There have been studies to try and eliminate BLW such as the quantized feedback baseline restoration [141], which aims to restore the missing frequency components with a feedback filter, or using a subcarrier frequency in order to avoid the signal attenuation. This method in particular is not ideal as it wastes the available bandwidth, thus reducing system capacity. It is noteworthy that BLW is approximately a random Gaussian process [41] so it

is not trivial to recover the original signal envelope and hence there is no ideal solution to date.

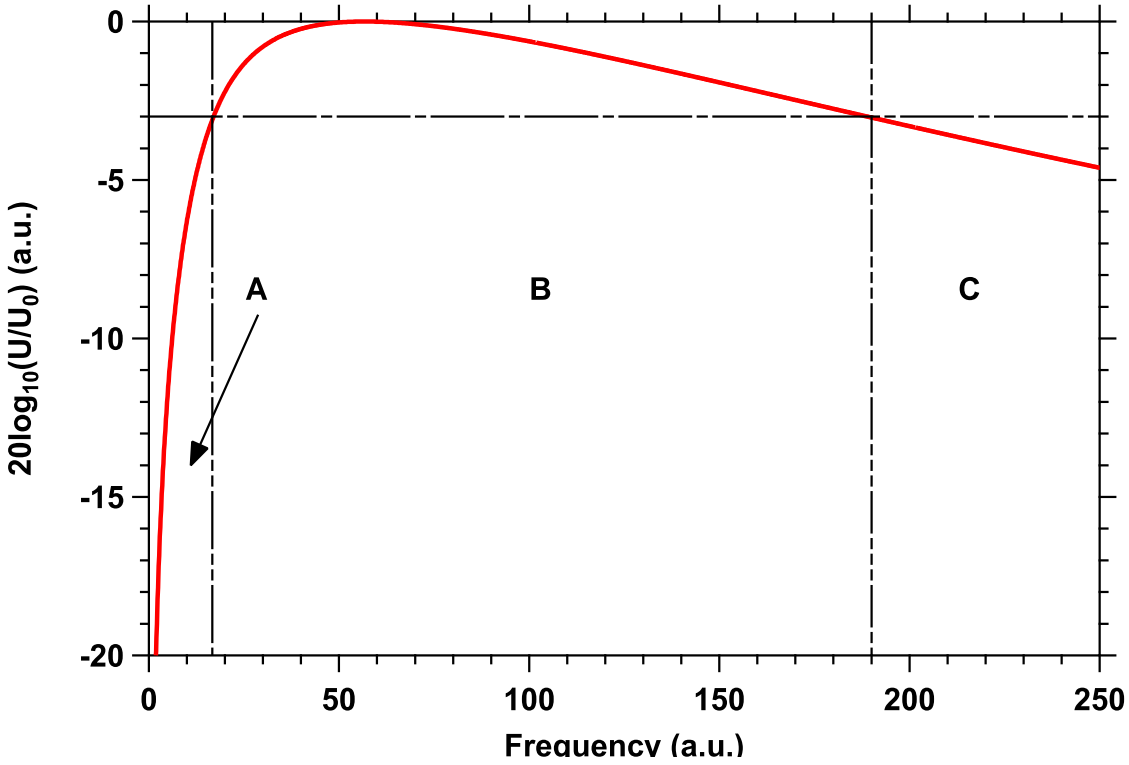

Fig. 4.11 Introduction of BLW from coupling capacitor of the bias tee

By isolating the AC data source using a NAND gate, there are no low frequency restrictions and therefore no BLW effect. It is for this reason that the data rate can be extended. In addition, the modulation depth increases from $< 10\%$ in bias-tee driver up to $\sim 100\%$ in the NAND driver as no signal power is dissipated through components, thus significantly improving SNR at the receiver which is also a major factor in the improvement. The advantage of bias-tee driver is that it is not restricted to digital pulse modulations; analogue formats and multi-level digital formats such as pulse amplitude modulation could be adopted, which is not possible with the NAND driver. No analogue or multi-level modulations are demonstrated in this thesis because the NAND driver is adopted as the preferred SMOLED driver.

4.2.2 Pulse Position Modulation

PPM is an attractive modulation format due to the low average power level, offering a natural protection to BLW as well as soft decision demodulation method offering an electrical

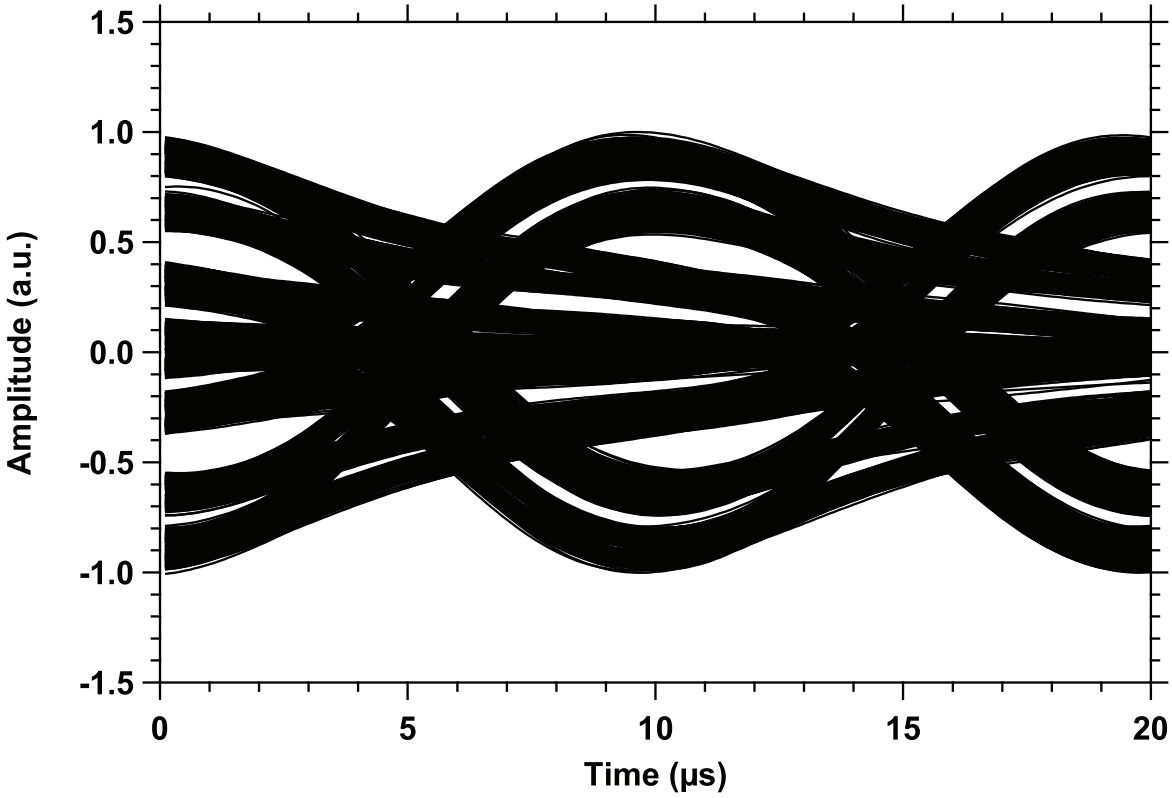

Fig. 4.12 Eye diagram for bias tee driving circuit at 100 kb/s; there is a clear BLW effect perturbing the link quality

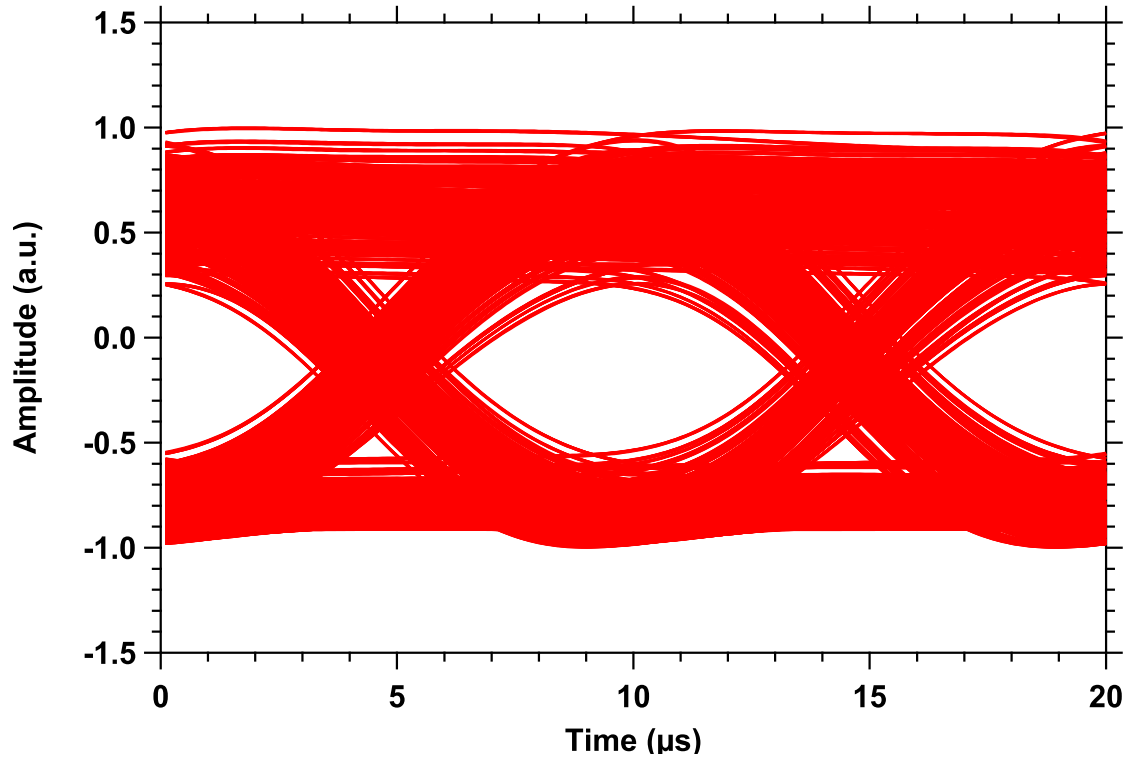

Fig. 4.13 Eye diagram for the NAND gate driving circuit with a clear improvement over the bias tee driver

SNR gain of 1.5 dB [115], however at the cost of increased bandwidth requirement [44]. Therefore in this thesis only the lower orders of PPM (i.e. 2 and 4-PPM) are used. The slot rate and amplitude of 4-PPM is set to twice that of 2-PPM; which is in turn set to twice that of OOK in order to provide the same transmission speeds. Therefore 4-PPM will require twice the bandwidth of 2-PPM (and four times that of OOK; since this system is bandlimited, no higher orders of PPM are tested i.e. 8-PPM because of the eight times bandwidth requirement of OOK. Soft decision demodulation is not covered here as it is well-known and can be referred to in [115]. The performance of all other pulse modulation formats lays somewhere between the bandwidth efficient OOK and the power efficient PPM [40] and this is the reason that only OOK and PPM are examined.

The BER performance of 2 and 4-PPM with hard decision decoding using a threshold detector is illustrated in Fig. 4.14 demonstrating transmission of 150 and 50 kb/s data rates along with the 250 kb/s OOK link for reference. In comparison to the $\sim$ 90 kHz system bandwidth bottleneck introduced by the SMOLED it was expected that OOK would offer the best performance with no equalization as it has half the bandwidth requirement of 2-PPM and four times less than 4-PPM. Furthermore, as expected 2-PPM also outperforms 4-PPM and this is also attributed to the lower bandwidth requirements.

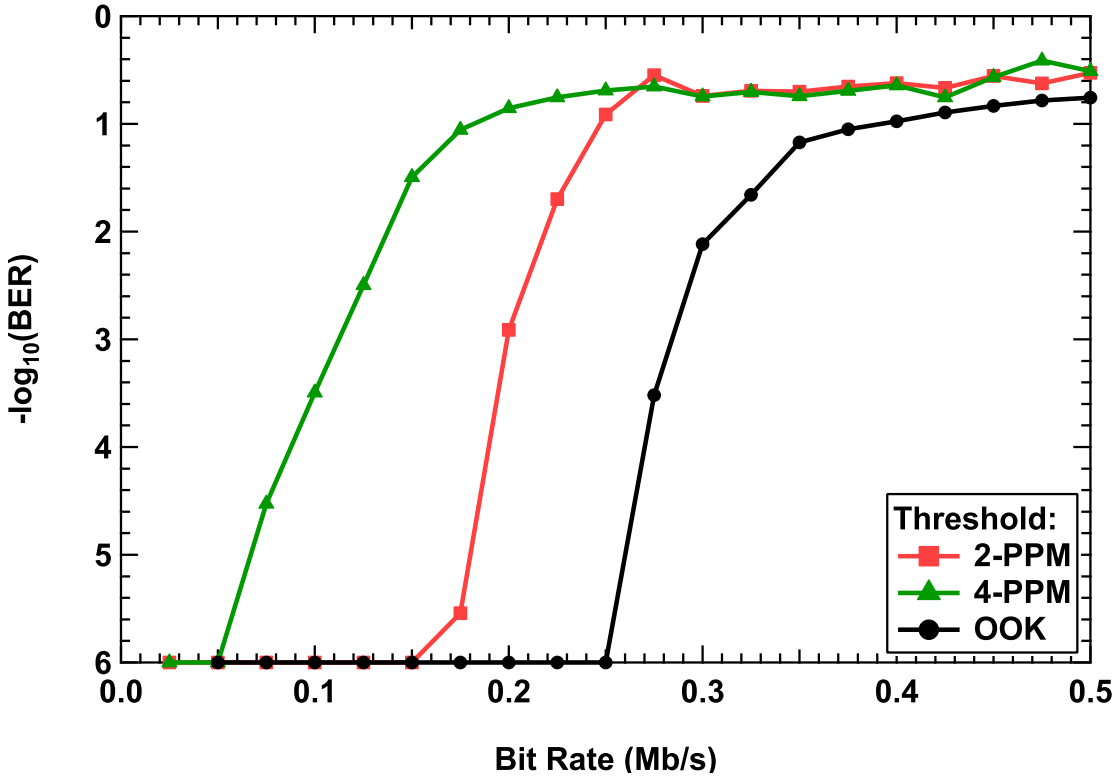

Fig. 4.14 Unequalized BER performance of each modulation

The system BER performance using soft decision demodulation as a function of the bit rate is shown in Fig. 4.15. It is not possible to use the soft decision algorithm with OOK so only 2 and 4-PPM with bit rates of 400 kb/s and 200 kb/s, respectively are used in this work. There is still a disparity between 2-PPM and 4-PPM caused by their respective bandwidth requirements. Using soft decision demodulation offers a significant improvement in the available data rate in comparison to threshold detection. More specifically, the improvement in data rates for 2 and 4-PPM are 250 kb/s and 150 kb/s, respectively. This means that 2-PPM has been able to double its capacity while 4-PPM has improved by four times, which is remarkable. These data rates obviously outperform OOK with threshold detection are just slightly short of the 550 kb/s as reported in [59] using an MLP-ANN equalizer.

In order to ensure that it is the filters that are being examined, a DSP board was selected where the synchronization can be performed in the MATLAB domain. The clock speed of the DSP is 225 MHz, which is clearly well in excess of the requirements for this system. The DSP board is programmed using the TI Code Composer Studio (CCS) software and the signal processing is implemented with the same features (i.e. number of taps in the equalizer case, or algorithm in soft demodulation case) as in the offline case for a like-for-like comparison. Since the adaptive algorithm was used it is not possible to give a general figure. The output of the DSP board is then recovered and transferred to the MATLAB domain for comparison with the offline DSP. It should also be noted that the data used in the offline and online cases is not the same data in order to ensure the thorough examination of the online filters and ensure the comparisons are not influenced by the data sequence; thus ensuring that the data is not biasing the result. This is reflected in Fig. 4.15 and Fig. 4.16, which show minor differences between the offline and online cases.

4.3 Equalization

As was outlined in Chapter 3 it is possible to observe equalization as a classification problem rather than an information theory problem and thus using an ANN as a system response equalizer. ANNs are the best performing transversal linear equalizer for both channel and system equalization [142]. This is because they are capable of mapping any input-output sequence (linear or otherwise) and nullifying the negative effects that other equalizers struggle to cope with such as large spectral nulls. The MLP ANN is implemented here in order to maximize the available data rates. The MLP is not the best performing ANN; however it is the least complex and supports the Levenberg-Marquardt back-propagation (LMBP) algorithm, which is very popular due to the ease of hardware implementation [142]. The LMBP algorithm is a supervised training method based on a gradient descent on the error cost func-

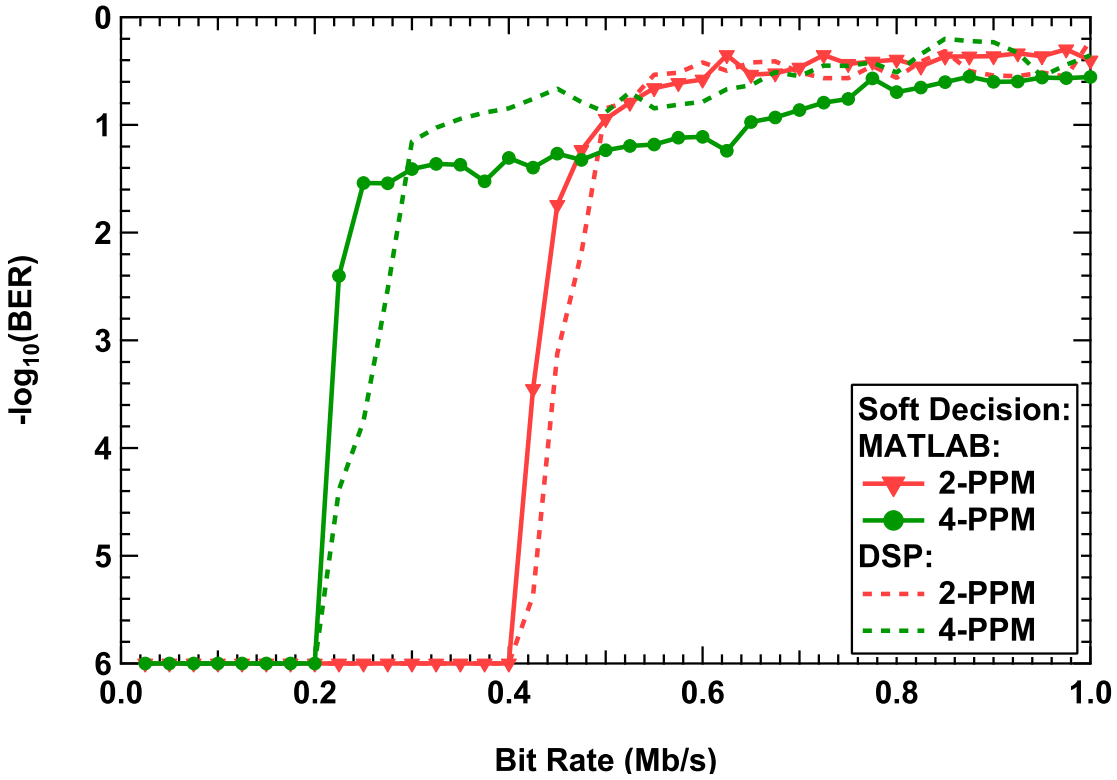

Fig. 4.15 Soft decision BER performance of 2-PPM and 4-PPM where 400 and 200 kb/s can be recovered, respectively

tion. That is, the difference between the received data and known data at the receiver for a certain number of training symbols. An adaptive algorithm is used to select the learning rate parameter [127]. The MLP-ANN equalizer is very well known so not fully covered here also to save space. For a more detailed overview including the mathematical analysis the reader should see [59, 124, 142]. The MLP-ANN is implemented offline in the MATLAB domain first and followed by the DSP based MLP-ANN. An FPGA could have been implemented for a fully real time result; however a full clock recovery and synchronization method would have been required.

Using MLP-ANN as an equalizer, it is possible to significantly improve data rates well into the Mb/s region as illustrated in Fig. 4.16. In every single case a higher data rate was recorded than the 1.4 Mb/s reported in [63] using a less complex system and modulation scheme. Firstly considering the offline case, 2-PPM, OOK and 4-PPM can transmit 2.7, 2.15 and 1.6 Mb/s, respectively. This is a significant improvement over the soft decision demodulation (for 2 and 4-PPM) and threshold detection (for OOK). The most unexpected and significant result in Fig. 4.16 is that 4-PPM offers the highest data rate, followed by OOK and then 2-PPM, especially as 4-PPM was the worst performing in each of the pre-

vious demodulation methods. Since the system is-band limited, it was expected that OOK would outperform 4-PPM due to the additional bandwidth requirement; however the experimental measurements show a contrary result. The cause of this is attributed to the fact that $P(0) = 0.75$ for 4-PPM and $P(0) = 0.5$ for OOK where $P(.)$ is the probability. Equalized 2-PPM and 4-PPM should have similar optical power penalties (OPPs). 4-PPM has a shorter pulse duration than 2-PPM so the OPP for 4-PPM should be higher as more power is required to reach the same average energy. However, the probability of occurrence of two consecutive pulses is much lower in 4-PPM than in 2-PPM, thus the significant improvement in BER performance [143]. At data rates > 2.7 Mb/s the presence of severe ISI in combination with degradation of SNR causes the MLP-ANN to fail.

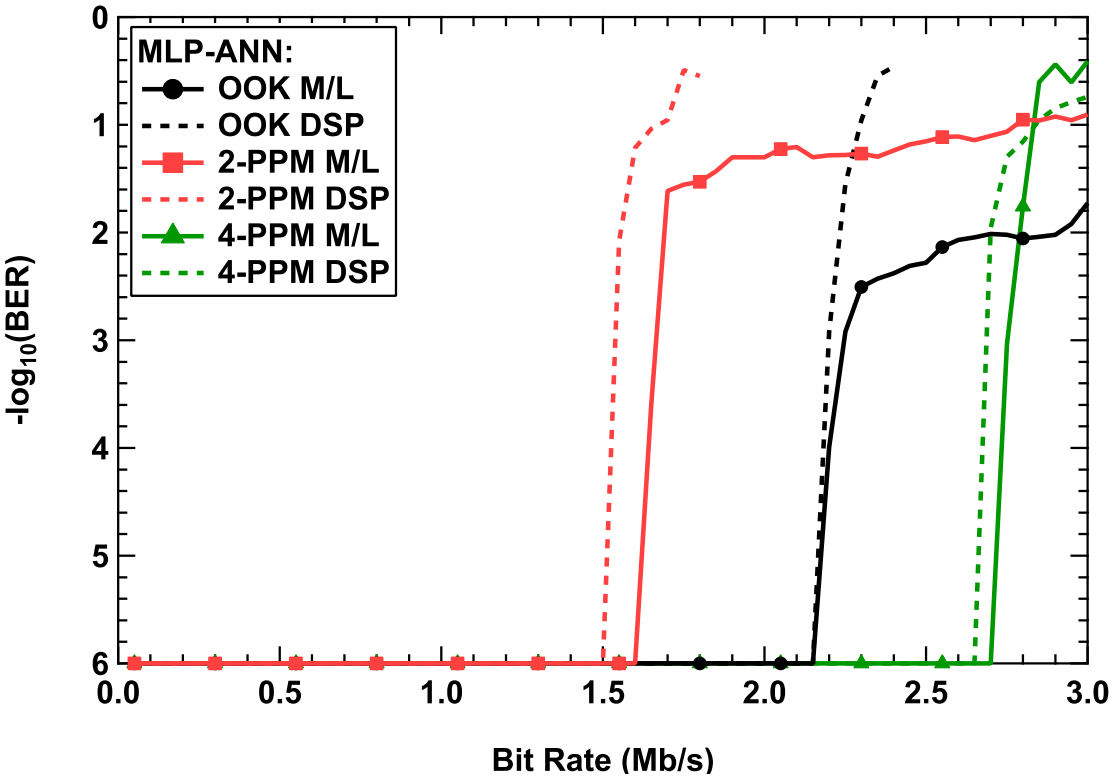

Fig. 4.16 Equalized BER performance of 2-PPM, OOK and 4-PPM in conjunction with the MLP-ANN in the MATLAB (M/L) domain, where data rates of 2.7, 2.15 and 1.6 Mb/s can be achieved, respectively. Significantly, using the DSP MLP-ANN, data rates of 2.65, 2.15 and 1.5 Mb/s can be achieved for the same modulation schemes which offer extremely good agreement in each case

The DSP MLP-ANN can offer similar data rates. For 4-PPM, OOK and 2-PPM data rates of 2.65, 2.15 and 1.5 Mb/s can be transmitted, respectively. This is a significant result as it qualifies the offline results and indicates that in a fully real time system including

clock recovery it would be feasible to achieve Mb/s data rates. The difference between each case is 0.05, 0 and 0.1 Mb/s for 4-PPM, OOK and 2-PPM, respectively which in terms of percentage is 1.85%, 0% and 6.25%, indicating a very small difference in each case. It should also be noted that in each case the MATLAB MLP-ANN outperforms the DSP based MLP-ANN.

4.4 Summary

In this chapter the optoelectronic characteristics of the SMOLED are outlined. Subsequently, a 2.7 Mb/s VLC link with the SMOLED as transmitter and a Si PD as receiver has been examined using an ANN equalizer in both offline and online (2.65 Mb/s) configurations. In comparison to previously reported works, the record data rate has been improved by two fold, from 1.4 Mb/s [63] up to 2.7 Mb/s for any state-of-the art organic VLC system. In terms of pulse modulation the improvement is four fold from 550 kb/s [59] to 2.15 Mb/s (for OOK) and five times from 550 kb/s to 2.7 Mb/s (for 4-PPM). The reason for this is due to the significantly reduced probability of occurrence of two consecutive pulses in 4-PPM in comparison to OOK. Furthermore, it is the first time online filtering has been demonstrated for any VLC system, offering good agreement with the offline results.

Chapter 5

Visible Light Communications with Organic Photodetectors

5.1 Introduction

This chapter will concentrate on VLC systems with an inorganic WPLED as the transmitter with an OPD receiver. The OPD under test is a P3HT:PCBM device with P3HT interlayer. It is a custom device that was manufactured under collaboration by Siemens AG, Corporate Technology. The external quantum efficiency of the P3HT:PCBM blend is outlined in Fig. 5.1, while in Fig. 5.2 the responsivity is shown in comparison to the ThorLabs PDA36A-EC Si PD.

From Fig. 5.2 it is clear that the OPD has some significant advantages over Si PDs. Firstly, the large ~ 2 eV band gap energy means that the cut-off wavelength is around 620 nm (red wavelengths) and no IR noise is absorbed. Secondly, the OPD responsivity is much higher (more than twice in some cases) than the Si PD at a significantly lower bias voltage ($>$ 20 V) across the entire active region. This is important for VLC systems, especially considering the common reliance on GaN (blue) based WPLEDs that often require blue filtering to recover their fast transient responses. The peak wavelength in such LEDs is typically 445 nm (see Fig. 1.4 in Chapter 1), which corresponds to a responsivity of $\sim$ 0.1 A/W for Si PDs and 0.25 A/W for the OPD under test meaning a better quality signal is obtained at the receiver. The major disadvantage is that the red wavelengths are not absorbed as mentioned which means that OVLC WDM capacity is reduced considering that a red light is required to contribute to the white balance and no information could be recovered from these wavelengths.

As reported in [61] the OPD bandwidth is heavily dependent on the incident light density

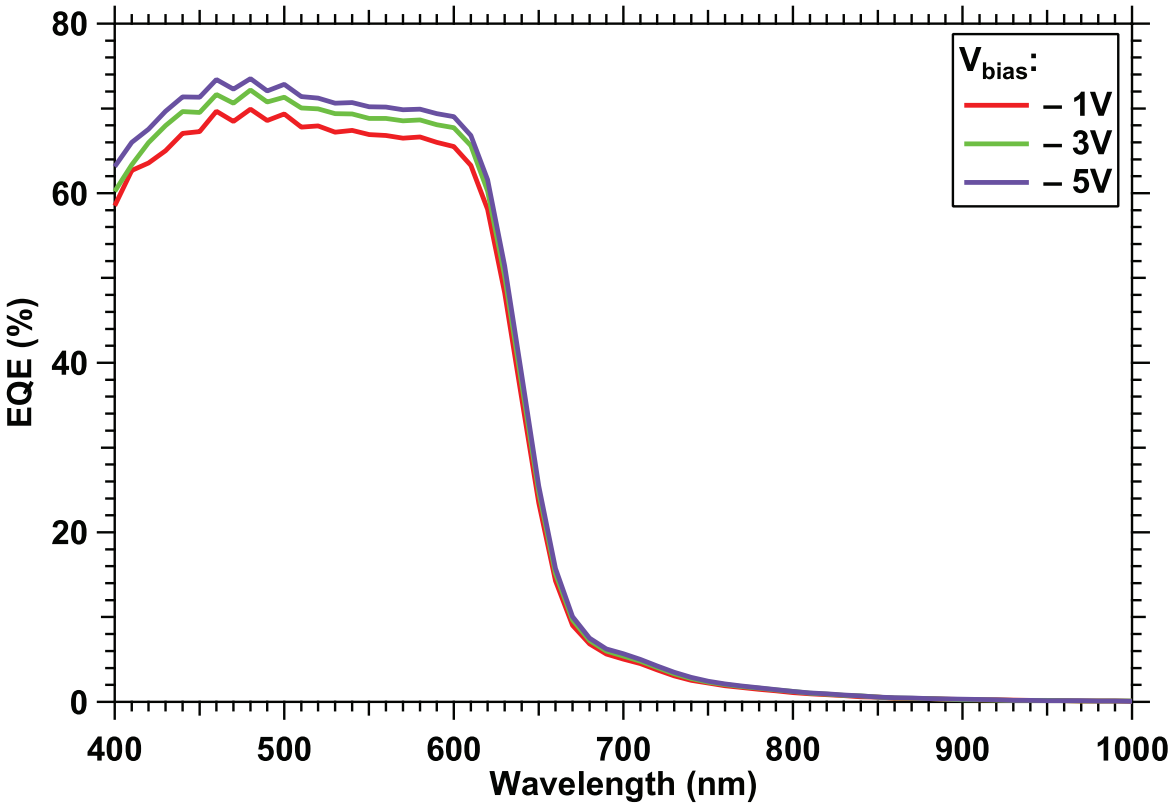

Fig. 5.1 EQE of the P3HT:PCBM OPD under test

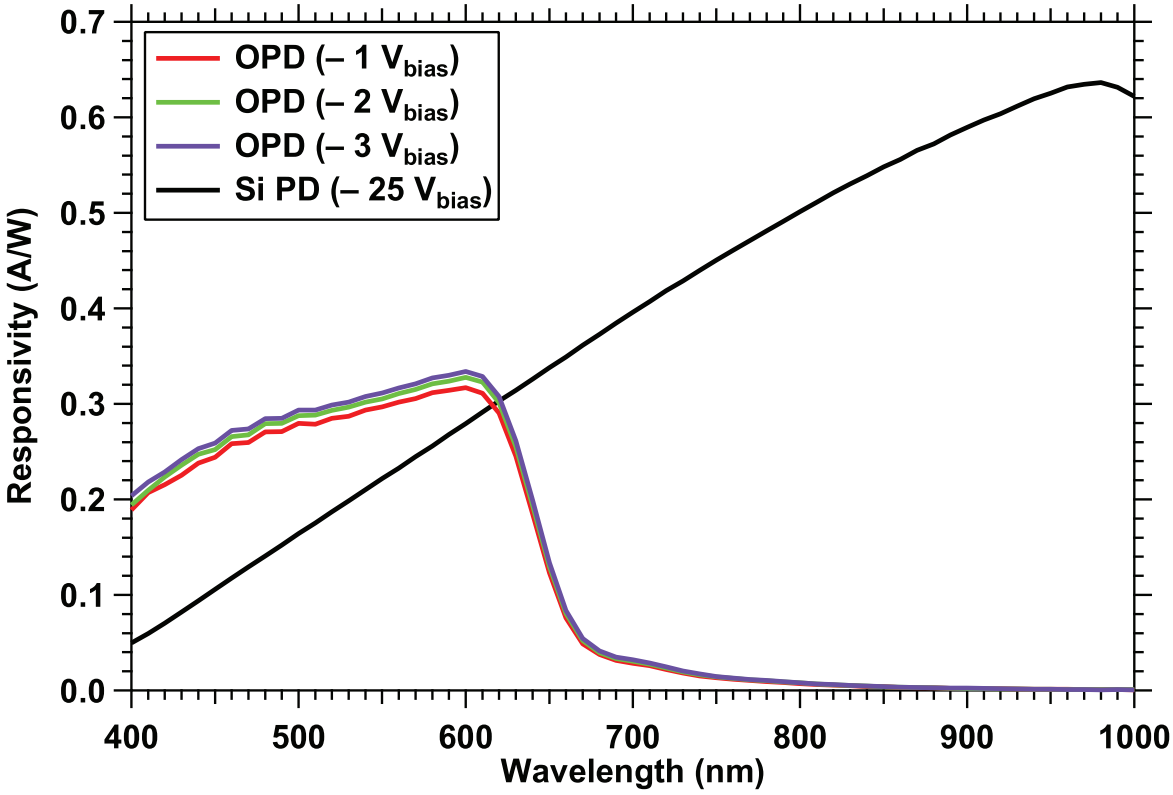

Fig. 5.2 Responsivity of the P3HT:PCBM OPD under test in comparison to a Si PD

(W/m^2) due to traps at the interface. Under a high light intensity ($>$ 300 μW/cm^2) the number of charge carriers generated exceeds the number of traps at the interface and the time constant of the plate capacitance controls the overall cut-off frequency as in Si PDs. Conversely, at low light intensities the number of traps exceeds the number of charge carriers meaning that the BW is controlled by the time constant of the interface traps and this can be illustrated in the bode plot of Fig. 5.3. The OPD is tested with a GaN WPLED as the transmitter, which has a BW that is around one order of magnitude higher than the organic devices ($\sim$ 4 MHz); ensuring that the equalizers under test are extending the operational range of the organic devices.

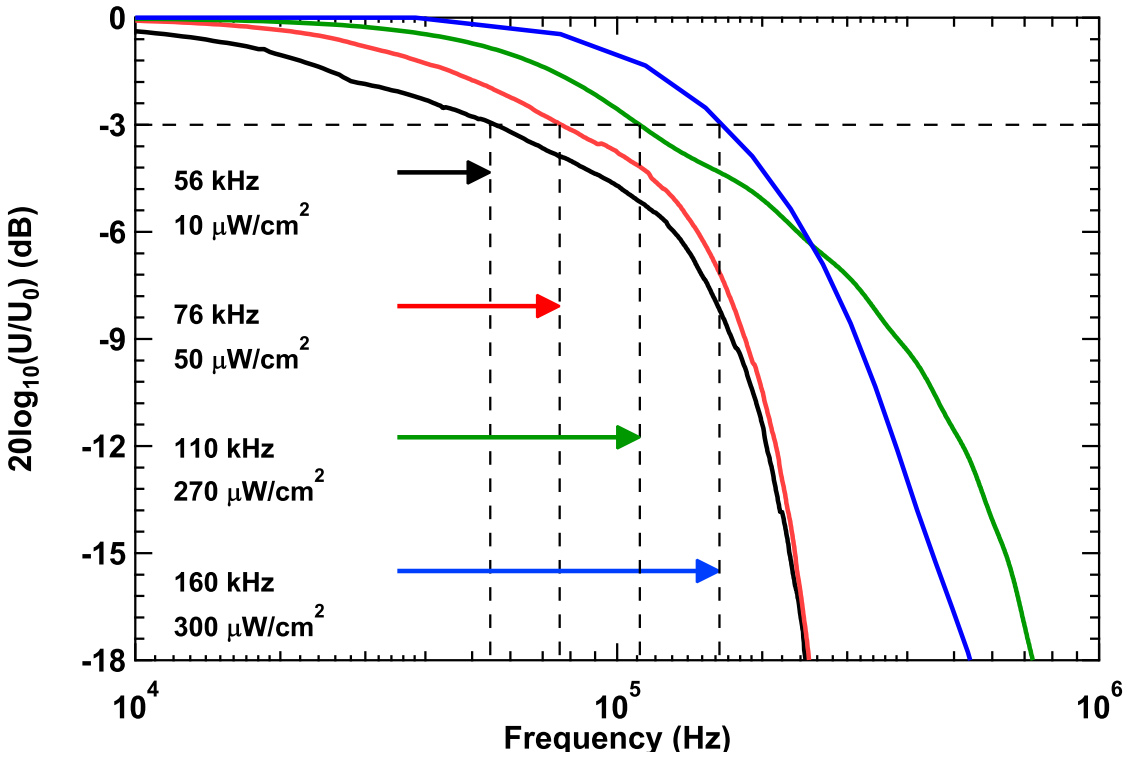

Fig. 5.3 OPD BWs for four light densities, varying from 10 to 300 μWcm^{-2} corresponds to BWs ranging between 56 $-$ $-$160 kHz, giving $\sim$ 100 kHz range

5.2 Communications Performance

OPDs are not expected to replace Si PDs in the near future in optical communications due to their strong market position and wide user base. On the other hand, OPDs can be of interest for applications where Si PDs are not suitable and therefore are an exciting technology for the future, also considering the significant cost reduction offered by spray-coating at room

temperature. Due to the low charge carrier mobility in organic semiconductors which are orders of magnitude lower than in Si, the BWs of OPDs are usually much lower than the BWs of Si devices; which is a major challenge.

The OPDs under test are produced under collaboration by Siemens AG Corporate Technology and are based on the BHJ principle [96]. Four diodes with 1 cm^2 active area each are fabricated on a single 5×5 cm^2 transparent glass substrate as previously illustrated in Fig. 2.14 and Fig. 2.15 in Chapter 2.

The thin film ($\sim$500 nm) organic semiconductor layer, a blend of P3HT as the donor material and PCBM as the acceptor material, is deposited by spray-coating from a xylene solution as in [54], which leads to extremely low material cost devices ($\sim$£0.17 cm^{-2}). This simple fabrication technique is extremely attractive for VLC systems. The OPD BW is dynamic and dependent on the incident light intensity, as reported in [61]. In high light densities, the number of charge carriers is greater than the number of interface traps and therefore the BW is proportional to the time constant of the plate capacitance. Conversely in low light densities, the number of interface traps outnumbers the number of charge carriers so the BW is proportional to the traps time constant.

Further, the OPD is also attractive for VLC systems due to its superior responsivity compared to Si photodetectors in the visible range under a much smaller reverse bias as shown in Fig. 5.2. It also has a sharp cut-off wavelength at $\sim$620 nm due to the larger band gap of P3HT ($\sim$2 eV) in comparison to Si ($\sim$1.16 eV). It should be noted that a band gap of 2 eV is relatively high and has a cut-off wavelength around 620 nm (red wavelengths) which could be a problem for VLC applications that take advantage of wavelength division multiplexing (WDM). The cut-off wavelength can be shifted to the NIR region by replacing P3HT in the BHJ blend with a low band gap material such as PCPDTBT as in [144, 145].

In this chapter BER measurements are made by varying the light densities between 10 and 300 μW/cm^2; obtaining a BW ranging between $\sim 50-160$ kHz. Furthermore, both OOK and 4-PPM are investigated. 2-PPM is not examined due to the fact that it has a higher spectral content around the DC and low frequencies regions while having the same BW requirements as 4-PPM. No higher orders of PPM are investigated due to the significant additional BW requirements as mentioned in the previous chapter. At the receiver an ANN equalizer is required to recover the data as in [59] since the required high data rates are much higher than the system BW.

5.2.1 Test Setup and Artificial Neural Network

The test setup is shown in Fig. 5.4. The PRBS in the OOK data format is generated in MATLAB and translated into the 4-PPM code. The data is output by a Tektronix AFG3022B

function generation controlled by LabVIEW (LV in Fig. 5.4) and buffered by a NAND gate with a high output impedance, then mixed with a DC level prior to intensity modulation of the LED (Philips Luxeon Rebel, BW 4.4 MHz). The white light is transmitted over the linearly attenuating line-of-sight channel h as given by [17]:

$$h(0) = \frac{A}{d^2} R_0(\theta) \cos(\varphi) \tag{5.1}$$

where A is the OPD active area (1 cm^2), d is the distance between the transmitter (LED) and receiver (OPD), θ is the angle of light emission, φ is the angle of incidence and R_0 is the Lambertian radiation pattern of the LED, given by [17]:

$$R_0(\theta) = \frac{m+1}{2\pi} \cos(\varphi)^m \tag{5.2}$$

where m is the Lambertian order.

At the receiver, the output of the photodetector is passed through an Analog Devices AD8015 (noise current density 2.4 pA Hz$^{-1/2}$) transimpedance amplifier the output of which is acquired by an Agilent DSO9254A oscilloscope.

The OPD was reverse biased at -5 V as in [61] using an Agilent 3631A controlled by LabVIEW. Then light was applied to the OPD through the transparent anode electrode. The applied light density was measured using a $\sim$1 cm diameter thermopile disk (14BT, Laser Instrumentation Ltd). In order to gain insight into the OPD performance under different light densities, the applied light intensity was varied by varying the transmission (LED-OPD) distance. Incident light densities of 10, 50, 270 and 300 μW/cm^2 were generated, and correspond to measured BWs of 56, 76, 110 and 160 kHz, respectively, as illustrated in Fig. 5.3. The BW difference between the lowest and highest light density is $\sim$100 kHz, which is a significant difference.

OOK is the most common modulation scheme for VLC systems due to its ease of implementation and BW efficiency [59]. Data is inferred by the presence or absence of a pulse of energy in the symbol period, see [108, 111]. Conversely PPM is the most power efficient modulation scheme, requiring half the power of OOK at the expense of a two-fold increase in BW requirement that follows [115]:

$$\frac{P_{PPM}}{P_{OOK}} = \sqrt{\frac{2}{L \log_2 L}} \tag{5.3}$$

where L is the order of PPM. This comes at the cost of decreased BW efficiency, following

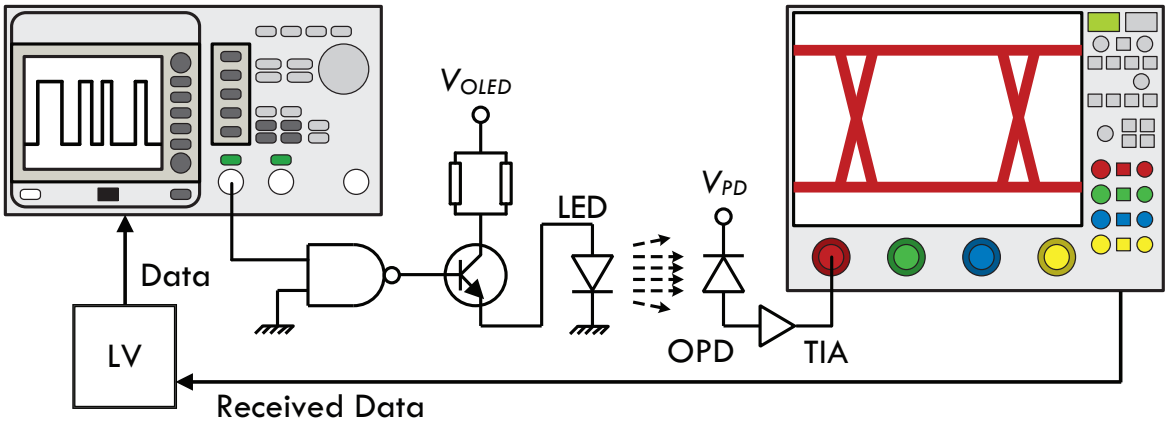

Fig. 5.4 Schematic system block diagram

[115]:

$$BW_{L-PPM} = \frac{LR_b}{\log_2 L} \tag{5.4}$$

where R_b is the bit rate. The spectral signature of 4-PPM contains little or no DC and low frequency components thus is ideal for reducing the high-pass filter induced BLW phenomena that occurs in indoor optical wireless communication links [59]. Soft demodulation can also be used with 4-PPM, offering an electrical SNR gain of more than 1.5 dB in the presence of signal distortion. Hence, threshold detection is not considered here for 4-PPM since it will yield an inferior result [115].

DMT is a popular option for increasing data rates in VLC systems and extremely high data rates have been demonstrated. In order to really maximize the bandwidth of such a DMT system three equalizers are required; a pre-equalizer, a time domain equalizer and a post-equalizer. Each of these equalizers requires knowledge of the system and channel responses (as stated in [146]). So far no widely accepted feedback channel has been used in VLC systems and therefore such as a system is not currently preferable as it may not be viable in the future.

Instead, a high performance equalizer such as the ANN can be used that does not require any knowledge of the channel because it acquires this information from a training sequence that consists of a known header file that is transmitted before the useful information. The MLP ANN is selected due to its superior performance in symbol error rate to transversal linear equalizers [125]. In theory, the MLP is not the optimal classifier, the DF or RBF ANNs should outperform the MLP, however these configurations have significantly higher computational intensity and complexity for only a slight increase in data rate [142]. The MLP consists of three layers; an input layer x, a hidden layer and an output layer y with

a single node. The N-input layer is the equivalent of an N-tap delay line in conventional filters; the number of nodes in the hidden layer is also made equal to N and is where the processing occurs. The output of the MLP is given by:

$$y = f\left(b + \sum_i w_i x_i\right) \tag{5.5}$$

where $i = 0,\ \ldots,\ N$ if a bias b exists and $i = 1,\ \ldots,\ N$ otherwise. The filter weights are given by w_i and are adjusted during the ANN training in order to find the correct coefficients to map the system response.

The ANN is trained by the Levenberg-Marquardt back propagation algorithm with an adaptive learning rate [127], which is supervised training that works on the basis of minimizing the error cost function E of a known bit sequence at the receiver and the transmitted data as follows [124]:

$$E(n) = |y(n) - d(n)|^2 \tag{5.6}$$

where d is the desired sample and y is the received sample. The back propagation algorithm updates the weights as follows [124]:

$$w_{ij}(n+1) = w_{ij}(n) - \eta \frac{\partial E(n)}{\partial w_{ij}(n)} \tag{5.7}$$

Once the ANN is fully trained it can be used to correct the received data.

The ANN is capable of generalizing, which is another advantage over linear equalizers. This means that if the sequence contains transitions that are unknown to the equalizer due to not being present in the training sequence, the ANN has a higher probability of recovering the data than any other linear equalizer [124]. The downside of this is that an excessive number of neurons tend to lead to over-fitting, a big problem with ANNs. Therefore it is crucial to select the correct number of neurons for the system. The ANN is implemented in MATLAB.

5.3 Results

In Fig. 5.5 the BER performance for OOK using both threshold detection (denoted T/H) and the ANN equalizer is shown in high light density conditions with 160 kHz system BW. Furthermore the performance of 4-PPM with soft demodulation and the ANN equalizer is also shown. First considering the unequalized case, data rates of 500 and 300 kb/s can be

achieved with 4-PPM and OOK, respectively (1000 and 300 kHz BW requirement, respectively), showing that 4-PPM significantly outperforms OOK by offering ∼66% additional data rate.

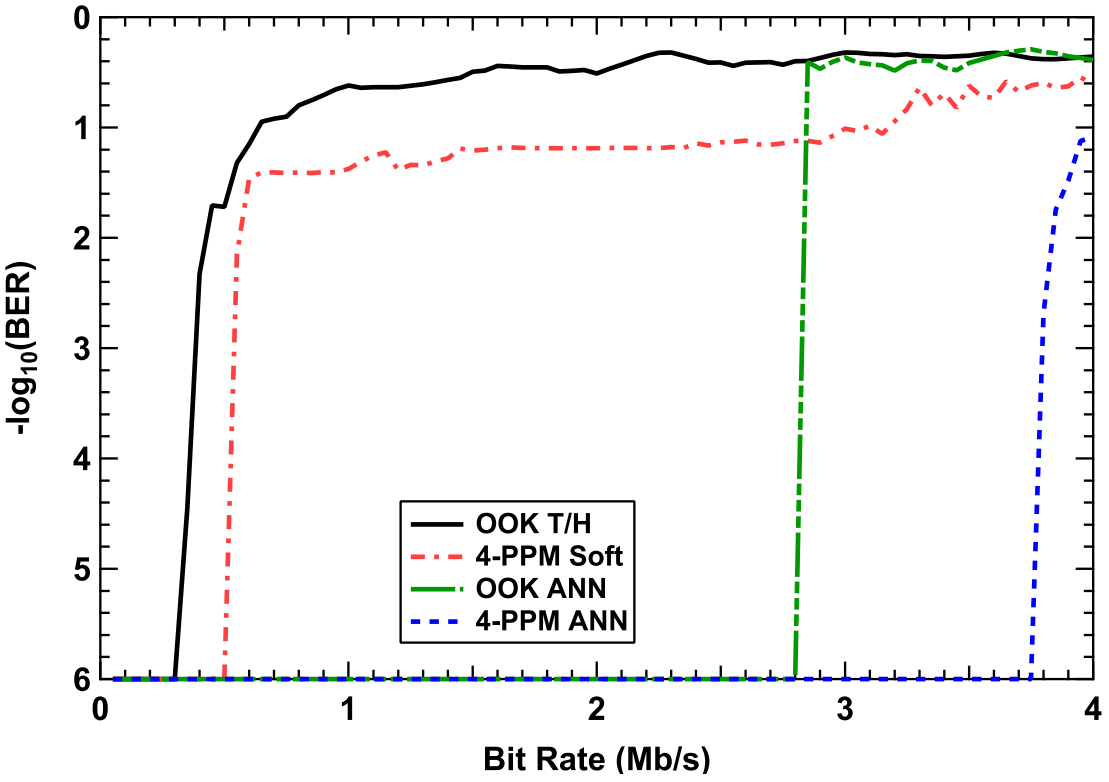

Fig. 5.5 BER performance for OOK and 4-PPM with and without ANN equalization

The reason for this is attributed to the fact that soft demodulation depends on the signal gradient. As opposed to threshold detection, where the bit levels are assigned with reference to an average value, soft demodulation reshapes the incoming signal into an L column matrix. The highest value is assigned a 1-level and the rest are assigned 0-levels. Failure of soft decoded 4-PPM is therefore caused by the rapid transmission of alternative states where the transient response of the OPD is not sufficient and the signal gradient cannot become negative to be assigned a 0-level.

Considering the ANN equalizer performance, 4-PPM and OOK can offer 3.75 and 2.8 Mb/s, respectively. As with the unequalized case, 4-PPM significantly outperforms OOK. Over ∼1 Mb/s extra data rate can be recovered with 4-PPM than OOK. The BW requirements are 7.5 and 2.8 MHz, respectively. The reason for the additional performance is that the ANN can easily differentiate between single pulses of energy followed by long streams of 0-levels in a highly multipath induced ISI environment. While in OOK each level is

equiprobable and there is therefore too much signal distortion in order to accurately estimate of the system response that is required for the ANN to undo the ISI effect.

It is established that 4-PPM outperforms OOK in high light density conditions. Therefore now the BER performance of 4-PPM with the ANN equalizer is investigated over the four BWs (56, 76, 110 and 160 kHz) that are obtained by using four different light densities (10, 50, 270 and 300 μW/cm^2), see Fig. 5.6. The case of the 160 kHz BW has already been covered and can support 3.75 Mb/s. Data rates up to 2.4, 1.45 and 1.15 Mb/s can be supported for the BW in the descending order.

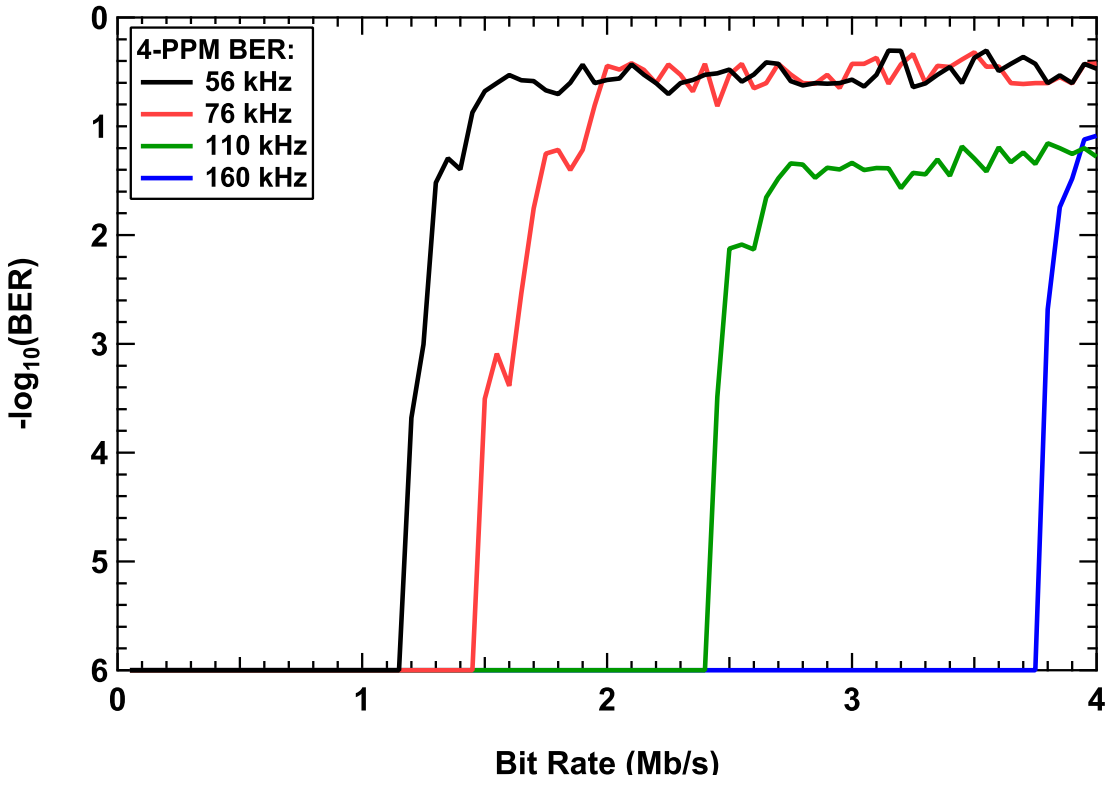

Fig. 5.6 BER performance of 4-PPM across the system with varying light density - in each case, over 1 Mb/s can be supported

Each of the system BWs are separated by between $\sim 20-40$ kHz and the performance decreases proportionally to the difference between them as expected. For example, there is a drop of 1.45 Mb/s between the 160 and 110 kHz cases (40 kHz difference) which is significant. Furthermore there are drops of $\sim$1 Mb/s between the 110 and 76 kHz cases (34 kHz difference) while between 76 and 56 kHz the drop in data rate is only 0.3 Mb/s (20 kHz). Therefore the performance is clearly related to the decrease in SNR with decreasing light density and the increasing influence of ISI, thus making the data unrecoverable. Nevertheless, data rates $>$1 Mb/s can be recovered across the entire system, which is an important

result for OPD-VLC systems as MHz devices are starting to emerge [147] that could use this technology in order to provide high speed and low cost VLC systems.

5.4 Multiple-Input Multiple-Output

5.5 Introduction

MIMO systems based on the concept of channel matrix inversion [148] are an excellent way to increase the aggregate bit rates in visible light communications (VLC) systems. As a result they have garnered a significant amount of interest in the research community with many different methods of implementing the MIMO technique being proposed [148–153]. For example, different modulation schemes are reported in [149] and [152] while [151] offers a spatially diverse scheme where only one transmitter is active at any given time. Furthermore, based on the simulation results in [150] there is a strong claim that a complex imaging receiver is required in order to receive an error free link [148–150] due to an ill-conditioned channel matrix rank.

This is not the case, however and here verification that it is possible to recover a 4×4 MIMO link without employing a complex imaging receiver is presented. A data rate of 1.8 Mb/s is achieved using this technique.

While the benefits of using WPLEDs for VLC and SSL are well known (high output power, bandwidths of several MHz [26]), using OPDs as the receiver for VLC systems is a subject in its infancy. Single-input single-output (SISO) links have been covered in the previous chapters and an ANN equalizer has been used to increase the data rate to 3.75 Mb/s from a system bandwidth of 160 kHz. In this section, a MIMO system based on four individual commercial WPLEDs and four OPDs that are mounted on the same substrate.

The OPD used is based on the BHJ concept [96], which is an interpenetrated blend of electron donor and electron acceptor, as opposed to the common p-n junction that Si PDs utilizes. It was manufactured by Siemens AG Corporate Technology by the spray deposition technique as reported in [54]. When comparing organic technologies with their Si counterparts, the real advantage is the price. The total bill of materials for the P3HT:PCBM system implemented here is $\sim$£0.17 cm^{-2}, which is very inexpensive. The materials can be processed into a solution that can be sprayed onto the substrate, allowing very low cost and straightforward manufacturing. Besides spray coating there are other ways to produce devices, see [154] for further details on a number of methods. Additionally, the OPD BW is dynamic [61], and its performance is controlled by the incident light intensity. Under a high light intensity (> 300 μW/cm^2) the number of charge carriers generated is greater than

the number of traps at the interface meaning that the time constant of the plate capacitance controls the cut-off frequency as in Si PDs. Conversely at low light intensities the number of traps is greater than the number of charge carriers, meaning that the BW is controlled by the time constant of the interface traps.

A further advantage of the OPD under test is that is has four independent diodes spaced 1.2 cm apart each with 1 cm^2 photoactive area meaning that 4×4 (4-transmitters and 4-receivers) MIMO is a natural progression on SISO links. No additional electronics or photodetectors are required at the receiver as in Si based MIMO, and therefore there is no additional cost. Since there are four diodes on the OPD substrate, 4×4 MIMO is investigated in this Chapter. While the theory of demodulating a MIMO link is extremely simple (outlined mathematically in Section 5.6), a series of pilot tones are transmitted from the first transmitter to all receivers in order to find the channel response (while keeping the rest of the transmitters off) and repeating for each transmitter. A matrix of channel coefficients is produced, inverted and multiplied with the received data in order to find the transmitted data. In practice this is a significant challenge for bandlimited systems due to the ISI induced distortion of the reference signals [59] that make up the channel matrix coefficients.

MIMO systems are typically implemented in the radio frequency domain where a multipath environment is inherent. There are many reports of using an ANN to find the channel response [155, 156]; however to the best of the author's knowledge there are no reports of applying an ANN at all in VLC MIMO systems. This is because they are mostly used for correcting ISI at the receiver. One cause of ISI is transmitting data outside of the modulation BW, which is not a problem that is observed in MIMO systems explicitly, since the quality of the channel coefficient matrix has more impact in recovering the data than the ISI. In this Chapter it is demonstrated that not only is it possible to implement the ANN to equalize the received signal but it is also possible to use the ANN to set a new record data rate based upon the ANN for a large coverage area beneath the transmitter array.

5.6 MIMO Theory

The concept of MIMO is outlined in Fig. 5.7. Over the next few subsections the transmitter, channel and receiver are outlined.

5.6.1 Transmitters

A pseudorandom binary sequence is generated and shaped into an OOK signal in MATLAB. Two arbitrary function generators (AFGs) with a peak-to-peak output voltage of 5 V

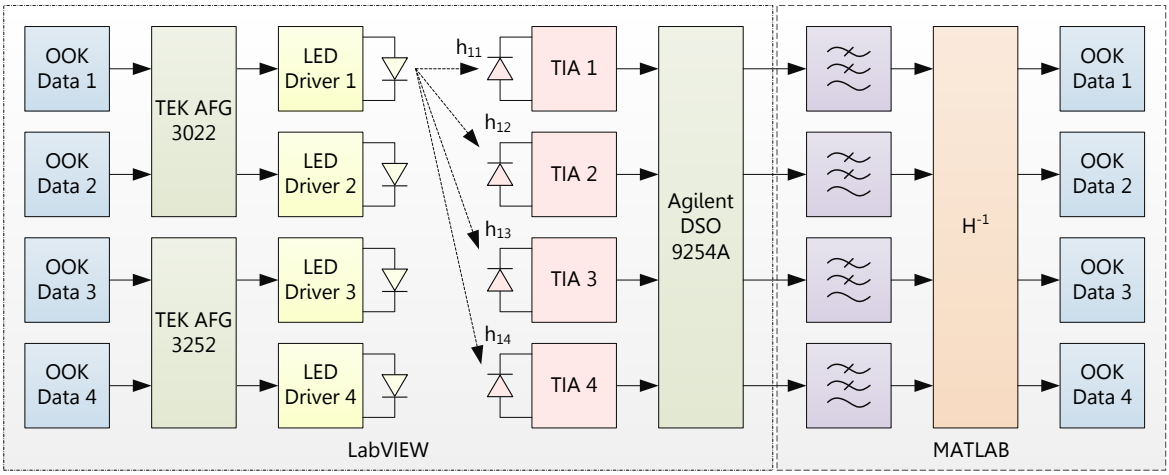

Fig. 5.7 MIMO system block diagram: The transmission side is controlled by LabVIEW whereas the demodulation is performed in MATLAB

are synchronized. Synchronization of the AFGs is not required as the data is recoverable regardless; however it does simplify the demodulation process. Autocorrelation will only be required once for all channels as the relative delay at the receiver will be the same. Each channel is buffered using a NAND gate with high output impedance then mixed with a bias current of 350 mA. The bias current is generated by a simple transistor circuit given in [138] to eschew the use of a coupling capacitor and therefore avoid the baseline wander phenomena that occurs in organic VLC links [59]. The transmitter array is made up of four yellow phosphor blue chip Philips Luxeon Rebel DS64 LEDs. The blue chip LED has a high order modulation BW; however the slow response of the yellowish phosphor limits the BW to several MHz. This BW is still approximately an order of magnitude higher than that of the OPD, which means that the OPD is limiting the link BW. The LED is a Lambertian emitter as given by [157]:

$$R_0(\theta) = \frac{m+1}{2}\cos(\theta)^m \tag{5.8}$$

where m is the Lambertian number and θ is the angle of emission. The transmitter array is divided into four serial data streams, each transmitting a unique pseudorandom binary sequence.

5.6.2 Channel Matrix

At the receiver the incident light from each transmitter adds by superposition to form the MIMO symbol. The VLC channel gain from transmitter i to receiver j is given by [17]:

$$h_{ij} = \frac{A_r}{d_{ij}^2} R_0\left(\theta_{ij}\right) \cos\left(\varphi_{ij}\right) \tag{5.9}$$

where A_r is the photodetector area, d_{ij} is the distance between transmitter i and receiver j, θ_{ij} is the emission angle and finally φ_{ij} is the angle of incidence. Clearly, if there is no light is incident to the receiver, $h_{ij} = 0$. From (5.9), it is noteworthy that there is no phase component, meaning that no phase distortion occurs in the channel and only a flat attenuation is experienced i.e. it is a DC gain < 1. Each transmitter has a LOS path to each receiver; considering there are four transmitters this gives a total of 16 LOS paths. It should be noted that there is a set of reflected components; however studies show that the strongest multipath component is at least 7 dB lower than the line of sight component [150], so the multipath case is ignored in this experiment. Using these paths a channel matrix $\mathbf{H}$ containing all the useful information about the channel can be built [150]:

$$\mathbf{H} = \begin{bmatrix} h_{11} & h_{12} & h_{13} & h_{14} \\ h_{21} & h_{22} & h_{23} & h_{24} \\ h_{31} & h_{32} & h_{33} & h_{34} \\ h_{41} & h_{42} & h_{43} & h_{44} \end{bmatrix} \tag{5.10}$$

Hence, the received electrical signal vector immediately after the photodetector is given by [148]:

$$P_{rx} = \mathbf{H}P_{tx} + n \tag{5.11}$$

where P_{tx} and P_{rx} are transmit and receive vectors, respectively of size $4 \times \eta$, where η is the number of transmitted symbols and n is the noise vector. Therefore the transmitted symbols can be estimated by:

$$\Psi = \mathbf{H}^{-1}P_{rx} \tag{5.12}$$

where Ψ is the estimate of P_{tx}. Notice that for the recovery of data, the channel matrix $\mathbf{H}$ must be full rank. It is clear that the quality of the estimated data is dependent on $\mathbf{H}$. The quality of the $\mathbf{H}$-matrix consequently depends on the quality of measurement of the

individual channel coefficients. The channel coefficient h_{ij} is controlled by d_{ij}^2 as (θ_{ij} and φ_{ij} change as a function of modifying d_{ij}^2) while A_r is a constant. A further consideration is that Ψ is dependent on the noise n. So far, no studies have been carried out on the impact of the noise on **H**. Tracking d_{ij}^2 in real time to build the **H**-matrix would be very problematic experimentally as it would involve a feedback channel - something not implemented in this work.

A far more simplistic approach is a histogram method. One LED transmits data over the channel while the remaining receivers are not active. The DC level is removed from the signal and the electrical signal levels are found. Recalling $V_{pp} = 5$ V, removing the DC corresponds to signal levels of ± 2.5 V. Therefore it is easy to rapidly find the DC gain of the given channel with a simple division. The method is then repeated for each LED in the transmitter to build **H** - see Fig. 5.8 and 5.9 for an example.

There is a drawback to this method; when transmitting outside the BW of the OPD, the influence of ISI will be significant, degrading the peaks of the histogram meaning the estimate of the signal will not be optimal. In the presence of severe ISI the histogram will fail completely since the histogram will not find any distinction between the two levels. In this test, the histogram measurement is only performed once for the each channel because the receiver is not moving continuously. For a real time measurement, **H** would be periodically updated.

5.6.3 Receiver

The $x-z$ and $x-y$ plane geometries are illustrated in Fig. 5.10(a)and (b), respectively where Fig. 5.10(a) demonstrates the previously outlined concepts and Fig. 5.10(b) shows the receiver plane geometry. Only one quarter of the possible area is tested, since the performance is expected to be symmetrical around the centre. This area is separated into nine sections of 5 cm^2 (S1:S9) to give an outline of the position-dependent performance. However before the performance is analysed, it is necessary to characterize the OPD under test.

As mentioned, there are four diodes on the substrate, as illustrated in Fig. 5.11, which also shows the spatial characteristics of the OPD. The distance d_{ij} between the transmitter and receiver is set to maximize the light density while maintaining full coverage by all other LEDs. Within the receiving plane, the maximum light density is found directly beneath one of the LEDs, i.e. section S3, which corresponds to a light density of > 300 μW/cm^2 and a BW of 177 kHz. The minimum is found in the centre of the receiving plane; section S7 where the light density is ~ 300 μW/cm^2 and the BW is 133 kHz, see Fig. 5.12.

The light density is measured with a thermopile of area 12 cm^2 and the bandwidth is found by performing a fast Fourier transform on a short pulse (duration 1 μs with rise and

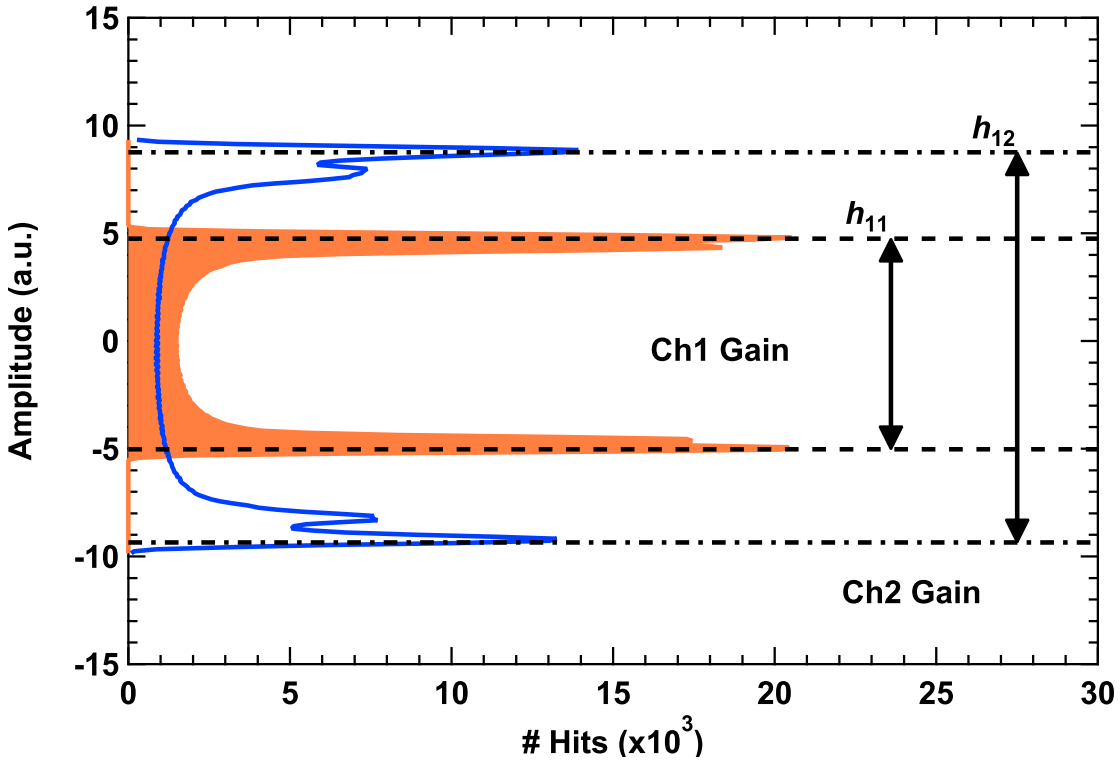

Fig. 5.8 Ch1 and Ch2 gain found using the histogram method

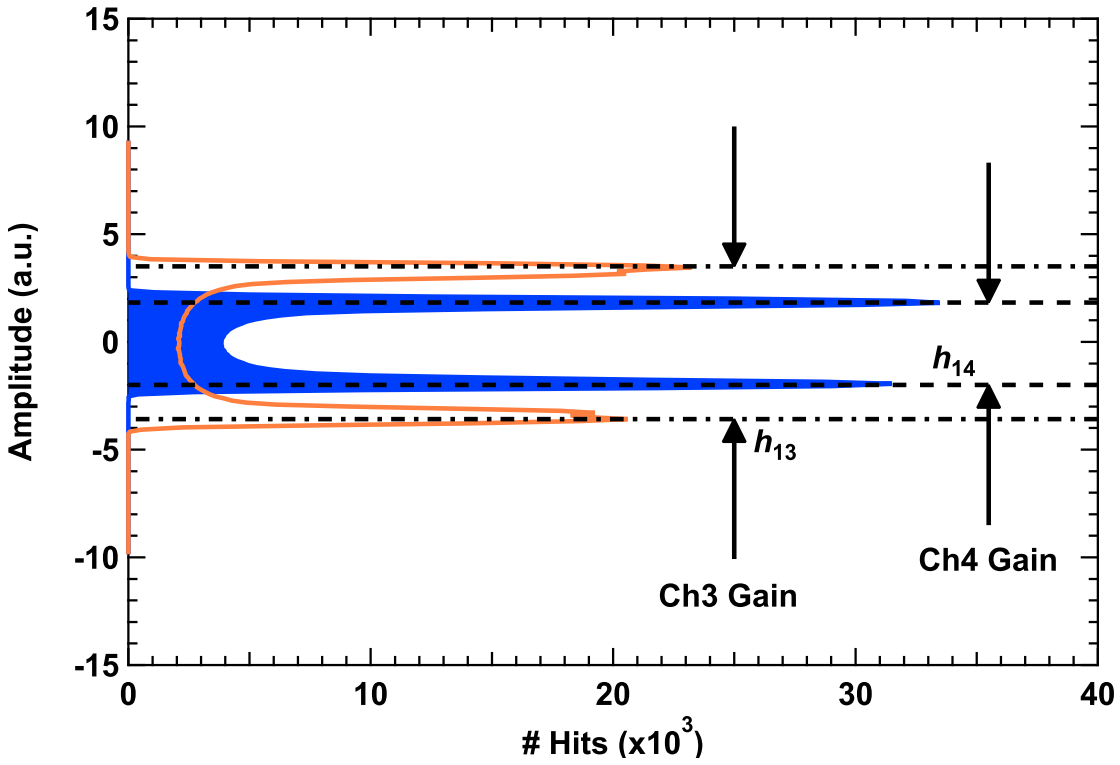

Fig. 5.9 Ch3 and Ch4 gain found using the histogram method

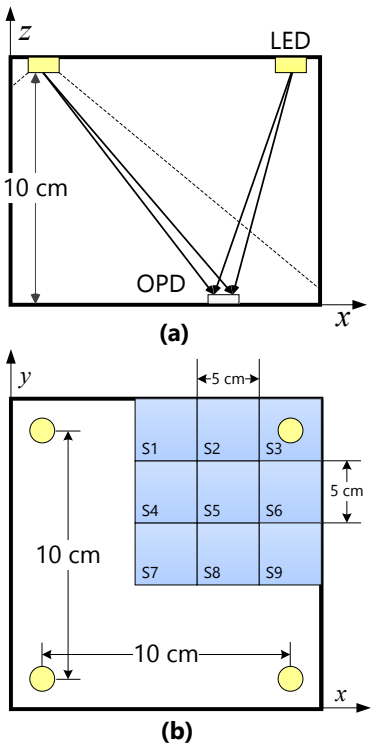

Fig. 5.10 (a) $x-y$ plane and (b) $x-y$ plane: the receiver plane divided into sections S1-S9 for BER measurements

fall times of 2 ns) transmitted over all 4-LEDs. The BW decreases from a maximum of 177 kHz to 133 kHz as the receiver approaches the centre of the receiving plane. This difference is quite large in relation to the magnitude of the BW. However, in terms of a MIMO signal at the centre of the receiving plane the contribution from each LED is much greater, so it is expected that this position will offer the largest data rate. Normally it would be predicted that the largest BW would offer the greatest data rate, yet since the bit rate will exceed the BW in all sections, ISI will distort the signals significantly thus causing the histogram method to fail.

The data is transferred in each section and sampled with an Agilent DSO9254A real time scope controlled by LabVIEW. In the histogram method, data demodulation and estimation are all performed in MATLAB. While an FPGA could have been implemented for a real time result, there was a strong indication from the literature that the experiment would not prove conclusive without an imaging lens. Therefore to avoid the costly development time MATLAB is selected for this first demonstration.

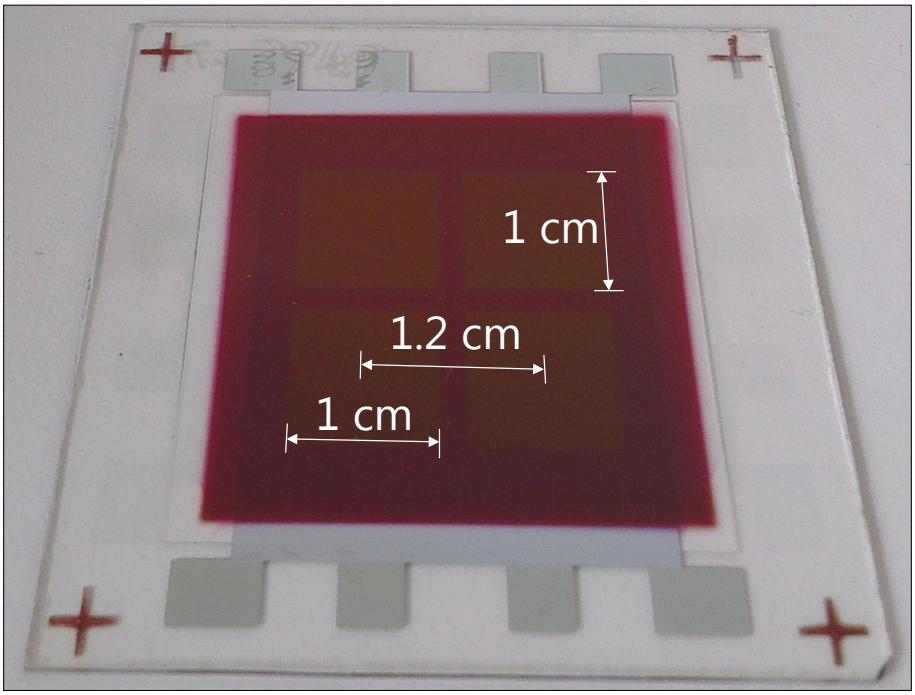

Fig. 5.11 Bottom view photograph of the OPD showing the spatial characteristics

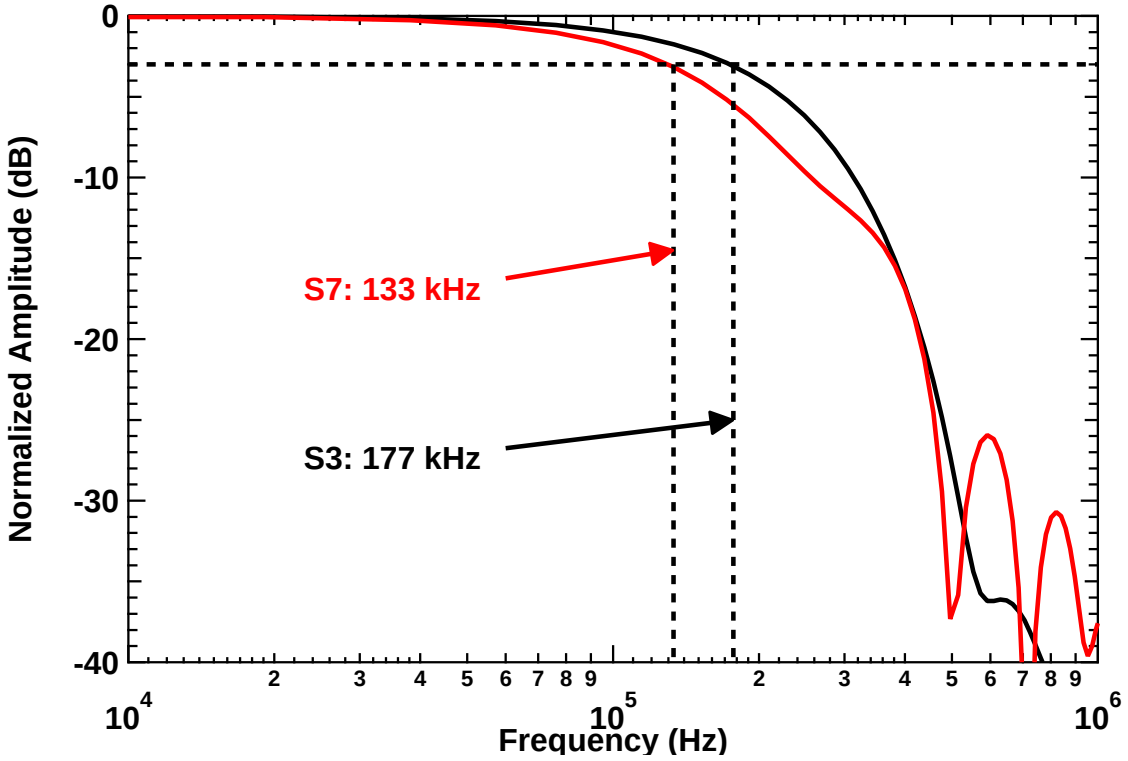

Fig. 5.12 BW in the highest and lowest light densities on the receiving plane

5.7 Results

The Q-factors of the four channels in every position were measured. The best results are found when the receiver is in section S7 as predicted with the results as well as the eye diagram shown in Fig. 5.13. Q–factor of 4.7 is equivalent to a BER of 10^{-6}, which is commonly accepted as error free in VLC. Fig. 5.13 also depicts that a 200 kb/s link can be established without an equalizer as two 100 kb/s channels could be demodulated error free (Chs.3 and 4). One possible reason for this is due to the fact that the measurement was made horizontally over the optical bench where the transmitters and receivers are perpendicular to the bench, as opposed to the case where transmitters and receivers are parallel to the bench; thus resulting in large multipath components for the two channels closest to the bench, i.e. Chs.1 and 2 in this case. As mentioned, the rank of $\mathbf{H}$ is crucial for recovering data; any loss of rank in the channel matrix means that the data can't be recovered. Since only two channels could be demodulated error free, $\mathbf{H}$ is an ill-conditioned matrix and as a result a portion of the data is lost as indicated by the condition number $\kappa(\mathbf{H}) = 70$.

It should be noted that a 200 kb/s link with no equalizer is significantly larger than the highest previously reported case of 30 kb/s in by around seven times. However a more effective method of increasing data rates without an equalizer might be to scale down the number of transmitters to two.

When considering the ANN equalizer, the achievable data rate for each section with all channels error free is illustrated in Fig. 5.14, where BER for all channels in sections S1, S3, S7 and S9 are averaged to produce a solitary curve rather than four curves per section. No other curves are illustrated since their performance lies between these sections. Sections S2 and S6 can offer 1.5 Mb/s while sections S5, S5 and S8 can offer 1.7 Mb/s. As predicted section S7 offers the highest data rate of 1.8 Mb/s while section S3 with the highest BW offers 1.4 Mb/s. This corresponds to four parallel channels transmitting 450 kb/s and 350 kb/s for each section, respectively. This represents an extremely large increase of over 1 Mb/s on the previously reported maximum data rate of 750 kb/s, not to mention exceeding the modulation BW by an order of magnitude. The performance difference of 300 kb/s observed between S1 - S9 is not a function of the BW as previously outlined, since the BW is maximized when the achievable data rate is minimized. Therefore considering section S3, the contribution to the MIMO symbol from the furthest LED is minimized in comparison to section S7 where the relative contributions from each LED are approximately equal meaning there it is more likely that the symbol will be recovered. This is reflected by the other sections, whereas the deviation from the centre point increases, the data rate decreases.

It was suggested in that section S7 would be impossible to recover due to the matrix

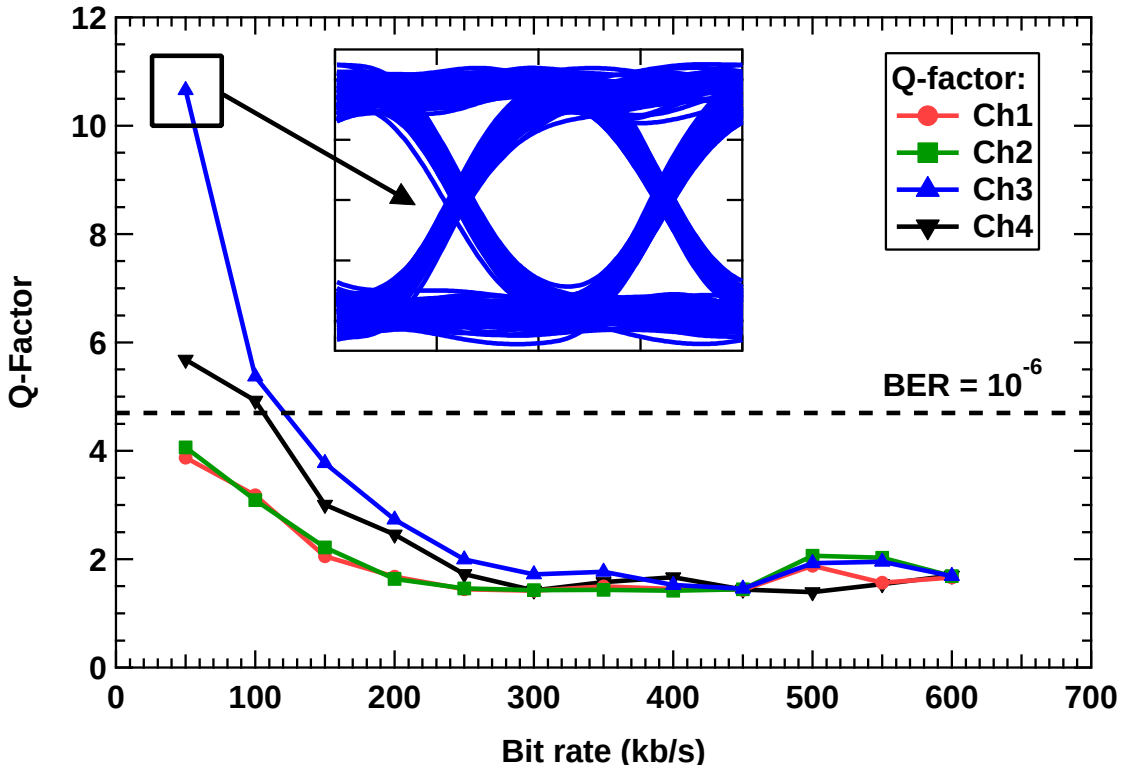

Fig. 5.13 Received Q-factor for section S7 with eye diagram inset at 50 kb/s; the dashed line represents $Q = 4.7$, corresponding to a BER of 10^{-6}

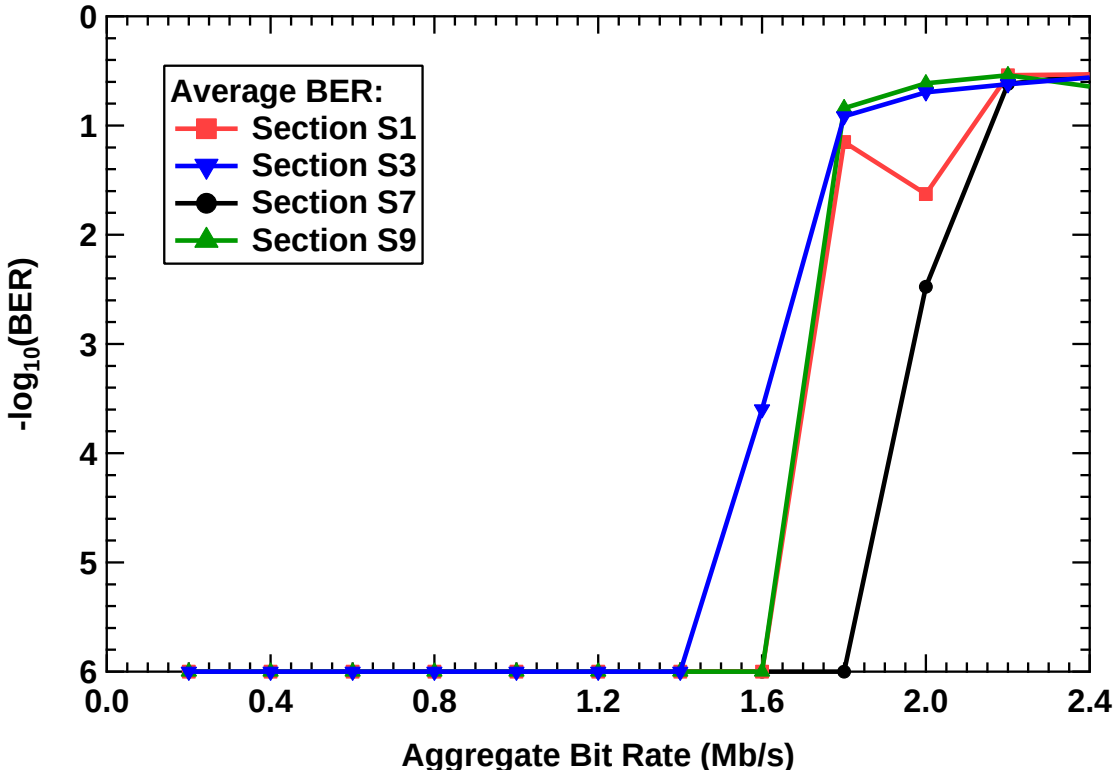

Fig. 5.14 Aggregate BER and bit rate for the four key sections tested

correlation; however the data could be recovered in these tests. While in theory, if the channel paths and transmission power are identical, the matrix will correlate. In practice, however this situation is extremely unlikely to occur due to the combination of the additive white Gaussian noise (AGWN) that exists in the system plus the fact that the LEDs are not perfectly identical so will have slightly different output characteristics.

In the worst case scenario, 1.4 Mb/s could be achieved, which still denotes a sizeable improvement as mentioned. This result is important not only for this reason, but because it means that data can be demodulated at all positions on the receiving plane indicating that MIMO is a valid technique for future organic VLC systems. It is important not to forget that in all cases an ANN was required to equalize the errors induced throughout the system. Without the ANN, only 100 kb/s could be transmitted over two channels. While not close to the 1.8 Mb/s reported above, in comparison to other unequalized LED to OPD links, this is still an increase over previously published work.

5.8 Conclusion

In this Chapter an experimental demonstration of a MIMO system for an organic VLC system is presented. Whilst providing this demonstration, the record data rate of 750 kb/s for VLC systems with Si LEDs and OPDs as transmitter and receiver, respectively has been well broken, as 1.8 Mb/s can now be transmitted, which is a significant step in the progression of organic VLC. The major challenge in this Chapter was to overcome the poorly conditioned matrix to recover the data at the receiver. In order to achieve this, an ANN equalizer was proposed to map the input-output sequence and correct the errors, which resulted in achieving extremely high data rates. The feasibility of VLC-MIMO without the use of an imaging receiver was demonstrated for the first time.

Future work on this topic considers what is missing from this preliminary experiment. Firstly, an FPGA development is required to provide a real time link which can fully explore the influence of white noise on $\mathbf{H}$, which will allow the derivation of new theory on the recovery of MIMO symbols for VLC links. Secondly, in order to provide a full scale demonstration, the number of OLEDs needs to be scaled up to provide full illumination of a small room. It would be expected that the link has the same performance as in the small scale link that is presented here, and so far a full scale demonstration has not been demonstrated.

Chapter 6

Visible Light Communications with All Organic Optoelectronic Components

6.1 Introduction

To date a VLC link employing exclusively organic optoelectronic components has not been demonstrated, despite enormous interest in both the organic based devices [67, 70, 100] and VLC [158–160] in the research community. This can be attributed to two main reasons; firstly there is a lack of commercially available organic devices - just a handful of SMOLEDs are available to purchase off-the-shelf while no OPDs are commercially available and must be custom made. Secondly, OVLC has only recently emerged as a serious topic for research and all of the reports so far have focused on either the transmitter [160] or receiver [158], as opposed to a full system evaluation. In spite of this it is necessary to perform such an evaluation because organics have outstanding properties that are ideally suited to the VLC domain. For instance, they can be processed into mechanically flexible, arbitrarily shaped panels with large photoactive areas. Such devices are processed by solution based processing at room temperature offering a real cost reduction; unlike inorganics which must be processed with epitaxial methods resulting in brittle crystals that do not scale well. Further, by careful selection of the semiconducting polymer it is possible to tune the emission or absorption wavelength to visible light as polymers and small molecules with band gap energies of 1 - 4 eV are abundant.

Even considering a forecasted market value of $\sim$£200 billion by 2027 [60], it is not anticipated that organic devices will become dominant over inorganics in optical communications and there are several reasons why. Firstly, a widespread infrastructure already exists for inorganics, which is well established and maintained. Secondly inorganic devices can be

easily and homogenously produced without defects or impurities. On the other hand, organics have the potential for applications in areas where inorganics are not perfectly suited or no optimized infrastructure exists. This could be in the screens and chassis of future mobile devices for device-to-device communications where OLEDs have already started appearing. Finally and most importantly, charge transport characteristics are orders of magnitude lower in organics and the direct result of this is that the bandwidths available for organics are in the kHz region (in comparison to MHz for inorganics). This is an open and timely challenge for OVLC links because the bandwidth is the most important factor for increasing capacity. The other is the SNR, which has an upper bound limit caused by the lighting requirements in VLC (max $\sim$400 lux) and also the quantum efficiencies and noise performance of the devices. However, having a low bandwidth is not necessarily a fatal perturbation for OVLC. In [159] a 10 Mb/s link was achieved using an organic polymer LED with 270 kHz bandwidth and a least mean squares equalizer. Although this report is a significant landmark for OVLC, a silicon photodetector was used instead of an OPD. Digital equalization techniques are an attractive option to increase transmission speeds as they restore link performance in the presence of ISI caused by the bandwidth limitation. The modulation format selected in this work is OOK due to its simplicity and popularity in the VLC domain [58, 158, 160]. Furthermore, OOK is compatible with transversal equalizers such as the MLP ANN which offer the best BER performance of any equalizer [142].

Aside from the bandwidth magnitude there is a further challenge in this setup. In [61] a detailed investigation was undertaken that reported OPD bandwidths can vary over several orders of magnitude from a few kHz to hundreds of kHz according to the incident light density (W/cm^2) due to interface charge traps. In high light density conditions, the number of charge carriers generated exceeds the number of interface traps, and therefore the BW is proportional to the time constant of the plate capacitance as with inorganic detectors (max bandwidth available $\sim$150 kHz [97]). Alternatively, in low light density conditions, the number of charge traps surpasses the number of charge carriers; so the overall bandwidth is proportional to the time constant of the traps, which varies with the ratio of empty/filled traps. In this work the worlds' first OVLC link operating at a link speed $>$ 1 Mb/s is proposed and demonstrated. In order to achieve this, the ANN equalizer is required to remove the effect of ISI. Furthermore, by varying the bias current of the OLED, the incident light density is reduced, thus reducing the bandwidth. Three cases are examined; a high (135 kHz), medium (100 kHz) and low bandwidth case (65 kHz) in order to find out the limitations of such links.

6.2 Organic Optoelectronic Devices

In this work the same SMOLED is used as in previous chapters as the transmitter and the same OPD as the receiver. While specific material details are not available for the OLED, the OPD is based on the bulk heterojunction concept - an interpenetrated blend of electron donor and electron acceptor (P3HT:PCBM) [96], which is dissolved into a solvent and sprayed onto the substrate.

P3HT:PCBM OPDs have higher responsivity than that of silicon detectors across the visible range whilst requiring a significantly lower reverse bias voltage of $\sim$3 - 5 V. Furthermore, P3HT:PCBM OPDs are infrared blind due to the higher band gap energy of $\sim$2 eV ($\sim$1.1 eV for silicon), which results in a sharp cut-off wavelength of $\sim$620 nm ($\sim$1100 nm for silicon). It should be noted that the 2 eV band gap is relatively high for VLC applications, which would benefit from a longer cut-off wavelength for applications such as wavelength division multiplexing, which can achieved by careful selection of the polymer [145]. On the other hand, as can be inferred from Fig. 6.1 (inset) the majority of the warm-white OLED optical power is absorbed by the OPD under test. The L-I-V is the main feature of Fig. 6.1 and the measured response shows good linearity up to 1 A, which is well beyond the 540 mA recommended operating limit set by the manufacturer.

In order to make bandwidth measurements and select an appropriate operating point, the DC level is varied between 0.1-0.8 A. The bandwidth of the system under test is shown in Fig. 6.2, which varies from 38 kHz to 146 kHz. It should be noted that in order to achieve 146 kHz a bias current of up to 0.8 A is required. Reducing the current to $\sim$0.5 A gives a slightly reduced bandwidth of $\sim$135 kHz while operating within the recommended region. Three bandwidths (bias currents) are selected for this work; 135 kHz (0.5 A) as the high bandwidth case, 100 kHz (0.35 A) as the mid-range case and 65 kHz (0.175 A) as the low case. A lower bandwidth was not selected because a symmetrical swing could not be achieved and the AC signal would therefore be clipped at the 0-level.

6.3 Test Setup

The experimental test setup is illustrated by the block diagram in Fig. 6.3. An arbitrary function generator (TEK AFG3022B) is loaded with a 2^{10}-1 (PRBS-10) generated in MATLAB and passed through a unit height rectangular pulse shaping filter $p(t)$. The rectangular signal is then mixed with a DC current using a bias tee to ensure operation in the linear region of the transmitter. The DC-biased signal then intensity modulates the OLED. The channel h is a less-than-unity DC gain that is not frequency selective for the required bandwidth in

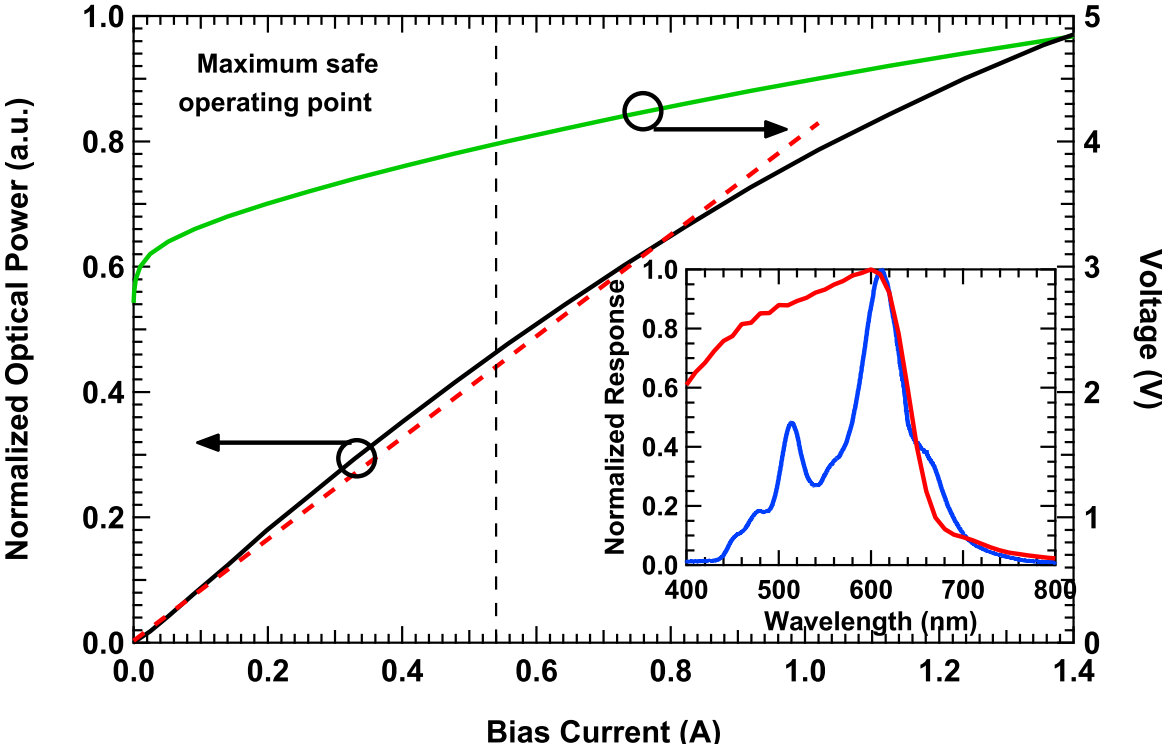

Fig. 6.1 The L-I-V curve of the OLED under test with linear fitting; normalized emission and absorption spectra of the OLED (blue) and OPD (red) respectively, noting that the vast majority of optical power is absorbed before the cut-off wavelength

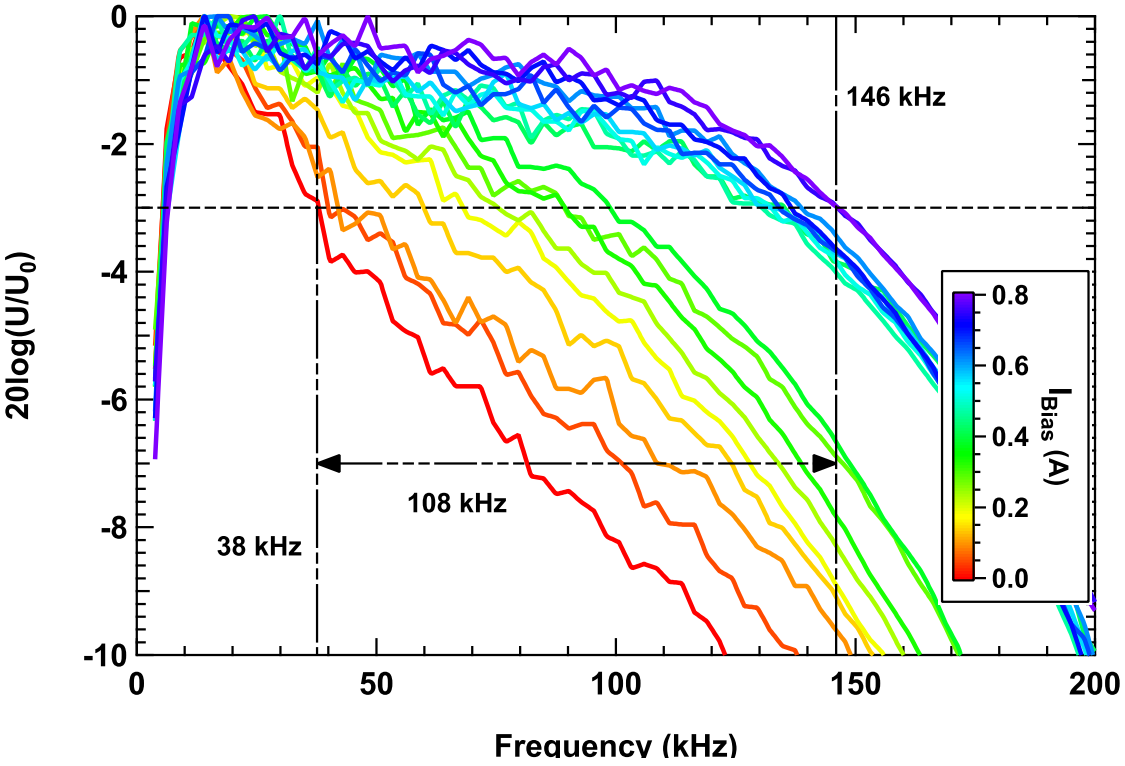

Fig. 6.2 Normalized and measured bandwidths of the OPD under test under different current bias conditions of the OLED, which control the light density

this work. The channel mathematics are given in [17] and the transmitter - receiver distance was 0.05 m as only a single device was used. The OPD substrate consists of four independent photodetectors of 1 cm^2 each as shown inset in Fig. 6.3. The incident signal on each detector is sampled by a real time Tektronix MDO4104-6 oscilloscope; with 10^6 samples acquired with maximum sampling frequency of 10 samples-per-symbol for further processing offline, meaning a BER target is 10^{-5} in this work. Ambient, shot and thermal additive white Gaussian noise sources at the receiver are dominant in this work [17]. The experiment was conducted in a controlled dark laboratory environment to minimize the ambient noise and electrical low pass filters were used in MATLAB to limit the other out-of-band noise sources.

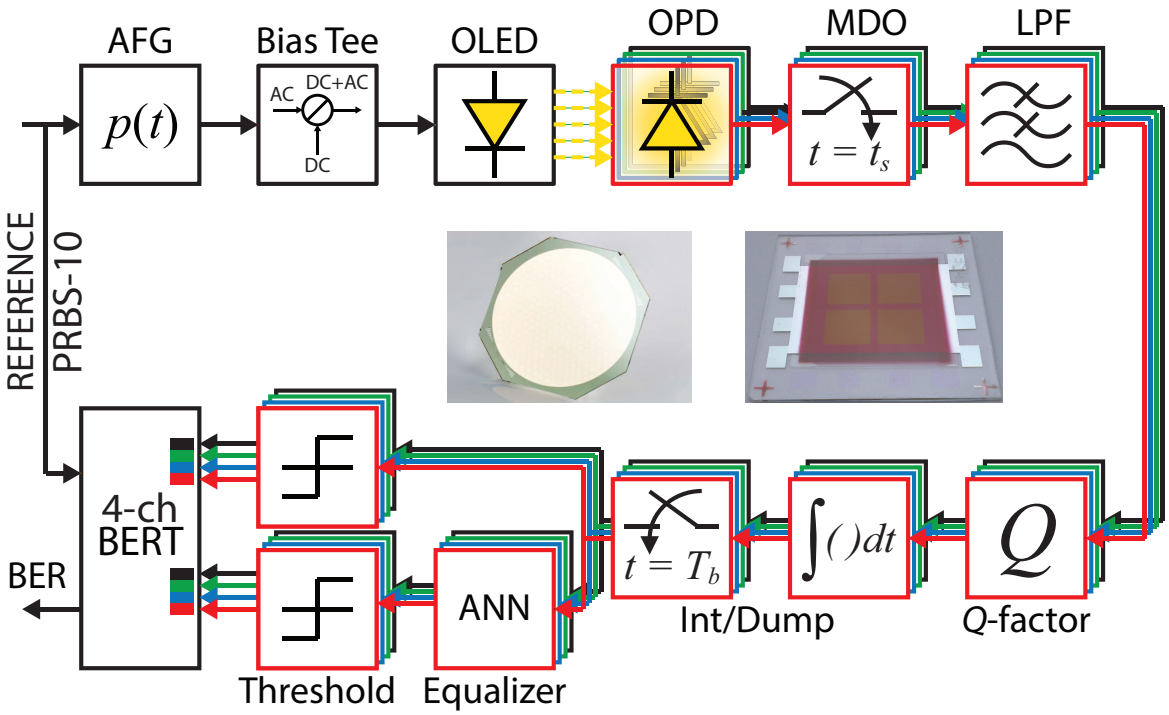

Fig. 6.3 Block diagram of the experimental setup used in this work with ANN equalizer implemented as a finite impulse response filter

The conditions for ISI are well known and therefore not covered here (refer to [161]). In order to remove ISI and achieve high data rates, an equalizer is required. The symbol spaced multilayer perceptron ANN with Levenberg-Marquardt (LM) training is used. This is because it is the best performing in terms of BER and the convergence to the error target in comparison to other equalizers [129, 142]. The mathematics of LM training can be found in [2, 124]. The output of the MLP is passed through a threshold detector and compared with the original transmitted data using a symbol-by-symbol BER tester (BERT). The ANN

and BERT are implemented in MATLAB.

6.4 Results

The unequalized BER and Q-factor performance of the link for a range of bandwidth will be illustrated in descending order followed by the equalized BER performances. Fig. 6.4 illustrates the BER envelope for the four diodes without equalization for 135 kHz bandwidth. The BER envelope is produced by analyzing the performance of each of the four diodes and selecting the maximum and minimum at each data rate. The average BER is calculated and used to represent the overall link performance. The average error free (BER $= 10^{-5}$) achievable transmission speed is 350 kb/s without equalization. Considering the BER envelope, the minimum and maximum available speeds are 350 and 450 kb/s, respectively, showing a different of 100 kb/s. As the light intensity striking each diode is equal, the reason for this difference can be attributed to the physical differences in the OPDs. The Q-factor (dB) profile for each diode is also shown for each individual channel; channels 1, 3 and 4 (red, gold, black) each offer a similar profile, while channel 2 (green) is the worst performing at each data rate. The reason for this is due to physical variations in the diodes as in the 135 kHz bandwidth case. It should be noted that the Q-factor peaks at a data rate of 150 kb/s. The reason for such a peak in the profile is due to the power penalty caused be the coupling capacitor in the bias tee of the transmitter, which has an associated cut-on frequency f_c. The power penalty decreases exponentially with decreasing f_c/R_b [41], hence the Q-factor peak. Subsequently, the Q-factor decreases with increasing data rate due to a separate power penalty introduced by the attenuation of high frequencies by the organic components (i.e. the ISI penalty), which is expected for such bandlimited components.

In Fig. 6.5 the BER and Q-factor performance for the 100 kHz link is shown in the same format as in the previous case. The available average data rate at a BER of 10^{-5} is reduced to 250 kb/s (300 kb/s is available at a BER $\sim 2 \times 10^{-5}$). The minimum available data rate was 250 kb/s and the maximum was 350 kb/s. Thus it is possible to determine that the 100 kHz case is operating at a similar level to the previous case; in both cases the achieved spectral efficiency is 350 kb/s$/$135 kHz $\approx$ 250 kb/s$/$100 kHz $\approx$ 2.5 b/s/Hz. This is slightly outside of the Nyquist limit and hence a slight reduction of transmission speed could be expected in real time applications. The Q-factor profile for each of the four channels is shown, which has the same characteristic peak as previously at $\sim$100 kb/s.

The 65 kHz case (Fig. 6.6) can support an error free (10^{-5}) link data rate of 150 kb/s. The maximum and minimum data rates are both 150 kb/s meaning that there is little variation across the four received channels and a similar envelope shape and Q-factor profile can be

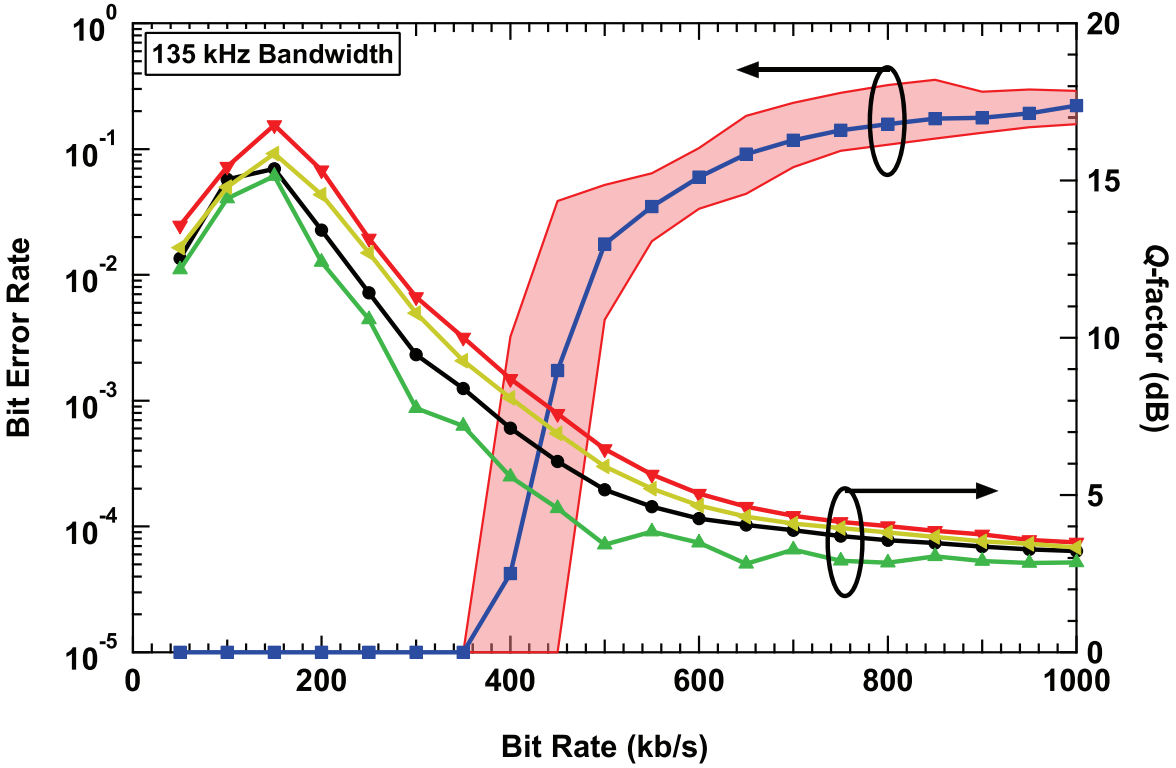

Fig. 6.4 Unequalized BER and Q-factor of the high bandwidth link; 350 kb/s can be recovered at a BER of 10^{-5}

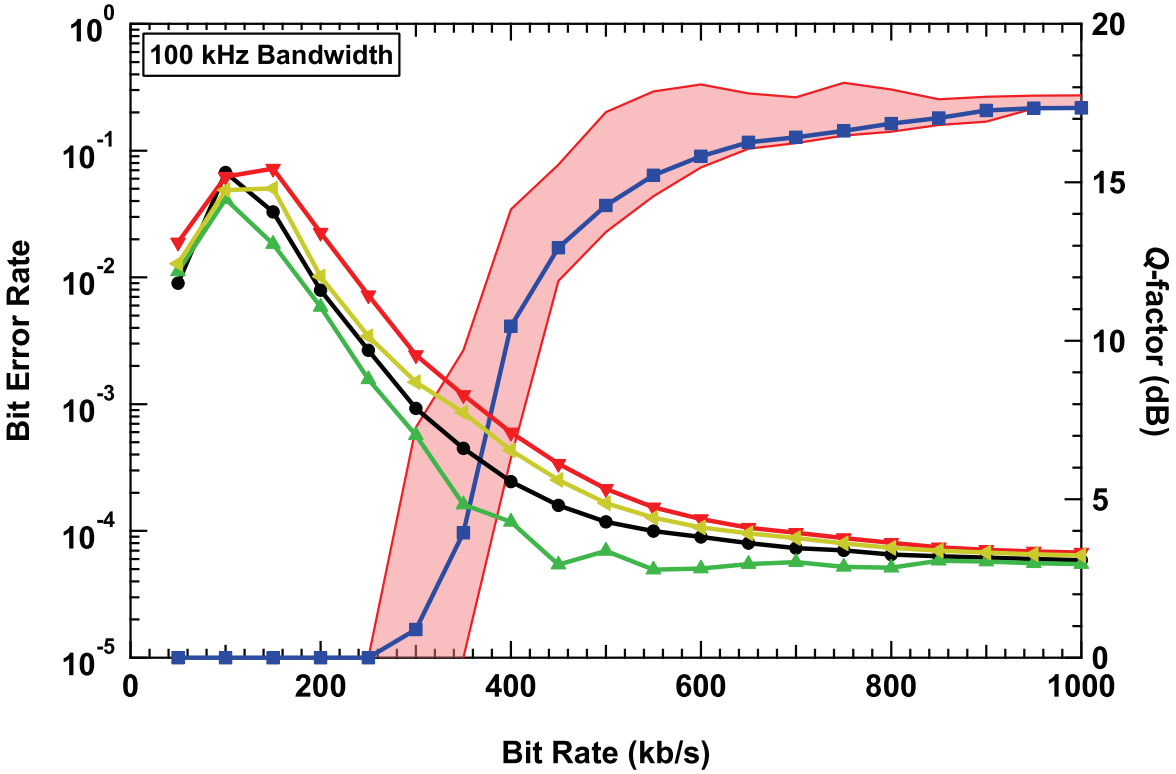

Fig. 6.5 Unequalized BER and Q-factor of the medium bandwidth link; 250 kb/s can be recovered at a BER of 10^{-5}

observed as in the previous two cases. It should be noted that channel 2 (green) is once again the worst performing. The spectral efficiency achieved using the 65 kHz case was $150/65 \approx 2.3$, thus there is a slight reduction in performance in comparison to the previous two cases. This can be attributed to the reduction in SNR observed due to the reduced optical power.ofile for each of the four channels is shown, which has the same characteristic peak as previously at $\sim$100 kb/s.

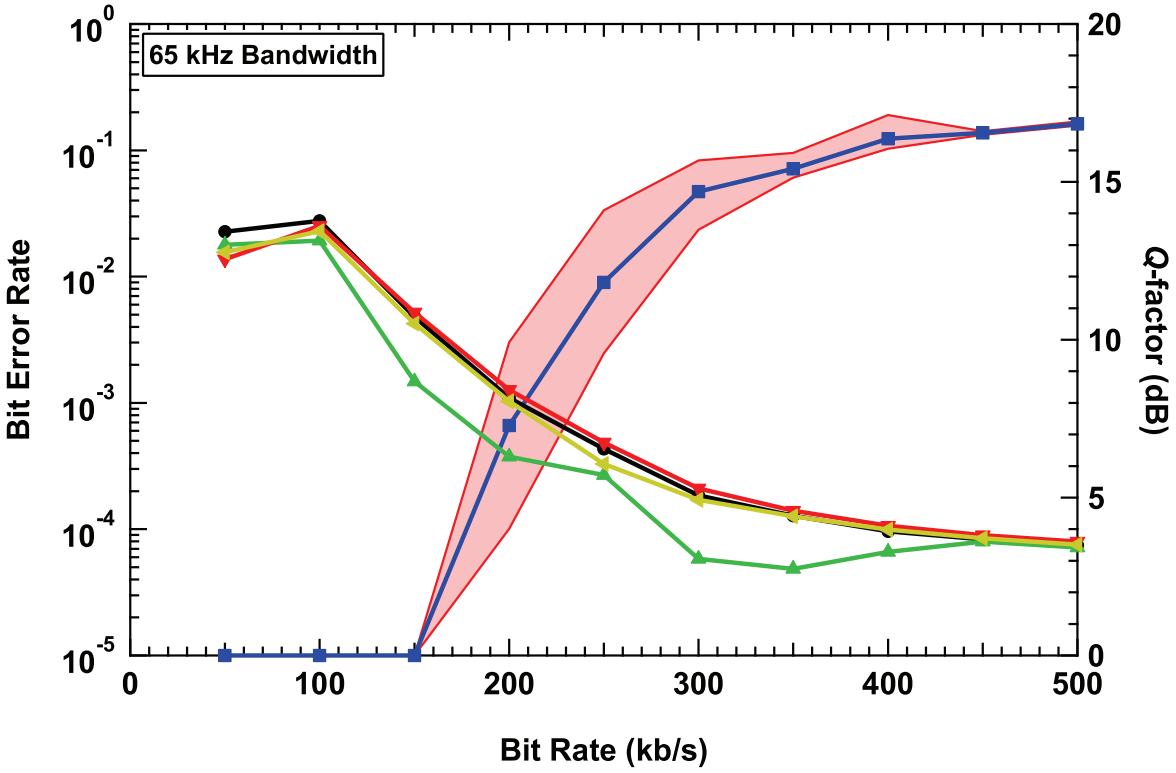

Fig. 6.6 Unequalized BER and Q-factor of the low bandwidth link; 150 kb/s can be recovered at a BER of 10^{-5}

In Fig. 6.7 the ANN equalized performance of each link is shown and will be discussed in descending order starting with the 135 kHz case. A data rate of 1100 kb/s can be supported at an average BER of 10^{-5} (1150 kb/s at 1.15×10^{-5} BER and, 1200 kb/s at 1.6×10^{-5}). This is approximately a threefold improvement over the unequalized case of 350 kb/s. This is due to the ANNs ability to map any input-output sequence given a sufficient SNR and number of neurons. This is the first ever report of a VLC link that consists entirely of organic optoelectronic components exceeding 1 Mb/s to the best of the author's knowledge, which is significant. For the 100 kHz case, a reduced equalized transmission speed of 850 kb/s is observed. Similarly to the 135 kHz case the level of performance shows an approximately threefold improvement in transmission speed over the unequalized case

(250 kb/s). Finally in the 65 kHz case, an equalized data rate of 450 kb/s can be achieved; once more offering similar performance improvement statistics as the previous two cases.

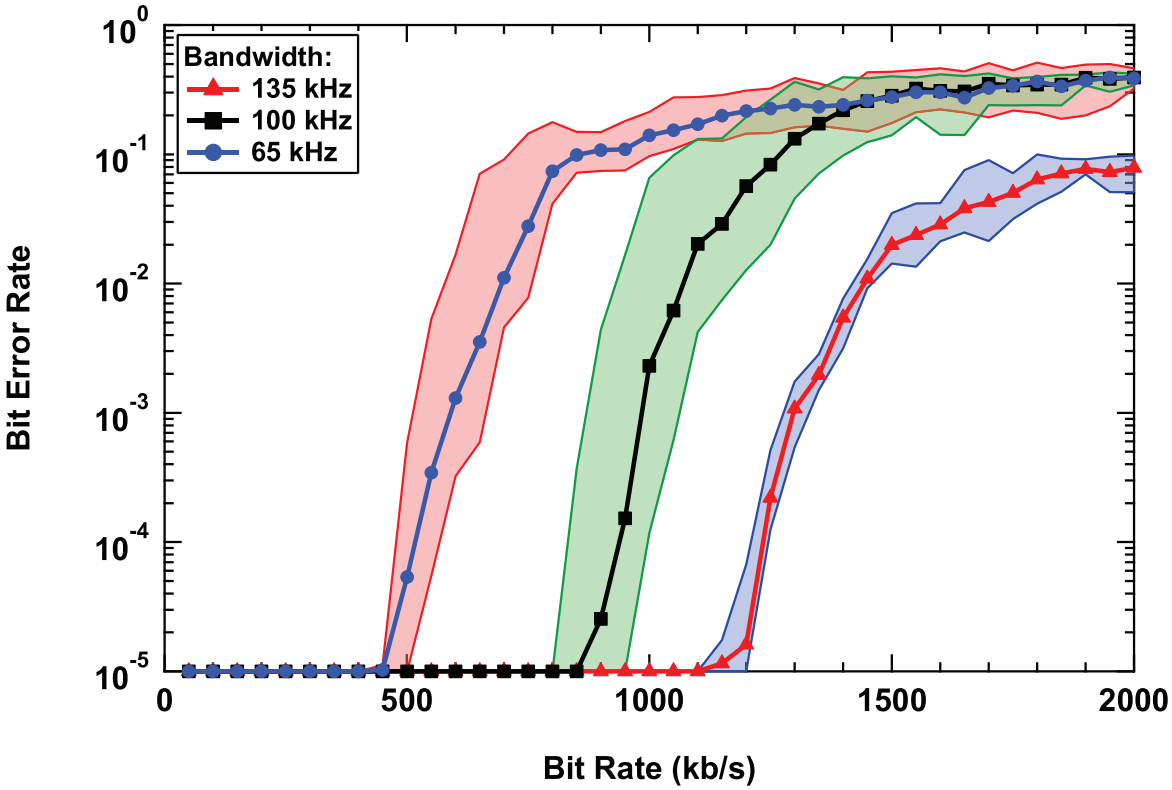

Fig. 6.7 Equalized BER performance of each of the three cases; data rates of 1100, 850 and 450 kb/s can be recovered at a BER of 10^{-5} for the 135, 100 and 65 kHz bandwidths, respectively

6.5 Summary

In this chapter the first ever OVLC link at a transmission speed exceeding 1 Mb/s has been demonstrated. The modulation format used was OOK due to its simplicity and compatibility with digital equalizers. The equalizer used to achieve such a transmission speed was the ANN due to its superiority over other equalizers. As mentioned, organic devices can be produced with low cost manufacturing methods such as spray coating (as in the OPDs used here) which are extremely attractive for implementation in future mobile devices. The final 1 Mb/s data rate is a significant result for the field of VLC as organic devices offer significant promise for applications that are not ideally suited for conventional devices such as mobile device communications.

Chapter 7

Visible Light Communications with Polymer Light-Emitting Diodes

7.1 Introduction

PLEDs have been gaining substantial attention in recent years due to their outstanding potential for future lighting and display applications [162]. Advantages of PLEDS include low-cost solvent-based processing, which in turn means large area devices are palpable with relative ease in comparison to inorganic LEDs.

As with white LEDs, white PLEDs are also seen as a viable source in VLC offering simultaneous illumination and data communications within rooms/offices environment. In both organic and inorganic VLC there is a common desire to drive up the data rate and this is reflected in the literature; PLEDs have reached 2.7 Mb/s transmission speeds using OOK and an 'offline' multi-layer perceptron ANN based equalizer [163]. On the other hand, inorganic VLC offers data rates up to 3.4 Gb/s [47] using discrete multi-tone modulation and wavelength division multiplexing of red, green and blue wavelengths. Thus it is clear that the state-of-the-art transmission speed in OLED-VLC currently lags LED-VLC by around three orders of magnitude. The reason for this disparity is because organic semiconductors are characterized by lower charge mobility than inorganic LEDs by several orders of magnitude. Typical hole mobilities of the semiconductors used in PLEDs are in the range 10^{-6}-10^{-2} cm^2/Vs, and similar or lower mobilities are found for electrons. Therefore, upon device switch off, extraction of the charge and extinction of the electroluminescence is therefore slow, despite an exciton lifetime of (typically) less than a nanosecond. The bandwidth is therefore several orders of magnitude smaller than for inorganic devices. In this chapter an increase in the transmission speed is reported for PLED-VLC up to 10 Mb/s;

using a custom designed PLED with a bandwidth of 270 kHz as the transmitter and a PIN photodetector as the receiver is reported. Such a data rate is achieved using a LMS adaptive equalizer implemented as a finite impulse response (FIR) filter on a Xilinx Virtex 6 ML605 FPGA in real time. All the previous literature on increasing data rates in organic VLC using equalizers has relied on offline processing in MATLAB [163] and hence this is the first time a real time system is reported.

7.2 Production and Characterization of the PLEDs

A schematic of the PLEDs used in this work is illustrated in Fig. 7.1. PLEDs were prepared starting with a transparent anode comprised of a thin layer ($\sim$120 nm) of ITO deposited via a sputtering process on a glass substrate. The ITO surface was cleaned in an acetone and isopropanol sonication bath followed by an oxygen plasma treatment [9, 12]. Immediately after the oxygen plasma treatment, a dispersion 2.8% w/w in H_2O of the polymer PEDOT:PSS (Sigma-Aldrich) is spin coated (4,500 rpm for 60 s plus 5,000 rpm for 10 s in air) to obtain a highly conductive polymeric film approximately 80 nm thick. The sample was then annealed at 140°C for 600 s in a nitrogen atmosphere. A solution 2% w/w in p-xylene of the polymer TFB (American Dye Source) with a molecular weight $M_w = 68,000$ is then spin coated (2,500 rpm for 60 s under nitrogen atmosphere) on the sample followed by annealing (140°C for $\sim$1 hour) and slow cooling to increase the crystallinity of the TFB layer. The amorphous portion of TFB is then removed via spin rinsing (1,000 rpm for 30 s and 4,500 rpm for 10 s) with p-xylene in which the solvent was added drop-by-drop while spinning.

To deposit the active layer a solution of poly[2-methoxy-5-(3',7'-dimethyloctyloxy)-1,4-phenylenevinylene] (MDMO-PPV) with a M_n of $\sim 23,000$ g/mol (Sigma-Aldrich) 1% w/w in toluene was spin coated (1,800 rpm for 60 s). A metallic calcium cathode 30 nm thick was evaporated onto the active layer and subsequently covered with a 150 nm layer of aluminium as a protection against oxidation. For the evaporation of the cathode a mask to produce eight different pixels was used, see Fig. 7.1. The active area of each pixel is of about 3.5 mm^2 and it is given by the intersection between the ITO stripe and the calcium layer. The corresponding energy levels are shown in Fig. 7.2.

The normalized optical emission intensity for each polymer were measured using an Andor spectrometer (Shamrock 163 spectrograph with an Andor Newton EMCCD camera) and are shown in Fig. 7.3. The PLEDs have a peak wavelength of 630 nm, with a pronounced shoulder at $\sim$595 nm. The voltage-current density and voltage-optical power (JLV) relationships were measured using a Keithley 2400 voltage source, which supplied and measured the drive voltage and current. A Keithley 2000 digital multi-meter is used

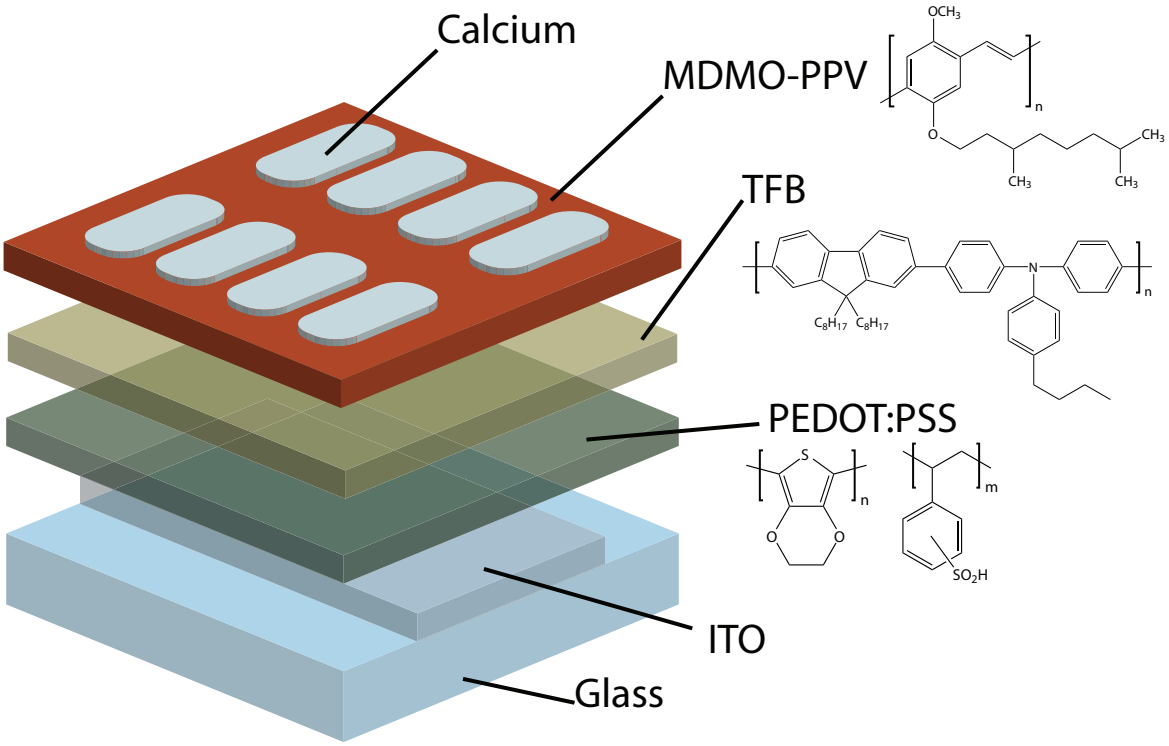

Fig. 7.1 A schematic of the PLED used in this work; the devices are composed of a stack of several thin polymeric layers encapsulated between two planar electrodes. The anode is a transparent conductive layer of ITO deposited on a glass substrate via a sputtering process. A hole injection layer made of a conjugated polymer poly(3,4-ethylenedioxythiophene) and poly(styrenesulfonate) (the mix is referred to as PEDOT:PSS) is in contact with the anode. On top of it, the conjugated polymer poly[(9'9'-dioctylfluorene-alt-N-(4-butylphenyl)diphenylamine] (TFB) acts as electron-blocking/hole-transporting interlayer [7–9]. The emissive polymer poly[2-methoxy-5-(3',7'-dimethyloctyloxy)-1,4-phenylenevinylene] (MDMO-PPV) is deposited on top of the TFB and is in direct contact with the metallic calcium cathode which is in turn covered by a layer of aluminium as a protection against oxidation

to measure the voltage from the photodetector, which was converted to the received optical power in MATLAB using the responsivity curve of the silicon photodetector. The JLV response was measured from 0 to 8 V as shown in Fig. 7.4. The operating voltage during the transmission tests was set at 8 VDC as this value is well above the turn-on for luminescence, therefore offering a milder non-linearity and less distortion to the transmission signal. Although at the limit of the range shown in Fig. 7.4, no significant degradation in the device operation was observed during the experiments.

The equalization of the Fermi levels of the electrodes generates a built-in voltage (V_{BI}) across the semiconductor layers inside the device. When the voltage supplied to the device

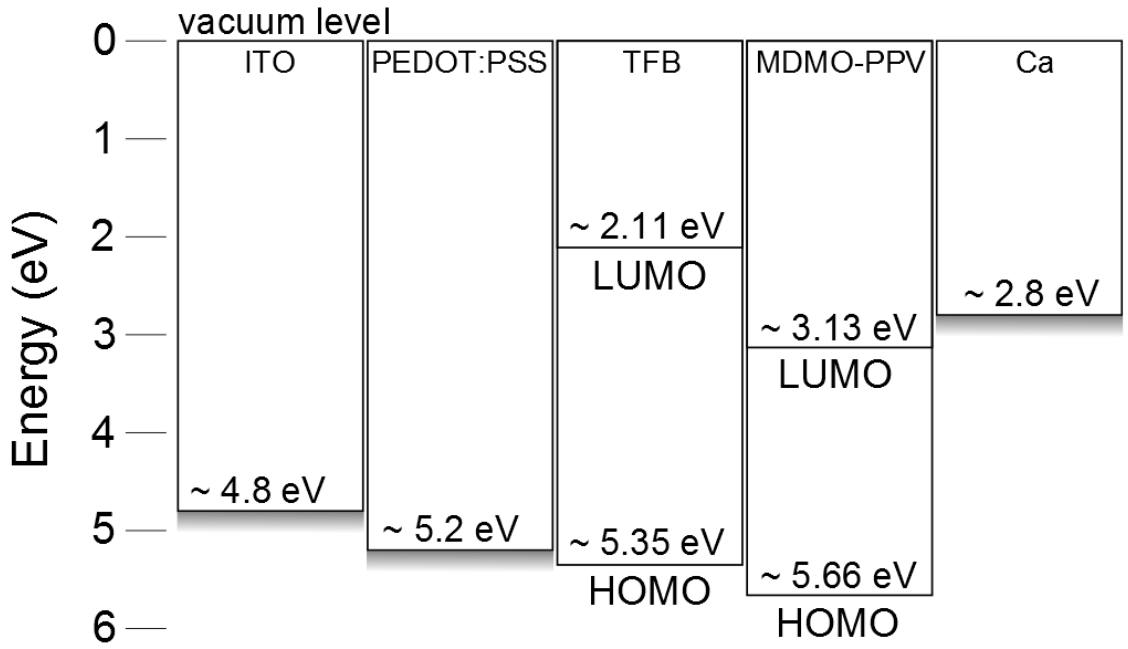

Fig. 7.2 The energy-level diagram, relative to vacuum, of the isolated materials used in the fabrication of the PLED. HOMO and LUMO stand for 'highest occupied molecular orbital' and 'lowest unoccupied molecular orbital' respectively. They indicate the two energy levels of the molecule that are responsible for its semiconductor behavior in the same way as valence and conduction bands in inorganic semiconductors. The HOMO and LUMO values for TFB and MDMO-PPV are measured by a combination of cyclic voltammetry and optical absorption [10, 11]. The Fermi levels of the electrodes are also reported [12]

is above V_{BI} a bipolar injection into the emitting polymer occurs and electroluminescence ensues. The device used in this work shows a peak external quantum efficiency of 1.9% when driving the LED with 72 mA/cm^2 current density and an applied voltage of 7.2 V as shown in Fig. 7.5. Finally, the device bandwidth was measured by transmission of a frequency swept sinusoid (20 kHz - 1 MHz) under the following operating conditions: 8 V_{DC}, 4 V_{AC}. At the receiver an Agilent N9010A electrical spectrum analyser measured the magnitude response of the received sinusoid over the given frequency range. Subsequently the light was switched off and a noise measurement was made over the same range. The bandwidth and noise measurements are illustrated in Fig. 7.6 along with the 270 kHz 3-dB point for the 270 kHz, which is the bandwidth under the operating conditions listed.

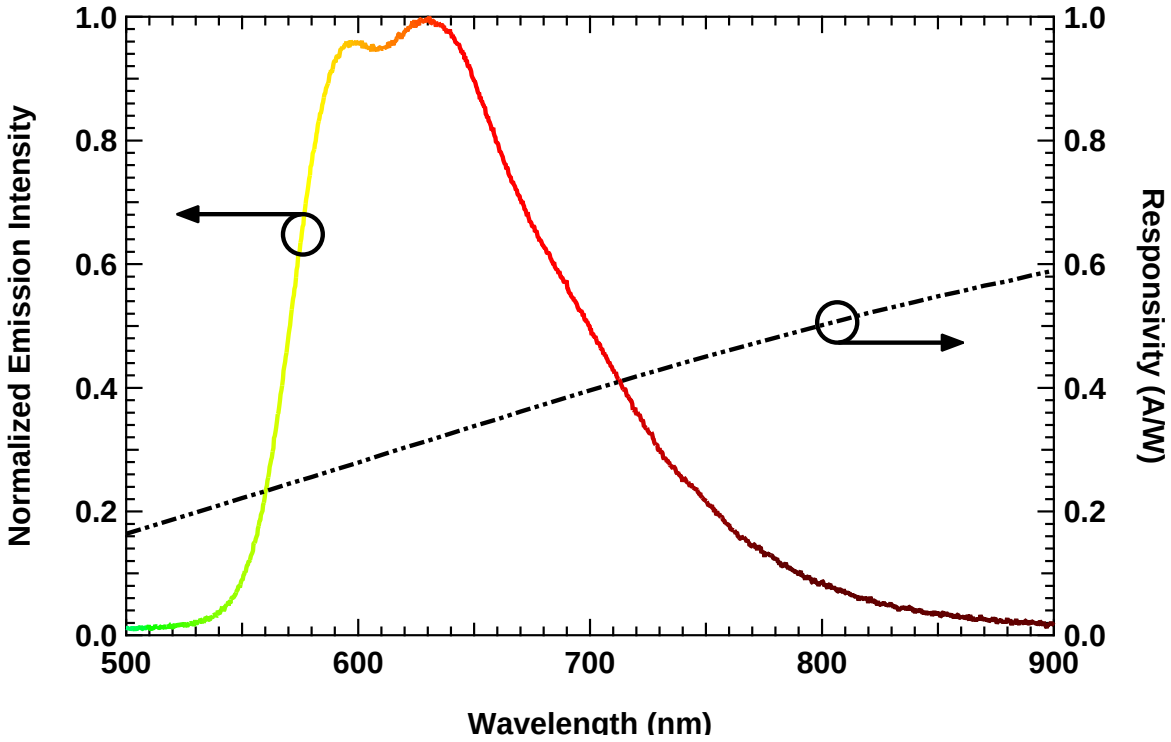

Fig. 7.3 Normalized PLED optical spectra and the responsivity of the ThorLabs PDA36A PD

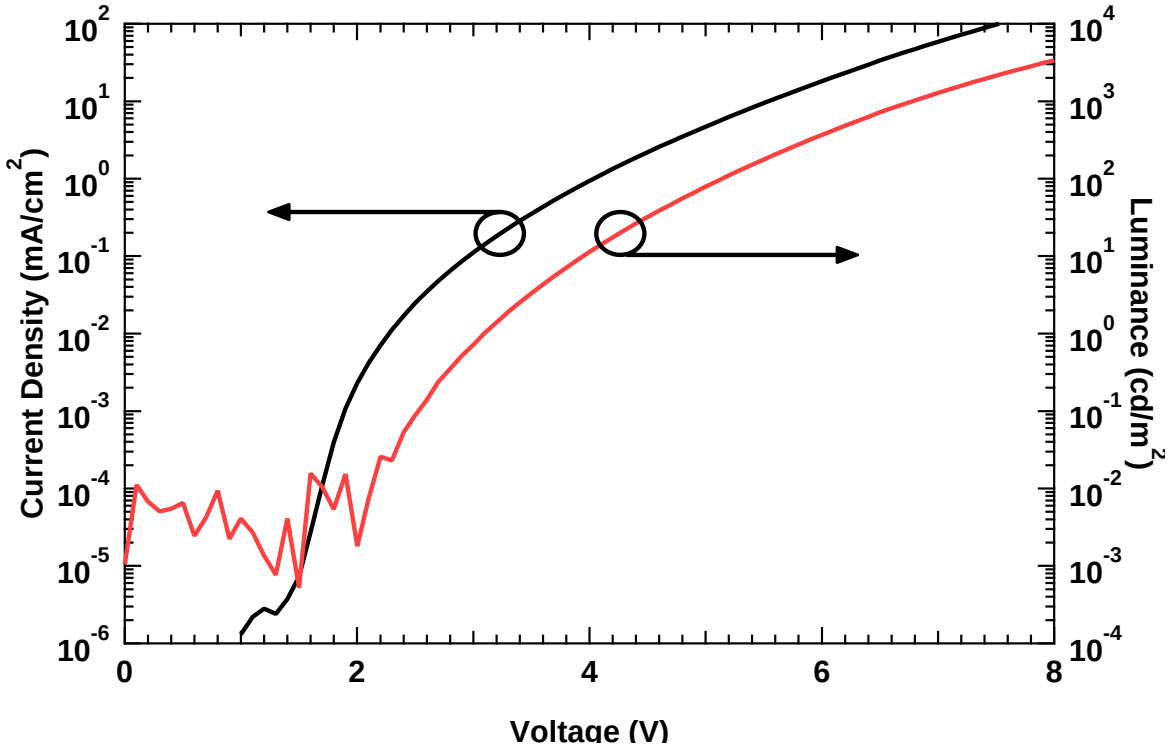

Fig. 7.4 PLED JLV relationship, with V_{ON} at $\sim$2 V; note the semi-logarithmic axes

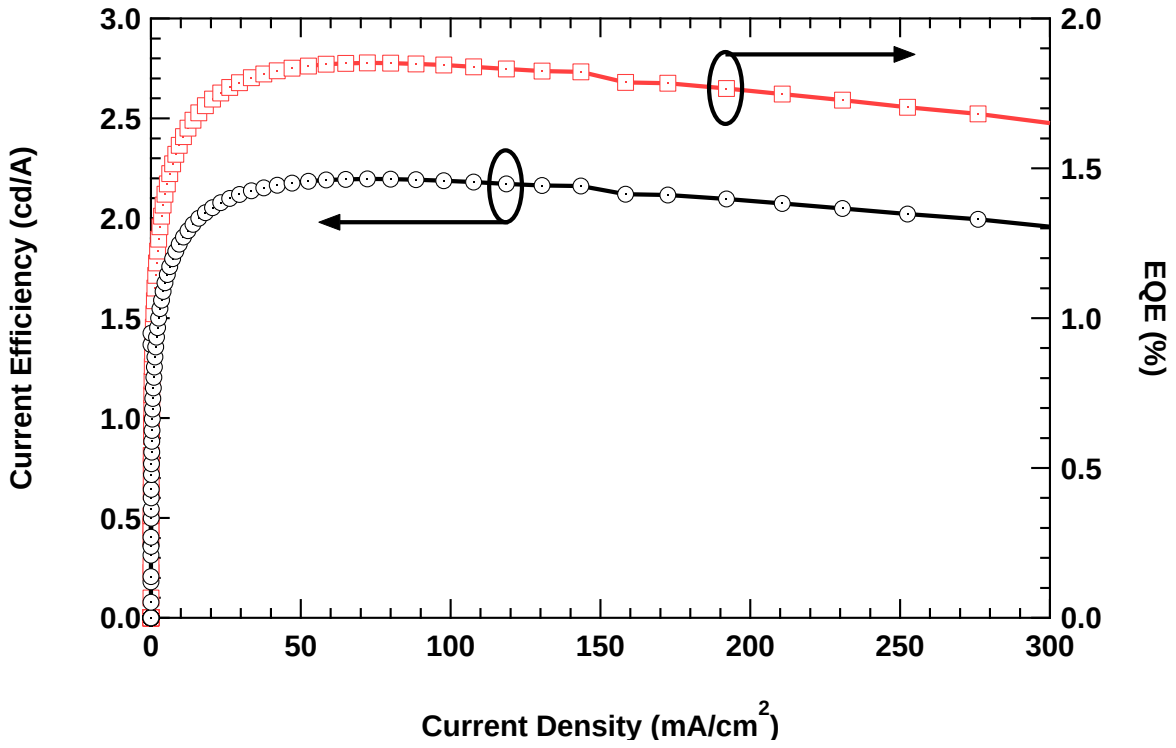

Fig. 7.5 The PLED current efficiency (cd/A) and external quantum efficiency (%) as a function of the current density

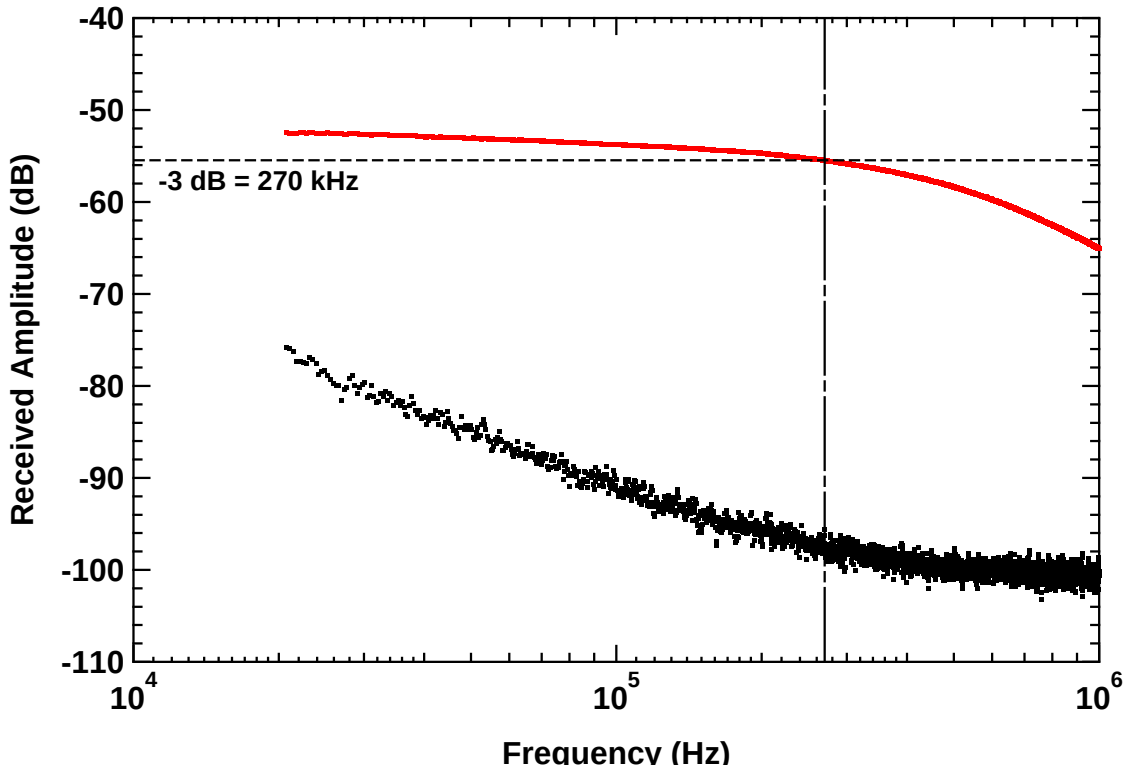

Fig. 7.6 The PLED the device frequency response for a variety of operating conditions

7.3 Experimental Test Setup and LMS Equalizer

The schematic block diagram of the experimental test setup is illustrated in Fig. 7.7.

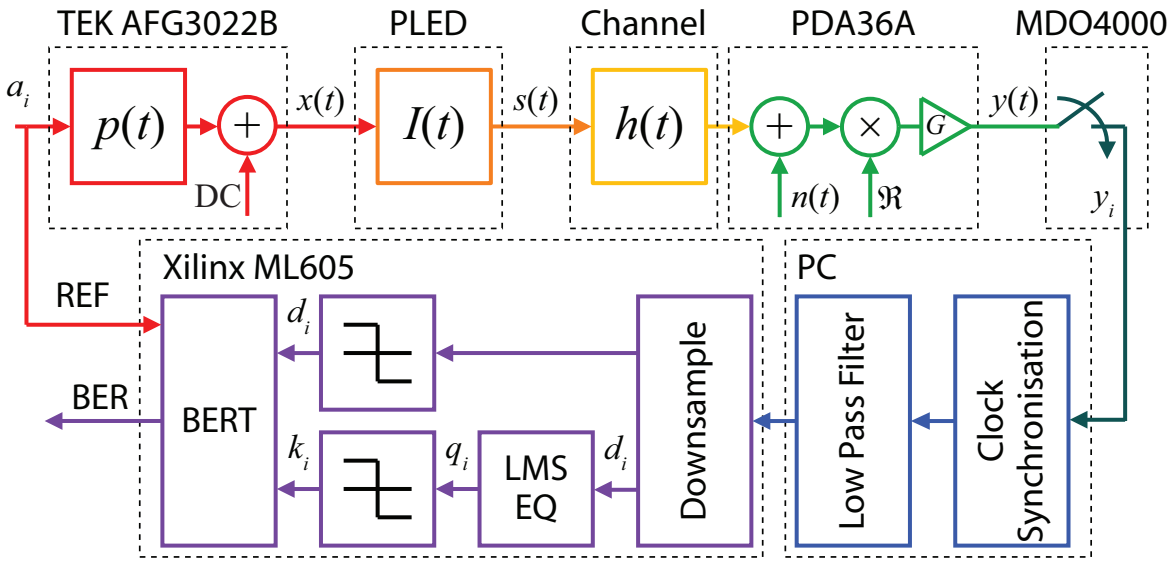

Fig. 7.7 Block diagram of the experimental test setup

A 2^{10}-1 length pseudorandom binary sequence data pattern a_i is generated in LabVIEW and mapped onto the OOK modulation format using a unit height pulse shaping filter $p(t)$. The output of the pulse shaping filter is loaded into the memory of the function generator and is internally shifted by a pre-defined DC level prior to driving the PLED to ensure operation in the linear region $x(t)$. The amplitude of the data is set to 4 V_{AC} and is biased at 8 VDC. The PLED converts the electronic data into an optical intensity $I(t)$. The radiation pattern of the PLED is assumed to be Lambertian and the mathematics can be referred to in [17]. The optical intensity propagates over the channel $h(t)$, which can be modelled as a DC gain less than unity [17]:

$$h = \xi \frac{A}{d^2} I(\theta) \cos(\varphi) \tag{7.1}$$

where A is the photodetector area (13 mm^2), d is the link distance (5 cm), θ and φ are the angles of emission and incidence from the PLED and to the photodetector, respectively. In order to achieve the best signal quality with the highest received optical power, a line of sight configuration with $\theta = \varphi = 0^\circ$ is adopted in this work. Note that the PLEDs were not encapsulated, instead they were set up in a pumped vacuum environment; however encapsulation is not expected to deteriorate the overall performance. The emitted light from the PLED propagates through a glass window with a small optical transmission loss

($\sim$ 10%). Therefore ξ is introduced as a proportionality factor to account for the silica window.

No focusing optics were used in the measurements and the distance between PLED and a ThorLabs PDA36A PIN photodetector (with 5.5 MHz bandwidth with an inbuilt transimpedance gain of 10 dB) was $\sim$0.05 m. This is a very short distance in comparison to a full room scale and the reason is because the experiment was performed using singular pixels ($\sim$3.5 mm^2) where the brightness was relatively low. To increase the transmission distance ($>$1 m) for future applications, the solution is to simply scale up the amount of PLEDs until the minimum desired optical power is collected at the receiver. There are several sources of noise $n(t)$ including ambient, thermal and shot noise. To minimize the ambient noise, the experiment was conducted in a pitch black laboratory. The thermal and shot noise sources are assumed to be AWGN as stated in [17, 111].

The received signal $y(t) = G\Re[h(t) \otimes s(t) + n(t)]$ is captured and sampled by a Tektronix MDO4104-6 real time oscilloscope with the output given by:

$$y_i = G\Re\left[y_i h_0 + \sum_{\substack{j=-\infty \\ j\neq i}}^{\infty} y_j h_{i-j} + n_i\right] \tag{7.2}$$

where $\Re$ is the photodiode responsivity, G is the 10 dB transimpedance gain, h_i is the sampled channel impulse response, i is the current sampling instance, j represents the contributions of the ISI and n_i is a zero mean Gaussian random variable with variance $N_0/2$ representing the noise at each sample. The data y_i is acquired by a PC via a LabVIEW script where synchronization with the transmitted data (clock synchronisation in Fig. 7.7) is carried out before being passed through a low pass filter (LPF) to remove the high frequency noise components. Both synchronisation and LPF are not performed in the FPGA domain; this is to ensure that any errors introduced in the system are due to the equalizer in this first demonstration of such a link.

To combat ISI, equalizers are the most effective solution; they are typically implemented as digital FIR transversal filters with adjustable coefficients. The adjustment of the equalizer coefficients is usually carried out adaptively during the transmission process. During the start-up period a short known training sequence is transmitted for the purpose of initial adjustment of the tapped weight coefficients of the filter. The accuracy of the channel estimation, which essentially resolves the convergence and performance of equalization, can be affected either by the length of the training or pilot sequence, or the period between channel estimations. Typically using a higher number of taps will result in better system response estimation. Likewise, a long training sequence will also result in a better estimation since

the impact of noise is reduced. On the other hand a high number of taps require more computational resources while a long training sequence introduces more redundancy into the system due to the requirement for retraining. The tap coefficients are determined using an iterative procedure. The most popular algorithms for determining the tap coefficients are the LMS, RLS and its derivatives, fast RLS, and gradient RLS. Here the LMS method is employed in conjunction with the (symbol spaced) linear transversal FIR filter since it is the least computationally complex of the training algorithms and requires no matrix inversion unlike RLS algorithms. The received samples di are streamed from a PC to the FPGA via a JTAG Ethernet connection and subsequently down-sampled to one sample-per-bit using a mid-point sampler before being passed through the filter. Down-sampling, equalization, threshold detection and BERT are all implemented on the FPGA board (Xilinx Virtex 6 ML605). The Xilinx ISE software is used to download the synthesized VHDL codes onto the board. The tap coefficients are updated as follows [161]:

$$w_{i+1}(m) = w_i(m) + \mu e_i d_i \tag{7.3}$$

where d_i is the incoming noise and interference perturbed downsampled symbol, $w_i(m)$ is the m^{th} filter weight at sample instant i, and μ is the learning rate parameter (set to 0.001) for every experiment in this work. Setting μ excessively will lead to instability in the equalizer (i.e. never converging) while setting μ insufficiently will result in slow convergence. The value selected for μ is relatively small; however the training length is set to the first 100,000 samples thus providing ample time for convergence. Reducing the training sequence length will deteriorate the channel estimation but reduces the SNR penalty and improves the data throughput.

Once the system response is estimated, the inverse of the system response is applied to the received symbols by means of tapped weight coefficients in order to recover the original symbols. The system is stationary meaning that training only occurs once at the start of each measurement. For non-stationary systems it would be expected that a shorter training sequence with a larger learning rate parameter would be used due to the need to retrain the tap coefficients when the system response is changing. The output of the equalizer is given as [161]:

$$q_i = \sum_{m=0}^{N} w_i(m)\, d_{i-m} \tag{7.4}$$

where N is the number of taps; $N = \{3;\ 5;\ 7;\ 10;\ 15;\ 20;\ 25\}$. The maximum number of taps available for this LMS transversal equalizer is 25. The bottleneck is clearly in the IOBs,

which are fully utilized with a 25-tap LMS filter. The rest of the resources are not close to the capacity (the next most utilized feature is the DSP48s at 27%).

7.4 Results

The BER performance of the system without an equalizer and measured with a symbol-by-symbol threshold detector is shown in Fig. 7.8. Also shown is the Q-factor. It is possible to transmit up to 3 Mb/s without the use of an equalizer in the real time scenario. This is a faster data rate than is currently available in the state-of-the-art organic VLC; which is currently limited to 2.7 Mb/s using a highly computationally complex ANN equalizer [163]. Aside from the device materials, which can't be controlled, the key difference between the devices is the bandwidth ($\sim$270 kHz in this work and $\sim$90 kHz in [163]) due to the photoactive areas; $\sim$3.5 mm^2 here and $\sim$4,900 mm^2 in [163]. The measured, smoothed and exponentially fitted SNR are shown in Fig. 7.9; the measurement was made by subtracting the system magnitude response from the system noise floor (refer to Fig. 7.6) between 20 kHz - 1 MHz. At 4 MHz the predicted SNR is $\sim$14 dB, which is sufficient for an OOK link at a BER of 10^{-6}. Thus it is possible to infer that the link fails as result of higher ISI contributions due to the transmission data rate far exceeding the modulation bandwidth. Also shown in inset are the captured eye diagrams.

In order to further improve the available data rate in PLED-VLC systems, it is necssary to utilise an equalizer as mentioned above. The LMS equalizer with N-taps as previously described is implemented on the ML605 FPGA board with the BER measurements repeated for a range of data rates. The BER performance of the FPGA filter in real time is depicted in Fig. 7.10 showing an improvement with an the increase in the number of taps. For $N = \{3;\ 5;\ 7;\ 10;\ 15\}$ taps and at a BER of 10^{-6} it is possible to increase the data rate by 3 Mb/s to 6 Mb/s compared to the simple threshold detection scheme. For $N = \{20;\ 25\}$ taps the available error free transmission speed is up to 7 Mb/s at the same BER. This is a significant increase in the available data rate not only in relation to the threshold detector case ($>$100%) but also in comparison to the literature [163] with a significantly less complex offline ANN equalizer and also in real time using the FPGA. For data rates $>$7 Mb/s symbols cannot be recovered with an acceptable BER. For example, at 8 Mb/s and referring to Fig. 7.9 the predicted SNR is $\sim$5 dB and it is for this reason that the equalizer fails because it cannot filter uncorrelated, and unbounded AWGN.

Thus it is necessary to introduce a BER limit for forward error correction (FEC) at 4.6×10^{-3}, at the cost of 7% increase in the overhead [164], as is a common practice in high speed VLCs [47, 58]. The limit is indicated by the dashed line in Fig. 7.10 and it

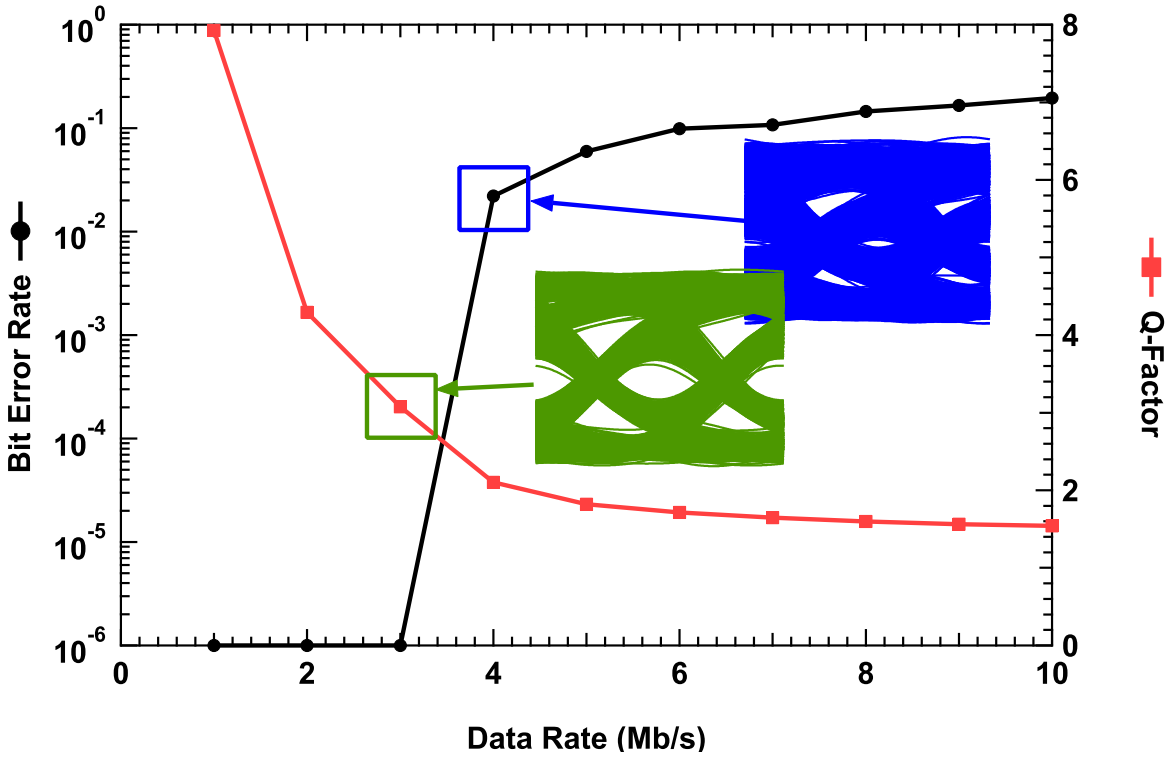

Fig. 7.8 The system BER and Q-factor performance as a function of data rate; 3 Mb/s can be achieved without the use of an equalizer. At 4 Mb/s the link fails and errors are introduced into the system; eye diagrams are shown inset

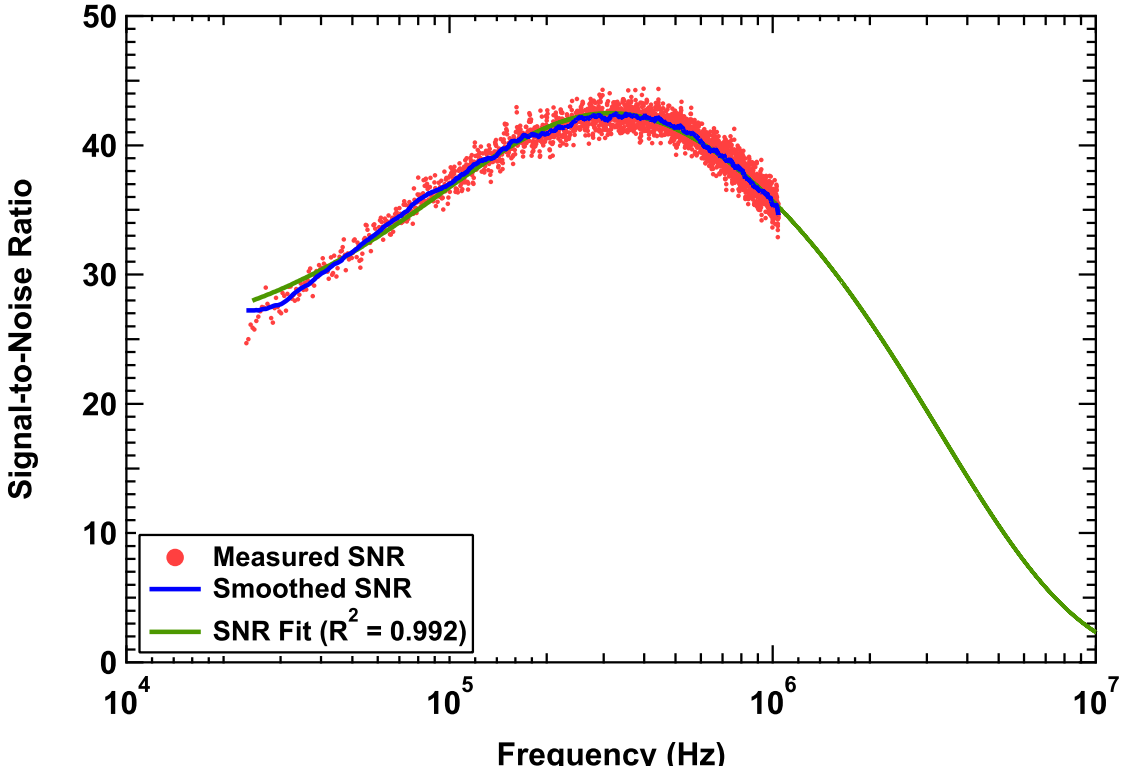

Fig. 7.9 The SNR measured throughout the system from 20 kHz – 1 MHz using an Agilent N9010A electrical spectrum analyser. The SNR is smoothed and fitted exponentially to predict the SNR at higher data rates

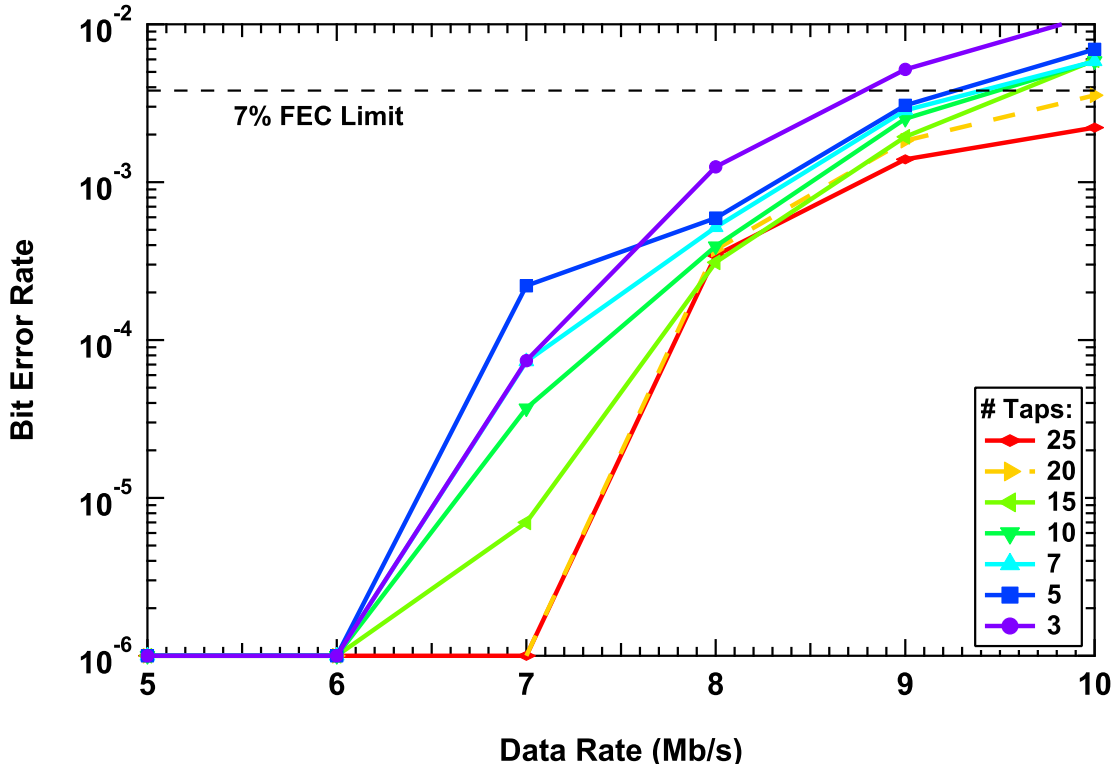

Fig. 7.10 BER performance of the PLED-VLC system with the FPGA based LMS equalizer; clearly there as an increase in performance with an increasing number of taps as expected; the key result is that the 10 Mb/s link has a BER within the FEC limit; meaning that the data can be recovered with an overhead of just 7%

is clear that data rates can be increased to 10 Mb/s using $N = 20$ and 25 tapped weight coefficients. The performance of an equalizer with $N = \{5; 7; 10; 15\}$ taps show BER of $\sim$0.006 - 0.007 and thus slightly exceeding the FEC limit, while $N = 3$ taps fails to converge to the target value. The predicted SNR at a frequency of 10 MHz is $<$5 dB, where the performance is descending into the noise floor, which is benefiting from the long training length with numerous tapped weight coefficients in order to compose an accurate account of the channel. Having a FEC overhead of 7% means that the line rate of 10 Mb/s would be reduced to 9.3 Mb/s.

Overall this demonstration of a real time PLED-VLC system operating at an overall data rate of 10 Mb/s is the first real landmark in high speed organic based VLC systems. This work represents three separate increases in the current state-of-the-art data rates over the 2.7 Mb/s reported in [163]. Firstly by using a custom produced PLED with $\sim$3 times larger bandwidth a data rate of 3 Mb/s was possible with simple threshold detection. Secondly using the FPGA based LMS equalizer at a BER target of 10^{-6} a data rate of 7 Mb/s can

be readily achieved. Finally by introducing the FEC BER limit of 4.6×10^{-3} an overall transmission speed of 10 Mb/s could be achieved. Removing the 7% redundancy gives an overall information rate of 9.3 Mb/s, or an increase over [163] by $\sim$3.5 times whilst using a significantly less computationally complex equalizer.

7.5 Conclusion

In this work a 10 Mb/s VLC link was implemented using a PLED for the very first time. This transmission speed was achieved at the FEC BER target of 4.6×10^{-3} at the cost of a 7% overhead. An LMS equalizer was also adopted and implemented on the Xilinx Virtex 6 ML605 FPGA board with 20 and 25 taps. Using 15-tap or fewer does not provide sufficient performance to achieve such a transmission speed. This is a significant step for the future of PLED-VLC systems as such a data rate is sufficient for an Ethernet connection.

Chapter 8

Conclusions and Future Work

8.1 Conclusions

The main objective of this thesis was to establish small molecule and polymer OVLC systems into the research community. VLC is an outstanding technology for future the future "last-metre" bottleneck caused by (*a*) the high capacity ubiquitous backbone networks provided by optical fibre links and (*b*) considerable overcrowding of the RF spectra. VLC possesses several serious advantages over RF such as license free use, no electromagnetic interference meaning deployment is possible in sensitive locations such as aircraft and hospitals and a wide 400 THz bandwidth (around 10,000 times larger than RF). Thus, VLC is worthy of further research to fulfil its potential. Normally this research has focused on using inorganic WPLEDs/RGBLEDs as the transmitters and Si PDs as the receivers due to several advantages: (*i*) high optical power output (transmitters) and (*ii*) reasonable bandwidths in the MHz region. On the other hand, such devices also have drawbacks. A few of the most noteworthy are scalability due to brittle crystals produced using epitaxial high vacuum processing methods (transmitters) and low responsivity in the visible range (receivers). Combine these disadvantages with the fact that PLEDs and SMOLEDs are emerging as serious candidates for future lighting systems due to extremely low cost solution-based processing methods and high electrical efficiencies and the main motivation for this thesis is established. Using organic components in general, however, is not an ideal solution. Due to highly disordered structures with low aggregation charge transport inside the semiconductor is roughly three orders of magnitude lower than amorphous Si which causes severely restricted bandwidths. Such is the desire of VLC to increase the capacity available to the end-user; the bandwidth limitation is the single most important problem facing OVLC dominance. As a result, equalizers are required which permit high transmission speeds by removal of ISI either via iterative procedures or by classification. In Chapter 1 this is firmly

established and aims/objectives are proposed.

In order to fully understand the proposed OVLC field, it was first necessary to establish the fundamental principles of inorganic and organic semiconductor photon generation, emission and absorption which are outlined in Chapter 2. The relationships established in Chapter 2 are important because they allow understanding into the behaviour of the devices which is beneficial for later understanding how to establish the best possible transmission system. Simplest-form equivalent circuits are derived from these principles along with governing equations.

Following this, Chapter 3 reviews the theory of optical communications using a mathematical approach. A full system model is presented including complete analysis of the optical emission patterns of the transmitters, channel model, reception methods and noise sources. The modulation formats under test in this thesis; OOK and L-PPM are examined in terms of their probability of error with varying SNR and also their bandwidth, power and spectral efficiency. Finally Chapter 3 covers equalization theory, starting with analogue RC equalization implemented as a passive HPF. It is shown that RC equalization is unsuitable for low bandwidth applications such as OVLC due to the high power penalty introduced by the capacitor that causes the BLW phenomenon. As such digital equalizers are introduced that offer an increase in performance alongside an increase in computational complexity. Digital equalizers can be divided into linear (adaptive and non-adaptive) and non-linear (adaptive) categories and the theory for both is outlined and compared. Finally ANNs are considered, in particular the MLP implementation which acts as a universal classifier between input and output sequences. The MLP is established as the best performing equalizer whilst being the most complex and hence is primarily used in this work.

The objectives of this thesis focus on analysing the performance of several links; a SMOLED to Si PD link and a WPLED to OPD link in the first instance. This allows the establishment of the BER performance limitations of the individual devices and as such, Chapter 4 marks the beginning of the authors' original contributions to knowledge. The full BER analysis of the SMOLED system is outlined. The modulation formats used are OOK and L-PPM. The target BER was set to 10^{-6} and unequalized (MLP equalized) transmission speeds achieved were 50 (2.7), 150 (2.15) and 250 (1.6) kb/s (Mb/s) for 4-PPM, 2-PPM and OOK, respectively. These results were confirmed using a TI TMS320C6713 DSP board that implemented the ANN equalizer in real time.

The WPLED/OPD link is analysed in Chapter 5 using OOK and 4-PPM. A further challenge in using OPDs emerges such that the available bandwidth is not constant and depends on the optical power impinging on the active area. The reason for this is due to charge traps at the interface at energy levels close to those of the HOMO and LUMO. Charge car-

riers propagating through the device may occupy the traps which have an associated time constant, which is slower than both the exciton lifetime and the capacitive limit. The time constant varies depending on the quantity of filled traps; hence if the impinging light density is high, the whole population of traps are filled and hence the bandwidth becomes proportional to the capacitance which has an upper limit ∼150 - 160 kHz for the devices used in this thesis. Otherwise the bandwidth is set by the number of traps filled. It should be noted that the upper bandwidth limitation can be improved by reducing the thickness of the BHJ (∼500 nm in this work); however this is not done here. Therefore Chapter 5 also compares the performance of each modulation scheme for a number of incident light densities. The bandwidths achieved (light densities required) were 160 (300), 110 (270), 76 (50) and 56 (10) kHz (μW/cm^2). The maximum BER performance of the link with a bandwidth of 160 kHz was 500 and 300 kb/s for 4-PPM and OOK, respectively. Using the MLP equalizer and 4-PPM, transmission speeds above 1 Mb/s could be achieved in all light densities; (*i*) 160 kHz bandwidth: 3.75 Mb/s transmission speed; (*ii*) 110 kHz: 2.4 Mb/s; (*iii*) 76 kHz: 1.45 Mb/s and (*iv*) 56 kHz: 1.15 Mb/s.

The next objective in this thesis was to establish a fully OVLC system that makes use of organic components at each optoelectronic node and this is carried out in Chapter 6. The link consisted of the same SMOLED and OPD used in the previous two chapters. The modulation format used was OOK and the unequalized and MLP equalized cases are presented across three separate link bandwidths (135, 100 and 65 kHz). The bandwidth is varied by controlling the light density of the SMOLED by varying the bias current. The maximum unequalized (equalized) transmission speeds are 350 (1150), 250 (850) and 150 (450) kb/s for 135, 100 and 65 kHz bandwidths, respectively. This is the first demonstration of a free space OVLC system and it is remarkable that with such low bandwidths, speeds above 1 Mb/s can be supported, which shows a considerable potential for future systems that will offer improvement on this work.

PLEDs are introduced in Chapter 7 with a view to future solution-processed lighting solutions that are deployable with extremely low costs. The idea behind the PLEDs used in this work is to integrate them into active matrices and embed them into display technologies for smart homes. Therefore a real time system using an FPGA is proposed and demonstrated with an LMS linear adaptive equalizer. An error free (10^{-6}) transmission speed of 9.3 Mb/s could be recovered, considering a 7 % FEC code. The gross transmission speed was 10 Mb/s which is approaching Ethernet speeds for the first time. Subsequently a remarkable improvement up to 20 Mb/s could be achieved using the better performing and more complex MLP equalizer. A transmission speed of 20 Mb/s is of the upmost importance to the VLC research community because it demonstrates that Ethernet-speed connectivity can be

achieved using extremely cheap devices which is truly an exciting prospect.

8.2 Future Work

As the author has introduced an entirely new domain for research, it was never intended that this work would finish with a complete standalone product. As such there is a huge scope for future work. The main suggestions of the author are as follows:

8.2.1 Discrete Multi-tone Modulation

DMT has shown remarkable improvements in throughput in the inorganic VLC domain, where transmission speeds at $\sim$3.4 Gb/s region have been experimentally demonstrated over RGB using links that have bandwidths $\sim$30 MHz/channel. Therefore DMT is worthy of further investigation for OVLC systems and is not covered at all in this thesis. A detailed investigation of the various DMT implementations (asymmetrical, DC-offset, flip) would be advantageous, followed by analysis of the adaptive bit- and power-loading algorithms in order to further drive up transmission speeds.

8.2.2 Pixel Combining for SNR Improvement

In Chapter 7 PLEDs are introduced for the first time. Despite there being six individual pixels on each substrate only a solitary pixel is used for communications at any given time. The reason for this was due to a shared ITO electrode that means the pixels are not independent. A lack of independence means a MIMO system is impossible to produce and hence no further measurements were made. The author recommends that a detailed investigation is necessary in order to establish the bandwidth/SNR trade-off that occurs with a varying number of active pixels. If the entire device can simultaneously provide six active pixels at a minimal bandwidth cost, it is expected that a substantial improvement could be made on the 20 Mb/s transmission speed reported in Chapter 7 which would be of considerable interest to the research community.

8.2.3 Reduction of Pixel Size

Considering that the PLEDs used have active area of 3 mm2 they are in an intermediate state where they are, realistically, too large for smart displays and too small for full room illumination. A reduction in pixel size would demonstrate an intention to move towards smart display technologies and would also result in greatly increased bandwidths, estimated

to be in the MHz region, thus rivalling WPLEDs. If such devices could be produced, independent of each other on the same substrate then this would be an extremely important development for future OVLC systems. Massively MIMO systems could be implemented to offer device-to-device communications in the context of smart homes. Furthermore, the previous two suggestions can be replicated using the new high-speed independent devices with a Gb/s transmission speed target.

References

[1] ThorLabs.

[2] S. Haykin, *Adaptive Filter Theory*. New Jersey, USA: Prentice Hall International, 2001.

[3] "American society for testing and materials (astm) terrestrial reference spectra for photovoltaic performance evaluation."

[4] W. Popoola, *Subcarrier intensity modulated free-space optical communication systems*. Thesis, 2009.

[5] S. Tedde, *Design, Fabrication and Characterization of Organic Photodiodes for Industrial and Medical Applications*. Walter Schottky Institut, Technische Universitat Munchen, 2009.

[6] A. K. Jain, M. Jianchang, and K. M. Mohiuddin, "Artificial neural networks: a tutorial," *Computer*, vol. 29, no. 3, pp. 31–44, 1996. 0018-9162.

[7] G. M. Lazzerini, F. Di Stasio, C. Flechon, D. J. Caruana, and F. Cacialli, "Low-temperature treatment of semiconducting interlayers for high-efficiency light-emitting diodes based on a green-emitting polyfluorene derivative," *Applied Physics Letters*, vol. 99, no. 24, pp. –, 2011.

[8] J.-S. Kim, R. H. Friend, I. Grizzi, and J. H. Burroughes, "Spin-cast thin semiconducting polymer interlayer for improving device efficiency of polymer light-emitting diodes," *Applied Physics Letters*, vol. 87, no. 2, pp. –, 2005.

[9] N. Johansson, F. Cacialli, K. Z. Xing, G. Beamson, D. T. Clark, R. H. Friend, and W. R. Salaneck, "A study of the ITO-on-PPV interface using photoelectron spectroscopy," *Synthetic Metals*, vol. 92, no. 3, pp. 207–211, 1998.

[10] O. Fenwick, S. Fusco, T. N. Baig, F. Di Stasio, T. T. Steckler, P. Henriksson, C. Fléchon, M. R. Andersson, and F. Cacialli, "Efficient red electroluminescence from diketopyrrolopyrrole copolymerised with a polyfluorene," *APL Materials*, vol. 1, no. 3, pp. –, 2013.

[11] B. W. D'Andrade, S. Datta, S. R. Forrest, P. Djurovich, E. Polikarpov, and M. E. Thompson, "Relationship between the ionization and oxidation potentials of molecular organic semiconductors," *Organic Electronics*, vol. 6, no. 1, pp. 11–20, 2005.

[12] T. M. Brown and F. Cacialli, "Contact optimization in polymer light-emitting diodes," *Journal of Polymer Science Part B: Polymer Physics*, vol. 41, no. 21, pp. 2649–2664, 2003.

[13] D. Mange and M. Tomassini, *Bio-inspired computing machines: towards novel computational architectures*. PPUR presses polytechniques, 1998.

[14] R. M. R. Ltd, "Uk radio frequency allocations chart," 2013.

[15] Y. Ito, "A new paradigm in optical communications and networks," *IEEE Communications Magazine*, vol. 51, no. 3, pp. 24–26, 2013.

[16] L. Hanzo, H. Haas, S. Imre, D. O'Brien, M. Rupp, and L. Gyongyosi, "Wireless myths, realities, and futures: From 3g/4g to optical and quantum wireless," *Proceedings of the IEEE*, vol. 100, no. Special Centennial Issue, pp. 1853–1888, 2012.

[17] J. Kahn and J. Barry, "Wireless infrared communications," *Proceedings of the IEEE*, vol. 85, no. 2, pp. 265–298, 1997.

[18] J. R. Barry, *Wireless Infrared Communications*. Boston: Kluwer Academic Publishers, 1994.

[19] F. K. Yam and Z. Hassan, "Innovative advances in led technology," *Microelectronics Journal*, vol. 36, no. 2, pp. 129–137, 2005.

[20] R. D. Dupuis and M. R. Krames, "History, development, and applications of high-brightness visible light-emitting diodes," *Lightwave Technology, Journal of*, vol. 26, no. 9, pp. 1154–1171, 2008.

[21] A. Laubsch, M. Sabathil, J. Baur, M. Peter, and B. Hahn, "High-power and high-efficiency ingan-based light emitters," *Electron Devices, IEEE Transactions on*, vol. 57, no. 1, pp. 79–87, 2010.

[22] Y. Tanaka, S. Haruyama, and M. Nakagawa, "Wireless optical transmissions with white colored led for wireless home links," in *Personal, Indoor and Mobile Radio Communications, 2000. PIMRC 2000. The 11th IEEE International Symposium on*, vol. 2, pp. 1325–1329 vol.2.

[23] Y. Tanaka, T. Komine, S. Haruyama, and M. Nakagawa, "Indoor visible communication utilizing plural white leds as lighting," in *Personal, Indoor and Mobile Radio Communications, 2001 12th IEEE International Symposium on*, vol. 2, pp. F–81–F–85 vol.2.

[24] Y. Tanaka, T. Komine, S. Haruyama, and M. Nakagawa, "A basic study of optical ofdm system for indoor visible communication utilizing plural white leds as lighting," *Proceeding of 8th International Symposium on Microwave and Optical Technology (ISMOT)*, pp. 303–306, 2001.

[25] K. Fan, T. Komine, Y. Tanaka, and M. Nakagawa, "The effect of reflection on indoor visible-light communication system utilizing white leds," in *Wireless Personal Multimedia Communications, 2002. The 5th International Symposium on*, vol. 2, pp. 611–615 vol.2.

[26] T. Komine and M. Nakagawa, "Fundamental analysis for visible-light communication system using led lights," *Consumer Electronics, IEEE Transactions on*, vol. 50, no. 1, pp. 100–107, 2004.

[27] IEEE, "IEEE standard for local and metropolitan area networks–part 15.7: Short-range wireless optical communication using visible light," 2012.

[28] K. Lee and H. Park, "Modulations for visible light communications with dimming control," *IEEE Photonics Technology Letters*, vol. 23, no. 16, pp. 1136–1138, 2011.

[29] B. Bo, X. Zhengyuan, and F. Yangyu, "Joint led dimming and high capacity visible light communication by overlapping ppm," in *Wireless and Optical Communications Conference (WOCC), 2010 19th Annual*, pp. 1–5.

[30] K. Jae Kyun, "Inverse source coding for dimming in visible light communications using nrz-ook on reliable links," *IEEE Photonics Technology Letters*, vol. 22, no. 19, pp. 1455–1457, 2010.

[31] G. Ntogari, T. Kamalakis, J. Walewski, and T. Sphicopoulos, "Combining illumination dimming based on pulse-width modulation with visible-light communications based on discrete multitone," *IEEE/OSA Journal of Optical Communications and Networking*, vol. 3, no. 1, pp. 56–65, 2011.

[32] C. Joon-ho, C. Eun-byeol, K. Tae-Gyu, and L. Chung Ghiu, "Pulse width modulation based signal format for visible light communications," in *OptoeElectronics and Communications Conference (OECC), 2010 15th*, pp. 276–277.

[33] J. Hyung-Joon, C. Joon-Ho, Z. Ghassemlooy, and L. Chung Ghiu, "PWM-based PPM format for dimming control in visible light communication system," in *Communication Systems, Networks & Digital Signal Processing (CSNDSP), 2012 8th International Symposium on*, pp. 1–5.

[34] A. Mirvakili and V. J. Koomson, "High efficiency LED driver design for concurrent data transmission and pwm dimming control for indoor visible light communication," in *Photonics Society Summer Topical Meeting Series, 2012 IEEE*, pp. 132–133.

[35] C. Eunbyeol, C. Joon-Ho, P. Chulsoo, K. Moonsoo, S. Seokjoo, Z. Ghassemlooy, and L. Chung Ghiu, "NRZ-OOK signaling with LED dimming for visible light communication link," in *Networks and Optical Communications (NOC), 2011 16th European Conference on*, pp. 32–35.

[36] T. Borogovac, M. B. Rahaim, M. Tuganbayeva, and T. D. C. Little, ""lights-off"; visible light communications," in *GLOBECOM Workshops (GC Wkshps), 2011 IEEE*, pp. 797–801.

[37] H. Le Minh, D. O'Brien, G. Faulkner, L. Zeng, K. Lee, D. Jung, and Y. Oh, "80 mbit/s visible light communications using pre-equalized white LED," in *Optical Communication, 2008. ECOC 2008. 34th European Conference on*, pp. 1–2, IEEE.

[38] H. Le Minh, D. O'Brien, G. Faulkner, L. Zeng, K. Lee, D. Jung, and Y. Oh, "High-speed visible light communications using multiple-resonant equalization," *Photonics Technology Letters, IEEE*, vol. 20, no. 14, pp. 1243–1245, 2008.

[39] H. Le Minh, D. O'Brien, G. Faulkner, L. Zeng, K. Lee, D. Jung, Y. Oh, and E. Won, "100-mb/s NRZ visible light communications using a postequalized white LED," *Photonics Technology Letters, IEEE*, vol. 21, no. 15, pp. 1063–1065, 2009.

[40] Z. Ghassemlooy, "Investigation of the baseline wander effect on indoor optical wireless system employing digital pulse interval modulation," *IET Communications*, vol. 2, no. 1, pp. 53–60, 2008. 1751-8628.

[41] A. M. Street, K. Samaras, D. C. Obrien, and D. J. Edwards, "Closed form expressions for baseline wander effects in wireless IR applications," *Electronics Letters*, vol. 33, no. 12, pp. 1060–1062, 1997.

[42] A. R. Hayes, Z. Ghassemlooy, N. L. Seed, and R. McLaughlin, "Baseline-wander effects on systems employing digital pulse-interval modulation," *IEE Proceedings - Optoelectronics*, vol. 147, no. 4, pp. 295–300, 2000.

[43] J. R. Barry, E. A. Lee, and D. Messerschmitt, *Digital Communication*. Boston: Kluwer Academic Publishers, 3rd ed., 2003.

[44] J. G. Proakis and M. Salehi, *Fundamentals of communication systems*. Pearson Prentice Hall, 2005.

[45] A. M. Khalid, G. Cossu, R. Corsini, P. Choudhury, and E. Ciaramella, "1-Gb/s transmission over a phosphorescent white LED by using rate-adaptive discrete multitone modulation," *IEEE Photonics Journal*, vol. 4, no. 5, pp. 1465–1473, 2012.

[46] R. A. Shafik, S. Rahman, and R. Islam, "On the extended relationships among EVM, BER and SNR as performance metrics," in *Electrical and Computer Engineering, 2006. ICECE '06. International Conference on*, pp. 408–411.

[47] G. Cossu, A. M. Khalid, P. Choudhury, R. Corsini, and E. Ciaramella, "3.4 Gbit/s visible optical wireless transmission based on RGB LED," *Opt Express*, vol. 20, no. 26, pp. B501–6, 2012.

[48] E. Biglieri, J. Proakis, and S. Shamai, "Fading channels: information-theoretic and communications aspects," *IEEE Transactions on Information Theory*, vol. 44, no. 6, pp. 2619–2692, 1998.

[49] H. Li, X. Chen, B. Huang, D. Tang, and H. Chen, "High bandwidth visible light communications based on a post-equalization circuit," *Photonics Technology Letters, IEEE*, vol. 26, no. 2, pp. 119–122, 2014.

[50] P. A. Haigh, Z. Ghassemlooy, S. Rajbhandari, I. Papakonstantinou, and W. Popoola, "Visible light communications: 170 mb/s using an artificial neural network equalizer in a low bandwidth white light configuration," *Journal of Lightwave Technology*, vol. 32, no. 9, pp. 1807–1813, 2014.

[51] J. H. Burroughes, D. D. C. Bradley, A. R. Brown, R. N. Marks, K. Mackay, R. H. Friend, P. L. Burns, and A. B. Holmes, "Light-emitting diodes based on conjugated polymers," *Nature*, vol. 347, no. 6293, pp. 539–541, 1990. 10.1038/347539a0.

[52] C. W. Tang and S. A. VanSlyke, "Organic electroluminescent diodes," *Applied Physics Letters*, vol. 51, no. 12, pp. 913–915, 1987.

[53] C. D. Muller, A. Falcou, N. Reckefuss, M. Rojahn, V. Wiederhirn, P. Rudati, H. Frohne, O. Nuyken, H. Becker, and K. Meerholz, "Multi-colour organic light-emitting displays by solution processing," *Nature*, vol. 421, no. 6925, pp. 829–833, 2003. 10.1038/nature01390.

[54] S. F. Tedde, J. Kern, T. Sterzl, J. Furst, P. Lugli, and O. Hayden, "Fully spray coated organic photodiodes," *Nano Lett*, vol. 9, no. 3, pp. 980–3, 2009.

[55] J. Shinar, *Organic Light-Emitting Devices: A Survey*. Springer, 2003.

[56] Y. Zhao, L. Duan, D. Zhang, L. Hou, J. Qiao, L. Wang, and Y. Qiu, "Small molecular phosphorescent organic light-emitting diodes using a spin-coated hole blocking layer," *Applied Physics Letters*, vol. 100, no. 8, p. 083304, 2012.

[57] F. Villani, P. Vacca, G. Nenna, O. Valentino, G. Burrasca, T. Fasolino, C. Minarini, and D. della Sala, "Inkjet printed polymer layer on flexible substrate for oled applications," *The Journal of Physical Chemistry C*, vol. 113, no. 30, pp. 13398–13402, 2009.

[58] J. Vucic, C. Kottke, S. Nerreter, K. Habel, A. Buttner, K. D. Langer, and J. W. Walewski, "230 Mbit/s via a wireless visible-light link based on OOK modulation of phosphorescent white LEDs," in *Optical Fiber Communication (OFC), collocated National Fiber Optic Engineers Conference, 2010 Conference on (OFC/NFOEC)*, pp. 1–3.

[59] P. A. Haigh, Z. Ghassemlooy, H. L. Minh, S. Rajbhandari, F. Arca, S. F. Tedde, O. Hayden, and I. Papakonstantinou, "Exploiting equalization techniques for improving data rates in organic optoelectronic devices for visible light communications," *Journal of Lightwave Technology*, vol. 30, no. 19, pp. 3081–3088, 2012.

[60] R. Das and P. Harrop, "Organic and printed electronics - forecasts, players and opportunites 2007-2027," report, IDTechEx, 2010.

[61] F. Arca, S. F. Tedde, M. Sramek, J. Rauh, P. Lugli, and O. Hayden, "Interface trap states in organic photodiodes," *Sci Rep*, vol. 3, p. 1324, 2013.

[62] R. Noriega, J. Rivnay, K. Vandewal, F. P. V. Koch, N. Stingelin, P. Smith, M. F. Toney, and A. Salleo, "A general relationship between disorder, aggregation and charge transport in conjugated polymers," *Nat Mater*, vol. 12, no. 11, pp. 1038–1044, 2013.

[63] P. A. Haigh, Z. Ghassemlooy, and I. Papakonstantinou, "1.4-Mb/s white organic LED transmission system using discrete multitone modulation," *IEEE Photonics Technology Letters*, vol. 25, no. 6, pp. 615–618, 2013.

[64] N. P. Vlannes and T. M. Lu, "Organic photonics: materials and devices strategy for computational and communication systems," in *Telesystems Conference, 1992. NTC-92., National*, pp. 9/7–915.

[65] J. Clark and G. Lanzani, "Organic photonics for communications," *Nat Photon*, vol. 4, no. 7, pp. 438–446, 2010. 10.1038/nphoton.2010.160.

[66] S. Valouch, M. Nintz, S. W. Kettlitz, N. S. Christ, and U. Lemmer, "Thickness-dependent transient photocurrent response of organic photodiodes," *IEEE Photonics Technology Letters*, vol. 24, no. 7, pp. 596–598, 2012.

[67] B. Arredondo, C. de Dios, R. Vergaz, G. del Pozo, and B. Romero, "High-bandwidth organic photodetector analyzed by impedance spectroscopy," *IEEE Photonics Technology Letters*, vol. 24, no. 20, pp. 1868–1871, 2012.

[68] L. Salamandra, G. Susanna, S. Penna, F. Brunetti, and A. Reale, "Time-resolved response of polymer bulk-heterojunction photodetectors," *IEEE Photonics Technology Letters*, vol. 23, no. 12, pp. 780–782, 2011.

[69] E. S. Zaus, S. Tedde, J. Furst, D. Henseler, and G. H. Dohler, "Dynamic and steady state current response to light excitation of multilayered organic photodiodes," *Journal of Applied Physics*, vol. 101, no. 4, pp. 044501–044501–7, 2007.

[70] I. A. Barlow, T. Kreouzis, and D. G. Lidzey, "High-speed electroluminescence modulation of a conjugated-polymer light emitting diode," *Applied Physics Letters*, vol. 94, no. 24, pp. 243301–3, 2009.

[71] H. Sasabe, J.-i. Takamatsu, T. Motoyama, S. Watanabe, G. Wagenblast, N. Langer, O. Molt, E. Fuchs, C. Lennartz, and J. Kido, "High-efficiency blue and white organic light-emitting devices incorporating a blue iridium carbene complex," *Advanced Materials*, vol. 22, no. 44, pp. 5003–5007, 2010.

[72] T. Chiba, Y.-J. Pu, R. Miyazaki, K.-i. Nakayama, H. Sasabe, and J. Kido, "Ultra-high efficiency by multiple emission from stacked organic light-emitting devices," *Organic Electronics*, vol. 12, no. 4, pp. 710–715, 2011.

[73] S. Sze and K. Ng, *Physics of semiconductor devices*. John Wiley & Sons Inc., 3rd ed., 2007.

[74] S. Pimputkar, J. S. Speck, S. P. DenBaars, and S. Nakamura, "Prospects for LED lighting," *Nat Photon*, vol. 3, no. 4, pp. 180–182, 2009. 10.1038/nphoton.2009.32.

[75] F. A. Ponce and D. P. Bour, "Nitride-based semiconductors for blue and green light-emitting devices," *Nature*, vol. 386, no. 6623, pp. 351–359, 1997. 10.1038/386351a0.

[76] B. Saleh and M. Teich, *Fundamentals of Photonics*. John Wiley & Sons, 2007.

[77] E. Schubert, *Light-Emitting Diodes*. Boston Univ., 2002.

[78] S. Chuang, *Physics of Photonic Devices*. Wiley, 2012.

[79] U. Ozgur, H. Liu, L. Xing, X. Ni, and H. Morkoc, "Gan-based light-emitting diodes: Efficiency at high injection levels," *Proceedings of the IEEE*, vol. 98, no. 7, pp. 1180–1196, 2010.

[80] W. Shockley, "The theory of p-n junctions in semiconductors and p-n junction transistors," *The Bell System Technical Journal*, vol. XXVIII, pp. 335–600, 1949.

[81] F. Trager, *Springer Handbook of Lasers and Optics*. Springer, 2012.

[82] H. Le Minh, Z. Ghassemlooy, A. Burton, and P. A. Haigh, "Equalization for organic light emitting diodes in visible light communications," 2011.

[83] A. Fox, *Optical Properties of Solids*. Oxford University Press, 2001.

[84] K. Myny, E. van Veenendaal, G. H. Gelinck, J. Genoe, W. Dehaene, and P. Heremans, "An 8-bit, 40-instructions-per-second organic microprocessor on plastic foil," *Solid-State Circuits, IEEE Journal of*, vol. 47, no. 1, pp. 284–291, 2012.

[85] G. E. Moore, "Cramming more components onto integrated circuits," *Proceedings of the IEEE*, vol. 86, no. 1, pp. 82–85, 1998.

[86] J. Clayden, N. Greeves, and S. Warren, *Organic Chemistry*. OUP Oxford, 2012.

[87] P. Atkins and J. de Paula, *Physical Chemistry*. W. H. Freeman, 2009.

[88] J. Frenkel, "On the transformation of light into heat in solids. i," *Physical Review*, vol. 37, no. 1, pp. 17–44, 1931. PR.

[89] J. Frenkel, "On the transformation of light into heat in solids. ii," *Physical Review*, vol. 37, no. 10, pp. 1276–1294, 1931. PR.

[90] G. H. Wannier, "The structure of electronic excitation levels in insulating crystals," *Physical Review*, vol. 52, no. 3, pp. 191–197, 1937. PR.

[91] W. Brutting, *Physics of Organic Semiconductors*. Wiley, 2006.

[92] M. Pope and C. Swenberg, *Electronic processes in organic crystals and polymers*. Oxford University Press, 1999.

[93] Y. Roichman and N. Tessler, "Generalized einstein relation for disordered semiconductors—implications for device performance," *Applied Physics Letters*, vol. 80, no. 11, pp. 1948–1950, 2002.

[94] L. G. Kaake, P. F. Barbara, and X. Y. Zhu, "Intrinsic charge trapping in organic and polymeric semiconductors: A physical chemistry perspective," *The Journal of Physical Chemistry Letters*, vol. 1, no. 3, pp. 628–635, 2010.

[95] A. Miller and E. Abrahams, "Impurity conduction at low concentrations," *Physical Review*, vol. 120, no. 3, pp. 745–755, 1960. PR.

[96] C. Brabec, N. Sariciftci, and J. Hummelen, "Plastic solar cells," *Adv. Funct. Mater.*, vol. 11, no. 15, 2001.

[97] P. A. Haigh, Z. Ghassemlooy, I. Papakonstantinou, F. Arca, S. F. Tedde, O. Hayden, and S. Rajbhandari, "A MIMO-ANN system for increasing data rates in organic visible light communications systems," in *IEEE ICC 2013 - Wireless Communications Symposium (ICC'13 WCS)*.

[98] F. Eder, H. Klauk, M. Halik, U. Zschieschang, G. Schmid, and C. Dehm, "Organic electronics on paper," *Applied Physics Letters*, vol. 84, no. 14, pp. 2673–2675, 2004.

[99] T. Someya, "Flexible electronics: Tiny lamps to illuminate the body," *Nat Mater*, vol. 9, no. 11, pp. 879–880, 2010. 10.1038/nmat2886.

[100] Z. B. Wang, M. G. Helander, J. Qiu, D. P. Puzzo, M. T. Greiner, Z. M. Hudson, S. Wang, Z. W. Liu, and Z. H. Lu, "Unlocking the full potential of organic light-emitting diodes on flexible plastic," *Nat Photon*, vol. 5, no. 12, pp. 753–757, 2011.

[101] T.-H. Han, Y. Lee, M.-R. Choi, S.-H. Woo, S.-H. Bae, B. H. Hong, J.-H. Ahn, and T.-W. Lee, "Extremely efficient flexible organic light-emitting diodes with modified graphene anode," *Nat Photon*, vol. 6, no. 2, pp. 105–110, 2012.

[102] J. Lambert, *Photometria sive de mensura et gradibus luminis colorum et umbrae*. Vidvae Eberhardi Klett, 1760.

[103] D. C. O'Brien, L. Zeng, H. Le-Minh, G. Faulkner, J. W. Walewski, and S. Randel, "Visible light communications: Challenges and possibilities," in *Personal, Indoor and Mobile Radio Communications, 2008. PIMRC 2008. IEEE 19th International Symposium on*, pp. 1–5.

[104] C. L. Mulder, K. Celebi, K. M. Milaninia, and M. A. Baldo, "Saturated and efficient blue phosphorescent organic light emitting devices with lambertian angular emission," *Applied Physics Letters*, vol. 90, no. 21, p. 211109, 2007.

[105] S. Rajbhandari, *Application of wavelets and artificial neural network for indoor optical wireless communication systems*. Thesis, 2010.

[106] L. Couch, *Digital and Analog Communication Systems*. Prentice Hall, 2007.

[107] A. Carlson, P. Crilly, and P. Crilly, *Communication Systems*. McGraw-Hill Higher Education, 2009.

[108] J. Proakis, *Digital Communications*. New York: McGraw-Hill, 2004.

[109] G. L. Turin, "An introduction to matched filters," *Information Theory, IRE Transactions on*, vol. 6, no. 3, pp. 311–329, 1960.

[110] S. Sheikh Muhammad, T. Javornik, I. Jelovcan, Z. Ghassemlooy, and E. Leitgeb, "Comparison of hard-decision and soft-decision channel coded m-ary ppm performance over free space optical links," *European Transaction on Telecommunications*, pp. 12, DOI: 10.1002/ett.1343, 2008.

[111] Z. Ghassemlooy, W. Popoola, and S. Rajbhandari, *Optical Wireless Communications: System and Channel Modelling*. CRC PressINC, 2012.

[112] J. Proakis, *Wiley encyclopedia of telecommunications*. Wiley-Interscience, 2003.

[113] T. Ohtsuki, "Turbo-coded atmospheric optical communication systems," in *Communications, 2002. ICC 2002. IEEE International Conference on*, vol. 5, pp. 2938–2942 vol.5.

[114] A. J. Phillips, R. A. Cryan, and J. M. Senior, "An optically preamplified intersatellite ppm receiver employing maximum likelihood detection," *Photonics Technology Letters, IEEE*, vol. 8, no. 5, pp. 691–693, 1996.

[115] S. Rajbhandari, Z. Ghassemlooy, and M. Angelova, "Bit error performance of diffuse indoor optical wireless channel pulse position modulation system employing artificial neural networks for channel equalisation," *IET Optoelectronics*, vol. 3, no. 4, pp. 169–179, 2009.

[116] S. Haykin, *Communication Systems, 4th Ed.* Wiley India Pvt. Limited, 2008.

[117] K. Samaras, A. M. Street, D. O"Brien, and D. J. Edwards, "Error rate evaluation of wireless infrared links," in *Communications, 1998. ICC 98. Conference Record. 1998 IEEE International Conference on*, vol. 2, pp. 826–831 vol.2.

[118] W. S. McCulloch and W. Pitts, "A logical calculus of the ideas immanent in nervous activity," *The Bulletin of Mathematical Biophysics*, vol. 5, no. 4, pp. 115–133, 1943.

[119] F. Rosenblatt, "Principles of neurodynamics," 1962.

[120] J. Anderson, E. Rosenfeld, and A. Pellionisz, *Neurocomputing*. MIT Press, 1993.

[121] L. J. Cao and F. E. H. Tay, "Support vector machine with adaptive parameters in financial time series forecasting," *Neural Networks, IEEE Transactions on*, vol. 14, no. 6, pp. 1506–1518, 2003.

[122] S. C. B. Lo, S. L. A. Lou, L. Jyh-Shyan, M. T. Freedman, M. V. Chien, and S. K. Mun, "Artificial convolution neural network techniques and applications for lung nodule detection," *Medical Imaging, IEEE Transactions on*, vol. 14, no. 4, pp. 711–718, 1995.

[123] B. Widrow and R. Winter, "Neural nets for adaptive filtering and adaptive pattern recognition," *Computer*, vol. 21, no. 3, pp. 25–39, 1988.

[124] S. Haykin, *Neural networks: A comprehensive foundation*. New Jersey, USA: Prentice Hall, 2nd ed., 1998.

[125] K. Hornik, M. Stinchcombe, and H. White, "Multilayer feedforward networks are universal approximators," *Neural Networks*, vol. 2, no. 5, pp. 359 – 366, 1989.

[126] S.-I. Amari and A. Cichocki, "Adaptive blind signal processing-neural network approaches," *Proceedings of the IEEE*, vol. 86, no. 10, pp. 2026–2048, 1998.

[127] L. Behera, S. Kumar, and A. Patnaik, "On adaptive learning rate that guarantees convergence in feedforward networks," *IEEE Transactions on Neural Networks*, vol. 17, no. 5, pp. 1116–1125, 2006.

[128] A. Toledo, M. Pinzolas, J. J. Ibarrola, and G. Lera, "Improvement of the neighborhood based levenberg-marquardt algorithm by local adaptation of the learning coefficient," *IEEE Trans Neural Netw*, vol. 16, no. 4, pp. 988–92, 2005.

[129] S. Rajbhandari, J. Faith, Z. Ghassemlooy, and M. Angelova, "Comparative study of classifiers to mitigate intersymbol interference in diffuse indoor optical wireless communication links," *Optik - International Journal for Light and Electron Optics*, no. 0, 2013.

[130] S. Trenn, "Multilayer perceptrons: Approximation order and necessary number of hidden units," *Neural Networks, IEEE Transactions on*, vol. 19, no. 5, pp. 836–844, 2008. 1045-9227.

[131] H. Zhang, W. Choy, and K. Li, "Blue organic LEDs with improved power efficiency," *IEEE Transactions on Electron Devices*, vol. 57, no. 1, pp. 125–128, 2010.

[132] H. Sasabe, K. Minamoto, Y.-J. Pu, M. Hirasawa, and J. Kido, "Ultra high-efficiency multi-photon emission blue phosphorescent OLEDs with external quantum efficiency exceeding 40%," *Organic Electronics*, vol. 13, no. 11, pp. 2615–2619, 2012.

[133] C. Waechter, D. Michaelis, and N. Danz, "Approaches for tailoring organic LED emission patterns by microoptics arrays," in *Solid-State and Organic Lighting*, Optical Society of America.

[134] T. Bocksrocker, J. B. Preinfalk, J. Asche-Tauscher, A. Pargner, C. Eschenbaum, F. Maier-Flaig, and U. Lemme, "White organic light emitting diodes with enhanced internal and external outcoupling for ultra-efficient light extraction and lambertian emission," *Optics Express*, vol. 20, no. 106, pp. A932–A940, 2012.

[135] P. Freitag, A. A. Zakhidov, B. Luessem, A. Zakhidov, and K. Leo, "Lambertian white top-emitting organic light emitting device with carbon nanotube cathode," *Journal of Applied Physics*, vol. 112, no. 11, pp. 114505–114505–5, 2012.

[136] H. T. Nicolai, M. Kuik, G. A. Wetzelaer, B. de Boer, C. Campbell, C. Risko, J. L. Bredas, and P. W. Blom, "Unification of trap-limited electron transport in semiconducting polymers," *Nat Mater*, vol. 11, no. 10, pp. 882–7, 2012.

[137] K. Szczerba, P. Westbergh, E. Agrell, M. Karlsson, P. A. Andrekson, and A. Larsson, "Comparison of intersymbol interference power penalties for OOK and 4-PAM in short-range optical links," *Journal of Lightwave Technology*, vol. 31, no. 22, pp. 3525–3534, 2013.

[138] A. R. Hayes, *Digital Pulse Interval Modulation for Indoor Optical Wireless Communication Systems*. Phd, 2002.

[139] ThorLabs, "PDA36A Si switchable gain detector," 2012.

[140] D. Dilaura, K. Houser, R. Mistrick, and G. Steffy, *IES Lighting Handbook*. Illuminating Engineering.

[141] F. D. Waldhauer, "Quantized feedback in an experimental 280-Mb/s digital repeater for coaxial transmission," *IEEE Transactions on Communications*, vol. 22, no. 1, pp. 1–5, 1974.

[142] K. Burse, R. N. Yadav, and S. C. Shrivastava, "Channel equalization using neural networks: A review," *IEEE Transactions on Systems, Man, and Cybernetics, Part C (Applications and Reviews)*, vol. 40, no. 3, pp. 352–357, 2010.

[143] S. Rajbhandari, Z. Ghassemlooy, and D. Lee, "Wavelet-artificial neural network receiver for indoor optical wireless communications," *Journal of Lightwave Technology*, vol. 29, no. 17, pp. 2651–2659, 2011.

[144] C. Soci, I.-W. Hwang, C. Yang, D. Moses, Z. Zhu, D. Waller, R. Gaudiana, C. J. Brabec, and A. J. Heeger, "Charge carrier photogeneration and transport properties of a novel low-bandgap conjugated polymer for organic photovoltaics," pp. 63340D–63340D, 2006. 10.1117/12.680781.

[145] F. Arca, M. Sramek, S. F. Tedde, P. Lugli, and O. Hayden, "Near-infrared organic photodiodes," *IEEE Journal of Quantum Electronics*, vol. 49, no. 12, pp. 1016–1025, 2013.

[146] A. H. Azhar, T. Tran, and D. O'Brien, "A gigabit/s indoor wireless transmission using MIMO-OFDM visible-light communications," *IEEE Photonics Technology Letters*, vol. 25, no. 2, pp. 171–174, 2013.

[147] W.-W. Tsai, Y.-C. Chao, E.-C. Chen, H.-W. Zan, H.-F. Meng, and C.-S. Hsu, "Increasing organic vertical carrier mobility for the application of high speed bilayered organic photodetector," *Applied Physics Letters*, vol. 95, no. 21, p. 213308, 2009.

[148] K. Dambul, D. O'Brien, and G. Faulkner, "Indoor optical wireless MIMO system with an imaging receiver," *IEEE Photonics Technology Letters*, vol. 23, no. 2, pp. 97–99, 2011.

[149] A. Azhar, T.-A. Tran, and D. O'Brien, "Demonstration of high-speed data transmission using MIMO-OFDM visible light communications," *IEEE GLOBECOM 2010 Workshops (GC Wkshps)*, pp. 1052 –1056, 2010.

[150] L. Zeng, D. O'Brien, H. Minh, G. Faulkner, K. Lee, D. Jung, Y. Oh, and E. Won, "High data rate multiple input multiple output (MIMO) optical wireless communications using white led lighting," *IEEE Journal on Selected Areas in Communications*, vol. 27, no. 9, pp. 1654–1662, 2009.

[151] R. Mesleh, R. Mehmood, H. Elgala, and H. Haas, "Indoor MIMO optical wireless communication using spatial modulation," in *IEEE International Conference on Communications (ICC) 2010*, pp. 1–5.

[152] T. Fath, M. Di Renzo, and H. Haas, "On the performance of space shift keying for optical wireless communications," in *IEEE GLOBECOM 2010 Workshops (GC Wkshps)*, pp. 990–994.

[153] Y. A. Alqudah and M. Kavehrad, "MIMO characterization of indoor wireless optical link using a diffuse-transmission configuration," *IEEE Transactions on Communications*, vol. 51, no. 9, pp. 1554–1560, 2003.

[154] H. Klauk, *Organic Electronics: Materials, Manufacturing, and Applications*. Wiley, 2006.

[155] K. K. Sarma and A. Mitra, "Ann based rayleigh multipath fading channel estimation of a mimo-ofdm system," in *First Asian Himalayas International Conference onInternet, 2009. AH-ICI 2009*, pp. 1–5.

[156] L. Zhang and X. Zhang, "Mimo channel estimation and equalization using three-layer neural networks with feedback," *Tsinghua Science and Technology*, vol. 12, no. 6, pp. 658–662, 2007.

[157] J. Barry, J. Kahn, W. Krause, E. Lee, and D. Messerschmitt, "Simulation of multipath impulse response for indoor wireless optical channels," *IEEE Journal on Selected Areas in Communications*, vol. 11, no. 3, pp. 367 – 379, 1993.

[158] Z. Ghassemlooy, P. A. Haigh, F. Arca, S. F. Tedde, O. Hayden, I. Papakonstantinou, and S. Rajbhandari, "Visible light communications: 3.75 mbits/s data rate with a 160 khz bandwidth organic photodetector and artificial neural network equalization [invited]," *Photon. Res.*, vol. 1, no. 2, pp. 65–68, 2013.

[159] P. A. Haigh, F. Bausi, Z. Ghassemlooy, I. Papakonstantinou, H. Le Minh, C. Fléchon, and F. Cacialli, "Visible light communications: real time 10 mb/s link with a low bandwidth polymer light-emitting diode," *Optics Express*, vol. 22, no. 3, pp. 2830–2838, 2014.

[160] P. A. Haigh, Z. Ghassemlooy, S. Rajbhandari, and I. Papakonstantinou, "Visible light communications using organic light emitting diodes," *IEEE Communications Magazine*, vol. 51, no. 8, pp. 148–154, 2013.

[161] S. U. H. Qureshi, "Adaptive equalization," *Proceedings of the IEEE*, vol. 73, no. 9, pp. 1349–1387, 1985.

[162] S. Reineke, F. Lindner, G. Schwartz, N. Seidler, K. Walzer, B. Lussem, and K. Leo, "White organic light-emitting diodes with fluorescent tube efficiency," *Nature*, vol. 459, no. 7244, pp. 234–238, 2009. 10.1038/nature08003.

[163] P. A. Haigh, Z. Ghassemlooy, I. Papakonstantinou, and H. L. Minh, "2.7 mb/s with a 93-khz white organic light emitting diode and real time ANN equalizer," *IEEE Photonics Technology Letters*, vol. 25, no. 17, pp. 1687–1690, 2013.

[164] F. Chang, K. Onohara, and T. Mizuochi, "Forward error correction for 100 G transport networks," *IEEE Communications Magazine*, vol. 48, no. 3, pp. S48–S55, 2010.